



Doctoral Programme in Electrochemistry. Science and Technology

Autónoma University of Madrid

DOCTORAL THESIS

Development of Redox Electrolytes and their Application in New Electrochemical Energy Storage Devices

**Desarrollo de Electrolitos Redox para su Aplicación en Nuevos
Dispositivos Electroquímicos de Almacenamiento de Energía**

A thesis submitted to Autónoma University of Madrid in fulfilment of the requirements for the degree of Doctor of Philosophy

by:

Paula Navalpotro Molina

Supervisors:

Dr. Rebeca Marcilla García

Dr. Jesús Palma del Val

Electrochemical Processes Unit –IMDEA Energy Institute

Academic tutor:

Dr. Pilar Ocón Esteban

Autónoma University of Madrid

Madrid, 2018

Dedicated to my family

Acknowledgments

Now that the end of this PhD period is near, it is time to thank all the people who have helped me during these years, teaching me and making me grow professionally and personally, since they have made it possible for me to get here. Considering how personal it is, please, let me continue in my own language.

En primer lugar, quiero agradecer a mis directores Dra. Rebeca Marcilla y Dr. Jesús Palma haberme dado la oportunidad de trabajar a su lado, el tiempo y paciencia invertidos en enseñarme y su ayuda y consejo a nivel personal y profesional. *Muchas gracias*. En especial, me gustaría resaltar el gran ejemplo que Rebeca ha sido para mí como mujer e investigadora. Gracias Rebeca por aquel “hazte grande Paula, saldrá bien” que marcó un antes y un después para mí. También me gustaría agradecer a Dr. Marc Anderson su cercanía, su consejo y sus ideas con ese “American style” que siempre me han hecho pensar.

Quiero agradecer a Dra. Pilar Ocón, mi tutora académica, su gran disponibilidad para ayudarme durante este tiempo y en especial estos últimos meses.

Me gustaría agradecer al grupo de investigación PATH (Products and Processes of Applied Thermodynamics) del CICECO-Universidad de Aveiro por acogerme durante mi estancia en Portugal y en especial al Prof. Joao A. P. Coutinho, Dra. Mara G. Freire y Dra. Catarina S. Neves por enseñarme y ayudarme en el desarrollo de sistemas bifásicos acuosos.

Muchas gracias a los miembros de la unidad de Procesos Electroquímicos de IMDEA Energía. Desde el primer día me sentí muy cómoda trabajando con vosotros y sin duda voy a echar de menos trabajar en un grupo tan especial. Quiero agradecer a Dr. Enrique García-Quismondo su ayuda y consejo, así como los momentos y charlas divertidas que hemos tenido. También quiero agradecer a Dr. Afshin Pendashteh, que ha sido un ejemplo de investigador y gran compañero, dentro y fuera de IMDEA. Agradezco a Dr. Edgar Ventosa y Dr. Julio Lado su ayuda y las conversaciones científicas y no científicas que hemos tenido durante el último año, *ha sido un placer*. Echando la vista atrás, recuerdo al ahora doctor Girum A. Tiruye, entrando con su “flow” y haciendo electrodos juntos, con “because I’m happy...” como B.S.O. de fondo, gracias por tu ayuda y tu cariño Girum. Así mismo quiero agradecer a Evgeny su cariño y apoyo, ¡ya casi lo tenemos rusito! A David, Jaime, Mayte y Antonio gracias por los buenos momentos, el trabajo día a día en el lab y las charlas de todo tipo. Mucho ánimo chic@s ¡a por ello! Por otro lado, espero haber ayudado y deseo mucha suerte en su futuro a Diego, Pablo, Andrés y especialmente a Noemí y Carlos, gracias por vuestra ayuda chicos.

No quiero extenderme mucho, pero he tenido la fortuna de compartir este periodo con una gran amiga, que ha sido clave para mí; Cleis, gracias por tu apoyo, cariño y consejo en los momentos buenos y regulares, por las conversaciones telepáticas y sobre electroquímica, las risas descontroladas...bueno qué te voy a decir, sencillamente seguiremos sumando, *muchas gracias*.

Quiero agradecer a los míticos imdean@s, las risas, el buen ambiente y los buenos recuerdos que me llevo de esta etapa.

Muchas gracias también a “mis compis”, Adrián, Vicent, Aser, Alex fue una suerte encontraros en el camino y por supuesto a María y Nerea, grandes futuras doctoras, por su apoyo y cariño y por las aventuras que vendrán, *gracias compis*.

Gracias también a mis amigos Jesús, Adrián y Juan por animarme y hacerme pasar siempre buenos ratos. Por supuesto, este agradecimiento también va para mi amiga Leticia, la distancia no es un impedimento si la amistad es real y 26 años no son nada, *gracias Leti*, aquí te espero.

Especialmente quiero dar las gracias a Nacho, porque empezaste siendo mi compañero de enfrente y has terminado cambiando mi vida y haciendo que estos años fueran casi tan increíbles como tú. Gracias por tu apoyo incondicional, por tu comprensión y paciencia con mis jaleos mentales electroquímicos, por estar ahí siempre en lo bueno y malo, por el sacrificio y tu voluntad de mejorar cada día, por tu esfuerzo por hacerme sonreír y reír incluso en los días grises, por hacer que sueñe despierta. *GRACIAS Nachete* por estos años y por todo lo que vendrá.

Por último, aunque por supuesto no con menos intensidad, quiero dar las gracias a mi familia, a mis tíos, Pepe, Carlos, Marivi, Araceli, M^aLuz y Juan, a Ciri, a mi abuela Viti, a mi primo Alex, a mi tata/chachita Raquel y a los que ya no están pero siguen conmigo. Gracias por vuestro apoyo y cariño desmedido, que me hacen fuerte y sentir orgullosa de ser una Navalpotro Molina. Estos apellidos los comparto con mi hermano Mario, a quien solo puedo dar las gracias por ser el mejor chache, por empujarme siempre hacia adelante y creer en mí. Evidentemente si he llegado hasta aquí, ha sido gracias a mis padres, Juana y Cecilio y a su amor, apoyo y ayuda de manera incondicional; por su esfuerzo y sacrificio para darme siempre lo mejor; por su comprensión, paciencia y confianza en mí, por enseñarme a mejorar cada día y el gusto por el trabajo bien hecho y tantas otras cosas...muchas gracias por todo se queda corto.

GRACIAS a todos de corazón

Finalmente me gustaría acabar con una reflexión que escuché hace tiempo, he corroborado a lo largo de esta tesis y que me repito a mí misma de vez en cuando:

En la vida, el conocimiento y la habilidad siempre suman, pero la actitud multiplica.

This thesis was financed by a personnel grant through the “FPI” program “Ayudas para contratos predoctorales para la formación de doctores” (BES-2013-063098) from the Spanish Government.

TABLE of CONTENT

Abstract	i
Resumen	v
CHAPTER 1: INTRODUCTION	1
1.1 Renewable Energy System.....	3
1.2 Energy Storage	4
1.2.1 Applications.....	4
1.2.2 Technologies.....	6
1.2.2.1 Mechanical Energy Storage Systems.....	6
1.2.2.2 Thermal Energy Storage Systems.....	7
1.2.2.3 Chemical Energy Storage Systems.....	8
1.2.2.4 Electrical Energy Storage Systems.....	8
1.2.2.5 Electrochemical Energy Storage Systems.....	9
1.3 Electrochemical Energy Storage.....	11
1.3.1 Supercapacitors.....	12
1.3.1.1 Types of Supercapacitors.....	13
Electrochemical Double Layer Capacitors (EDLC).....	15
Pseudocapacitors.....	21
Hybrid SCs.....	23
1.3.2 Batteries.....	26
1.3.2.1 Conventional Redox Flow Batteries (RFB).....	27
1.3.2.2 Next Generation in Redox Flow Battery Systems.....	34
1.4 Organic Redox Molecules in Energy Storage.....	37
1.4.1 Organic Redox Molecules for Supercapacitors.....	40
1.4.2 Organic Redox Molecules as Active Species for RFBs.....	44
1.5 Challenges in the Development of New Redox Electrolytes.....	50
1.6 References	53
CHAPTER 2: OBJECTIVES	61

CHAPTER 3: ELECTROCHEMICAL STUDY OF HYBRID SUPERCAPACITORS BY USING para-BENZOQUINONE IONIC LIQUID REDOX ELECTROLYTE..... 67

3.1	Introduction.....	69
3.2	Results and Discussion.....	73
3.2.1	Electrochemical Characterization of Electrolytes.....	73
3.2.2	Electrochemical Characterization of Hybrid Supercapacitors.....	75
3.2.2.1	Cyclic Voltammetry Experiments.....	76
3.2.2.2	Galvanostatic Charge-Discharge Experiments.....	79
3.2.2.3	Cycling experiments.....	84
3.2.3	Insights into the Energy Storage Mechanism by Electrochemical Impedance Spectroscopy Study.....	86
3.3	Conclusions.....	100
3.4	Experimental.....	102
3.4.1	Electrode and Electrolyte Preparation.....	102
3.4.2	Assembly of Supercapacitors.....	103
3.4.3	Electrochemical Characterization of Supercapacitors.....	104
3.4.3.1	Cyclic voltammetry experiments.....	104
3.4.3.2	Galvanostatic Charge-Discharge experiments.....	105
3.4.3.3	Electrochemical Impedance Spectroscopy Experiments.....	107
3.5	References.....	109

CHAPTER 4: MEMBRANE-FREE REDOX FLOW BATTERIES BY USING TWO IMMISCIBLE REDOX ELECTROLYTES 113

4.1	Introduction.....	115
4.2	Results and Discussion.....	122
4.2.1	Proof-of-concept of Membrane-Free Battery.....	122
4.2.1.1	Electrochemical Characterization of Redox Electrolytes.....	123
4.2.1.2	Assembly and Electrochemical Characterization of Membrane-Free Battery.....	126
4.2.2	Versatility of Membrane-Free Redox Flow Battery Concept.....	134
4.2.2.1	Electrochemical Characterization of Immiscible Electrolytes.....	137
4.2.2.2	Electrochemical Performance of Membrane-Free Redox Flow Batteries.....	145
4.3	Conclusions.....	157
4.4	Experimental.....	159
4.4.1	Reagents.....	159
4.4.2	Preparation of Electrolytes.....	159

4.4.3	Electrochemical characterization of redox electrolytes.....	160
4.4.4	Battery Assembly.....	162
4.4.5	Electrochemical Characterization of Membrane-Free RFB.....	163
4.5	References	165

CHAPTER 5: MEMBRANE-FREE REDOX FLOW BATTERIES BASED ON AQUEOUS BIPHASIC SYSTEMS..... 169

5.1	Introduction.....	171
5.2	Results and Discussion.....	173
5.2.1	Partitioning Characterization and Design of Aqueous Biphasic System (ABS) as Suitable Immiscible Electrolytes for Membrane-Free RFB.....	173
5.2.1.1	Phase Diagrams of ABS.....	173
5.2.1.2	Partition Coefficients of Organic Molecules in the ABS.....	177
5.2.2	Electrochemical characterization of redox-active ABS.....	180
5.2.3	Electrochemical Characterization of Total Aqueous Membrane-Free Battery based on an ABS	187
5.2.3.1	Polarization Experiments.....	192
5.2.3.2	Charge-Discharge Experiments.....	193
5.2.3.3	Self-discharge Phenomenon.....	194
5.2.3.4	Cycling Experiments.....	197
5.3	Conclusions.....	199
5.4	Experimental.....	201
5.4.1	Reagents.....	201
5.4.2	ABS Phase diagrams.....	202
5.4.3	Partition coefficients determination.....	203
5.4.4	Preparation of Redox-active ABS.....	204
5.4.5	Electrochemical characterization.....	204
	Electrochemical characterization of the electrolytes.....	204
	Assembly and Electrochemical characterization of the battery.....	205
5.5	References.....	207

CHAPTER 6: FINAL CONCLUSIONS AND RECOMMENDATIONS..... 209

6.1	Final Conclusions.....	211
6.2	Future Work and Recommendations	214

Abstract

Transportation and energy production activities based on fossil fuels have important environmental impacts. In order to minimize them, alternatives to fossil fuel vehicles and an efficient use of renewable energy resources are needed. Energy storage can provide a safe and cost-effective solution to the inherent irregular energy supply from those sources and to the massive implementation of the electric vehicle. Thus, remarkable investments are being done in the development of electrochemical energy storage technologies, such as supercapacitors and batteries, due to their high efficiency, variety of power and energy rates, long cycle life and low maintenance. One of the main challenges in this field is to improve their energy density while reducing their cost.

With respect to supercapacitors, the development of redox electrolytes for hybrid devices is becoming one of the hottest topics, since they are an easier alternative than the complex development of new electrode materials. In this way, by simple dissolution of active species into the supporting electrolyte, important parameters such as capacity, energy and power density, can be enhanced. Regarding Redox Flow Batteries, different approaches are being investigated such as the replacement of vanadium species by organic redox molecules or the substitution of problematic ion-selective membranes by less expensive separators.

Despite all the scientific efforts, many challenges still remain to be faced both in supercapacitors (SCs) and Redox Flow Batteries (RFB). This thesis addresses some of them and aims to provide new insights to the matter.

The aim of this thesis is to contribute to the field of electrochemical energy storage by developing new organic redox electrolytes with application in different devices. Specifically, the formulation of new redox electrolytes containing commercially available organic molecules has been studied, as well as their electrochemical characterization. Thus, important parameters such as solubility, redox potential, reversibility, kinetics and diffusion coefficients were determined. Moreover, the electrochemical performance of these new redox electrolytes in devices such as hybrid supercapacitors and in an innovative concept of Membrane-Free Redox Flow Battery was analyzed with the main goal of improving their performance.

This PhD thesis is organized in 6 different chapters whose content is described below:

Chapter 1 consists on an introduction in which the state-of-art and the current main challenges of the electrochemical energy storage devices, especially those containing redox electrolytes, are commented. In **chapter 2** the main objectives of this PhD thesis are described as well as the initial hypothesis and the scientific questions that are pursued to be answered. **Chapters 3, 4 and 5** contained the main scientific results related to the challenges and the objectives expounded previously, including the specific methodology and bibliography in each chapter.

In **chapter 3**, the effect of using a organic redox electrolyte based on ionic liquids on a hybrid SC was investigated. Thus, a solution of 0.4 M para-Benzoquinone (pBQ) in the ionic liquid (IL) N-butyl-N-methylpyrrolidinium bis(trifluoromethanesulfonyl) imide (PYR₁₄TFSI) was used as a redox electrolyte in hybrid supercapacitors. Two carbons with very different textural properties, Pica carbon and Vulcan carbon, were used as electrode material. Electrochemical performance of these energy storage systems was investigated by cyclic voltammetry (CV) and galvanostatic charge-discharge (CD). Unlike SCs with pure IL electrolyte, new battery-like features appeared in the CV curves and CD profiles. This electrochemical performance, associated with the faradaic contribution of the redox electrolyte, results in a significant improvement of the electrochemical performance of the hybrid system. For Vulcan carbon with low specific surface area ($S_{\text{BET}}=240 \text{ m}^2\cdot\text{g}^{-1}$), specific capacitance (C_s) and specific real energy (E_{real}) values as high as $70 \text{ F}\cdot\text{g}^{-1}$ and $10.3 \text{ Wh}\cdot\text{kg}^{-1}$ were obtained at $5 \text{ mA}\cdot\text{cm}^{-2}$ with hybrid SC operating at 3 V. This represents an increment of 300 % in C_s and E_{real} with respect to the SC based on pure PYR₁₄TFSI. For high surface area carbon such as Pica ($S_{\text{BET}}=2410 \text{ m}^2\cdot\text{g}^{-1}$), the addition of the redox quinone molecule resulted in a moderate enhancement, reaching values of $156 \text{ F}\cdot\text{g}^{-1}$ and $30 \text{ Wh}\cdot\text{kg}^{-1}$ under the same experimental conditions (36 % and 10 % increment, respectively).

Moreover, the energy storage mechanism of these hybrid devices was assessed in detail by Electrochemical Impedance Spectroscopy (EIS). In this thesis, EIS was used for the first time to analyse the energy storage mechanism in supercapacitors with non-aqueous electrolytes with organic redox molecules dissolved, as a function of the frequency and bias voltage.

In addition, a simple electrical model was developed to describe the behaviour of the supercapacitor with a very good correlation with the experimental results. This investigation provides useful information delving into the behaviour of the devices which is fundamental for their future practical applications.

In **chapter 4**, a new concept of Membrane-Free RFB that relies on the immiscibility of redox electrolytes and where the vanadium species are replaced by organic molecules was presented. It was demonstrated that the biphasic system formed by one acidic solution and one ionic liquid, both containing dissolved quinoyl redox-active species, behaves as a reversible battery without any membrane or separator. This proof-of-concept of Membrane-Free Battery exhibits an open circuit voltage (OCV) of 1.4 V with a high theoretical energy density of $22.5 \text{ Wh}\cdot\text{L}^{-1}$ and it is able to deliver 90 % of its theoretical capacity. Moreover, this battery shows excellent long-term performance with coulombic efficiency close to 100 % and energy efficiency of 70 % upon cycling.

In addition, the versatility of this concept was investigated. Hence, the electrochemical performance of 10 immiscible redox electrolytes based on different solvents such as propylene carbonate, 2-butanone or neutral media and containing different organic molecules such as TEMPO or substituted anthraquinones was explored. Those showing promising electrochemical performance were paired and used as anolyte and catholyte in Membrane-Free RFBs that exhibited different performance. For instance, a 50 % improved OCV (2.1 V), an operating voltage of 1.75 V and 35 % higher power density compared with the first battery were revealed in batteries with substituted anthraquinones. Moreover, cycling-life was evaluated over 300 cycles for a battery containing propylene carbonate-based anolyte achieving excellent (85 %) capacity retention. Thus, these results demonstrated the huge versatility and countless possibilities of this new Membrane-Free RFB concept which can be tailored to several applications with different requirements.

With the aim of extending the applicability of this new concept beyond the aqueous-nonaqueous combination, the feasibility of using Aqueous Biphasic Systems (ABS) was investigated in **chapter 5**. ABS in which the two immiscible phases are aqueous are a successful tool employed in extraction/separation processes. In this chapter, ABS containing one redox organic molecule selectively dissolved in each phase were

proposed as redox electrolytes for Membrane-Free RFB for the first time. In this concept, the cross-contamination typically occurring through the ineffective membranes is determined by the partition coefficients of the active molecules between the two phases. Thus, a series of ABS with different compositions and the partition of several redox organic molecules on these systems were tested. In addition, the electrochemistry of these redox-active immiscible phases was evaluated. Combining thermodynamics and electrochemistry, several redox ABS that might be used in Total Aqueous Membrane-Free RFB were proposed exhibiting theoretical battery voltages as high as 1.6 V. Among them, the ABS based on the polymer PEG₁₀₀₀ and containing methylviologen (MV) and 2,2,6,6-Tetramethyl-1-piperidinyloxy (TEMPO) as active species was selected to become an unprecedented Total Aqueous Membrane-Free Battery. When connected electrically, this redox-active ABS becomes a Membrane-Free Battery with an open circuit voltage (OCV) of 1.23 V, high peak power density (23 mW·cm⁻²) and excellent long-cycling performance (99.99 % capacity retention over 550 cycles). Moreover, essential aspects of this technology such as the crossover, controlled here by partition coefficients, and the inherent self-discharge phenomena were addressed for the first time. These results point out the potential of this pioneering Total Aqueous Membrane-Free RFB as a new energy storage technology.

Finally, this thesis includes a **chapter 6** in which general conclusions and future work are explained. In the **appendix A** the scientific contributions of this work are gathered. In the **appendix B**, the figures, tables and acronyms used in this thesis are listed.

Resumen

Las actividades de transporte y producción de energía basadas en combustibles fósiles tienen importantes impactos ambientales. Para minimizarlos, se necesitan alternativas a los vehículos con combustibles fósiles y un uso eficiente de las energías renovables. El almacenamiento de energía puede proporcionar una solución segura y económica para la inherente irregularidad en el suministro de energía de esas fuentes y para la implementación masiva del vehículo eléctrico. Por ello, se están llevando a cabo inversiones notables en el desarrollo de tecnologías de almacenamiento de energía electroquímica, como supercondensadores y baterías, debido a su alta eficiencia, variedad de potencia y energía, larga vida útil y bajo mantenimiento. Uno de los principales desafíos en este campo es mejorar la densidad de energía de los dispositivos y simultáneamente reducir su coste.

Con respecto a los supercondensadores, el desarrollo de electrolitos redox para dispositivos híbridos, se está convirtiendo en uno de los temas más candentes, ya que son una alternativa más fácil que el complejo desarrollo de nuevos materiales de electrodos. De esta forma, mediante la simple disolución de especies activas en el electrolito soporte, se pueden mejorar parámetros importantes tales como capacidad, energía y densidad de potencia. En relación a las Baterías de Flujo Redox, diferentes estrategias están siendo investigadas tales como el reemplazo del vanadio por moléculas redox orgánicas o la sustitución de las problemáticas membranas de intercambio iónico por separadores más asequibles económicamente.

A pesar de todos los esfuerzos científicos, todavía quedan algunos desafíos por enfrentar tanto en el campo de los supercondensadores (SC) híbridos como en el de las Baterías de Flujo Redox (BFR). Esta tesis aborda algunos de ellos y tiene como objetivo aportar nuevos conocimientos en esta materia.

En esta tesis, el objetivo es contribuir al campo del almacenamiento electroquímico de energía mediante el desarrollo de nuevos electrolitos redox con moléculas orgánicas y su aplicación en diferentes dispositivos. Específicamente, se ha estudiado la formulación de nuevos electrolitos redox que contienen moléculas orgánicas disponibles

comercialmente, así como su caracterización electroquímica. Así mismo, se determinaron parámetros importantes tales como solubilidad, potencial redox, reversibilidad, cinética y coeficientes de difusión. Además, se analizó el rendimiento electroquímico de estos nuevos electrolitos redox en dispositivos como los supercondensadores híbridos y en un concepto innovador de Baterías de Flujo Redox Sin Membrana con el objetivo principal de mejorar su funcionamiento. Esta tesis doctoral está organizada en 6 capítulos diferentes cuyo contenido se describe a continuación:

El **capítulo 1** consiste en una introducción en la que se comenta el estado del arte y los principales desafíos de los dispositivos de almacenamiento de energía electroquímicos, especialmente los que contienen electrolitos redox. En el **capítulo 2** se describen los principales objetivos de esta tesis doctoral, así como las hipótesis iniciales y las preguntas científicas que se quieren responder. Los **capítulos 3, 4 y 5** contienen los principales resultados científicos relacionados con los desafíos y los objetivos expuestos previamente, incluida la metodología y la bibliografía específicas en cada capítulo.

En el **capítulo 3**, se investigó el efecto del uso de un electrolito redox orgánico basado en líquido iónico en un SC híbrido. Para ello, se usó una disolución de para-benzoquinona 0,4 M (pBQ) en el líquido iónico (LI) N-butil-N-metilpirrolidinio bis(trifluorometanosulfonil) imida (PYR₁₄TFSI) como electrolito redox en supercondensadores híbridos. Dos materiales carbonosos con propiedades texturales muy diferentes, carbón Pica y carbón Vulcan, se emplearon como material de electrodo. El comportamiento electroquímico de estos sistemas de almacenamiento de energía se investigó mediante voltametría cíclica (CV) y carga-descarga galvanostática (CD). A diferencia de los SC con LI puro como electrolito, aparecieron nuevas características, similares a las de las baterías, en las curvas de CV y los perfiles de CD. Este comportamiento electroquímico, asociado con la contribución faradaica del electrolito redox, da como resultado una mejora significativa del rendimiento electroquímico del sistema híbrido. Para aquellos SC que contenían el carbón Vulcan con baja área superficial específica ($S_{BET} = 240 \text{ m}^2 \cdot \text{g}^{-1}$), se obtuvieron valores de capacitancia específica (C_s) y de energía real específica (E_{real}) de hasta $70 \text{ F} \cdot \text{g}^{-1}$ y $10,3 \text{ Wh} \cdot \text{kg}^{-1}$ a $5 \text{ mA} \cdot \text{cm}^{-2}$, respectivamente, con un voltaje de operación de 3 V. Esto representa un incremento de

300 % en C_s y E_{real} con respecto al SC basado en $PYR_{14}TFSI$ puro. Para los SC que contenían carbón de alta área superficial específica como Pica ($S_{BET} = 2410 \text{ m}^2 \cdot \text{g}^{-1}$), la adición de la molécula redox quinónica resultó en una mejora moderada que alcanzó valores C_s y E_{real} de $156 \text{ F} \cdot \text{g}^{-1}$ y $30 \text{ Wh} \cdot \text{kg}^{-1}$, respectivamente, bajo las mismas condiciones experimentales, lo que corresponde con un 36 % y 10 % de incremento, respectivamente.

Además, el mecanismo de almacenamiento de energía de estos dispositivos híbridos se evaluó en detalle mediante un estudio de Espectroscopía de Impedancia Electroquímica (EIE). En esta tesis por primera vez, la EIE se utilizó para analizar el mecanismo de almacenamiento de energía en supercondensadores con electrolitos no convencionales con moléculas redox orgánicas disueltas, en función de la frecuencia y el voltaje de polarización. Además, se desarrolló un modelo eléctrico simple para describir el comportamiento del supercondensador con una muy buena correlación con los resultados experimentales. Esta investigación proporciona información útil para profundizar en el comportamiento de los dispositivos que es fundamental para sus futuras aplicaciones prácticas.

En el **capítulo 4**, se presentó un nuevo concepto de Batería de Flujo Redox Sin Membrana que se basa en la inmiscibilidad de los electrolitos redox y donde las especies de vanadio son reemplazadas por moléculas orgánicas. Se demostró que el sistema bifásico formado por una disolución ácida acuosa y un líquido iónico, que contienen especies activas quinónicas, se comporta como una batería reversible sin membrana o separador. Esta prueba de concepto de Batería Sin Membrana exhibe un voltaje de circuito abierto de 1,4 V con una alta densidad de energía teórica de $22,5 \text{ Wh} \cdot \text{L}^{-1}$ y es capaz de descargar el 90 % de su capacidad teórica. Además, esta batería muestra un excelente funcionamiento a largo plazo con una eficiencia coulombica cercana al 100 % y una eficiencia energética del 70 % en los ensayos de ciclabilidad.

También, se investigó la versatilidad de este concepto. Para ello, se analizó el comportamiento electroquímico de 10 electrolitos redox inmiscibles basados en diferentes disolventes así como carbonato de propileno, 2-butanona o medios neutros con diferentes moléculas orgánicas tales como TEMPO o antraquinonas sustituidas. Aquellos que mostraron un comportamiento electroquímico prometedor se emparejaron y se usaron como anolito y catolito en Baterías de Flujo Redox Sin

Membrana que exhibieron diferentes comportamientos. Por ejemplo, en baterías con antraquinonas sustituidas como especie activa se obtuvo un voltaje a circuito abierto (VCA) con una mejora del 50 % (2,1 V), un voltaje de funcionamiento de 1,75 V y una densidad de potencia 35% mayor en comparación con la batería con la que se demostró el concepto. Además, la ciclabilidad se evaluó a lo largo de 300 ciclos para una batería que contenía un anolito basado en carbonato de propileno y se observó una excelente retención de la capacidad (85 %). Por lo tanto, estos resultados demostraron la gran versatilidad e innumerables posibilidades de este nuevo concepto de Batería Sin Membrana que puede ser ajustado a varias aplicaciones con diferentes requisitos.

Con el objetivo de extender la aplicabilidad de este nuevo concepto a otras combinaciones de electrolitos, además de las combinaciones de electrolito acuoso-no acuoso, en el **capítulo 5**, se investigó la viabilidad de utilizar sistemas acuosos bifásicos (SAB). Los SBA en los cuales las dos fases inmiscibles son acuosas, son una herramienta exitosa en procesos de extracción/separación. En este capítulo, los SAB con una molécula redox orgánica disuelta selectivamente en cada fase se propusieron, por primera vez, como electrolitos redox para una Batería de Flujo Redox Sin Membrana. En este concepto, la contaminación cruzada (*crossover*, en inglés) que se produce típicamente a través de las ineficaces membranas está determinada por los coeficientes de reparto de las moléculas activas entre las dos fases. Por ello, se probaron una serie de SAB con diferentes composiciones y se estudió el coeficiente de reparto de varias moléculas redox orgánicas en dichos sistemas. También se evaluó la electroquímica de estas fases inmiscibles con actividad redox. Combinando termodinámica y electroquímica, se propusieron varios SAB con actividad redox que podrían usarse en Baterías Redox de Flujo Sin Membrana Totalmente Acuosas, que presentaron voltajes teóricos de batería de hasta 1,6 V. Entre ellos, el SAB basado en el polímero PEG₁₀₀₀ con metilviologen (MV) y 2,2,6,6-Tetrametil-1-piperidiniloxi (TEMPO) como especies activas, se seleccionó para convertirse en una Batería Sin Membrana Totalmente Acuosa sin precedentes. Una vez conectado eléctricamente, este SAB con actividad redox se convierte en una Batería Sin Membrana con un voltaje a circuito abierto (VCA) de 1,23 V, una alta densidad de potencia máxima (23 mW·cm⁻²) y una excelente ciclabilidad (99,99% de retención de capacidad a lo largo de 550 ciclos). Además, por primera vez

fueron abordados aspectos esenciales de esta tecnología como el crossover, controlado aquí por los coeficientes de reparto, y el inherente fenómeno de autodescarga. Estos resultados subrayan el potencial de esta pionera Batería Sin Membrana Totalmente Acuosa como una nueva tecnología de almacenamiento de energía.

Finalmente, en esta tesis se ha incluido un último capítulo, **capítulo 6**, en el que se explican las conclusiones generales y el trabajo futuro. En el **apéndice A** se recogen las contribuciones científicas a las que ha dado lugar este trabajo. En el **apéndice B** se enumeran las figuras, tablas y acrónimos usados en esta tesis.

Chapter 1 . Introduction

1.1 Renewable Energy System

Energy is one of the main sources of socioeconomic development, welfare and progress. Since the energy production activities have especially important environmental impacts, it is crucial an advancement to reach an energy system which fulfills the techno-economical needs and conserves the ecosystems.

Behind the structural changes in the energy system there are three important drivers: secure energy supply, increasing competitiveness due to least-cost strategies and environmental concerns. The appearance of new technologies and resources generates new opportunities as well as increases the complexity and the number of challenges that have to be faced. The energy production from renewable sources is growing every year. For instance, today it represents around 9.5% of the global energy production and the outlook for the next decades predicts a relevant increase for the energy generation from wind and solar sources (Figure 1.1) ¹.

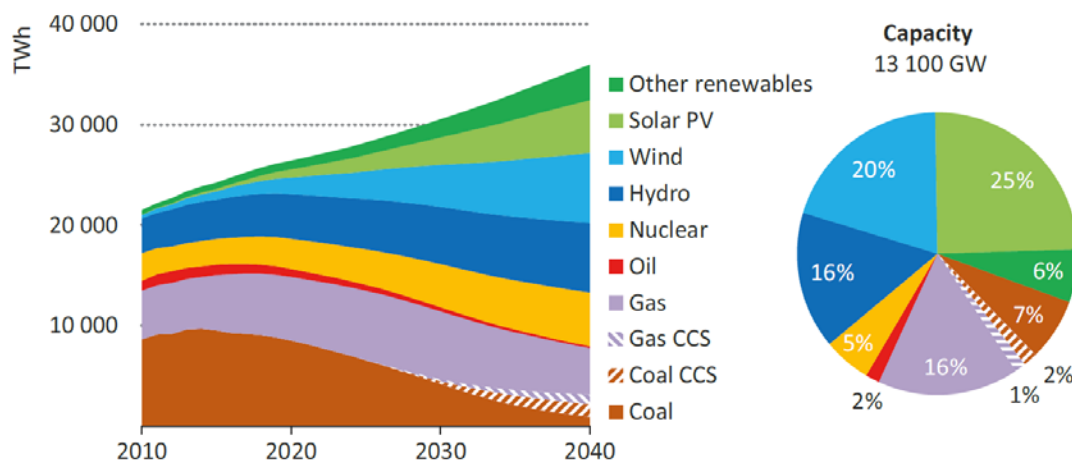


Figure 1.1. Outlook of the power generation by source (left) and the total installed capacity (right) in 2040 for a Sustainable Development Scenario (figure taken from¹).

However, the main drawback for the massive energy production from these sources is the volatile output of wind farms and photovoltaics due to its dependency on climatology. These intermittence and fluctuation in the production put the reliability of grid operation in risk ². In Figure 1.1 a forecast for the power generation by source in 2040 developed by the International Energy Agency is represented. In this sustainable development scenario, 45% of the total installed capacity comes from Solar PV and

Wind. Nevertheless, the power generation from these sources will be around 33%. This means an important part of the installed capacity is idle due to the periods of time of high energy consumption usually do not fit in with the intervals of production. In this situation, energy storage technologies emerges as a solution to counteract these shortcomings and are being intensively investigated globally ³.

1.2 Energy Storage

Energy storage is a very varied field with multiple technologies. The appearance of new requirements and applications has given rise to rapid change in some technologies. At the end of 2015 the global installed storage capacity was 146 GW and is expected to continue increasing in the next years ⁴.

1.2.1 Applications

The applications of the energy storage systems can be classified according to different criteria. Usually, applications of the energy storage technologies depend on the technical requirements based on terms of power rating, storage capacity, cycle life and storage time (seconds, hours, days...). Typical energy applications are defined as those in which a continuous supply of energy over a large period of time is needed ^{5,6}. In contrast, power applications require fast injection and absorption of energy but the operation time is usually much shorter. Typical energy applications include peak shifting or energy arbitrage. On the other hand, common power applications are frequency regulation or ramp rate control for intermittent renewable generation ⁷⁻⁹. A combination of power and energy requirements simultaneously is demanded by transport applications. Other classification can be done in which the applications are divided by the operational level. Thus, two different groups can be distinguished: generation/grid level and end-user level (Figure 1.2).

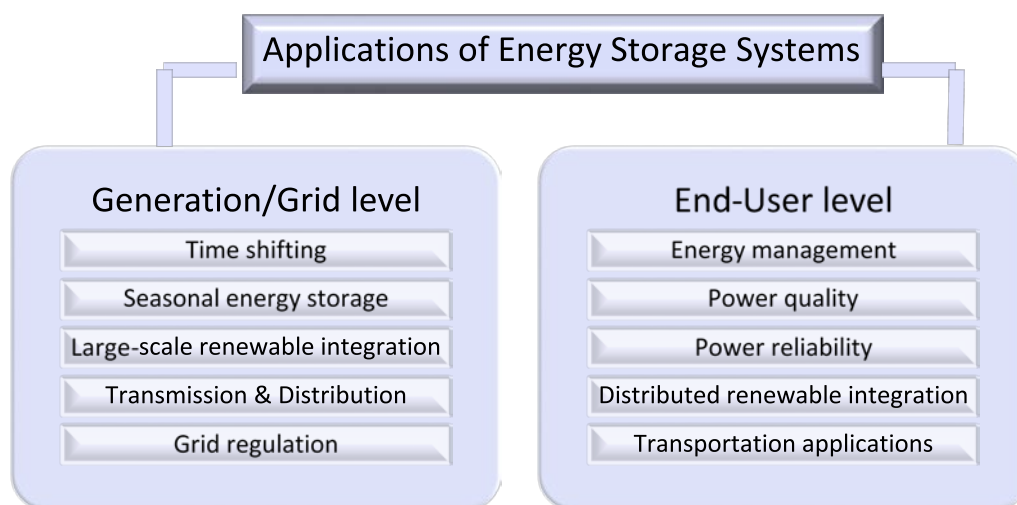


Figure 1.2. Applications of energy storage systems.

- **Generation/Grid Level:**

- Since the renewable sources have an intermittent inherent nature, the energy storage are indispensable systems to ensure the energy supply during time periods between hours and days.
- At this level, the storage systems also enable to supply energy and fulfill consumption peaks, power-grid failures and act as frequency regulators.
- In order to guarantee the energy supply, during the grid operation, the energy storage systems can help to stabilize the transmission and distribution since they can avoid voltage drops and keep it constant ^{7,8}.

- **End-User Level:**

- The storage systems can be a possible solution to energy distribution in remote areas and islands where interconnections are weak and flexible power sources are lacking.
- These systems can ensure the power quality. This application counterbalances disturbances from electricity grid to maintain and guarantee stable supply.
- Storage systems can be applied in transportation. High energy density and high specific energy are the most important requirements for this application, but a fast response time is also important. A combination of different technologies can enable using electric vehicles in smart grids ⁷.

1.2.2 Technologies

The classification of the different storage technologies relies on many different criteria; in Figure 1.3 the division is based on the conversion process ¹⁰. Following this classification, a brief description of each technology is presented below:

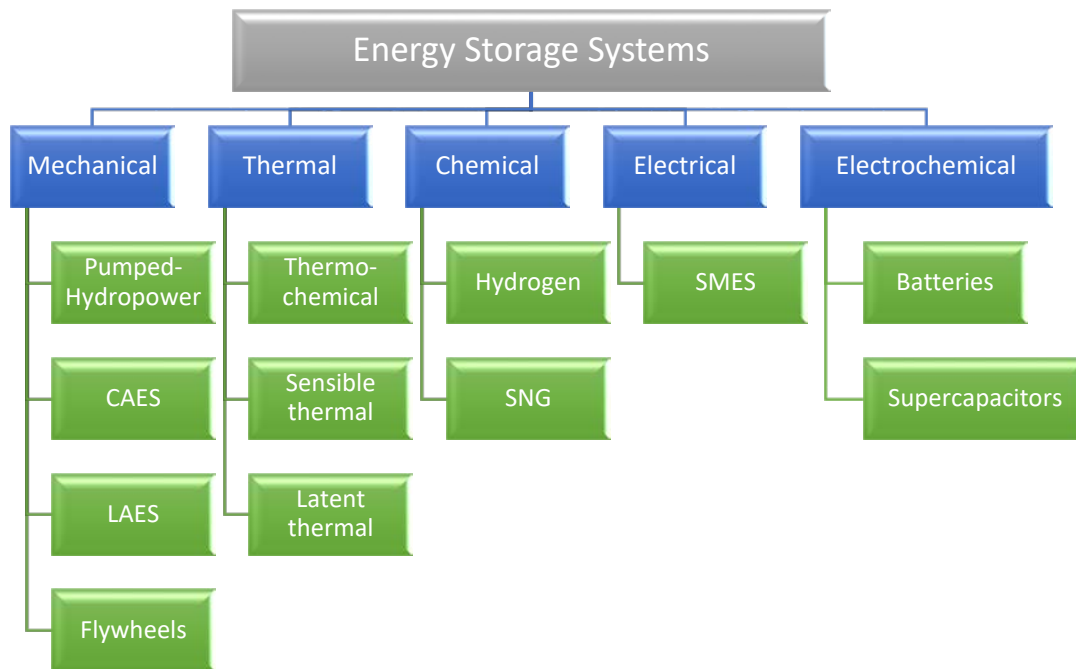


Figure 1.3. Classification of the energy storage systems. CAES in Compressed Air Energy Storage; LAES is Liquid Air Energy Storage; SMES is Superconducting Magnetic Electrical Systems; SNG is Synthetic Natural Gas ¹⁰.

1.2.2.1 Mechanical Energy Storage Systems

- **Pumped- Hydropower Storage (PHS).** This system is based on two water reservoirs located in different elevations. Energy is stored by pumping water from the lower to the upper reservoir, when energy is demanded water is turbined back to the lower reservoir. The power rate of these systems is in the range of hundreds to thousands of MW, while energy storage capacity is proportional to the height difference between lower and upper reservoir and the volume of water stored. Thus, the main disadvantage is the geographical requirements which limit its installation. Conventional PHS also presents a

moderate to high efficiency (65–85%). It was first used in Italy and Switzerland in the 1890s and the first large-scale commercial application was in the USA in 1929^{10,11}.

- **CAES (Compressed Air Energy Storage).** These systems use electricity of periods of low consumption to compress air and store it in underground caverns or tanks. During peak-consumption the air is released to a combustor in a gas turbine to generate electricity. This technology is characterized by high power rating (100–300MW), large storage capacity and moderate response time (around ten minutes). The same as PHS, its main disadvantage is the geographical requirements. The first CAES plant is in Huntorf, Germany, and has been in operation since 1978 with 42% efficiency^{10,12}.
- **LAES (Liquid Air Energy Storage)** is a promising storage alternative, currently at the demonstration stage. It consists in compressing and cooling air in a refrigeration plant and storing in an insulated tank during low-demand energy periods. When the energy is needed the air is converted in gas and used to produce electricity in a turbine. High efficiency (75–85%) is shown if waste heat is used during discharge cycle^{7,13}.
- **Flywheels.** This technology stores energy in the angular momentum of a spinning mass. During charge, a disc is rotated suspended on magnetic bearings by a motor; during discharge, the same motor acts as a generator producing electricity from the kinetic energy of the flywheel. The total energy of a flywheel system is dependent on the weight and speed of the rotor, and the power rating is dependent on the motor-generator. Usually power rating is in the range of hundreds of kW, the discharge takes from seconds to minutes with high efficiency (75–85%). Nevertheless, flywheels usually have a very high self-discharge rate (55–100%/day)^{10,14}.

1.2.2.2 Thermal Energy Storage Systems

They can be classified according to the form in which the heat is stored:

- **Sensible:** uses the heat associated to the increase or decrease the temperature of a medium (e.g. water, oil, rocks).

- **Latent:** uses the heat associated to changes in the state of aggregation, as per phase change materials (PCMs) which undergo melting or solidification when energy is exchanged (e.g. molten salts, water/ice).
- **Thermochemical:** uses reversible chemical reactions to store thermal energy in the form of chemical compounds. During charge the material absorbs heat and dissociates into two components that can be stored separately and allow this technology to reduce heat losses ¹⁵.

1.2.2.3 Chemical Energy Storage Systems

- **Hydrogen.** In this system hydrogen is released by breaking the water molecule using electricity (electrolysis), heat (thermolysis) or any other method. Then, hydrogen is stored under pressure, low temperature or by chemical conversion in products such as methanol, ammonia, metallic hydride or liquid hydrocarbons. The storage efficiency is almost 100%. When the energy is demanded, electricity is generated converting the hydrogen through fuel cells. The hydrogen injected in the Natural Gas network is called Power-to-Gas¹⁶.
- **SNG.** In this technology hydrogen is converted into methane. The main advantage is that the methane can be stored in the existing natural gas infrastructure while the amount of hydrogen that can be kept in the gas pipeline is limited to 10 - 15% by the technical characteristics ¹⁶. This technology is also named as *Power-to-Gas* ¹⁶

1.2.2.4 Electrical Energy Storage Systems

- **Superconducting Magnetic Electrical Systems (SMES).** These systems store energy in a magnetic field. They consist in a super-cooled coil in which a magnetic field is created by the flow of direct current (DC). There is almost no resistance in low-temperature superconducting materials, so they can cycle for a long time without losing energy. Besides high efficiency (80–90%), SMES main features are very fast response time (a few milliseconds) and a very high power density (1–4MW/m³)⁷.

1.2.2.5 *Electrochemical Energy Storage Systems*

- **Supercapacitors.** These devices rely on electrostatic forces to store charge as conventional electrolytic capacitors. The so-called supercapacitors, or electrochemical capacitors, were developed to have greater capacitance and energy density and are mainly characterized by having high power density ¹⁷.
- **Batteries.** These systems consist in an electrolyte and two electrodes composed by materials with different electrochemical potential and use reversible electrochemical reactions which enable the flow of electrons to store energy. Several types of batteries with different characteristics can be distinguished depending on the chemistry involved in the reactions ¹⁸.

The described technologies are gathered in the following diagram (Figure 1.4) where their energy capacity and the discharge time are represented. According to these parameters the technologies will perform different services.

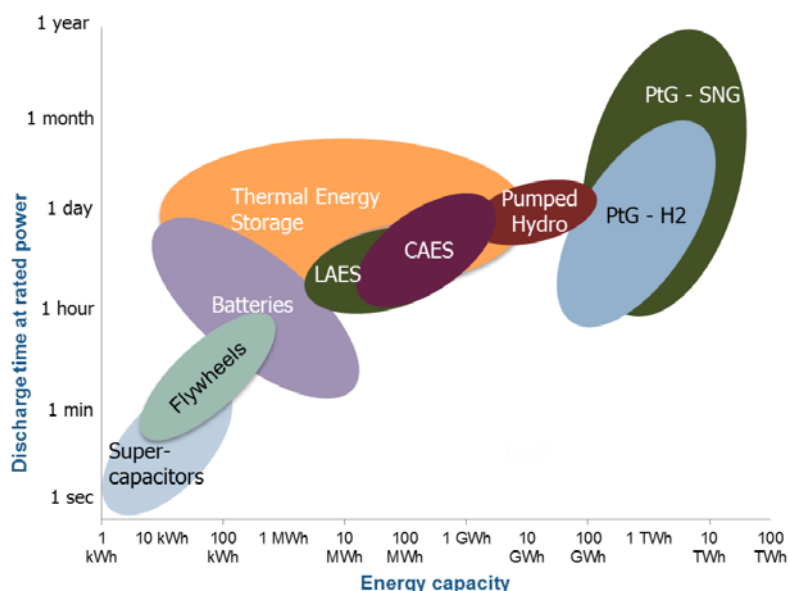


Figure 1.4. Relationship between the different technologies based on their energy capacity and time response ⁴. (PtG- H2: hydrogen injected in the Natural gas network; PtG-SNG: hydrogen converted into methanol).

Pumped hydro energy storage has dominated energy storage for over a century (accounts for over 99% of the global installed energy storage capacity) since it is a mature technology with high energy capacity (Figure 1.5). Other technology that could be used for energy management due to its capacity is compressed air but currently there are only two commercial plants (in total 400 MW)⁴. In the opposite part of the Figure 1.4, it can be found technologies which energy capacity is in the range of KWh-MWh with a discharge time between seconds and hours. Among these technologies are supercapacitors and batteries.

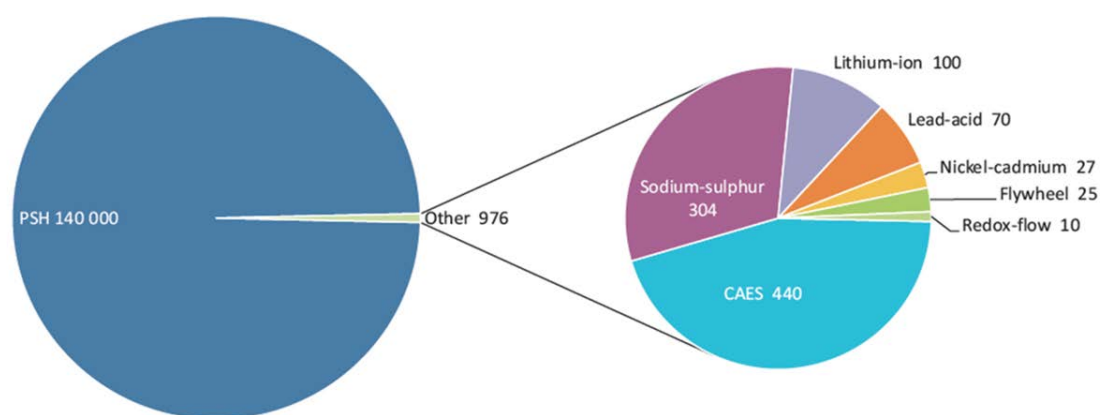


Figure 1.5. Current global installed grid-connected electricity storage capacity in MW (taken from ¹⁹).

Although these electrochemical devices have been used for energy storage since the 19th century ²⁰, they have not been used extensively, only in small-scale applications, such as mobile power sources, and in the automotive industry and the total installed capacity is around 1.7 GW ²¹. However, the growth of interest in the electric vehicles and the need to integrate renewable power technologies such as solar and wind are driving huge investments in the development of electrochemical energy storage technologies. In the following section a deep description of the electrochemical energy storage devices, their components and the mechanisms involved are presented.

1.3 Electrochemical Energy Storage

In general, electrochemical energy storage has many desirable characteristics such as almost pollution-free operation, high efficiency, a variety of power and energy rates to fulfill different requirements, long cycle life and low maintenance without the current restrictions related to the location or severe environmental issues existing in pumped-hydro or compressed air technologies.

According to the materials employed in the manufacture of these elements the energy storage mechanism will be different and as a consequence the characteristics of the device. The different electrochemical technologies can be divided in two main groups: supercapacitors and batteries.

The main differences between batteries and supercapacitors (SCs) are gathered in Table 1.1. Compared to supercapacitors, batteries are characterized by having higher energy density, longer discharge times, but also lower power density and cycle life. For better understanding the basic of these differences, both technologies (SCs and batteries) are described deeply in the next sections.

Table 1.1. Comparison between batteries and supercapacitors ¹⁷.

Parameter	Battery	Supercapacitor
Storage mechanism	Chemical	Physical
Power limitation	Reaction kinetics, mass transport	Electrolyte conductivity
Energy storage	High (bulk)	Limited (surface area)
Charge rate	Kinetically limited	High, same as discharge
Cycle life limitations	Mechanical stability, chemical reversibility	Side reactions

1.3.1 Supercapacitors

Supercapacitors (SCs) are electrochemical energy storage devices characterized by having high power density, good cyclability but low energy density^{22,23}. These devices are interesting because they fill the gap between electrolytic capacitors and batteries. Thus, it should be noted that SCs cannot only be discharged in a matter of seconds, but also be charged in such a short time with almost 100% efficiency. In terms of cycle life, these devices can perform millions of cycles maintaining high efficiency values²⁴. This characteristic is due to their charge storage mechanism in which the charges are stored by electrostatic forces, so it is a physical process in contrast to the batteries' mechanism. Other important parameter is the temperature operation, SCs have demonstrated good performances at low temperatures such as -40°C ²⁴ that are too low for batteries.

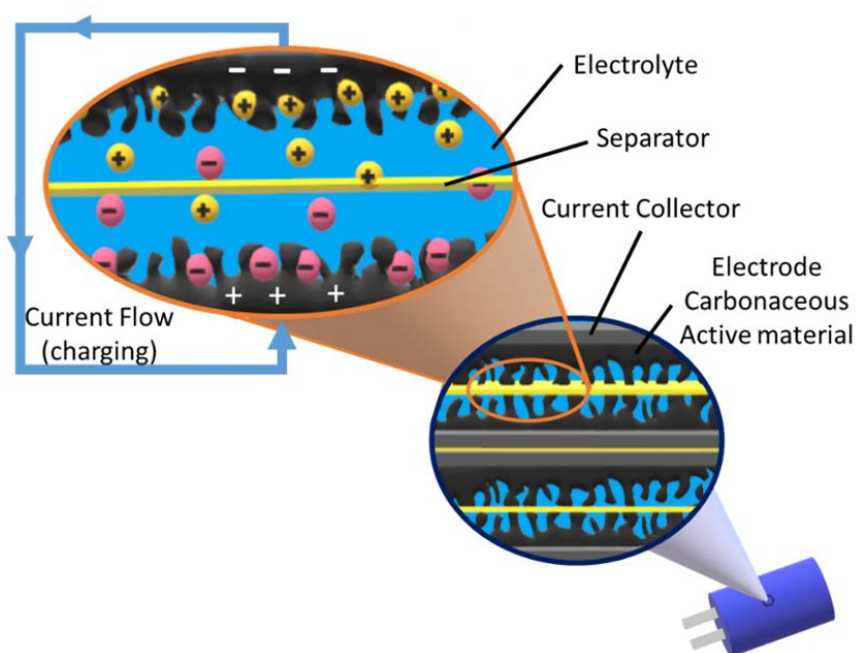


Figure 1.6. Scheme of a supercapacitor (based on²⁵).

The basic components of a SC are two electrodes and between them there is a separator soaked in the electrolyte (Figure 1.6). Each component is briefly described as follows:

- **Separator.** The separator should avoid the direct contact of the electrodes (it would cause a short-circuit) and but also should have ion permeability to allow

the ionic transport. It is also important that the material exhibit high electrical resistance and the lower possible thickness to achieve good performance ^{24,26}.

- **Electrolyte.** The electrolyte is chemically inert and should have high ionic conductivity and wide electrochemical stability window (ESW). These properties depend on the nature of the electrolyte. Thus, different types of electrolytes can be distinguished: aqueous, organic, ionic liquids and polymer electrolytes ²⁷.
- **Current collector.** This component is usually a metal with high chemical and electrochemical stability in the selected electrolyte. In addition, in order to have a good performance, it is important to ensure good electric contact between the electrode active material and the current collector, since a homogenous distribution of the current inside the cell is crucial to obtain low internal resistance values ^{17,28}.
- **Electrodes.** The electrode active material should have high electric conductivity and high surface area. If both the positive and the negative electrodes are equal then the SC will be symmetrical whereas if they are different each other the SC is asymmetric ^{29,30}.

According to the materials employed in the manufacture of the electrodes or the electrolyte, different storage mechanism will be found and in consequence different types of SCs.

1.3.1.1 Types of Supercapacitors

Depending on the materials and the charge storage mechanism it is possible to distinguish between different types of SCs: Electrical Double Layer Capacitors (EDLC), pseudocapacitors and hybrid SCs (Figure 1.7)^{17,30,31}.

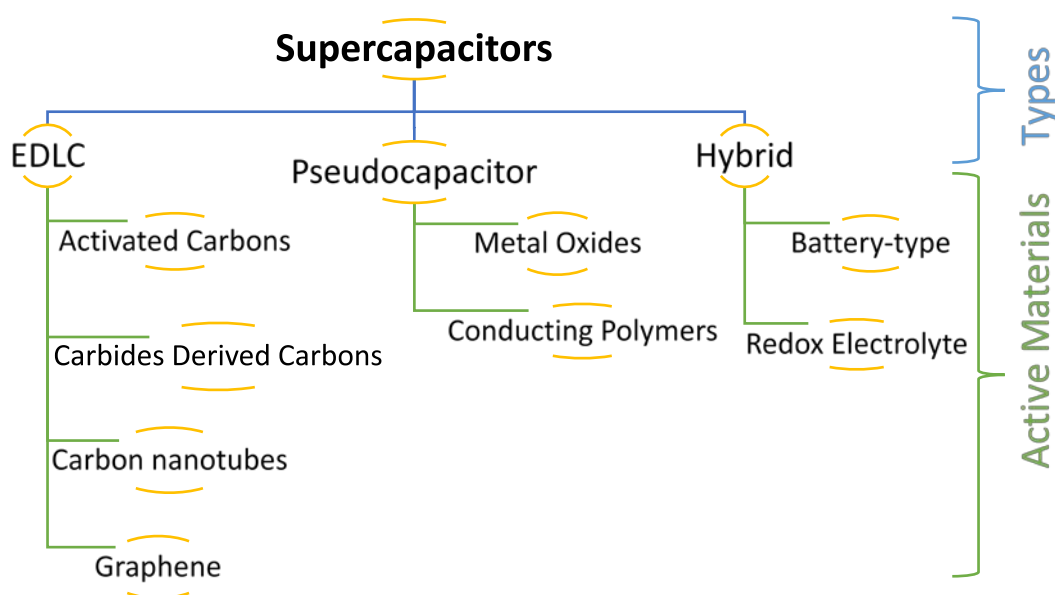


Figure 1.7. Classification of supercapacitors (adapted from ¹⁷).

EDLC is the first type of supercapacitors discovered and most commercial supercapacitors belongs to this kind. The energy storage mechanism is based on electrostatic forces and the electrodes are made of carbonaceous materials. As it was commented before, one possibility to enhance the properties of the supercapacitors is the modification of the electrode materials and as a consequence their energy storage mechanism. Thus, two additional types of SC can be defined: pseudocapacitors (using metal oxides or conducting polymers) and hybrid SCs in which battery type materials are used in the electrode (Battery-type) or in the electrolyte (Redox Electrolyte). In these two types of devices, not only electrostatic processes occurs but electron transfer processes are also involved. The main different between EDLC, pseudocapacitors and hybrid devices is their electrochemical response (Figure 1.8). The performance difference between capacitive and non-capacitive faradaic processes could be the effect of localized and delocalized valence electrons and can be explained by the electron energy states. In non-capacitive faradaic processes, the electron energy states are separated in molecules, so the process for electron injection (or removal) may take place in very well separated redox active sites (hybrid supercapacitors as per Figure 1.8 c). However, if these redox active sites can interact

between each other due to either short separation or/and good conductivity their energy states can merge into a broad band. As a result electron transfer becomes continuous over a wide range of potentials and a capacitive-faradaic response is obtained^{31–33} (pseudocapacitors as per Figure 1.8 b).

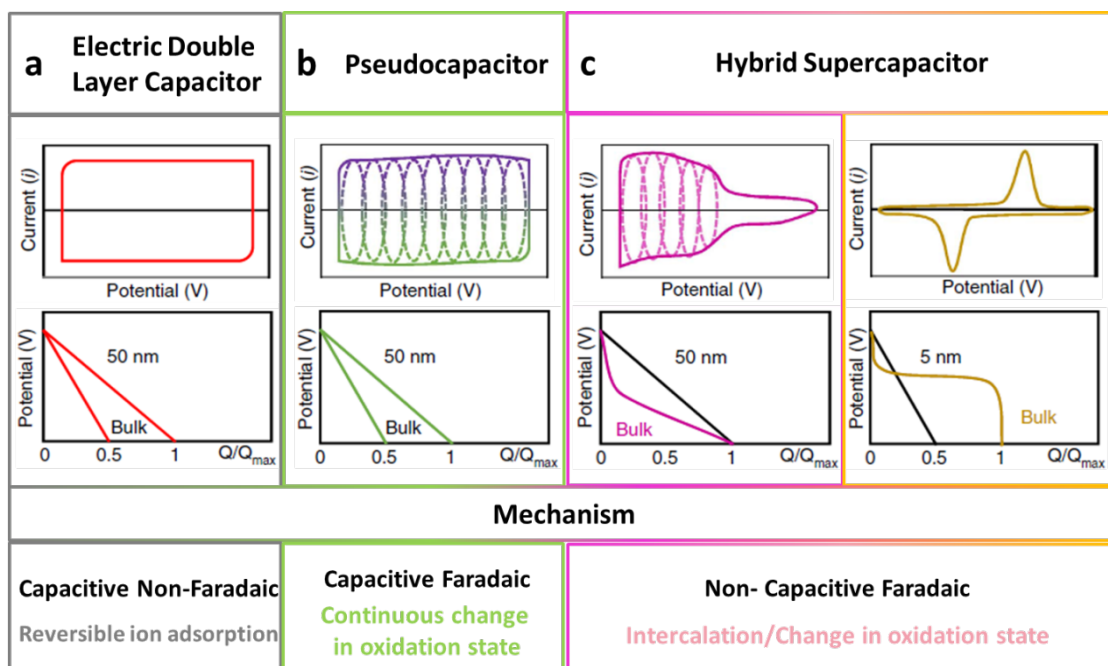


Figure 1.8. Types of supercapacitors classified by their electrochemical response and storage mechanism (adapted from³⁴).

Electrochemical Double Layer Capacitors (EDLC)

In conventional capacitors the electrodes are metallic plates that are separated by a dielectric characterized by its permittivity (ϵ_r) and the charge stored (Q) depends on the applied potential (V) and the capacitance (C) which depends on the accessible area (A) of the plates and the distance (d) between them, following the equation (1.1), where ϵ_0 is the permittivity of the vacuum.

$$C = \frac{Q}{V} = \frac{\epsilon_r \epsilon_0 A}{d} \quad (1.1)$$

In the case of EDLC the dielectric material is substituted by an electrolyte and the electrodes are made of microporous or nanoporous carbonaceous materials with high specific surface area ($>1000 \text{ m}^2\text{g}^{-1}$). This huge active area and the nanometric size of

the electric double layer (d) leads to capacitance values orders of magnitude higher than electrolytic capacitors^{17,26}.

- **Electric double layer**

In EDLCs the charge is stored in the accessible surface area of the electrodes forming an electric double layer. This structure is created when a voltage difference is applied between the two electrodes. Then, the carbonaceous material of the electrodes is electrostatically charged (one positively and the other negatively) and the ions (anions and cations) of the electrolyte migrate to the electrode with the opposite charge to keep a charge balance in the device. This process takes place at the electrode-electrolyte interface and is very fast (10^{-8} s). Thus, each interface represents a capacitor and a EDLC can be described as two capacitors connected in series (Figure 1.9)²⁶.

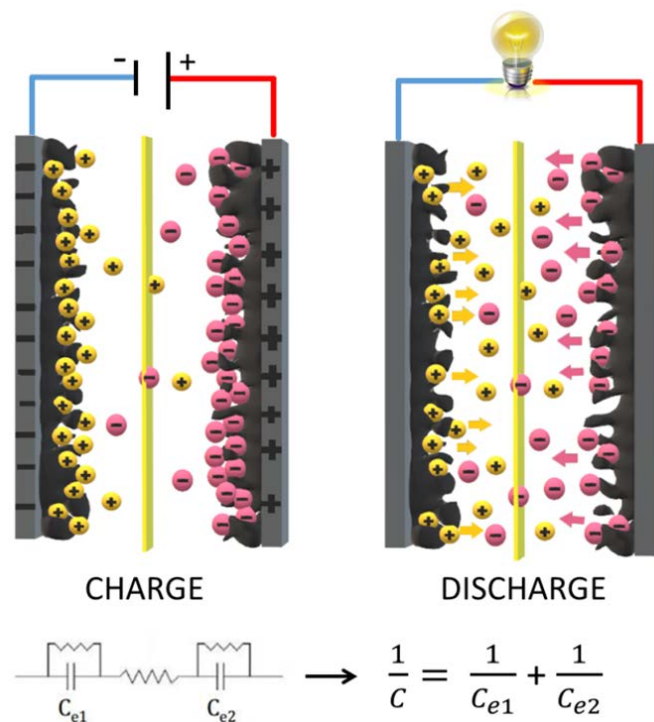


Figure 1.9. Scheme of EDLC and its behavior during charge and discharge processes.

Several models have been developed to describe the behavior at the electrode-electrolyte interface and the creation of the double layer, Helmholtz model, Gouy-Chapman model and Stern model¹⁷.

According to Helmholtz theory, the charge generated in the electrode is neutralized by opposite sign ions of the electrolyte at a “d” distance. But this model does not take into account several factors such as ion diffusion. Then, Gouy-Chapman proposed a more complex model. It describes the creation of a diffusive layer in which a concentration gradient of ions is generated and decreases towards the bulk solution. However, this model is still insufficient for highly charged double layers and Stern suggested in 1924 a model combining both models by accounting for the hydrodynamic motion of the ions in the diffuse layer and the accumulation of ions close to the electrode surface (Figure 1.10). Thus the capacitance of the double layer has two different contributions Helmholtz capacitance (C_H) and Diffuse-layer capacitance (C_{diff}) which are connected in series. The thickness of the double layer is in a magnitude order about 100 nm, and the specific-surface area of the electrode materials is ($100\text{-}1000\text{ m}^2\text{g}^{-1}$), therefore the capacitance of the EDLC is much higher than the one obtained with conventional capacitor (equation 1.1)²⁶.

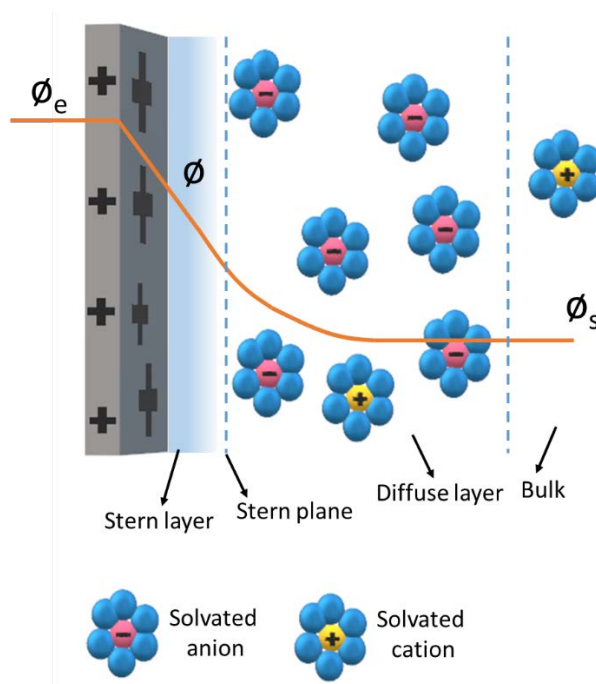


Figure 1.10. Stern model of the electrical double-layer formed at a positively charged electrode in an aqueous electrolyte. The electrical potential, ϕ , decreases from the electrode to the bulk electrolyte. The Stern plane marks the distance of closest approach of the ions to the charged surface. The diffuse layer starts in the range of 10 – 100 nm from the electrode surface (adapted from ³⁵).

- **Electrode Active Materials for EDLC**

In EDLC the electrodes are usually made of porous carbonaceous materials. They have several desirable properties such as: high electric conductivity and specific-surface area, good thermal and chemical stability and low cost. The most important electrode materials³⁶ are gathered here and briefly described:

❖ **Activated carbons.** These are the most widely employed active material for SCs. They are characterized by having high surface area as a result of a chemical or physical activation process in which a porous network in the carbon particles is formed. The size of these pores leads to different types of nanoporous materials (micropores <2nm, mesopores 2-50nm, macropores >50nm) the pore size distribution and the pore volume are also important characteristics³⁷⁻⁴¹.

❖ **Carbide derived carbons (CDC).** These materials are prepared by high temperature extraction of metals from carbides. Its main characteristic is that their pore size distribution is very narrow and it can be tailored by changing the synthesis temperature. This is useful to study the effect of the pore size in a specific application⁴²⁻⁴⁴.

❖ **Carbon nanotubes (CNT).** These materials are prepared by catalytic decomposition of hydrocarbons as well as carbon nanofibers. Depending on the synthesis parameters it is possible to control their crystalline structure thus, single walled carbon nanotubes (SWCNTs) and multi-walled carbon nanotubes (MWCNTs) can be produced⁴⁵⁻⁴⁷. They have a high electric conductivity and the electrodes can be prepared without any binder or current collector giving rise to self-standing devices.

❖ **Graphene.** It is a one-atom thick sheet made of sp^2 bonded carbon atoms in a polyaromatic honeycomb crystal lattice. Its excellent physicochemical properties such as large surface area, good flexibility, high electrical conductivity lead to high rate and cycle capability. It is usually combined with metal oxides in composites which result in improved performance of the devices⁴⁸⁻⁵⁰.

❖ **Onion-like carbon.** This type of carbonaceous materials is also called 'carbon onions' and 'multiwalled fullerenes'. They are made of concentric spherical graphitic

sheets and are characterized by having moderate surface area (400-600 m²g⁻¹), low cost, ability to be dispersed in polar and non-polar solvents and often can provide higher specific capacitance than MWCNTs⁵¹.

- **Energy & Power Density in EDLC**

The electrode material is one of the main components of the SC, since it has a very strong influence in the total capacitance. However, important parameters such as energy and power are also influenced by other factors.

Energy and power densities are among the main properties of an energy storage system as it was explained before, since they define the amount of energy that can be stored and the time response. They are described by equations (1.2-1.3) and (1.4-1.5), where Capacitance (C), maximum operating voltage (V), and the Equivalent Series Resistance (ESR) are related. The latter is the sum of all the resistances associated to the cell (materials resistance, electrical contact resistance, bulk electrolyte resistance, ion diffusion resistance and separator resistance)²⁶.

$$E_{max} = \frac{1}{2} C V^2 \quad (1.2); \quad E_{real} = \int_{t_i}^{t_f} I \cdot V dt \quad (1.3)$$

$$P_{max} = \frac{V^2}{4 ESR} \quad (1.4); \quad P_{real} = \frac{E_{real}}{t_{discharge}} \quad (1.5)$$

Where I is the current density applied and $t_{discharge}$ is the discharge time at that current density ($t = t_f - t_i$). It should be mentioned Eq 1.2 is only applicable for EDLC, where a capacitive non-faradic behavior is revealed, whereas the Eq 1.3 is valid for any type of SC or battery.

The difference between the maximum and real energy/power values lies in the inability of extracting the 100% of energy stored. Even in so highly efficient devices as SC, the real energy that can be extracted depends on the current density and the discharge time and is always smaller than the maximum.

In order to boost the energy density of the devices, different strategies are pursued either by increasing capacitance (C) or voltage (V), according to equations 1.2 and 1.3. These strategies are related to the modifications of the different components of the SC either the electrode material or the electrolyte which are detailed next²⁶.

- **Electrolytes**

The electrolyte plays an important role in the device performance, since the operating voltage is mainly limited by this component, as well as it can have strong influence in the ESR. Thus, the main properties of the electrolyte are the Electrochemical Stability Window (ESW) and its ionic conductivity (σ). Other desirable features also are: low viscosity, low flammability and volatility, high purity and low cost. Three classes of electrolytes can be found : aqueous, organic or ionic liquids⁵².

❖ **Aqueous Electrolytes.** Aqueous solutions are widely employed at different pH (eg. H_2SO_4 or KOH). These electrolytes can operate up to 1.2- 1.5 V since they are limited by water electrolysis. The ionic conductivity of this type of solutions is around $1 \text{ S}\cdot\text{cm}^{-1}$ and the ionic radius is smaller than the one exhibited by the salts used in non-aqueous electrolytes, which is beneficial to obtain low ESR. On account of these properties, the power density of the aqueous devices is higher than for organic ones²⁶.

❖ **Organic Electrolytes.** The usual organic electrolytes are based on tetraalkylammonium salts dissolved in common solvents such as propylene carbonate (PC) or acetonitrile (ACN, forbidden in Japan). These electrolytes can achieve operating voltages close to 2.7 V. Thus, their wider ESW allows these SCs for having higher energy density than the aqueous devices which is the main advantage in comparison with the aqueous ones and the reason because these electrolytes are mostly used in the commercial SCs. On the contrary, the power density is much lower due to their lower conductivity ($0.01 \text{ S}\cdot\text{cm}^{-1}$). In addition, the cost is higher since any water contamination should be avoided^{17,26}.

❖ **Ionic liquids (ILs).** The ionic liquids are salts which are in liquid state at low temperatures (their melting point is $<100 \text{ }^\circ\text{C}$). They are composed by asymmetric and large size cations and anions (Figure 1.11). They are characterized by having low volatility, high thermal and chemical stability and large ESW (4-6 V). The main drawbacks are their low conductivity, which is typically less than $10 \text{ mS}\cdot\text{cm}^{-1}$ and the high viscosity at room temperature. However, both are improved by increasing the temperature^{27,53}.

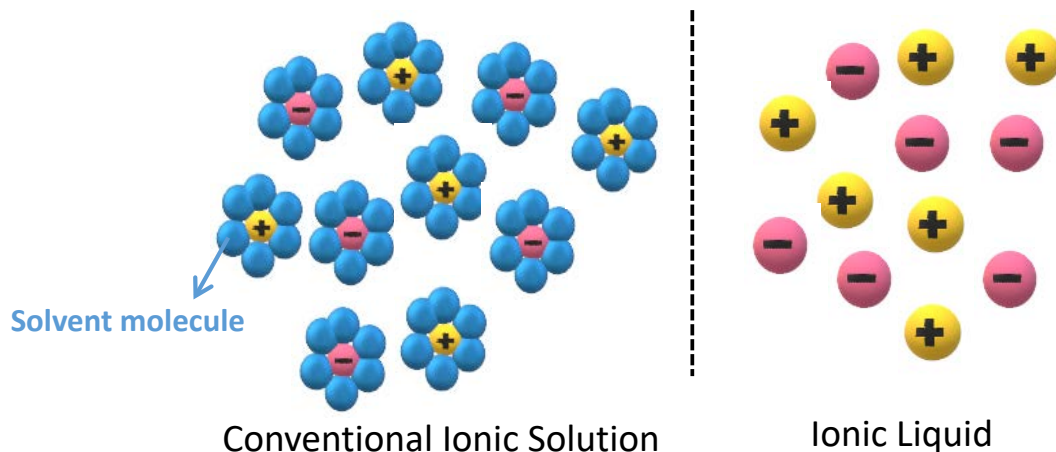


Figure 1.11. Schematic difference between ionic liquids and conventional electrolytes based on dissolved salts.

Pseudocapacitors

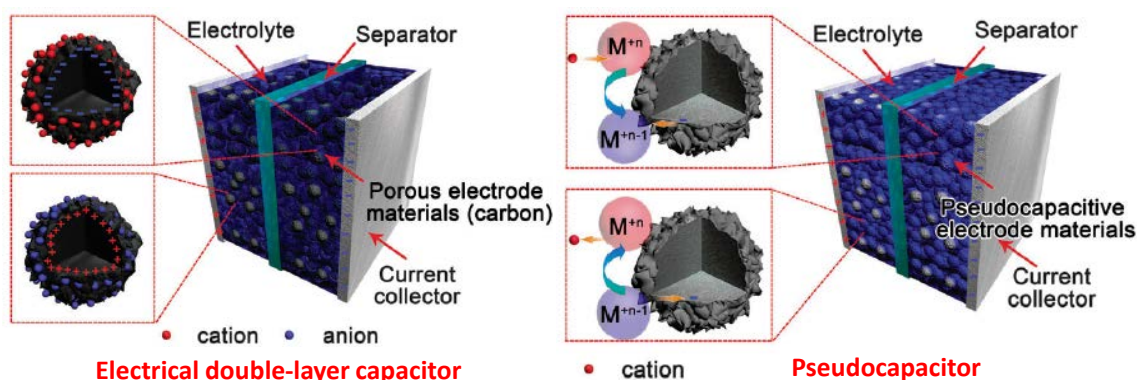


Figure 1.12. Scheme of an EDLC and a pseudocapacitor (adapted from ⁵²).

In these devices, in contrast to EDLC, the charge storage mechanism has two contributions: the electrostatic forces (electrical double layer) and capacitive-faradaic processes ^{26,54} (Figure 1.12). For this reason, in these devices instead of capacitance, the accurate term is “pseudocapacitance”. Thus, the pseudocapacitance values and the energy density of these SCs is usually higher than those obtained with EDLCs. However, the time response of a pseudocapacitor is usually slower than the EDLC due to the faradaic process. It should be mentioned, that the charge storage mechanism relies on fast redox reactions occurring on the electrode surface but not in the bulk.

Besides this, the electrical response of a pseudocapacitive material is quite similar to an EDLC (see typical discharge profiles in Figure 1.8), and the pseudocapacitance must be constant in all operating voltage range^{32,55}. Contrarily, if the cyclic voltammetry or galvanostatic charge-discharge experiments are far away from their respective rectangular and triangular shape, then these materials should not be considered “pseudocapacitive” but “battery-type” and their corresponding devices will be hybrid Supercapacitors. In general, the materials used in pseudocapacitors are some metal oxides or conducting polymers.

❖ **Metal oxides.** These materials have high specific capacitance but poor electrical conductivity making them a suitable material to be combined with highly conductive materials, such as graphene or CNTs. A variety of metal oxides⁵⁴ has been used, in SCs achieving capacitance values above 400 Fg^{-1} . The most investigated is based on RuO_2 ⁵⁶, but its high cost and toxicity promoted the use of other oxides such as MnO_2 ⁵⁷, Nb_2O_5 ⁵⁸.

❖ **Conducting Polymers.** These polymers exhibit conductivity due to conjugated double bonds located in the chain⁵⁹. The conductivity is usually enhanced with some doping species. With these materials it is possible to achieve high values of pseudocapacitance and can be produced in thin films. In addition, they have lower cost than metal oxides. Polymers based on polypyrrole⁶⁰, polyaniline⁶¹ and thiophene⁶² are being intensively studied using organic electrolytes^{59,63}.

Respect to the design, pseudocapacitors can be asymmetric. Thus, one electrode is made of carbonaceous material (typical EDLC) and in the opposite one the electrode material is pseudocapacitive (e.g, MnO_2 ⁶⁴ or polyaniline (PANI)⁶⁵). In addition, the pseudocapacitive electrode is made of a composite in which a carbonaceous material is mixed with the pseudocapacitive material to enhance its conductivity and surface area. The main advantage of the asymmetric design is the improved capacitance obtained. Moreover, if the electrodes are mass balanced to compensate their different specific capacitances, the device can operate in the whole electrochemical stability window of the electrolyte.

Hybrid SCs

As it was mentioned before if the materials employed to provide faradaic contribution do not allow for having a constant value of pseudocapacitance, then they should be called battery-type materials and the device in which they were used it is a Hybrid SC.

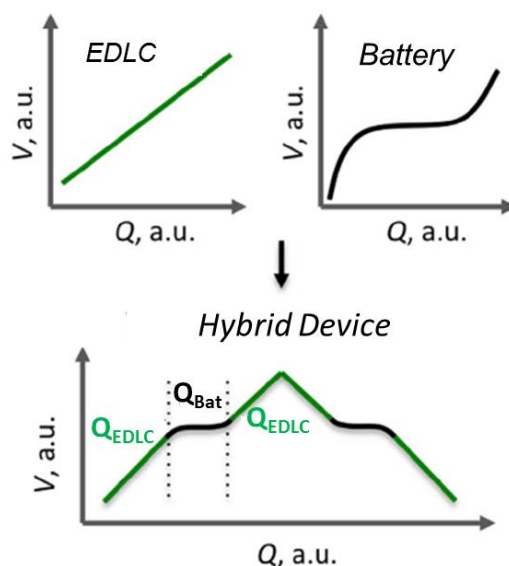


Figure 1.13. Scheme of the storage mechanism in a hybrid device (adapted from ⁶⁶).

In these devices the combination of a double layer mechanism and a faradaic contribution non-capacitive are used to devices with much higher energy density values. A scheme of the storage mechanism in a hybrid device is shown in Figure 1.13 ^{33,34,66–68}. In the last years, new devices are emerging as result of mixing different types of materials, so far, two types of hybrid SCs can be distinguished depending on where the active material is located. Thus, Battery-type Hybrid SC (double layer + faradaic contributions from electrode) and Redox electrolyte-SC (double layer + faradaic contribution from electrolyte) can be distinguished.

❖ **Battery-type Hybrid Supercapacitors (BtHSC).** In this type of device one electrode is battery-type (intercalation or conversion reaction) whereas the other electrode is a typical EDLC electrode.

○ In a first category, there is an intercalation compound, which supports reversible intercalation of ions (usually Li^+ or Na^+). This allows for improving the energy

density, however, the rate capability of these devices is limited by the intercalation, since it is a slower process in comparison with the EDL formation. Materials that have been employed in these devices are $\text{Li}_4\text{Ti}_5\text{O}_{12}$ ⁶⁹, graphite⁷⁰, $\text{Li}_2\text{FeSiO}_4$ ⁷¹ for negative electrodes, and $\text{LiNi}_{0.5}\text{Mn}_{1.5}\text{O}_4$ ⁷², $\text{Li}_3\text{V}_2(\text{PO}_4)_3$ ⁷³, $\text{Na}_3\text{V}_2(\text{PO}_4)_3$ ⁷⁴, $\text{Li}_2\text{CoPO}_4\text{F}$ ⁷⁵ for positive ones.

○ A second category gathers the functionalization of carbonaceous electrode material with metal oxides or organic redox molecules. Thus, in the SC an EDLC material is used in one electrode and in the other one a metal oxide or an organic molecule is used for decorating the carbon material. In the case of the metal oxides-based materials, the reason to incorporate them into the electrode is the same as mentioned in the pseudocapacitors section, but considering that some of them such as NiCo_2O_4 ⁷⁶, Co_3O_4 ⁷⁷ and Fe_3O_4 ⁷⁸, exhibit a non-capacitive faradaic response, the final device should be classified as hybrid.

With respect to the organic molecules, the growing interest in these molecules is mainly due to their fast and reversible redox reactions, low cost, a commercial availability. The most investigated family is quinones. Prof. Compton's group was the first one which reported the performance of SC based on carbonaceous material in which quinones are covalently bonded. Since then, several studies have been reported based on the functionalization of carbon electrodes with organic redox molecules^{79–82}. This combination leads to higher capacity values at lower cost.

In addition, in this type of devices different combinations of materials are possible. Recently, devices in which pseudocapacitive + battery-type mechanisms are mixed have been developed^{66,67}.

❖ **Redox-Electrolytes Hybrid SC.** In these devices the solvents are used both as redox and conducting mediator since the active redox material is dissolved into the electrolyte such as in Redox Flow Batteries (RFB). Thus, the redox source comes from the electrolyte and the active species have to migrate from the bulk of the electrolyte to the electrode surface where the faradaic reaction takes place as is represented in Figure 1.14⁸³. The oxidized species migrates inside the pores from the bulk of the electrolyte to the electrode surface where some transition states are formed and

finally it gets reduced accepting an electron. Then the reduced species should make the opposite way and go from the electrode surface to the bulk. As mentioned before, similar redox electrolytes are employed in redox-flow batteries but in those devices the electrolytes are flowing through the cell and the faradaic reactions are the only ones contributing to the energy storage. Contrarily, Hybrid SC are closed systems in which the electrolytes are static and the contribution of the EDL is important because carbonaceous materials with high specific surface area are used as electrode materials. The application of such redox active couples presents a new trend in SC development to increase the energy density as will be discussed in this thesis. Some examples of redox couples that have been used and demonstrated enhanced capacity in this type of hybrid systems include organic and inorganic compounds such as transition metal ions^{84,85}, halide ions^{86,87}, quinones⁸⁸ and phenylamide⁸⁹.

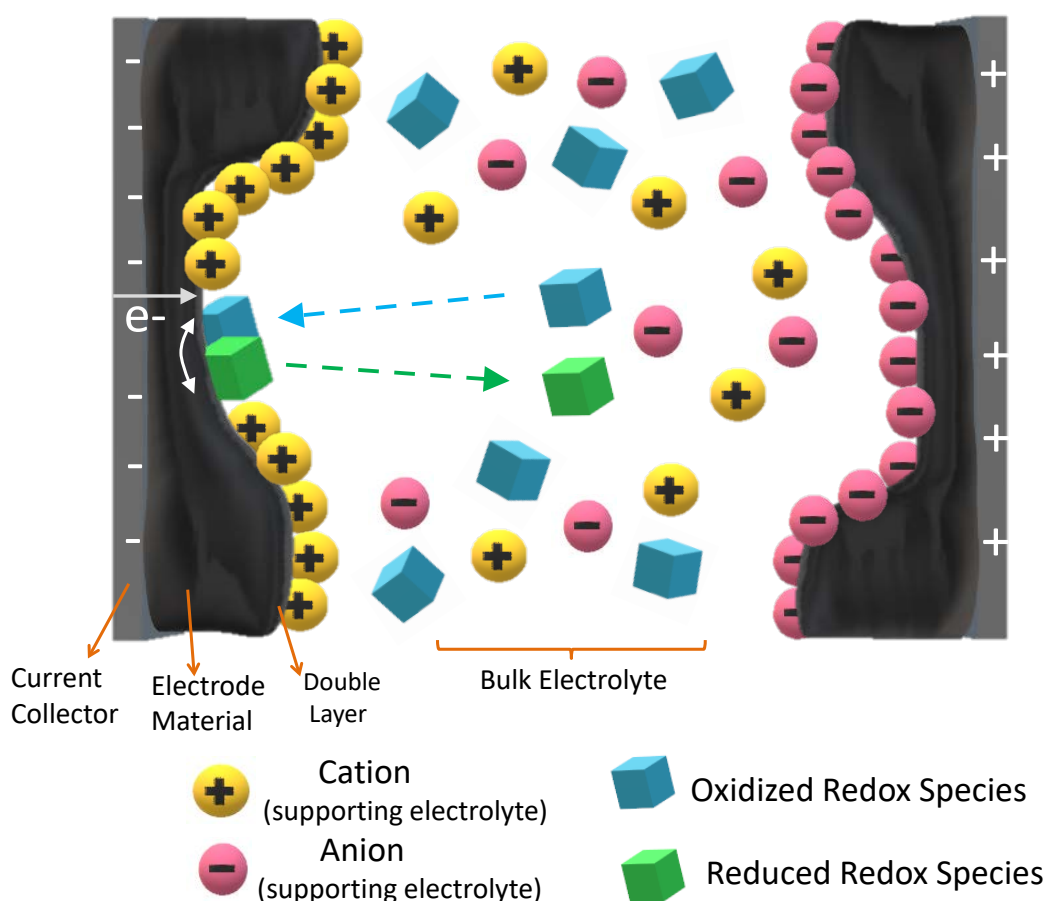


Figure 1.14. Illustration of the charge storage mechanisms in porous carbon based supercapacitor with a redox electrolyte.

1.3.2 Batteries

Many different types of batteries with different chemistries have been developed during the last decades including Alkaline, Lead-acid, Ni-MH, Zn-air, Lithium-ion, etc. Among them, Lithium-ion battery (LIB) technology is one of the most promising because of its good electrochemical performance and its successful application in consumer electronics and in electric vehicles⁹⁰ (Figure 1.15). All these mentioned batteries belong to a category that can be named as “static batteries” in which the active material is solid in form of electrode and compressed and fixed to the current collector. In this category a subdivision can be done based on the reaction type. Thus, two groups can be distinguished; batteries in which the reaction relies on chemical conversion reactions such as Pb- acid or batteries in which the energy is stored by ion intercalation, such as Li-ion. However, there is another type of batteries in which the active materials are dissolved into the liquid electrolytes that are stored in external tanks, and are pump into the cell/reactor during battery operation. This technology is named as “Redox Flow Batteries” and main differences with respect to conventional static batteries are gathered in the Table 1.2. Although providing a revision of all battery technologies it is out of the scope of this thesis, it is pertinent to present the state-of-the-art and future prospects of Redox Flow Batteries.

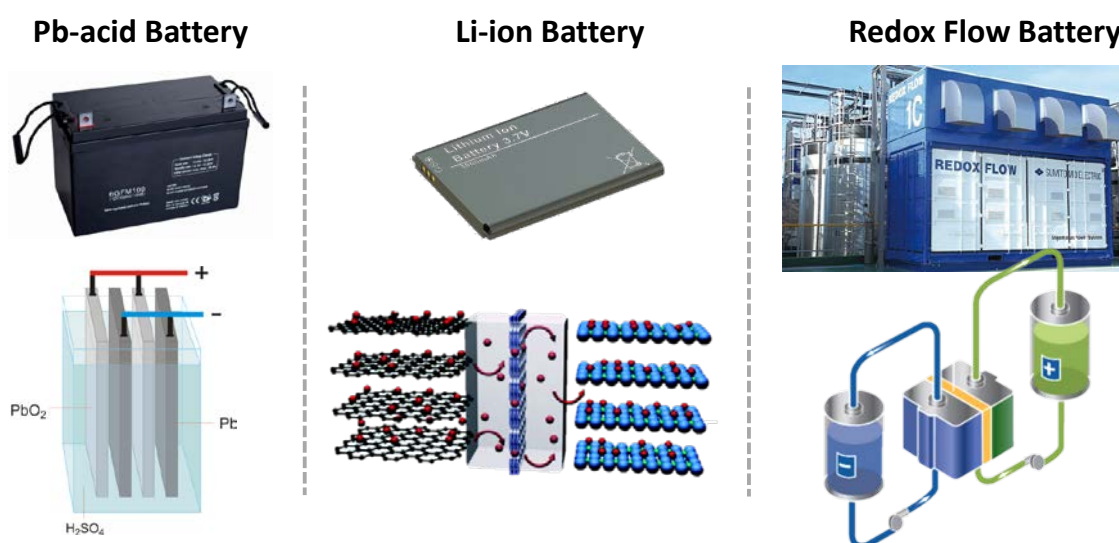


Figure 1.15. Illustration of different types of batteries.

Table 1.2. General comparison between static and redox flow batteries^{91,92}.

Features	Static (standard LIB)	Redox Flow
Site of reactants/products	Active electrode material	Electrolytes in tanks
Electrolyte conditions	Static and held within cell	Flowing through the cell
Separator	Microporous polymer separator	Ion exchange membrane
Energy & Power relation	Coupled	Uncoupled
Energy related cost (€/kWh)	Higher	Lower
State of charge	Narrow range	Larger range
Efficiency	Higher	Lower
Cycle Life	< 5000 cycles	>10000 cycles

1.3.2.1 Conventional Redox Flow Batteries (RFB)

A redox flow battery is an electrochemical energy storage device in which active materials are dissolved into the electrolytes that are stored in two external tanks. On account of this, energy and power densities can be scaled independently from each other which is the differentiating feature of these batteries and provides them with a huge versatility. In Figure 1.16 a simplified schematic is represented. During the operation the electrolytes are pumped into the cell and the reactions take place at the electrode surface. Thus, the electrodes are just a conductive material that allows for having electron transfer, but they do not suffer from any chemical change which causes variations in their volume or chemical structure. Figure 1.17 shows the stacking of the cell components to build a filter-press type flow cell. The cell is divided in two compartments by an ion exchange membrane which is permeable to some specific ions to balance the charge in both electrolytes, but should be impermeable to the redox-active materials to avoid the mixture between the electrolytes (crossover). The most conventional electrolytes consist of soluble redox metallic species (usually based on vanadium) which are dissolved into the solvent and undergo reversible and fast oxidation-reduction reactions during the operation of the battery. Thus, the active

species dissolved in the anolyte (negative electrolyte) are reduced during the charge and oxidized during the discharge. In the catholyte (positive electrolyte) the process is the opposite one, i.e. during the charge the species are oxidized and during the discharge they are reduced. The difference between the reaction potential in the anolyte and in the catholyte determines the voltage of the battery as illustrated in Figure 1.16. The voltage of the battery (V) together with the capacity (Q) define the energy density of the battery (eq 1.6)

$$E = Q \cdot V \quad (1.6)$$

The volumetric capacity of the electrolyte indicates the amount of charge that can be stored in a certain amount of electrolyte and is defined by equation 1.7.

$$Q = C_n e^- F \quad (1.7)$$

Where C_n is the concentration of the active species in molarity; e^- are the number of electrons exchanged in the reaction; and F is Faraday's constant.

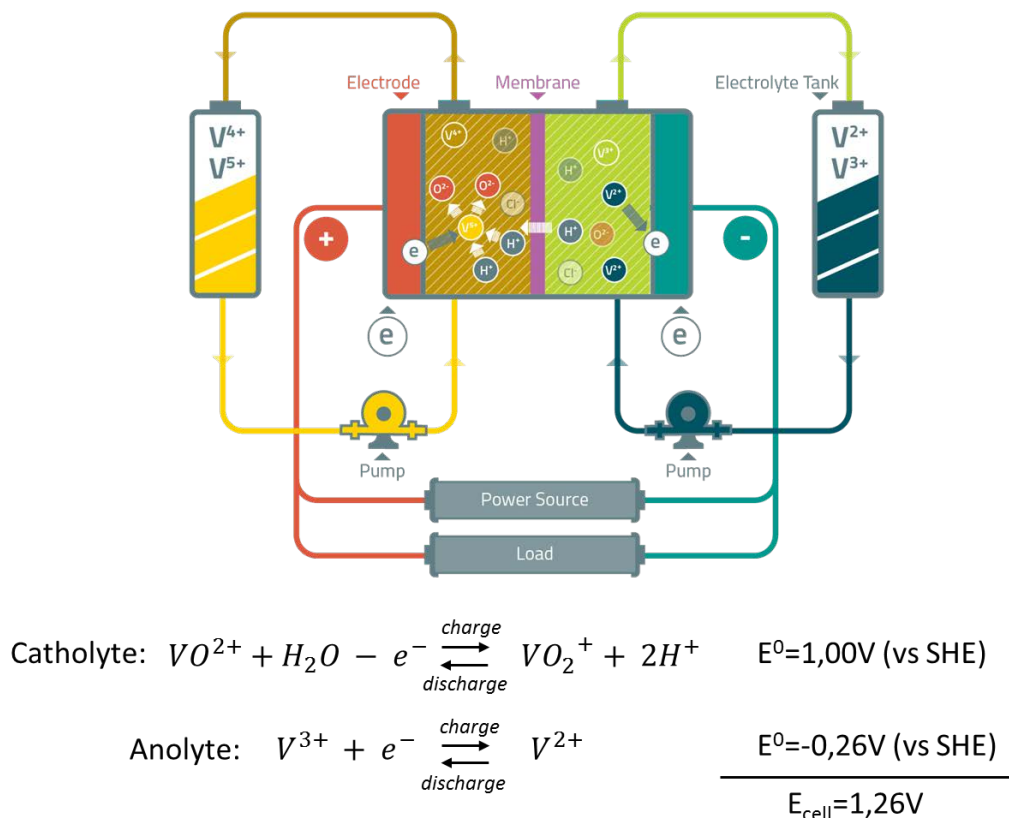


Figure 1.16. Illustration of an All-Vanadium Redox Flow Battery System ⁹³.

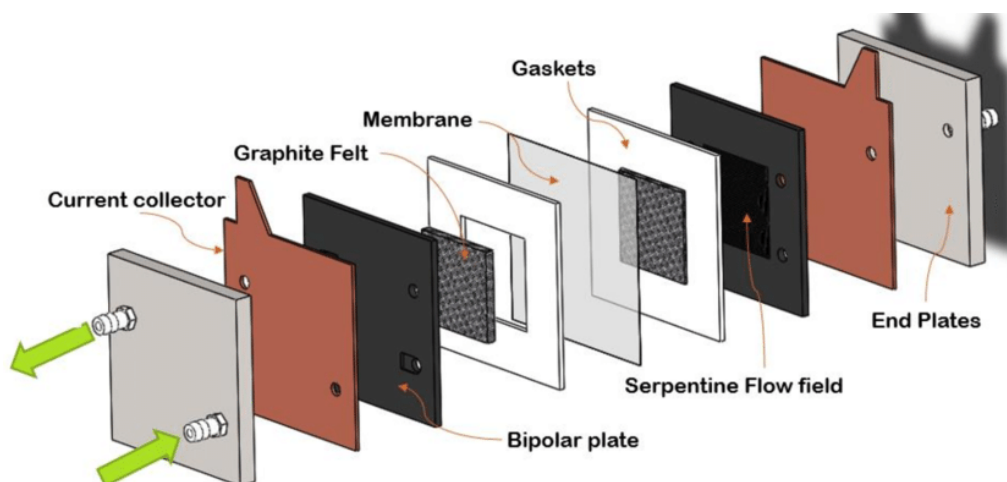


Figure 1.17. Components of a filter-press redox flow cell ⁹⁴.

- Redox-Active Electrolytes

The electrolytes used in conventional RFBs are mainly based on aqueous solutions of redox pairs such as chromium, iron, vanadium or copper. Hence, different systems have been developed based on: Fe-Cr, Br-polysulfide, Zn-Br, all-Fe and all-Vanadium ⁹⁵ (Table 1.3). The latter is the most widely studied system and the one which has achieved higher development degree. It was discovered by Prof. Skyllas-Kazakos and co-workers in 1986 and is based on soluble vanadium pairs in acid media. This system incorporates vanadium in four different oxidation states (V^{2+}/V^{3+} for the anolyte and VO^{2+}/VO_2^+ for the catholyte) (Figure 1.16). Since both electrolytes just contain vanadium in different oxidation states, if the species migrate from one compartment to the other, the capacity decay resulting from this crossover will not produce cross-contamination and can be counterbalanced so the initial state can be recovered via a simple “rebalancing” process ⁹⁶. This system has been scaled up and there are several large demonstration projects around the world based on All-Vanadium RFBs ²¹. The biggest one is being built in China by Rongke Power with 200MW and 800MWh which is the largest battery in the world²⁵.

Table 1.3. Chemistry of the different developed RFB systems

Battery	Catholyte	Anolyte	Electrolyte	OCV (V)
Fe/Cr	$\text{Fe}^{2+} \leftrightarrow \text{Fe}^{3+}$	$\text{Cr}^{3+} \leftrightarrow \text{Cr}^{2+}$	HCl	1.18
Br/PS	$3\text{Br}^- \leftrightarrow \text{Br}_3^-$	$\text{S}_4^{2-} \leftrightarrow 2\text{S}_2^{2-}$	NaBr/Na ₂ S	1.27
Zn-Br	$3\text{Br}^- \leftrightarrow \text{Br}_3^-$	$\text{Zn}^{2+} \leftrightarrow \text{Zn}$	ZnBr ₂	1.80
All-Fe	$\text{Fe}^{2+} \leftrightarrow \text{Fe}^{3+}$	$\text{Fe}^{2+} \leftrightarrow \text{Fe}$	Fe^{2+} in HCl	1.00
All-V	$\text{V}^{4+} \leftrightarrow \text{V}^{5+}$	$\text{V}^{3+} \leftrightarrow \text{V}^{2+}$	H ₂ SO ₄	1.26

- Separators

The main purpose of the ion exchange membranes is to avoid the contact between the electrodes (short-circuit) and the mixture of the electrolytes (crossover). Besides, the material must exhibit high ionic conductivity to allow the ions' movement without increasing the internal resistance of the cell. Depending on their permeability, they can be classified in two groups: anionic (only anions can go through the membrane) or cationic (only cations can go through the membrane)⁹⁷. The most employed ones in RFB as well as in fuel cells are from the latter group, and were developed by Dupont in the 60's. They are made of a polymer-based material called Nafion[®], which exhibits high chemical stability in acidic aqueous media. However, they show poor performance in terms of vanadium crossover, since the migration of some electrolyte species through the membrane is not completely avoided. This migration or crossover leads to loss of efficiency due to self-discharge and imbalance of electrolyte. Consequently, huge efforts are being made by the scientific community to develop new separators either by modification of Nafion or using other materials (adding other polymers, inorganic particles, etc)⁹⁸⁻¹⁰⁰. However, nowadays, there are no membranes that exhibit good performance with low cost. In non-aqueous systems, these Nafion-based membranes exhibit really poor-performance since they need to be soaked in aqueous media, otherwise they exhibit extremely restricted ion conductivity which increases the internal resistance of the cell and limits the applicable current densities.

Thus, other separators/membranes such as porous separators (Celgard)¹⁰¹, ion exchange membranes (Neosepta, Fumasep)¹⁰¹ or porous polymeric composite separators (PTFE)¹⁰² are being investigated.

According to the characteristic mentioned above, the main advantage of the current RFB is their huge versatility due to the decoupling of the energy and the power densities. This feature allows for having a more adapted design to the applications requirements without oversizing the battery in terms of capacity/power as happens in static-batteries. In addition, since the electrodes do not suffer from structure transformations, these batteries are more suitable for long cycles (>10000 cycles, 10-20 years)¹⁰³. Despite their advantages, RFB have not been commercialized on a massive scale. Until now, the reason behind this poor penetration in the market is the high cost of the electrolytes and the ion exchange membranes used as separators. These two components represent up to 70% of the total cost of the battery (Figure 1.18) ^{104,105}. However, this situation could change in the next years due to: lowering prices of membrane material and the emerging business models based on electrolyte leasing. In the future, the limiting factor for these batteries could be the high initial capital cost and the operating cost for batteries with lower energy density and lower efficiency than Li-ion technology.

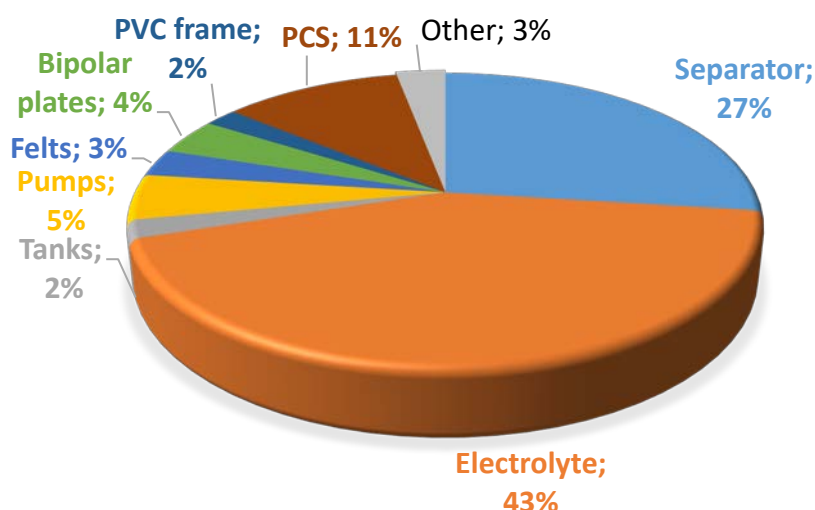


Figure 1.18. Distribution of cost for all-Vanadium for a 1MW system (4MWh-450 \$kWh⁻¹)¹⁰⁴.

The reasons behind the high cost of the electrolytes and the membranes are:

- The electrolyte active materials are transition metal ions which are expensive ($2.5 \text{ €}\cdot\text{mol}^{-1}$)¹⁰⁵, scarce¹⁰⁶ and some of them are toxic. In addition, they are mostly based on acid aqueous media which limits the voltage operation because of the water electrolysis ($\sim 1.23 \text{ V}$).
- The ion-exchange membranes used as separators are made of Nafion which price used to be high (from $\$500$ to $\$1000$ per m^2 ; although nowadays the prices are dropping below $\$250$ per m^2)¹⁰⁷. Besides their high cost it is worth to mention that they are poor performing since the crossover of active species is not completely avoided.

To overcome these disadvantages related to the conventional metal based aqueous RFBs a growing effort has been focused on developing novel systems to increase energy density and operating voltage. Many studies are being focused on new catalysts, redox couples and membranes since the chemistry and the materials used in the system determine all the main properties of the battery. In terms of electrolytes, new redox couples with tailored structure have been proposed to improve the redox potential, the solubility, the kinetics and the stability. In the electrode materials new research is being done to improve the conductivity and the kinetics and to reduce the overpotentials. In the case of the membrane the new approaches involve devices in which the use of ion-exchange membrane is not needed. Instead, the alternatives are: i) using size exclusion separators, which consist of porous separators and big size active molecules or redox-polymers ¹⁰⁸; ii) making hybrid flow batteries in which one active material of the battery is a solid metal electrode ¹⁰⁹; and iii) formulating mixed-reactant electrolytes, where the catholyte and the anolyte contain both the negative and the positive active molecules. In this way the migration due to the different concentration is avoided ¹¹⁰. All of these strategies are intriguing alternatives but have also some associated disadvantages such as low specific capacity due to the large size of the active molecules, coupled power and energy density or lower material utilization, respectively. The most important requirements of the electrolytes,

electrodes and membrane for the development of new and improved redox electrolytes are enumerated in Figure 1.19

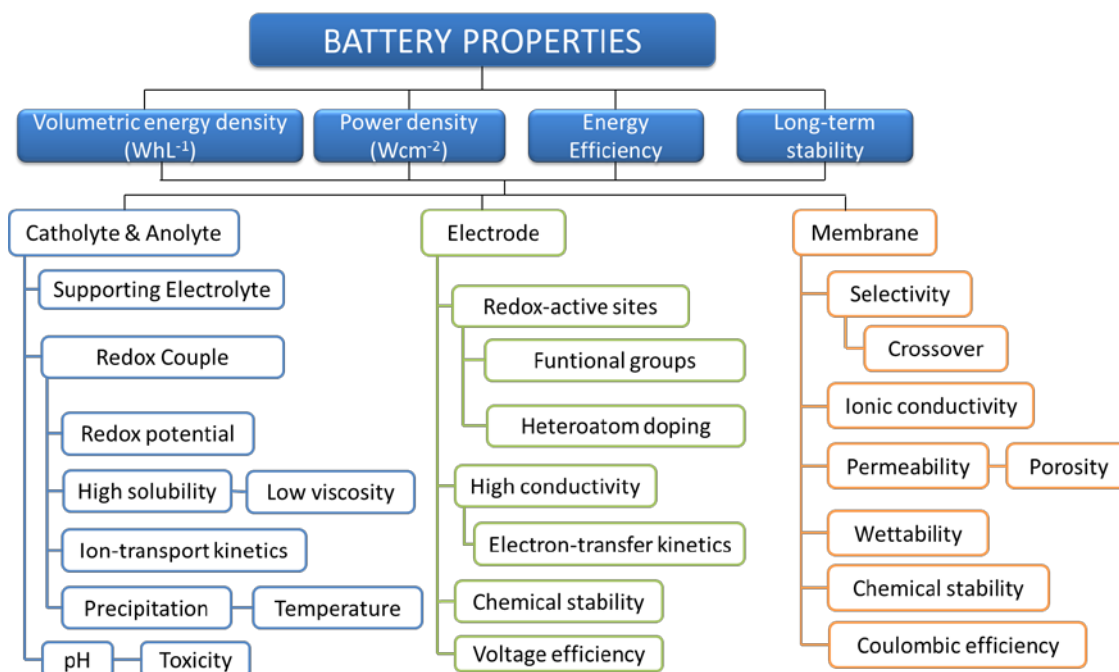


Figure 1.19. Requirements and considerations for the development of flow batteries (Adapted from ⁹⁰).

1.3.2.2 *Next Generation in Redox Flow Battery Systems*

Recently, novel flow batteries have been reported which have a new architecture and novel chemistries break away from the traditional frameworks. Some of these new designs are following described and illustrated in Figure 1.20:

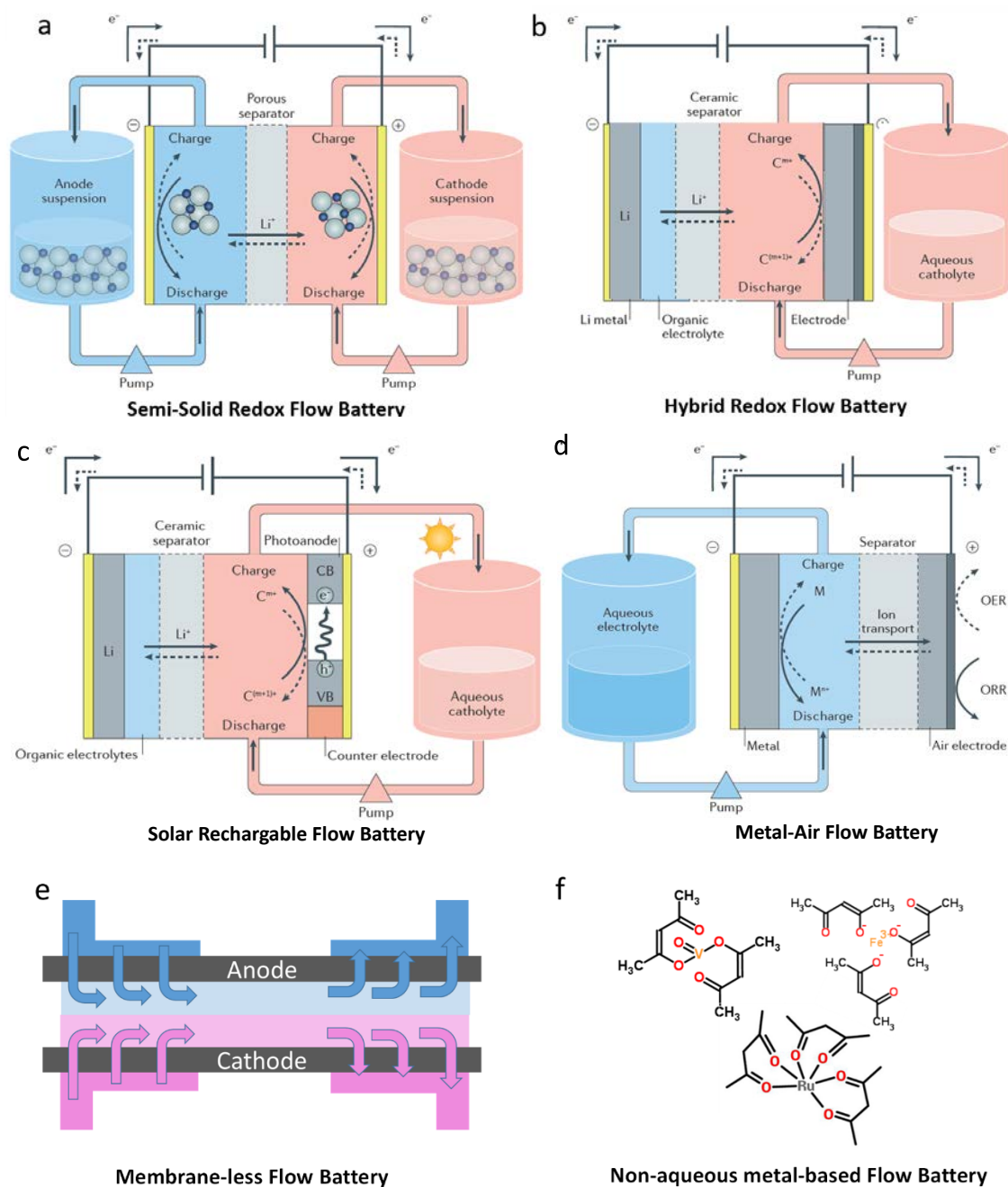


Figure 1.20. Schematic Illustration of different design of redox flow batteries. a) semisolid Redox Flow Battery; b) Hybrid Redox Flow Battery; c) solar- Rechargeable Flow battery; d) metal-air Flow Battery; e) Detail of the reactor of Membrane-less Flow Battery design; f) Metal based complexes used in Non-aqueous Flow Battery. Adapted from ^{90 111}.

- **Semi-solid flow batteries.** This approach is based on using the conventional cathode and anode materials used in Li-ion technology but making them flowable. Thus the electrolytes are solid suspensions of active materials with high capacity and a conductive additive dispersed in the solvent which commonly is non-aqueous. Their main disadvantages are the poor conductivity and the high viscosity of the electrolyte which can produce difficulties to pump them. This configuration tries to solve the limitations of solubility of active species and battery voltage, since they use suspensions instead of solutions and non-aqueous electrolytes with wider electrochemical voltage window. In addition, the utilization of suspensions enables the use of microporous separators instead of ion-exchange membranes ^{112,113}.

- **Hybrid Flow batteries.** These batteries take the advantage of using an extendable storage vessel and flowable redox active materials for increasing the energy density in one side of the battery and the other part is a conventional metallic electrode. In this category one of the widely studied are lithium-metal based flow batteries in which the anode is lithium metal and for the positive side of the battery a flowable solution containing redox active material dissolved is used ¹¹⁴.

- **Solar rechargeable flow batteries.** In these batteries, instead of vanadium species, photoactive materials are dissolved into one electrolyte and are used to generate photoelectrons. Thus, it enables to store solar energy directly. Two different configurations have been studied. In the first one the photochemical cell and a RFB are physically connected by an external electrolyte circuit ¹¹⁵ whereas in the second one both are co-located ¹¹⁶.

- **Metal-air flow batteries.** These systems have only one electrolyte tank in which the negative electrolyte is stored in the positive side of the battery, while for the other side, the oxygen from the pumped air is used as active material. Thus, this technology merges the RFB and metal-air batteries. In comparison with conventional RFB the cost of the active species is significantly decreased and comparing with conventional metal-air batteries the metal dendrite growth problem is mitigated ^{117,118}.

- **Membrane-less flow batteries.** In these designs the membrane is removed, since the mixing of the electrolytes is avoided by limiting the flow of the electrolytes to laminar regime ¹¹⁹. On account of this restriction, this configuration is restricted to be used only in microfluidic systems. The main advantage is the elimination of the expensive membrane of conventional RFB.

- **Non-aqueous metal-based redox flow batteries.** This approach offers the opportunity to broaden the RFB applications by using organic solvents since they make possible to achieve wider working temperature, higher cell voltage and potentially higher energy density. Instead of simple metal ions which have very limited solubility metal-organic ligand coordination complexes are used in these devices. A metal ligand complex is formed by a metal center and several chelating ligands. The metals used are Ru, V, Fe, Cr, Co and the organic ligands can be divided in different groups such as double-oxygen bidentate ligands, double-nitrogen bidentate ligands, double sulfur bidentate ligands and hybrid atom bidentate ligands. Among these organic ligands the double-oxygen bidentate ligand (“acac”) is mostly used ^{95,120–122}. The main drawback of these batteries is their low power density due to the low conductivity of the organic electrolytes and the high resistance that the membranes exhibit in this media. Thus, the overpotentials increase and consequently these batteries provide low voltage efficiency ¹²³.

- **Organic redox flow batteries.** In these devices the metal active species are replaced by organic active molecules either using aqueous or non-aqueous electrolytes. Organic molecules are cheaper and abundant and some of their properties can be tuned by functionalization. These are great advantages in comparison with the expensive, scarce and less soluble inorganic species commonly used ^{124,125}. More detailed information about this type of organic batteries has been included in next section.

All of the abovementioned next-generation technologies are in a nascent stage and represent a notable progress in RFBs technology. In particular, a great interest in RFBs based on redox organic molecules has growth in the last 5 years among the scientific community. In the next section of this introduction, some examples are described.

1.4 Organic Redox Molecules in Energy Storage

There is a growing interest in using organic redox molecules in energy storage due to the advantages that organic molecules provide in comparison with inorganic or metal-based materials.

These organic active materials are interesting for electrochemical energy storage devices since they are abundant, lightweight, low cost and environmental friendly. On account of this, they are not considered just an alternative to traditional energy storage materials; rather they have excellent features to lead innovative technologies.

Despite of being abundant and relatively inexpensive, other main advantage is their structural diversity that can be tailored by relative simple synthesis methods. These changes in the structure are a way to tune their redox potential and other important properties such as solubility, electron transfer rate and chemical and electrochemical stability that definitely have a strong effect on the characteristics of the final devices. Organic compounds are hugely diverse due to the large number of possibilities offered by synthetic chemists. The number of possible organic compounds that can be interesting for electrochemical energy storage is enormous. Therefore, exploring and testing all the possibilities, even only the synthetically and practically relevant, by experimental trial and error is a really time and resource consuming activity. In order to reduce the number of candidates, great efforts are being done in the development of computational chemistry to provide high-throughput screening tools for electrode materials and electrolytes ^{126–131}.

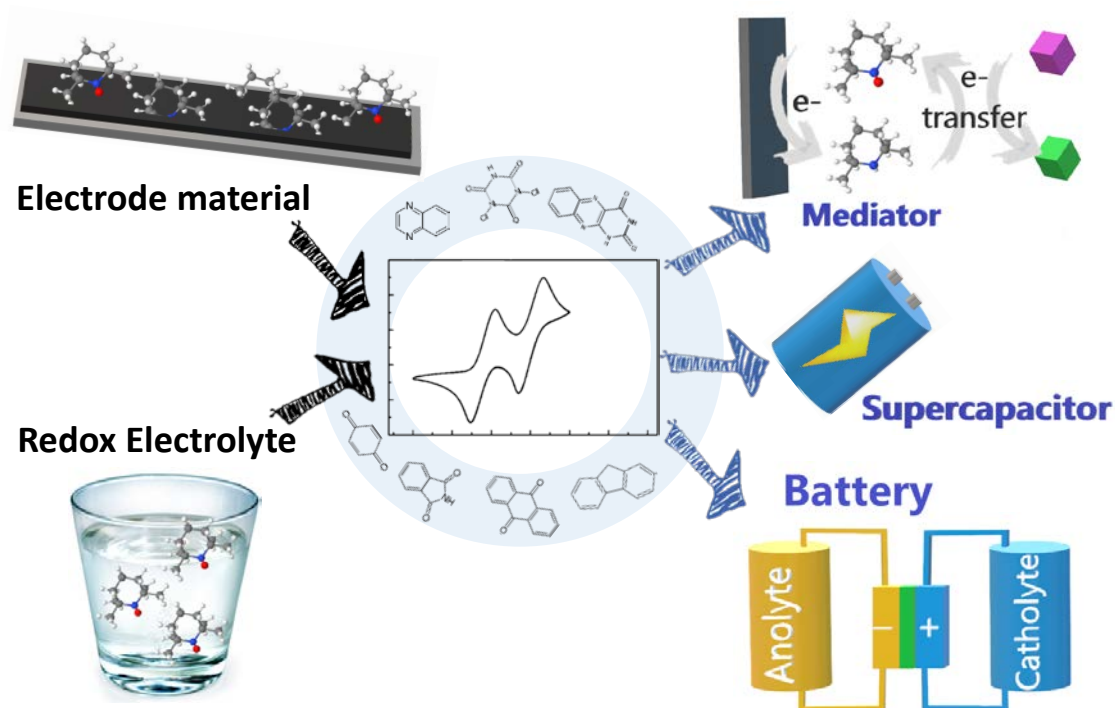


Figure 1.21. Schematic representation of redox organic molecules and their applications in energy storage.

Organic materials can be applied to different energy storage devices depending upon their physicochemical and electrochemical properties. It is important to highlight that, the same organic compound can be applied in different materials and components, for example, they can be incorporated in polymers¹³², be mixed with porous carbon and binders¹³³ and act as electrodes in Li-ion batteries or be dissolved into the electrolytes. As illustrated in Figure 1.21, they can be used as active component within the electrodes or as soluble active material in redox electrolytes. Thus, one of the main differences is that organic molecules for electrode materials should not be soluble into the electrolyte whereas organic molecules for redox active electrolytes should exhibit as high solubility as possible. These redox-active organic materials have been applied to different devices such as: mediators/redox shuttles in Li-ion batteries, supercapacitors and redox flow batteries^{130,131,134,135} (Figure 1.21).

Among the immense number of organic molecules, the majority of the work performed on organic materials for energy storage has been focused on quinones^{128,129,136}.

Quinones

One of the main families of organic molecules used in energy storage are quinones. Quinones are a class of redox-active organic compounds that contain two carbonyl groups in an unsaturated six-member ring structure. Depending on the number of rings different types of quinones can be distinguished (Figure 1.22); One ring: benzoquinones; Two-rings: naftaquinones; Three-rings: anthraquinones.

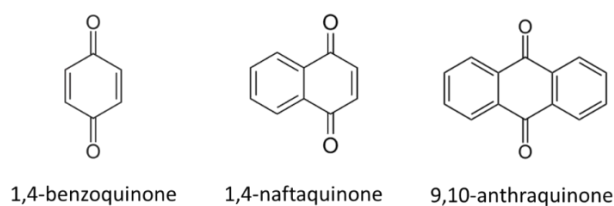


Figure 1.22. Molecular structure of different quinones.

In nature, quinones play a vital role in numerous electrochemical reactions for energy transduction and storage. These redox reactions involve two electrons due to the two carbonyl ligands contained into the quinone structure and exhibit high reversibility and fast kinetics, which are important features for their applications in electrochemical devices. Electrochemical studies of quinones in different media were performed previously to understand their redox behavior (Figure 1.23)¹³⁷. In general, the reaction mechanism pathway depends on the protic or aprotic nature of the media. Thus, the reduction process can occur through the formation of the protonated hydroquinone or via the formation of charged radicals (semiquinone). Consequently, the potential of the redox reaction changes and therefore, the final properties of the devices are also modified.

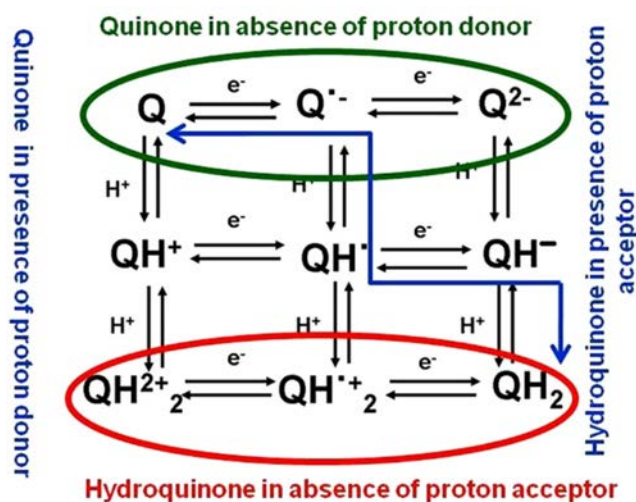


Figure 1.23. Mechanistic pathways of quinones ¹³⁸.

In addition to the nature of the electrolyte, it has been demonstrated that the position and the type of substituents also affect the electrochemistry of quinones significantly ^{128,139}. The substitution with electron donating groups (EDG) leads to lower reduction potentials, whereas substitution with electron withdrawing groups (EWG) leads to increased reduction potentials. It has been also discovered that addition of functional groups near to the carbonyl groups has the largest effect on the reduction potential whereas the substitution away from the carbonyl groups leads to the greatest improvement in solubility ¹²⁸.

Considering all these characteristic of organic redox active molecules, the results of applying them on SC and RFB are described in the next sections of this chapter.

1.4.1 Organic Redox Molecules for Supercapacitors

SC are described by having high power density, but low energy density. Two different strategies are being pursued to increase energy density without impairing power density: the incorporation of the organic redox- active material into the electrode or its dissolution into the electrolyte, as shown in Figure 1.21.

- **Organic Redox Molecules as Active Electrode Materials for SC**

As it was mentioned in previous sections of this introduction, conducting polymers, nitroxyl radical polymers and conjugated carbonyl compounds such as quinones have been proposed as promising redox materials¹⁴⁰. Thus, the incorporation of quinones derivatives into carbon based materials (e.g CNTs, carbon onions, activated carbons and graphene) via impregnation or grafting have been proposed to enhance the energy density^{81,141–143} as it was mentioned previously (Figure 1.24).

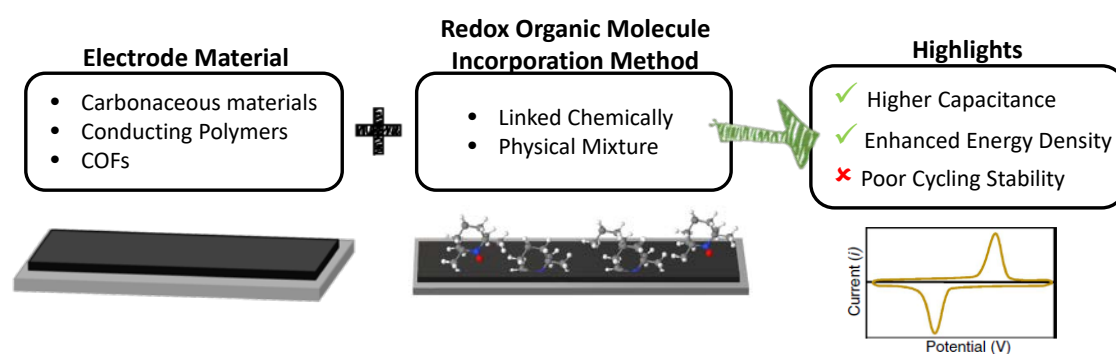


Figure 1.24. Schematic representation of the strategy for improving SC performance by adding organic redox molecules as active electrode material.

For example, Chen et al.¹⁴⁴ decorated hierarchical porous carbon nanotubes with anthraquinones achieving a twofold capacitance value. Pognon et al.¹⁴⁵ reported 66% enhanced specific capacitance of black pearl carbon by covalently attaching catechol groups. Anjos et al.¹⁴⁶ attached quinone derivatives through a simple hydrophobic interaction showing a good capacity retention of 97%. Quinones can also be hybridized with conducting polymers or covalent organic frameworks (COF). Dichtel's group¹⁴⁷ taking advantage of the useful properties of 2D COFs, incorporated 2,6-diaminoanthraquinone (DAAQ) into COFs linked by an electro active β -ketoenamine. The material exhibited a higher current density and also increased electron and proton transfer rates. Kim et al.¹⁴⁸ synthesized a 3D mesostructured hybrid electrode consisting of polypyrrole and catechol. As a result, the hybrid electrode showed an enhanced volumetric capacitance. Tomai et al.¹⁴⁹ showed the incorporation of two different organic molecules one in each electrode in a proton rocking chair-SC with a

large energy of 20 Whkg^{-1} . In Figure 1.25 some organic compounds used in electrode materials are shown.

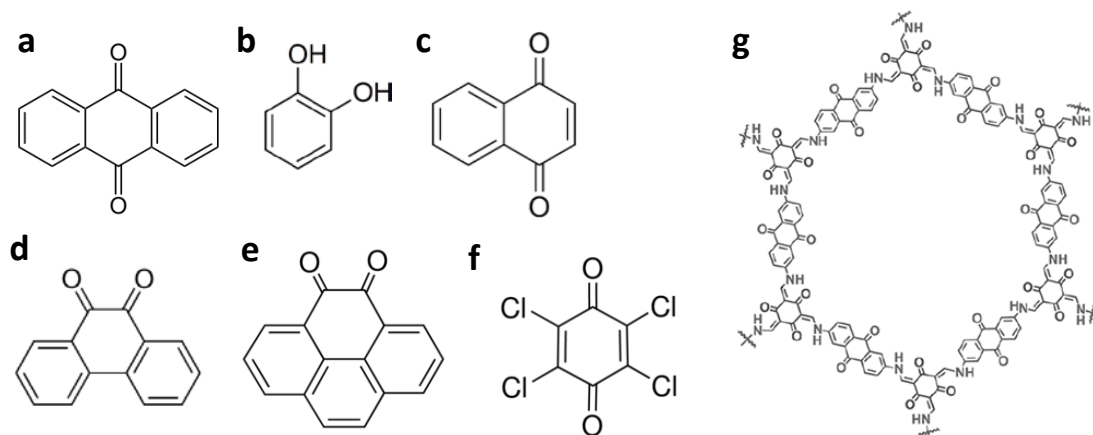


Figure 1.25. Organic materials used in SC. a) 9,10-anthaquinone ^{144,149}; b) catechol ^{145,148}; c) 1,4-naphthoquinone ¹⁴⁶; d) 9,10-phenanthraquinone ¹⁴⁶; e) 4,5-pyrenedione ¹⁴⁶; f) tetrachloro-1,4-benzoquinone ¹⁴⁹; g) β -ketoenamine and 2,6-diamino anthraquinone linked COFs ¹⁴⁷.

The main challenge of these hybrid materials is achieving high capacitance values while keeping a good cycling stability. Unfortunately, the cycle life of the device is often decreased due to the gradual dissolution of the organic moieties into the electrolyte and the structural and volumetric changes associated to the redox reaction. Other approach is dissolve directly the redox molecule into the electrolyte ^{83,150,151} (Figure 1.26).

• Organic Redox Molecules in Redox Electrolytes for SC

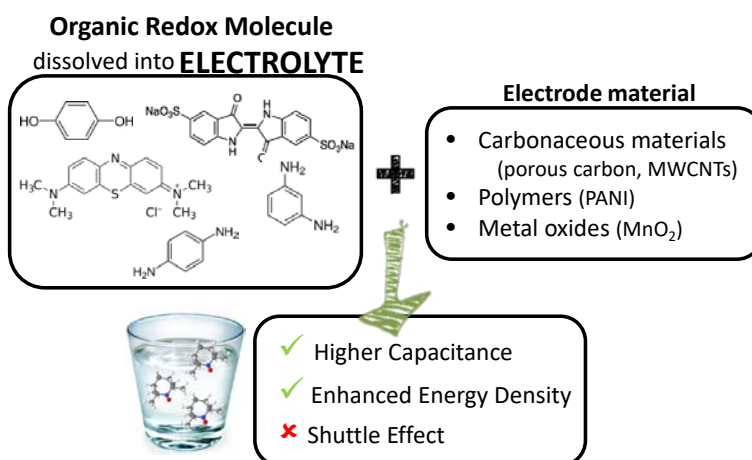


Figure 1.26. Schematic representation of the use of redox electrolytes in SC

Roldan et al.^{88,152} proposed for the first time the use of quinoid-aqueous electrolyte in a hybrid SC (Figure 1.27). In that study, the solution of hydroquinone (HQ) in acid aqueous solution leads to a 9-fold increase in capacitance. Using the same solvent and electrode material (MWCNTs), the same group proposed the use of methylene blue (MB) as active redox moieties instead of HQ and a Nafion[®] membrane as separator to avoid the shuttle effect of the generated reduced-MB which otherwise would migrate to the opposite electrode¹⁵³. In addition, in other work¹⁵⁴ they also proposed the use of indigo carmine as an active species which can be reduced and oxidized in two redox processes. However, an important capacitance reduction was observed over cycling which can be attributed to a decrease in the redox activity of the indigo carmine.

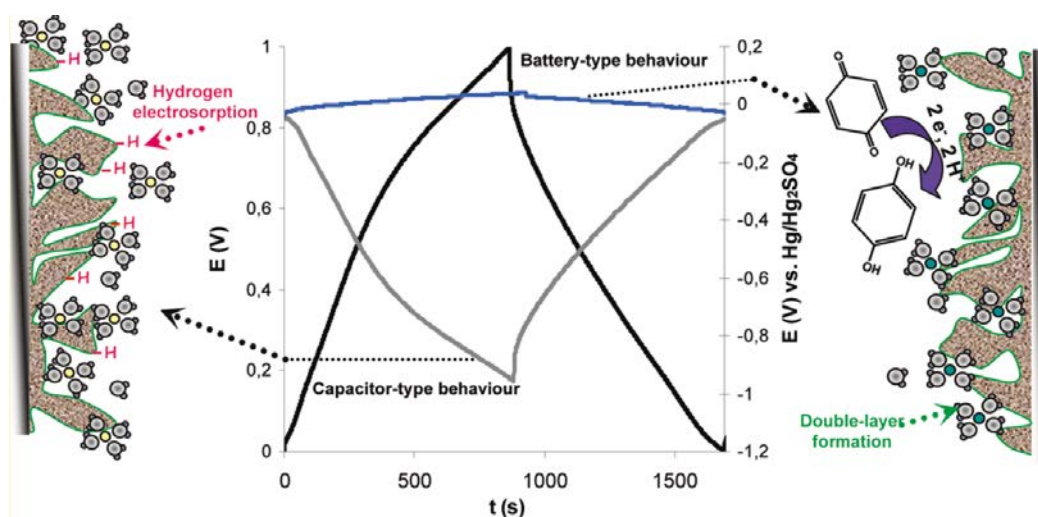


Figure 1.27. Charge-Discharge voltage profile of a hybrid SC using HQ-redox electrolyte and the potential profile of each electrode (in blue and grey). Taken from⁸⁸.

The importance of the carbonaceous material used as electrode was highlighted by Fontaine et al.^{155,156}. In these studies the electrolytes consist in a biredox ionic liquid in which both cations and anions were functionalized with organic redox molecules, OH-TEMPO (4-hydroxy-2,2,6,6-tetramethylpiperidiny-1-oxyl) and anthraquinone, respectively. Thus, the energy density was doubled and maintained over 2000 cycles. Using a protic ionic liquid as a solvent and HQ as active dissolved material Velayutham et al.¹⁵⁷ achieved a high specific energy density around 31 Wh·kg⁻¹. The hybrid device also showed low charge transfer resistance and improved ionic conductivity due the presence of the quinone, according to authors' claim. Wang et al.¹⁵⁸ used the same

active molecule (HQ) combined with functionalized CNTs as a strategy to improve the performance of the electrode. Wu et al.¹⁵⁹ presented an organic molecule from the amine family (m-phenylenediamine) dissolved into KOH to enhance (~114%) the specific capacitance of a carbon-based SC. The redox active electrolytes can be also combined with pseudocapacitive materials to achieve higher energy values. In this sense, Wu et al.⁸⁹ dissolved p-phenylenediamine into KOH as electrolyte, using ball-milled MnO₂ based-electrodes which allows for having a 10-fold higher energy density (10Wh·kg⁻¹). Also Su et al.¹⁶⁰ showed the performance at low temperature of the same redox-active electrolyte in a MnO₂-nanorods hybrid SC. In the same line, Xie et al.¹⁶¹ proposed the use of HQ dissolved in H₂SO₄ as electrolyte for polyaniline (PANI)-based hybrid SC. The authors turned out that the redox reactions proceed through an “inner-sphere” mechanism, which involves the adsorption of the molecule in an edgewise orientation that allows electronic transfer onto the electrode surface. Chun et al.¹⁶² proposed an enhanced design of hybrid SC in which two redox couples were dissolved into the electrolyte. In this case, the redox couple for the negative side was organic (methyl viologen dichloride) whereas the reaction of the positive side was undergone by KBr₂. The authors affirmed that the redox couples in the solution appear to be entirely utilized which brings this hybrid SC closer to a RFB concept. The approach of merging some SC and RFB characteristics was also followed by Hatzell et al.¹⁶³. These authors showed the use of flowing p-phenylenediamine redox active electrolyte in a so called “flow-capacitor”. As has been mentioned almost all the reported studies are based on aqueous media which limits the working voltage. Thus, the use of other types of electrolytes such as ionic liquids can help broaden the possibilities and improving the performance of these devices.

1.4.2 Organic Redox Molecules as Active Species for RFBs

Redox Flow Batteries have recently come back into the spotlight for research due to the need for inexpensive grid storage. Great efforts have also been done in replacing the expensive metallic species in both anolyte and catholyte by less-expensive organic redox molecules. In an ideal scenario these organic redox compounds can help to

achieve specific energy of $150 \text{ Wh}\cdot\text{kg}^{-1}$ or energy density of $210 \text{ Wh}\cdot\text{l}^{-1}$ which are values comparable to conventional lithium-ion batteries. It is important to note that this estimation is based on a RFB in which the molecular weight of the active species is $120 \text{ g}\cdot\text{mol}^{-1}$, 2 electrons transferred per molecule, cell voltage of 1.5 V and 75 % round trip energy efficiency¹¹⁴. Consequently, the development of organic materials specifically designed to be applied in RFBs has increased, with most research focused on quinones¹³⁵. Among the various quinone molecules, computational studies have suggested that the group containing 9,10-anthraquinone provides the most suitable redox couples for the negative electrolyte whereas naphthaquinones and benzoquinones are more appropriate for the positive electrolyte¹³⁹.

Although, several examples of organic-inorganic RFBs (one of the electrolyte is based on inorganic materials) have been reported, in this chapter only those RFBs in which both catholyte and anolyte involve organic materials are contemplated.

• Organic Aqueous RFBs

In this section several examples of RFB with organic molecules dissolved in aqueous electrolytes are described. Figure 1.28 shows the types of organic molecules used in this configuration and their most significant characteristics.

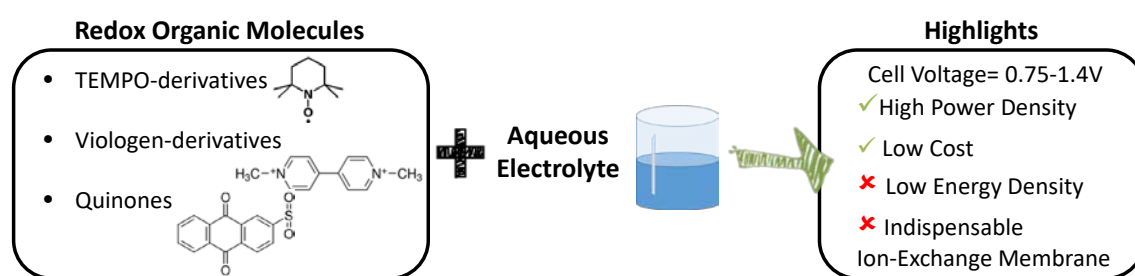


Figure 1.28. Schematic summary about the organic redox molecules used in Aqueous RFB and their characteristics.

The first example of organic aqueous RFB was proposed by Yang et al. in 2014¹⁶⁴. The negative (anolyte) and the positive (catholyte) electrolytes were aqueous and based on quinones, 9,10-anthraquinone-2-disulfonic acid and 1,2-benzoquinone-3,5-disulfonic

acid, respectively. The battery exhibited a capacity retention of 90% over 12 cycles and cell voltage around 0.75V. The degradation of the molecule in the positive side led to the decay of the battery voltage. After this all-quinone battery, other types of organic molecules were tested in aqueous RFB. Thus, Brushett et al.^{165,166} proposed the use of quinoxaline in alkaline media as anolyte and 1,2 dihydrobenzoquinone-3,5-disulfonic acid in acid media as catholyte which yield to a battery with a significant decrease in capacity attributable to the difficulties of keeping the proper pH in each side of the cell. In 2016 Liu et al.¹⁶⁷ proposed a RFB based on viologen (4,4'-bipyridine derivative) and TEMPO (2,2,6,6-tetramethylpiperidinyloxy) molecules for the anolyte and the catholyte respectively, dissolved in the neutral aqueous electrolyte. The TEMPO molecule was functionalized with a hydroxyl group to enhance its solubility in aqueous media. As a result, the open circuit voltage was 1.25V. Functionalization of TEMPO was also the strategy followed by Schubert et al.¹⁶⁸ to increase the performance of other battery based on the same molecules with a theoretical OCV of 1.4V. In addition, the cell exhibited good cyclability over 100 cycles.

Schubert and co-workers proposed the first polymer RFB in 2015¹³². In this battery the polymers are based on viologen and TEMPO dissolved in neutral-pH media. In this concept it is important to minimize the dynamic viscosity of the electrolyte. The main advantage of polymer RFBs¹⁶⁹ is that, due to the large size of polymers, the membrane can be replaced by a size-exclusion porous separator which is 90 % cheaper than usual ion-exchange membranes.

- **Organic Non-Aqueous RFB**

Previous research on organic molecules as redox-mediators in Li-ion batteries motivated that the first examples of organic redox flow batteries were non-aqueous. Non-aqueous electrolytes offer a wider voltage stability window which enables flow batteries to operate at higher voltages. Figure 1.29 shows the types of organic molecules used in this configuration and their most significant characteristics.

The active species were based on derivatives of quinoxaline¹⁷⁰, anthraquinone¹⁷¹, TEMPO¹⁷² and DBBB (2,5-Di-tert-butyl-1,4-bis(2-methoxyethoxy)benzene)¹⁷³. Since the

selected non-aqueous electrolytes are mainly aprotic, electron transfer reactions involve the formation of charged radicals that in some cases exhibit poor chemical stability in the long-term¹³⁴.

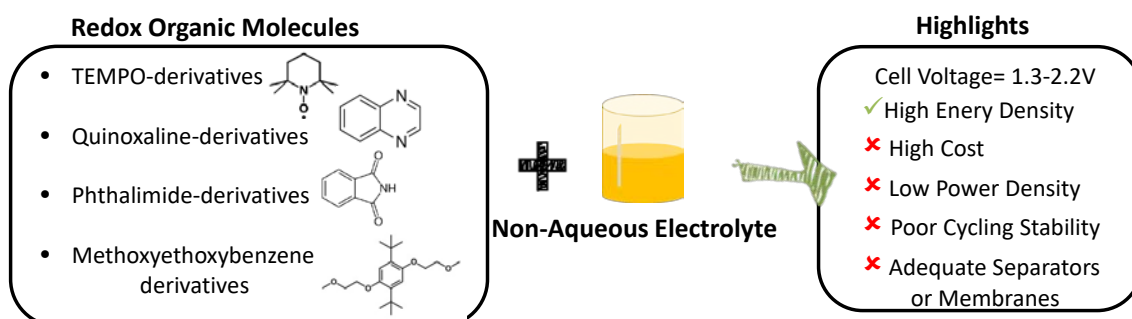


Figure 1.29. Schematic summary about the organic redox molecules used in Non-Aqueous RFB and their characteristics

The first organic non-aqueous RFB was proposed by Li et al. using N-methylphthalimide and TEMPO in acetonitrile for the anolyte and catholyte, respectively¹⁷². The cell voltage was 1.6 V and the kinetics were several orders of magnitude faster than those of V(II)/V(III)¹⁷⁴. The cycling test was conducted in a static cell, as many other examples due to some of these materials have been previously used in Li-ion systems. Another TEMPO-based system was proposed by Park et al.¹⁷⁵ In this case camphoquinone and oxo-TEMPO were used as active species in the anolyte and catholyte, respectively with an open circuit voltage of 2.12 V. The battery containing 0.2 M active species exhibited coulombic and energy efficiencies of 80 and 71 % at the third cycle. This poor cycling performance was attributed to the crossover and poor mass transport within the static cell configuration. The unsatisfactory cycle life of this type of RFBs is usually attributed to the use of ion-exchange membranes, which exhibit low conductivity and high resistance in this media. Thus, other kind of separators are being proposed such as porous inexpensive separators. However, these separators do not avoid the cross-mixing of the electrolytes and some groups have proposed the use of already mixed-electrolytes (the active species are mixed in the electrolyte and a single electrolyte is used). On example of this strategy is the study published by Brushett and co-workers¹⁷⁰. In addition, they introduced the use of quinoxaline and

DBBB for the first time in this application. However, the cell potential was still low (1.3 V) for non-aqueous systems. The proof-of-concept cell was cycled in a static coin cell with mixed-reactant electrolytes. The coulombic efficiency was quite low and attributed to the use of a single electrolyte in the coin cell configuration. Later Kaur et al.¹⁷⁶ investigated the replacement of DBB with 3,7-bis(trifluoromethyl)-N-ethylphenothiazine (BCF3EPT) which is more soluble (1.2 M) compared to DBBB. The performance of the battery was superior to the previous system, but it still showed a decline in capacity after 50 cycles due to the dimerization of radicals at high concentrations.

Wei and co-workers¹⁷⁷ proposed a new system based on 9-fluorenone (FL) and 2,5-di-tert-butyl-1-methoxy-4-[2'-methoxyethoxy]benzene (DBMMB) were used as negative and positive active species, respectively. The solubility was quite high (2M) in acetonitrile and the battery was cycled at high current density (15 mAcm⁻²) for 100 cycles. A highly porous separator was used and important crossover rates were detected. Finally, the battery suffered from capacity fade losing 80% of its initial capacity after 100 cycles, which is attributed to the reactivity of the free radical involved in the reaction mechanisms. The same research group developed other systems based on DBMMB which operate at even higher current density (35 mAcm⁻²)¹¹⁰. In this case the FL was replaced by N-methylphthalimide in the anolyte. Thus, the cell voltage was 2.1V and the authors suggested that the N-methylphthalimide radical anion cannot undergo any side reaction with the supporting electrolyte. During the cycling the battery maintained constant capacities and efficiencies with a high active material utilization (85-77%).

- **Symmetric Organic RFB**

The previous examples were asymmetric since different active species were used for the anolyte and the catholyte. Using the same compound could solve the issue of crossover contamination. On account of this, the group of prof. Abruña¹⁷¹ proposed a symmetric system using a commercial diaminoanthraquinone derivative (DAAQ) as active specie in both electrolytes. These anthraquinones have more than five discrete redox states over a wide range of potentials. During the charge the same molecules

are reduced in the anolyte and oxidized in the catholyte. The theoretical energy density of the battery is $120 \text{ Wh}\cdot\text{mol}^{-1}$ which is significantly higher than the one obtained with all-vanadium electrolytes ($34 \text{ Wh}\cdot\text{mol}^{-1}$). Its main drawback is the low solubility of the species. The performance was demonstrated in a static glass cell but it needs to be further improved to achieve an energy density comparable to existing aqueous systems. Other molecules such as nitroxide radicals have also studied in symmetric non-aqueous RFB due to its three redox states¹⁷⁸.

An example of highly water soluble organic molecules with different redox-states was published by Armand et al ¹⁷⁹. This work was based on indigo and anthraquinone derivatives that with a proper choice of aqueous electrolyte are able to both reversibly oxidize and reduce, developing two-sets of fast two proton- electron transfers separated by $\approx 1 \text{ V}$. Thus, using these molecules a symmetric aqueous RFB could be assembled.

The symmetric aqueous RFB was demonstrated by Winsberg et al using a “combi-molecule” in which the combination of TEMPO and phenazine yields an organic redox-active material that can be used as active specie for both, anolyte and catholyte. Thus, the cross-over is mitigated, but the main disadvantage is the amount of unusable active material and the high molecular weight.

Considering the results reported by the different research groups, an appropriate selection and modification of organic molecules and corresponding electrolytes will remain important. In fact, the current challenges to the RFB include: determine safe, sustainable, cost effective electrolytes and redox couples; and moreover, the implementation of adequate engineering approaches to design the cells and the systems.

1.5 Challenges in the Development of New Redox Electrolytes

The growing interest in this type of electrolytes is due to they are an easier alternative than the complex development of new electrodes materials. In this case by simple dissolution of active species into the supporting electrolyte, important parameters can be enhanced such as: capacity, operating voltage or energy and power density. In addition, using inexpensive redox organic molecules the cost of the devices can be significantly decreased in comparison with the inorganic compounds conventionally used. However, some challenges should still be faced in this field.

The active species used in redox electrolytes for energy storage devices may have desirable properties such as multi-electron transfers, increased solubility or fast kinetics in order to yield good performance^{134,180}. In addition, it is also important to use lower molar mass active molecules ($< 200 \text{ g mol}^{-1}$) to obtain high specific capacity. Based on the studies performed in the last years, several technical challenges should be faced in these systems:

1. Enhance the Solubility of Active Species

For aqueous systems it is still a hurdle to achieve highly soluble active species and high cell voltage simultaneously. In the case of non-aqueous systems, many of them suffer from low energy attributed to low concentrations of active species.

2. Increase Power Density

Non-aqueous systems are currently limited by their low power density, mainly due to the small operating current densities ($0.01\text{-}0.5 \text{ mAcm}^{-2}$), caused by the high resistance exhibited by the conventional ion-exchange membranes in these media ($\approx 10 - 100 \Omega \text{ cm}^2$)¹³⁴ and the low conductivity of these electrolytes.

3. Extend the Stability of Active Species

Other important issue is the compatibility of the organic solvents with the active species in non-aqueous cells. Hence, the effect of the supporting salt in the solubility of active species needs to be considered when selecting the supporting electrolytes and their concentration. Moreover, for most organic redox molecules in aprotic

solvents, the electron transfer process involves the formation of radicals. Most of these radicals are reactive which implies poor stability in the long term cycling. In this sense, the supporting salt can be a key element for further improvement the cycle life of the devices. In order to minimize the degradation of radicals, it is important to identify the mechanism to improve the chemical stability, for instance, by tailoring the molecular structure.

4. Deep investigation of the electrode/electrolyte interface

The interface electrode/electrolyte must be deeply understood for controlling interfacial reactions, as well as electrolyte ion dynamics, solvation/desolvation processes and degradation mechanisms that limits the cycle life of the devices.

5. Minimize Crossover Effect

A relevant parameter that has a strong influence in the capacity decay during cycling is the electrolyte contamination due to the crossover of the active species. This cross-migration of the active materials is usually attributed to the poor-performance of the membranes in terms of selectivity. Thus, new separators and strategies to avoid the use of membrane and avoid the crossover are being proposed, such as using already mixed-reactants, applying polymers as active materials, or implementing symmetric cells.

On account of all these limitations that should be further faced, huge efforts are being done in this field that has become in a hot topic in energy storage research.

New molecules and chemistries are being proposed elsewhere for the formulation of new electrolytes as well as new engineering approaches and new concepts to develop innovative designs of the devices. In this sense, some of these challenges have been faced in this thesis since it explores the development of new redox electrolytes based on ionic liquids with organic redox molecules as actives species and its application in novel devices such us hybrid supercapacitors and an innovative concept of membrane-free RFB.

Specifically, in this thesis, the formulation of new redox electrolytes containing commercial available organic molecules has been studied, as well as their

electrochemical characterization. Thus, important parameters such as solubility, redox potential, reversibility, kinetics and diffusion coefficients were determined. Moreover, the electrochemical performance of these new redox electrolytes in devices such as hybrid supercapacitors was analyzed with the main goal of improving their performance. In the characterization of these devices, important aspects like the efficiency, cycling stability and the energy storage mechanism were investigated.

With the aim of facing some of the current challenges of other devices such as Redox Flow Batteries, a new concept of Membrane-Free RFB based on immiscible electrolytes has been presented. This innovative concept relies on biphasic systems that work as a battery without any separator, avoiding the limitations associated with the currently used membranes. In addition, to explore the versatility of this device, different combinations of electrolytes (aqueous and non-aqueous with different organic active species) were studied.

In the next chapter, specific details are given on the objectives and the main goals of this thesis.

1.6 References

- 1 I. Energy Agency, *World Energy Outlook 2017*, 2017.
- 2 J. Rugolo and M. J. Aziz, *Energy Environ. Sci.*, 2012, **5**, 7151–7160.
- 3 S. Weitemeyer, D. Kleinhans, T. Vogt and C. Agert, *Renew. Energy*, 2015, **75**, 14–20.
- 4 World Energy Council, *World Energy Council Rep.*, 2016, **1**, 468.
- 5 X. Luo, J. Wang, M. Dooner and J. Clarke, *Appl. Energy*, 2015, **137**, 511–536.
- 6 H. Zhao, Q. Wu, S. Hu, H. Xu and C. N. Rasmussen, *Appl. Energy*, 2015, **137**, 545–553.
- 7 A. B. Gallo, J. R. Simões-Moreira, H. K. M. Costa, M. M. Santos and E. Moutinho dos Santos, *Renew. Sustain. Energy Rev.*, 2016, **65**, 800–822.
- 8 M. Yekini Suberu, M. Wazir Mustafa and N. Bashir, *Renew. Sustain. Energy Rev.*, 2014, **35**, 499–514.
- 9 A. Castillo and D. F. Gayme, *Energy Convers. Manag.*, 2014, **87**, 885–894.
- 10 T. M. I. Mahlia, T. J. Saktisahdan, A. Jannifar, M. H. Hasan and H. S. C. Matseelar, *Renew. Sustain. Energy Rev.*, 2014, **33**, 532–545.
- 11 The American Society of Mechanical Engineers, *A Natl. Hist. Mech. Engineering Landmark*, 1980.
- 12 F. Crotagino, K.-U. Mohmeyer and R. Scharf, *Solut. Min. Res. Inst. Spring Meet.*, 2001, 351–357.
- 13 Y. Ding, Y. Li, D. Li, J. Radcliffe and Y. Huang, *Highview Power Storage Handb. Clean Energy Syst.*
- 14 M. Lazarewicz and J. Arseneaux, in *Electrical Energy Storage Applications and Technologies (EESAT) Technical conference*, 2005.
- 15 C. Prieto, P. Cooper, A. I. Fernández and L. F. Cabeza, *Renew. Sustain. Energy Rev.*, 2016, **60**, 909–929.
- 16 M. Götz, J. Lefebvre, F. Mörs, A. McDaniel Koch, F. Graf, S. Bajohr, R. Reimert and T. Kolb, *Renew. Energy*, 2016, **85**, 1371–1390.
- 17 A. González, E. Goikolea, J. A. Barrena and R. Mysyk, *Renew. Sustain. Energy Rev.*, 2016, **58**, 1189–1206.
- 18 M. Armand and J.-M. Tarascon, *Nature*, 2008, **451**, 652–657.
- 19 I. Energy Agency, *Energy Technol. Perspect.*, 2014.
- 20 Z. Yang, J. Zhang, M. C. W. Kintner-meyer, X. Lu, D. Choi and J. P. Lemmon, *Chem. Rev.*, 2011, **111**, 3577–3613.
- 21 S. N. Laboratories, Doe Global Energy Storage Database.
- 22 M. Conte, *Fuel Cells*, 2010, **10**, 806–818.
- 23 A. Burke, *J. Power Sources*, 2000, **91**, 37–50.

- 24 R. Kötz and M. Carlen, *Electrochim. Acta*, 2000, **45**, 2483–2498.
- 25 Ultracapacitor, <http://www.ultracapacitors.org>.
- 26 F. Béguin, V. Presser, A. Balducci and E. Frackowiak, *Adv. Mater.*, 2014, **26**, 2219–2251.
- 27 A. Balducci, *J. Power Sources*, 2016, **326**, 534–540.
- 28 B. Panda, I. Dwivedi, K. Priya, P. B. Karandikar and P. S. Mandake, in *2016 - Biennial International Conference on Power and Energy Systems: Towards Sustainable Energy.*, 2016.
- 29 A. G. Pandolfo and A. F. Hollenkamp, *J. Power Sources*, 2006, **157**, 11–27.
- 30 G. Wang, L. Zhang and J. Zhang, *Chem. Soc. Rev.*, 2012, **41**, 797–828.
- 31 Y. Zhai, Y. Dou, D. Zhao, P. F. Fulvio, R. T. Mayes and S. Dai, *Adv. Mater.*, 2011, **23**, 4828–4850.
- 32 L. Guan, L. Yu and G. Z. Chen, *Electrochim. Acta*, 2016, **206**, 464–478.
- 33 L. Yu and G. Z. Chen, *J. Power Sources*, 2016, **326**, 604–612.
- 34 M. R. Lukatskaya, B. Dunn and Y. Gogotsi, *Nat. Commun.*, 2016, **7**, 12647.
- 35 F. Béguin, V. Presser, A. Balducci and E. Frackowiak, *Adv. Mater.*, 2014, **26**, 2219–2251.
- 36 W. Gu and G. Yushin, *Wiley Interdiscip. Rev. Energy Environ.*, 2014, **3**, 424–473.
- 37 X. Sun, X. Zhang, H. Zhang, D. Zhang and Y. Ma, *J. Solid State Electrochem.*, 2012, **16**, 2597–2603.
- 38 A. Balducci, R. Dugas, P. L. Taberna, P. Simon, D. Plée, M. Mastragostino and S. Passerini, *J. Power Sources*, 2007, **165**, 922–927.
- 39 A. Laheaar, S. Delpeux-Ouldriane, E. Lust and F. Beguin, *J. Electrochem. Soc.*, 2014, **161**, A568–A575.
- 40 S. Guo, F. Wang, H. Chen, H. Ren, R. Wang and X. Pan, *J. Solid State Electrochem.*, 2012, **16**, 3355–3362.
- 41 E. Taer, M. Deraman, I. A. Talib, A. Awitdrus, S. A. Hashmi and A. A. Umar, *Int. J. Electrochem. Sci.*, 2011, **6**, 3301–3315.
- 42 J. Chmiola, G. Yushin, R. Dash and Y. Gogotsi, *J. Power Sources*, 2006, **158**, 765–772.
- 43 Y. Gogotsi, R. K. Dash, G. Yushin, T. Yildirim, G. Laudisio and J. E. Fischer, *J. Am. Chem. Soc.*, 2005, **127**, 16006–16007.
- 44 R. Dash, J. Chmiola, G. Yushin, Y. Gogotsi, G. Laudisio, J. Singer, J. Fischer and S. Kucheyev, *Carbon N. Y.*, 2006, **44**, 2489–2497.
- 45 R. Lin, P. Taberna, S. Fantini, V. Presser, C. R. Pérez, F. Malbosc, N. L. Rupesinghe, K. B. K. Teo, Y. Gogotsi and P. Simon, *J. Phys. Chem. Lett.*, 2011, **2**, 2396–2401.
- 46 R. Z. Ma, J. Liang, B. Q. Wei, B. Zhang, C. L. Xu and D. H. Wu, *J. Power Sources*, 1999, **84**, 126–129.

- 47 E. Frackowiak, S. Delpeux, K. Jurewicz, K. Szostak, D. Cazorla-Amoros and F. Béguin, *Chem. Phys. Lett.*, 2002, **361**, 35–41.
- 48 M. D. Stoller, S. Park, Y. Zhu, J. An and R. S. Ruoff, *Nano Lett.*, 2008, **8**, 3498–3502.
- 49 C. Liu, Z. Yu, D. Neff, A. Zhamu and B. Z. Jang, *Nano Lett.*, 2010, **10**, 4863–4868.
- 50 J. Sato, Y. Takasu, K. Fukuda and W. Sugimoto, *Chem. Lett.*, 2011, **40**, 44–45.
- 51 M. Zeiger, N. Jäckel, V. N. Mochalin and V. Presser, *J. Mater. Chem. A*, 2016, **4**, 3172–3196.
- 52 C. Zhong, Y. Deng, W. Hu, J. Qiao, L. Zhang and J. Zhang, *Chem. Soc. Rev.*, 2015, **44**, 7484–7539.
- 53 M. Galiński, A. Lewandowski and I. Stępiak, *Electrochim. Acta*, 2006, **51**, 5567–5580.
- 54 V. Augustyn, P. Simon and B. Dunn, *Energy Environ. Sci.*, 2014, **7**, 1597–1615.
- 55 T. Brousse, D. Belanger and J. W. Long, *J. Electrochem. Soc.*, 2015, **162**, A5185–A5189.
- 56 J. P. Zheng, *J. Electrochem. Soc.*, 1995, **142**, 2699–2703.
- 57 O. Ghodbane, J. L. Pascal and F. Favier, *ACS Appl. Mater. Interfaces*, 2009, **1**, 1130–1139.
- 58 V. Augustyn, J. Come, M. A. Lowe, J. W. Kim, P. L. Taberna, S. H. Tolbert, H. D. Abruña, P. Simon and B. Dunn, *Nat. Mater.*, 2013, **12**, 518–522.
- 59 G. a. Snook, P. Kao and A. S. Best, *J. Power Sources*, 2011, **196**, 1–12.
- 60 J. Zhao, J. Wu, B. Li, W. Du, Q. Huang, M. Zheng, H. Xue and H. Pang, *Prog. Nat. Sci. Mater. Int.*, 2016, **26**, 237–242.
- 61 K. S. Ryu, K. M. Kim, N.-G. Park, Y. J. Park and S. H. Chang, *J. Power Sources*, 2002, **103**, 305–309.
- 62 S. Lehtimäki, M. Suominen, P. Damlin, S. Tuukkanen, C. Kvarnström and D. Lupo, *ACS Appl. Mater. Interfaces*, 2015, **7**, 22137–22147.
- 63 I. Shown, A. Ganguly, L. C. Chen and K. H. Chen, *Energy Sci. Eng.*, 2015, **3**, 1–25.
- 64 T. Brousse, P.-L. Taberna, O. Crosnier, R. Dugas, P. Guillemet, Y. Scudeller, Y. Zhou, F. Favier, D. Bélanger and P. Simon, *J. Power Sources*, 2007, **173**, 633–641.
- 65 B. B. Khatua, A. K. Das, R. Bera, A. Maitra, S. K. Karan, S. Paria, L. Halder, S. K. Si and A. Bera, *J. Mater. Chem. A*, 2017, **5**, 22242–22254.
- 66 A. Vlad, N. Singh, J. Rolland, S. Melinte, P. M. Ajayan and J.-F. Gohy, *Sci. Rep.*, 2014, **4**, 4315.
- 67 W. Zuo, R. Li, C. Zhou, Y. Li, J. Xia and J. Liu, *Adv. Sci.*, 2017, 1600539.
- 68 G. Z. Chen, *Int. Mater. Rev.*, 2017, **62**, 173–202.
- 69 G. G. Amatucci, F. Badway, A. Du Pasquier and T. Zheng, *J. Electrochem. Soc.*, 2001, **148**, A930–A939.
- 70 V. Khomeiko, E. Raymundo-Piñero and F. Béguin, *J. Power Sources*, 2008, **177**,

- 643–651.
- 71 K. Karthikeyan, V. Aravindan, S. B. Lee, I. C. Jang, H. H. Lim, G. J. Park, M. Yoshio and Y. S. Lee, *J. Alloys Compd.*, 2010, **504**, 224–227.
- 72 N. Arun, A. Jain, V. Aravindan, S. Jayaraman, W. Chui Ling, M. P. Srinivasan and S. Madhavi, *Nano Energy*, 2015, **12**, 69–75.
- 73 R. Satish, V. Aravindan, W. C. Ling and S. Madhavi, *J. Power Sources*, 2015, **281**, 310–317.
- 74 Z. Jian, W. Han, X. Lu, H. Yang, Y. S. Hu, J. Zhou, Z. Zhou, J. Li, W. Chen, D. Chen and L. Chen, *Adv. Energy Mater.*, 2013, **3**, 156–160.
- 75 K. Karthikeyana, S. Amaresha, K. J. Kima, S. H. Kima, K. Y. Chungb, B. W. Chob and Y. S. Lee, *Nanoscale*, 2013, **7**, 5958–5964.
- 76 T. Y. Wei, C. H. Chen, H. C. Chien, S. Y. Lu and C. C. Hu, *Adv. Mater.*, 2010, **22**, 347–351.
- 77 X.-H. Xia, J.-P. Tu, X.-L. Wang, C.-D. Gu and X.-B. Zhao, *Chem. Commun.*, 2011, **47**, 5786–5788.
- 78 S.-Y. Wang, K.-C. Ho, S.-L. Kuo and N.-L. Wu, *J. Electrochem. Soc.*, 2006, **153**, A75–A80.
- 79 S. Isikli, M. Lecea, M. Ribagorda, M. C. Carreño and R. Díaz, *Carbon N. Y.*, 2014, **66**, 654–661.
- 80 A. Le Comte, T. Brousse and D. Bélanger, *Electrochim. Acta*, 2014, **137**, 447–453.
- 81 K. W. Leitner, B. Gollas, M. Winter and J. O. Besenhard, *Electrochim. Acta*, 2004, **50**, 199–204.
- 82 M. Toupin and D. Bélanger, *Langmuir*, 2008, **24**, 1910–1917.
- 83 B. Akinwolemiwa, C. Peng and G. Z. Chen, *J. Electrochem. Soc.*, 2015, **162**, A5054–A5059.
- 84 Q. Li, K. Li, C. Sun and Y. Li, *J. Electroanal. Chem.*, 2007, **611**, 43–50.
- 85 E. Frackowiak, K. Fic, M. Meller and G. Lota, *ChemSusChem*, 2012, **5**, 1181–1185.
- 86 G. Lota and E. Frackowiak, *Electrochem. commun.*, 2009, **11**, 87–90.
- 87 G. Lota, K. Fic and E. Frackowiak, *Electrochem. commun.*, 2011, **13**, 38–41.
- 88 S. Roldán, M. Granda, R. Menéndez, R. Santamaría and C. Blanco, *J. Phys. Chem. C*, 2011, **115**, 17606–17611.
- 89 H. J. Yu, J. H. Wu, L. Q. Fan, Y. Z. Lin, S. H. Chen, Y. Chen, J. L. Wang, M. L. Huang, J. M. Lin, Z. Lan and Y. F. Huang, *Sci. China Chem.*, 2012, **55**, 1319–1324.
- 90 M. Park, J. Ryu, W. Wang and J. Cho, *Nat. Rev. Mater.*, 2016, **2**, 16080.
- 91 C. Ponce de León, A. Frías-Ferrer, J. González-García, D. A. Szánto and F. C. Walsh, *J. Power Sources*, 2006, **160**, 716–732.
- 92 M. Uhrig, S. Koenig, M. R. Suriyah and T. Leibfried, *Energy Procedia*, 2016, **99**, 35–43.
- 93 Vanadium Batteries- <http://australianvanadium.com.au/vanadium-batteries/>.

- 94 A. Roy, S. Patra and I. I. of E. S. and Technology, 2017.
- 95 A. Z. Weber, M. M. Mench, J. P. Meyers, P. N. Ross, J. T. Gostick and Q. Liu, *J. Appl. Electrochem.*, 2011, **41**, 1137–1164.
- 96 M. Skyllas-Kazacos, M. Rychcik, R. G. Robins and A. G. Fane, *J. Electrochem. Soc.*, 1986, **133**, 1057–1058.
- 97 H. Prifti, A. Parasuraman, S. Winardi, T. M. Lim and M. Skyllas-Kazacos, *Membranes (Basel)*, 2012, **2**, 275–306.
- 98 D. Chen, S. Kim, V. Sprenkle and M. A. Hickner, *J. Power Sources*, 2013, **231**, 301–306.
- 99 J. Xi, Z. Wu, X. Qiu and L. Chen, *J. Power Sources*, 2007, **166**, 531–536.
- 100 J. Zeng, C. Jiang, Y. Wang, J. Chen, S. Zhu, B. Zhao and R. Wang, *Electrochem. commun.*, 2008, **10**, 372–375.
- 101 N. S. Hudak, L. J. Small, H. D. Pratt and T. M. Anderson, *J. Electrochem. Soc.*, 2015, **162**, A2188–A2194.
- 102 X. Wei, B. Li and W. Wang, *Polym. Rev.*, 2015, **55**, 247–272.
- 103 B. Dunn, H. Kamath and J.-M. Tarascon, *Science*, 2011, **334**, 928–935.
- 104 V. Viswanathan, A. Crawford, D. Stephenson, S. Kim, W. Wang, B. Li, G. Coffey, E. Thomsen, G. Graff, P. Balducci, M. Kintner-Meyer and V. Sprenkle, *J. Power Sources*, 2014, **247**, 1040–1051.
- 105 J. Noack, L. Wietschel, N. Roznyatovskaya, K. Pinkwart and J. Tübke, *Energies*, 2016, **9**, 627–642.
- 106 U. National Minerals Information Center, *U.S. Geol. Surv. Miner. Commod. Summ.*, 2017, 182–183.
- 107 The Electric Power Research Institute, 2007, 3.
- 108 E. C. Montoto, G. Nagarjuna, J. S. Moore and J. Rodríguez-López, *J. Electrochem. Soc.*, 2017, **164**, A1688–A1694.
- 109 J. Winsberg, S. Muench, T. Hagemann, S. Morgenstern, T. Janoschka, M. Billing, F. H. Schacher, G. Hauffman, J.-F. Gohy, S. Hoepfener, M. D. Hager and U. S. Schubert, *Polym. Chem.*, 2016, **7**, 1711–1718.
- 110 X. Wei, W. Duan, J. Huang, L. Zhang, B. Li, D. Reed, W. Xu, V. Sprenkle and W. Wang, *ACS Energy Lett.*, 2016, **1**, 705–711.
- 111 J. W. Lee, M.-A. Goulet and E. Kjeang, *Lab Chip*, 2013, **13**, 2504–2507.
- 112 M. Duduta, B. Ho, V. C. Wood, P. Limthongkul, V. E. Brunini, W. C. Carter and Y. M. Chiang, *Adv. Energy Mater.*, 2011, **1**, 511–516.
- 113 E. Ventosa, M. Skoumal, F. J. Vazquez, C. Flox, J. Arbiol and J. R. Morante, *ChemSusChem*, 2015, **8**, 1737–1744.
- 114 Y. Zhao, Y. Ding, Y. Li, L. Peng, H. R. Byon, J. B. Goodenough and G. Yu, *Chem. Soc. Rev.*, 2015, **44**, 7968–7996.
- 115 K. Wedege, J. Azevedo, A. Khataee, A. Bontien and A. Mendes, *Angew. Chemie -*

- Int. Ed.*, 2016, **55**, 7142–7147.
- 116 M. Yu, W. D. McCulloch, D. R. Beauchamp, Z. Huang, X. Ren and Y. Wu, *J. Am. Chem. Soc.*, 2015, **137**, 8332–8335.
- 117 Y. G. Zhu, C. Jia, J. Yang, F. Pan, Q. Huang and Q. Wang, *Chem. Commun.*, 2015, **51**, 9451–9454.
- 118 M. Bockelmann, U. Kunz and T. Turek, *Electrochem. commun.*, 2016, **69**, 24–27.
- 119 W. A. Braff, M. Z. Bazant and C. R. Buie, *Nat. Commun.*, 2013, **4**, 2346.
- 120 Q. Liu, A. E. S. Sleightholme, A. A. Shinkle, Y. Li and L. T. Thompson, *Electrochem. commun.*, 2009, **11**, 2312–2315.
- 121 Q. Liu, A. A. Shinkle, Y. Li, C. W. Monroe, L. T. Thompson and A. E. S. Sleightholme, *Electrochem. commun.*, 2010, **12**, 1634–1637.
- 122 M. H. Chakrabarti, R. A. W. Dryfe and E. P. L. Roberts, *Electrochim. Acta*, 2007, **52**, 2189–2195.
- 123 D. H. Evans, *Chem. Rev.*, 2008, **108**, 2113–2144.
- 124 W. Wang and V. Sprenkle, *Nat. Chem.*, 2016, **8**, 204–206.
- 125 J. Winsberg, T. Hagemann, T. Janoschka, M. D. Hager and U. S. Schubert, *Angew. Chemie - Int. Ed.*, 2016, **55**, 2–28.
- 126 E. V. Carino, J. Staszak-Jirkovsky, R. S. Assary, L. A. Curtiss, N. M. Markovic and F. R. Brushett, *Chem. Mater.*, 2016, **28**, 2529–2539.
- 127 Y. Moon and Y.-K. Han, *Curr. Appl. Phys.*, 2016, **16**, 939–943.
- 128 S. Er, C. Suh, M. P. Marshak and A. Aspuru-Guzik, *Chem. Sci.*, 2015, **6**, 885–893.
- 129 D. Tomerini, C. Gatti and C. Frayret, *Phys. Chem. Chem. Phys.*, 2015, **17**, 8604–8608.
- 130 L. Cheng, R. S. Assary, X. Qu, A. Jain, S. P. Ong, N. N. Rajput, K. Persson and L. A. Curtiss, *J. Phys. Chem. Lett.*, 2015, **6**, 283–291.
- 131 S. D. Pineda Flores, G. C. Martin-Noble, R. L. Phillips and J. Schrier, *J. Phys. Chem. C*, 2015, **119**, 21800–21809.
- 132 T. Janoschka, N. Martin, U. Martin, C. Friebe, S. Morgenstern, H. Hiller, M. D. Hager and U. S. Schubert, *Nature*, 2015, **527**, 78–81.
- 133 Y. Xu, Y. Wen, J. Cheng, G. Cao and Y. Yang, *Electrochem. commun.*, 2009, **11**, 1422–1424.
- 134 K. Gong, Q. Fang, S. Gu, S. F. Y. Li and Y. Yan, *Energy Environ. Sci.*, 2015, **8**, 3515–3530.
- 135 T. B. Schon, B. T. McAllister, P.-F. Li and D. S. Seferos, *Chem. Soc. Rev.*, 2016, **45**, 6345–6404.
- 136 Y. Ding, Y. Li and G. Yu, *Chem*, 2016, **1**, 790–801.
- 137 P. S. Guin, S. Das and P. C. Mandal, *Int. J. Electrochem.*, 2011, **2011**, 1–22.
- 138 M. A. Bhat, *Electrochim. Acta*, 2012, **81**, 275–282.

- 139 K. Wedege, E. Dražević, D. Konya and A. Bentien, *Sci. Rep.*, 2016, **6**, 39101.
- 140 E. J. Son, J. H. Kim, K. Kim and C. B. Park, *J. Mater. Chem. A*, 2016, **4**, 11179–11202.
- 141 S. Isikli and R. Diaz, *J. Power Sources*, 2012, **206**, 53–58.
- 142 G. Pognon, T. Brousse, L. Demarconnay and D. Bélanger, *J. Power Sources*, 2011, **196**, 4117–4122.
- 143 Z. Algharaibeh and P. G. Pickup, *Electrochem. commun.*, 2011, **13**, 147–149.
- 144 X. Chen, H. Wang, H. Yi, X. Wang, X. Yan and Z. Guo, *J. Phys. Chem. C*, 2014, **118**, 8262–8270.
- 145 C. Cougnon and D. Mayilukila, *ACS Appl. Mater. Interfaces*, 2012, **4**, 3788–3796.
- 146 D. M. Anjos, J. K. McDonough, E. Perre, G. M. Brown, S. H. Overbury, Y. Gogotsi and V. Presser, *Nano Energy*, 2013, **2**, 702–712.
- 147 C. R. Deblase, K. E. Silberstein, T. T. Truong, H. D. Abruña and W. R. Dichtel, *J. Am. Chem. Soc.*, 2013, **135**, 16821–16824.
- 148 S. K. Kim, J. Cho, J. S. Moore, H. S. Park and P. V. Braun, *Adv. Funct. Mater.*, 2016, **26**, 903–910.
- 149 T. Tomai, S. Mitani, D. Komatsu, Y. Kawaguchi and I. Honma, *Sci. Rep.*, 2014, **4**, 3591.
- 150 S. T. Senthilkumar, R. K. Selvan and J. S. Melo, *J. Mater. Chem. A*, 2013, **1**, 12386–12394.
- 151 W. Chen, C. Xia, R. B. Rakhi and H. N. Alshareef, *J. Power Sources*, 2014, **267**, 521–526.
- 152 S. Roldán, C. Blanco, M. Granda, R. Menéndez and R. Santamaría, *Angew. Chemie Int. Ed.*, 2011, **50**, 1699–1701.
- 153 S. Roldán, M. Granda, R. Menéndez, R. Santamaría and C. Blanco, *Electrochim. Acta*, 2012, **83**, 241–246.
- 154 S. Roldán, Z. González, C. Blanco, M. Granda, R. Menéndez and R. Santamaría, *Electrochim. Acta*, 2011, **56**, 3401–3405.
- 155 E. Mourad, L. Coustan, P. Lannelongue, D. Zigah, A. Mehdi, A. Vioux, S. A. Freunberger, F. Favier and O. Fontaine, *Nat. Mater.*, 2017, **16**, 446–455.
- 156 C. Bodin, E. Mourad, D. Zigah, S. Le Vot, S. A. Freunberger, F. Favier and O. Fontaine, *Faraday Discuss.*, 2018, **206**, 393–404.
- 157 S. Sathyamoorthi, V. Suryanarayanan and D. Velayutham, *J. Power Sources*, 2015, **274**, 1135–1139.
- 158 G. Wang, R. Liang, L. Liu and B. Zhong, *Electrochim. Acta*, 2014, **115**, 183–188.
- 159 H. Yu, L. Fan, J. Wu, Y. Lin, M. Huang, J. Lin and Z. Lan, *RSC Adv.*, 2012, **2**, 6736.
- 160 L. Su, L. Gong, H. Lü and Q. Xü, *J. Power Sources*, 2014, **248**, 212–217.
- 161 H. Xie, Y. Zhu, Y. Wu, Z. Wu and E. Liu, *Mater. Res. Bull.*, 2014, **50**, 303–306.
- 162 S.-E. Chun, B. Evanko, X. Wang, D. Vonlanthen, X. Ji, G. D. Stucky and S. W.

- Boettcher, *Nat. Commun.*, 2015, **6**, 7818.
- 163 K. B. Hatzell, M. Beidaghi, J. W. Campos, C. R. Dennison, E. C. Kumbur and Y. Gogotsi, *Electrochim. Acta*, 2013, **111**, 888–897.
- 164 B. Yang, L. Hooper-Burkhardt, F. Wang, G. K. Surya Prakash and S. R. Narayanan, *J. Electrochem. Soc.*, 2014, **161**, A1371–A1380.
- 165 J. D. Milshtein, L. Su, C. Liou, A. F. Badel and F. R. Brushett, *Electrochim. Acta*, 2015, **180**, 695–704.
- 166 US2015/0236543 A1, 2015, 1–38.
- 167 T. Liu, X. Wei, Z. Nie, V. Sprenkle and W. Wang, *Adv. Energy Mater.*, 2016, **6**, 1501449.
- 168 T. Janoschka, N. Martin, M. D. Hager and U. S. Schubert, *Angew. Chemie - Int. Ed.*, 2016, **55**, 14427–14430.
- 169 M. Burgess, J. S. Moore and J. Rodríguez-López, *Acc. Chem. Res.*, 2016, **49**, 2649–2657.
- 170 F. R. Brushett, J. T. Vaughey and A. N. Jansen, *Adv. Energy Mater.*, 2012, **2**, 1390–1396.
- 171 R. A. Potash, J. R. McKone, S. Conte and H. D. Abruña, *J. Electrochem. Soc.*, 2016, **163**, A338–A344.
- 172 Z. Li, S. Li, S. Liu, K. Huang, D. Fang, F. Wang and S. Peng, *Electrochem. Solid-State Lett.*, 2011, **14**, A171–A173.
- 173 J. Huang, L. Cheng, R. S. Assary, P. Wang, Z. Xue, A. K. Burrell, L. A. Curtiss and L. Zhang, *Adv. Energy Mater.*, 2015, **5**, 1–6.
- 174 A. Bourke, M. A. Miller, R. P. Lynch, X. Gao, J. Landon, J. S. Wainright, R. F. Savinell and D. N. Buckley, *J. Electrochem. Soc.*, 2016, **163**, A5097–A5105.
- 175 S. K. Park, J. Shim, J. Yang, K. H. Shin, C. S. Jin, B. S. Lee, Y. S. Lee and J. D. Jeon, *Electrochem. commun.*, 2015, **59**, 68–71.
- 176 A. P. Kaur, N. E. Holubowitch, S. Ergun, C. F. Elliott and S. A. Odom, *Energy Technol.*, 2015, **3**, 476–480.
- 177 X. Wei, W. Xu, J. Huang, L. Zhang, E. Walter, C. Lawrence, M. Vijayakumar, W. A. Henderson, T. Liu, L. Cosimbescu, B. Li, V. Sprenkle and W. Wang, *Angew. Chemie - Int. Ed.*, 2015, **54**, 8684–8687.
- 178 W. Duan, R. S. Vemuri, J. D. Milshtein, S. Laramie, R. D. Dmello, J. Huang, L. Zhang, D. Hu, M. Vijayakumar, W. Wang, J. Liu, R. M. Darling, L. Thompson, K. Smith, J. S. Moore, F. R. Brushett and X. Wei, *J. Mater. Chem. A*, 2016, **4**, 5448–5456.
- 179 J. Carretero-González, E. Castillo-Martínez and M. Armand, *Energy Environ. Sci.*, 2016, **9**, 3521–3530.
- 180 R. M. Darling, K. G. Gallagher, J. A. Kowalski, S. Ha and F. R. Brushett, *Energy Environ. Sci.*, 2014, **7**, 3459–3477.

Chapter 2. Objectives

The main objective of this thesis is to contribute to the development of new redox electrolytes and their application in two types of electrochemical energy storage devices: i) High performance hybrid supercapacitors; ii) New concepts of redox flow batteries (RFB). Specifically, this thesis is focused on the study of new redox electrolytes containing organic redox molecules as active species and their application to high performance hybrid supercapacitors and to an innovative concept of Membrane-Free Redox Flow Battery.

In order to achieve this goal, specific objectives were defined and following described:

- 1) Formulation of redox electrolytes based on ionic liquids containing organic molecules as active species which can enhance the performance of the electrochemical energy storage devices.
- 2) Electrochemical characterization of hybrid supercapacitors with new organic redox electrolytes based on ionic liquids.
- 3) Analysis of the influence of the textural properties of carbonaceous electrode material on the performance of hybrid supercapacitors using organic redox electrolytes based on ionic liquids.
- 4) Design a new concept of Membrane-Free Redox Flow Battery based on aqueous-nonaqueous immiscible electrolytes and evaluation of its electrochemical behavior.
- 5) Investigation of the versatility of the innovative concept of Membrane-Free RFB by developing different combinations of aqueous-nonaqueous immiscible redox electrolytes with organic molecules. Evaluation of the electrochemical performance of different of Membrane-Free RFB.
- 6) Exploring the application of Membrane-Free concept to aqueous-aqueous immiscible systems through the thermodynamic study of Aqueous Biphasic Systems.
- 7) Development and electrochemical characterization of a Total Aqueous Membrane-Free RFB based on Aqueous Biphasic Systems.

The three first objectives are pursued in **Chapter 3** which seeks the answer to this research question: How can the use of redox electrolytes based on ionic liquids

containing organic molecules affect the electrochemical performance of supercapacitors? The initial hypotheses that were considered are:

- i) Ionic liquids have a wide electrochemical window stability, thus its application as electrolytes can enhance the applied potential and, as consequence, the energy density of the devices.
- ii) The solution of organic redox molecules into the electrolyte provides faradaic non-capacitive contribution which can also enhance the energy density of the device.

In **Chapter 4** the objectives 4 and 5 are pursued trying to solve the next research questions: Is it possible to develop a redox flow battery without any physical separator just by using aqueous-nonaqueous redox immiscible electrolytes? Is it possible to use redox electrolytes containing organic molecules is such type of Membrane-Free RFB? This disruptive concept emanates from the current difficulties which redox flow batteries are facing. These limitations are the scarcity, high price and toxicity of metallic active species, the high cost and low performance of ion-exchange membranes, and the low voltage and energy density of these batteries. All these issues limit the massive implementation of this technology. Therefore, the Chapter 4 is based on the following hypothesis:

- i) The replacement of the metallic active species by abundant, tunable and eco-friendly organic redox molecules and the elimination of the membrane can improve the performance of the batteries, making them versatile and suitable for different applications and reducing their cost.

Objectives 6 and 7 are pursued in **Chapter 5** in which we aim to answer to this question: Can an Aqueous Biphasic System be applied to an electrochemical energy storage device? The hypotheses in which the research activities are based on are:

- i) The innovative concept of Membrane-Free RFB can be applied to many different combinations of immiscible electrolytes. Among them, Aqueous Biphasic Systems used so far in extraction and separation processes might become a safer, cheaper and eco-friendly alternative.
- ii) Aqueous Biphasic Systems offer the advantage of controlling the partitioning behavior of different target molecules, thus they can be used as a strategy to control the cross-migration to the active species.

The methodology to achieve these abovementioned objectives involves the formulation of organic redox electrolytes, the use of electrochemical techniques to analyze the electrochemical behavior of these redox electrolytes as well as the assembly of lab-scale devices and prototypes and the evaluation of their performance.

Chapter 3 . Electrochemical
Study of Hybrid
Supercapacitors Based on
para-Benzoquinone Ionic
Liquid Redox Electrolyte

3.1 Introduction

As it was explained in chapter 1, supercapacitors (SCs), are electrochemical energy storage devices characterized by having high power density, good cyclability but low energy density ^{1,2}. Activated carbons with capacitances in the range of 80-150 F·g⁻¹ are widely employed as active material for SC electrodes ^{3,4} due to their high specific surface area (1000-2000 m²·g⁻¹), high electric conductivity and low cost. In order to boost energy density, different strategies are pursued either by increasing capacitance (C) or voltage (V), according to equation (3.1)

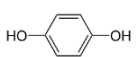
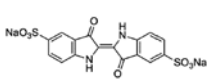
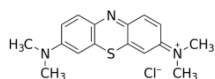
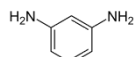
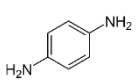
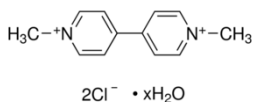
$$E_{\max} = 1/2 CV^2 \quad (3.1)$$

Since Prof. Compton's group ⁵ demonstrated the functionalization of carbon surface by covalent grafting of active redox molecules such as quinones, several authors have investigated the use of quinone-modified carbons as electrode material in aqueous carbon/carbon capacitors. In those systems, the energy storage mechanism is a combination of two phenomena occurring in the carbon electrode: the formation of the electrical double layer and the faradaic reactions of the quinone functional groups. As a result, the specific capacitance of the modified electrode increases even by a factor of two compared to the pristine carbon electrode in acid and basic aqueous electrolytes ⁶⁻¹³. However, the preparation of quinone-modified carbons implies additional and sometimes costly synthesis and purification steps that restrict their practical application. In this sense, the development of hybrid storage systems in which redox molecules are simply dissolved in the electrolyte similar to redox flow batteries, has been proposed in the last years as an advantageous strategy ¹⁴⁻¹⁶. These hybrid systems combine materials and concepts typical from supercapacitors (activated carbon electrodes and electrostatic storage mechanism) and from redox flow batteries (faradaic reactions involving redox couples dissolved in the electrolyte). First examples of redox pairs used in electrolytes for hybrid supercapacitors include inorganic compounds such as bromine/bromide ¹⁷ and iodine/iodide ¹⁸, the latter showing capacitance as high as 1840 Fg⁻¹ due to the redox reaction that occurs in the positive electrode ^{19,20}. The use of two redox electrolytes such as iodine/iodide and vanadium/vanadyl, reacting separately in each electrode, has further improved the electrochemical properties of the hybrid

3. Electrochemical study of Hybrid Supercapacitors Based on para-Benzoquinone Ionic Liquid Redox Electrolyte

supercapacitor presenting energy density values as high as $19 \text{ Wh}\cdot\text{kg}^{-1}$ ^{21,22}. Recently, redox electrolytes containing organic quinone/hydroquinone couples have been also used not only in organic redox flow batteries ^{23,24} but also in hybrid supercapacitors ^{25,26} due to the high reversibility and relatively fast redox reaction of quinones in aqueous electrolytes. Besides quinones, other organic molecules have been employed in redox electrolytes for SCs (Table 3.1).

Table 3.1. Summary of reported redox-electrolytes based on organic molecules for supercapacitors

Organic Active Molecule	Electrolyte	Electrode Material	Energy Density ($\text{Wh}\cdot\text{kg}^{-1}$)	C ($\text{F}\cdot\text{g}^{-1}$)	Year [ref]
Hydroquinone 	H_2SO_4	Porous carbon MWCNTs	31.3 N.A.	900 180 (@ $2.65\text{mA}\cdot\text{cm}^{-2}$)	2011 25
Indigo Carmine 	H_2SO_4	MWCNTs	1.7 (@ $0.88\text{mA}\cdot\text{cm}^{-2}$)	50 (@ $50\text{mV}\cdot\text{s}^{-1}$)	2011 27
Methylene Blue 	H_2SO_4	MWCNTs	N.A.	23 (@ $0.9\text{mA}\cdot\text{cm}^{-2}$)	2012 28
m-phenylenediamine 	KOH	Porous carbon	9.99 (@ $0.5\text{A}\cdot\text{g}^{-1}$)	78	2012 29
p-phenylenediamine 	KOH	Ball-milled MnO_2	10 (@ $1\text{A}\cdot\text{g}^{-1}$)	44.8	2012 30
p-phenylenediamine	KOH + carbon beads + carbon black		N.A.	140 (@ $0.2\text{A}\cdot\text{g}^{-1}$)	2013 31
p-phenylenediamine	KOH	MnO_2 Nanorods	N.A.	156 (@ $2\text{A}\cdot\text{g}^{-1}$)	2014 32
Hydroquinone	H_2SO_4	Functionalized CNTs	Only one electrode performance		2014 11
Hydroquinone	H_2SO_4	Polyaniline	N.A.	584 (@ $0.5\text{A}\cdot\text{g}^{-1}$)	2014 33
MVCl ₂ and KBr ₂ 	water	Porous carbon	13.9	13.3 ($\text{mAh}\cdot\text{g}^{-1}$)	2015 34

In those systems, the energy storage mechanism is a combination of electrical double layer formation and faradaic reaction at the electrode-electrolyte interface resulting in supercapacitors having higher capacitance and energy densities. However, similarly to other hybrid devices, they also present some drawbacks such as lower power and poorer cyclability compared with electric double layer capacitors. A new term 'supercapbatteries'^{14,35} has emerged to highlight the fact that in those systems, characteristics of batteries and supercapacitors are merged.

In all the previous examples the operating voltage of the devices was limited to 1.0-1.4 V due to the aqueous nature of the redox electrolytes. Although for conventional carbon-carbon capacitors this voltage has been extended up to 3.5 V by using ionic liquids (ILs)³⁶⁻³⁸, those ILs have not been used to broaden the electrochemical stability window of redox electrolytes in hybrid supercapacitors. It is worthy to mention that most of these studies are focused on their improved electrochemical behavior evaluated by cyclic voltammetry (CV) and galvanostatic charge discharge (CD). However, a profound analysis of the complex energy storage mechanism of these redox-active systems where it is difficult to discriminate faradaic from capacitive components is still missing. Although Electrochemical Impedance Spectroscopy (EIS) has been widely employed to characterize electrochemical double layer capacitors (EDLC) and to better understand the physicochemical phenomena involved in the formation of the double layer^{39,40} only scarce examples using this powerful tool for SCs with redox-active electrolytes can be found in literature⁴¹⁻⁴³.

In this chapter, the development of a redox electrolyte composed of parabenzoquinone (pBQ) dissolved in an ionic liquid electrolyte, N-butyl-N-methylpyrrolidinium bis(trifluoromethanesulfonyl)imide (PYR₁₄TFSI) is reported. This redox electrolyte is used in carbon based hybrid supercapacitors to simultaneously increase operating voltage (V) and capacitance (C) and to boost the energy density of devices. The effect of electrode textural properties in the electrochemical performance of this hybrid supercapacitor is also investigated by using two carbons with different textural properties; Pica activated carbon and Vulcan carbon³⁸.

In addition, in order to shed some light on the energy storage mechanism and better understanding of the physicochemical phenomena involved, a detailed and comprehensive electrochemical impedance spectroscopy study of the devices is carried out. Besides the analysis of the measurements, an equivalent electric circuit model is proposed with the aim of anticipating the performance of the devices in duty cycles demanding different time responses.

3.2 Results and Discussion

3.2.1 Electrochemical Characterization of Electrolytes

As it was commented in the introduction, different kinds of redox organic molecules have been tested as active species for redox electrolytes. Among them, quinones are especially interesting since their redox reactions involve two electrons, due to the two carbonyl ligands contained in the quinone structure, and exhibit high reversibility and fast kinetics, which are important features for their applications in electrochemical devices. Amid all the different quinones, parabenzoquinone is the smallest one and its simple structure contributes to have high theoretical capacity ($495 \text{ mAh}\cdot\text{g}^{-1}$). These characteristics have motivated the choice of pBQ as redox active molecule for this work. Electrochemical studies of quinone redox behavior in different media have been reported in literature^{44–46}. In general, the reaction mechanism pathway depends on the protic or aprotic nature of the media. In this sense, Roldan et al²⁵ tested it in acidic media and found a one-step redox process in which 2 electrons were exchanged (according to the mechanistic pathway highlighted in blue in Figure 3.1).

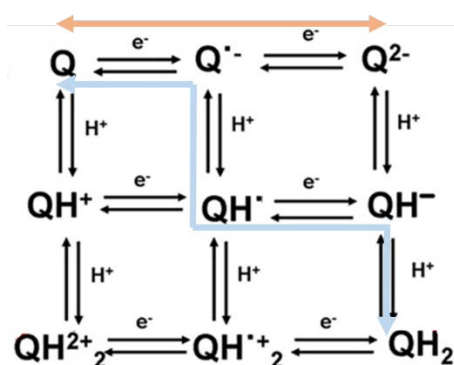


Figure 3.1. Mechanistic pathways of quinones. Blue arrow represents the reaction mechanism in protic media. Orange arrow indicates reaction mechanism in aprotic media (adapted from ⁴⁵).

Therefore, in order to investigate the redox behavior of pBQ in the IL, cyclic voltammetry of a 20 mM solution of pBQ in $\text{PYR}_{14}\text{TFSI}$ was performed in a 3-electrode cell using glassy carbon as working electrode, platinum mesh as counter electrode and silver wire as reference (Figure 3.2). CV curve shows two quasi-reversible redox peaks (peaks

separation ~ 150 mV) confirming that the reaction mechanism of pBQ in aprotic ionic liquid such as $\text{PYR}_{14}\text{TFSI}$ takes place in two one-electron reduction steps according to the mechanistic pathway highlighted in orange in Figure 3.1. The first step at -0.25 V (vs. NHE) corresponds to the formation of a semiquinone radical $\text{Q}^{\bullet-}$ while the second step at -0.75 V (vs. NHE) corresponds to the formation of quinone dianion Q^{2-} , as shown in Equations 3.2 and 3.3.

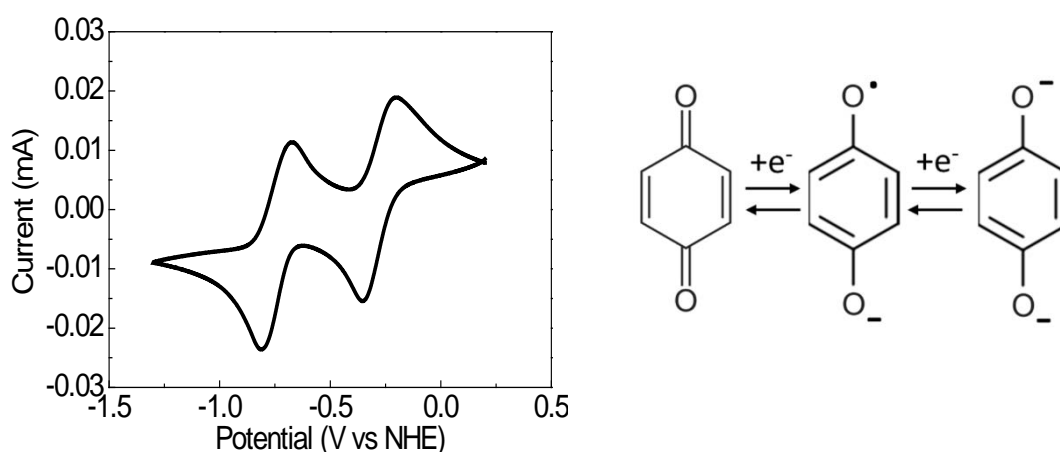


Figure 3.2. Cyclic voltammetry of a 20 mM solution of pBQ in $\text{PYR}_{14}\text{TFSI}$ in 3 electrode cell at $10 \text{ mV}\cdot\text{s}^{-1}$ in glassy carbon electrode 3 mm diameter.

In order to understand the nature of the faradaic process, CVs at different scan rate were recorded (from $10 \text{ mV}\cdot\text{s}^{-1}$ to $600 \text{ mV}\cdot\text{s}^{-1}$). A lineal relationship between the peak current and the square root of the scan rate was found for both process (anodic and cathodic), therefore the oxidation and reduction of pBQ are diffusion-controlled processes (Figure 3.3). Moreover, it was found that the scan rate mainly has two effects: i) increase the current of the redox peaks and ii) enlarge the potential separation between reduction and oxidation peaks (78 mV for the first step reaction and 50 mV for the second step). This behavior confirms that these processes are diffusion-controlled.

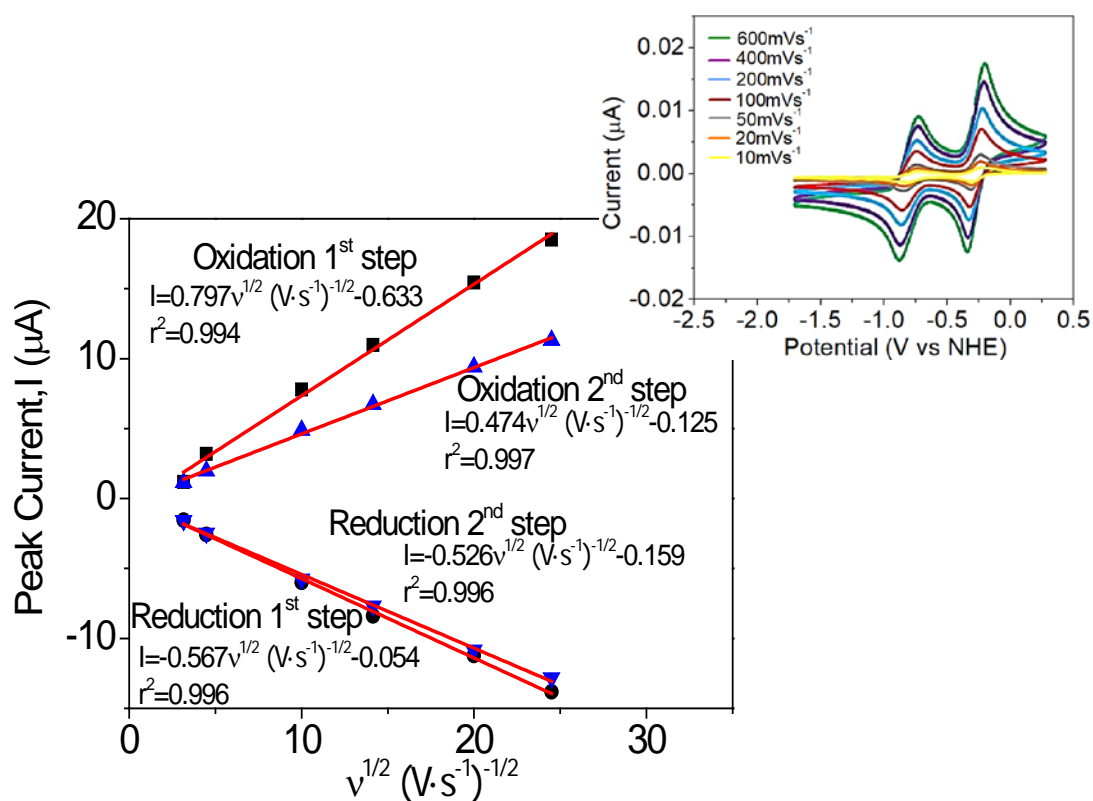


Figure 3.3. Anodic and cathodic peak current dependence on the square root of scan rate. Inset: cyclic voltammetry obtained in a three electrode cell of 20 mM solution of pBQ in PYR₁₄TFSI at different scan rate.

3.2.2 Electrochemical Characterization of Hybrid Supercapacitors

Once the electrochemical behaviour of the electrolyte was appraised, hybrid SCs based on Vulcan were assembled using a redox electrolyte solution containing different concentrations of pBQ in PYR₁₄TFSI. For the sake of comparison, SCs containing pure PYR₁₄TFSI were also assembled. Thus, the effect of the concentration of pBQ on the device performance was studied. Electrochemical characterization was performed at 60°C since some properties of ionic liquid such as the ionic conductivity improve with increasing temperature endowing SCs with lower resistance. Firstly, in order to select the optimal pBQ concentration, its effect on the specific real energy was investigated. As can be seen in Figure 3.4, the influence of the amount of pBQ dissolved in the IL on the E_{real} delivered by the SCs is significant in all the cases.

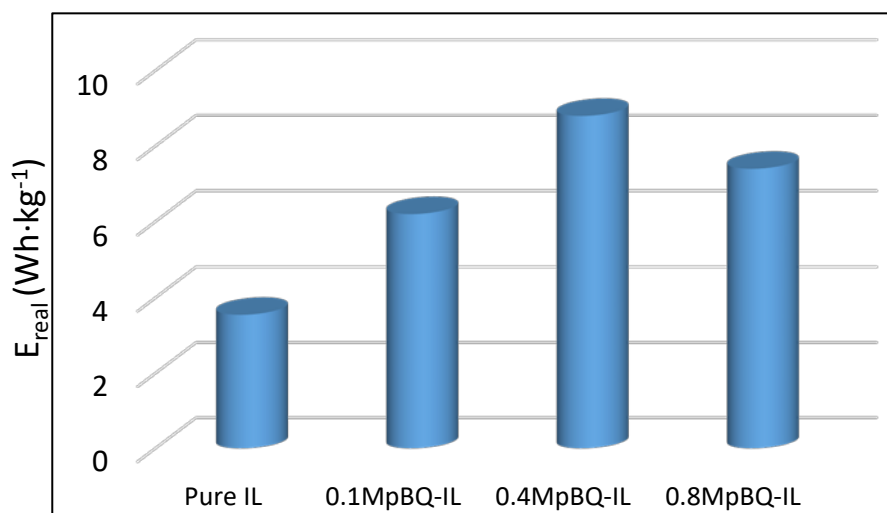


Figure 3.4. Real energy density (E_{real}) versus different concentration of pBQ dissolved into the IL. Obtained from galvanostatic Charge-Discharge experiments over a range in voltage from 0 V to 3 V at 10 mA·cm⁻². T^a=60 °C. Electrode material: Vulcan carbon.

Thus, an improvement of 74 % was attained by dissolving 0.1 M of pBQ in the IL and increasing the pBQ concentration from 0.1 M to 0.4 M causes an enhancement in E_{real} of 42 %. However, a further increase in concentration of pBQ (up to 0.8 M, maximum solubility of pBQ in the IL) provokes a decrease in the energy density value. This drop in the E_{real} when the pBQ concentration is increased up to 0.8 M, might be explained because physical adsorption of some quinone molecules can clog the pores of the carbonaceous material, hindering the diffusion of ions to the surface of the electrode. According to these results, optimal concentration of pBQ into the electrolyte was found to be 0.4 M.

Therefore, the redox electrolyte used in further experiments was based on a 0.4 M solution of pBQ into the IL. Hence, the influence on the performance of the devices of carbonaceous material used in the electrode, among other aspects, are investigated in the next section, by using this redox electrolyte.

3.2.2.1 Cyclic Voltammetry Experiments

Hybrid SCs based on two different carbons, Pica and Vulcan, were assembled using a redox electrolyte solution 0.4 M of pBQ in PYR₁₄TFSI. Figure 3.5a shows the cyclic voltammetry of SCs based on Pica activated carbon. Since one of the advantages of using

IL electrolytes is their high electrochemical stability window, the SCs where characterized from 0 V to 3.0 V. It is observed that the CV of hybrid SC with redox electrolyte is distorted in comparison with the typical rectangular shape that is obtained for pure $\text{PYR}_{14}\text{TFSI}$. During the anodic scan, a hump is observed at about 1.5 V that shifts to 0.8 V during the cathodic scan. In the case of hybrid SCs based on Vulcan (Figure 3.5b), the distortion of the CV curve is even more pronounced, with bigger and sharper humps that appear at 1.4 V and 1.1 V for anodic and cathodic sweeps, respectively. These protuberances are due to faradaic contribution associated with the redox reactions suffered by pBQ dissolved in $\text{PYR}_{14}\text{TFSI}$.

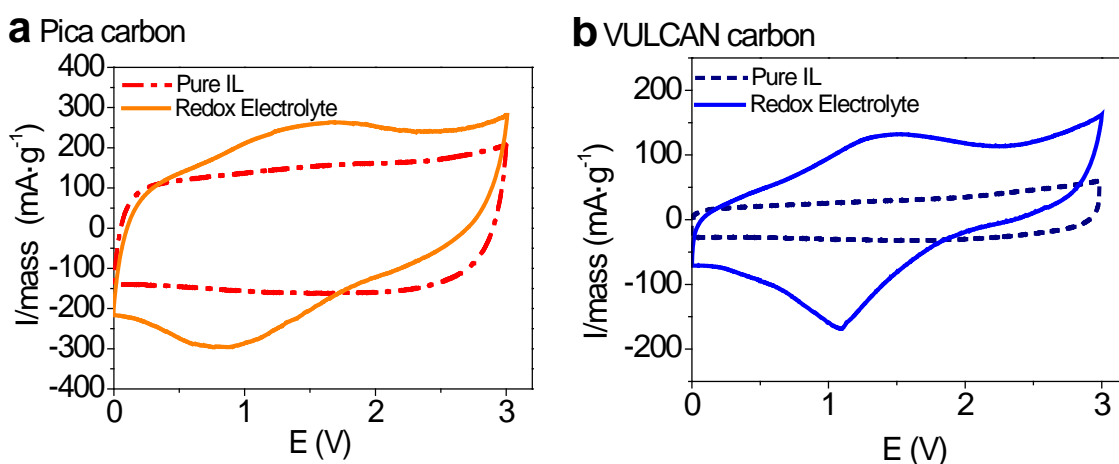


Figure 3.5. Cyclic voltammetry of hybrid SCs at a scan rate of $5 \text{ mV}\cdot\text{s}^{-1}$ for (a) Pica activated carbon and (b) Vulcan carbon. Electrolytes: Redox electrolyte (0.4 M pBQ in $\text{PYR}_{14}\text{TFSI}$) and pure $\text{PYR}_{14}\text{TFSI}$. $T=60^\circ\text{C}$.

Comparison between rectangular CVs of SCs with pure ionic liquid electrolyte and distorted CVs of hybrid SCs with redox electrolyte indicates the existence of a mixed energy storage mechanism. In this mechanism, the electrical double layer formation coexists with faradaic quinone reactions occurring at the interface electrode-electrolyte. Therefore, specific capacitance of the SCs will be the sum of the double layer capacitance and the faradaic contributions. The specific capacitance of the electrodes (C_s)[†] was calculated by the integrating the CV curves at different scan rates applying Ec. 3.6 and 3.7 (see section 3.4 of this chapter). The capacitance value (C_s) of Vulcan with pure

[†] Note: It should be clarified that the term *specific capacitance* ($\text{F}\cdot\text{g}^{-1}$) is used for evaluating the performance of SC with redox electrolyte just for doing a direct comparison with pure IL-SC and with reported results in literature. However, in systems with such high faradaic contribution the correct term, as it was explained in chapter 1 is *specific capacity* ($\text{mAh}\cdot\text{g}^{-1}$).

PYR₁₄TFSI is about 15-20 F·g⁻¹ whereas for Pica the values vary from 120 F·g⁻¹ at 5 mV·s⁻¹ to 90 F·g⁻¹ at 20 mV·s⁻¹ (see Figure 3.6). Those differences could be easily attributed to the high specific surface area (S_{BET}) of Pica activated carbon that is contributing to the formation of the electrical double layer and consequently to double layer capacitance. It is clear that the use of the quinone redox electrolyte (0.4 M pBQ in PYR₁₄TFSI) improves significantly the capacitance in both carbonaceous materials due to the additional faradaic contribution. In the case of Vulcan, the capacitance was increased about threefold reaching maximum values of about 70 F·g⁻¹. In the case of Pica, this increment is about 36 % reaching a maximum of 156 F·g⁻¹ at 5 mV·s⁻¹. Therefore, although the presence of quinonyl groups in the electrolyte results in hybrid SCs having higher capacitance, the faradaic contribution of the redox electrolyte to the total capacitance depends on the type of carbonaceous material used in constructing the electrode.

Figure 3.6 also shows that capacitance decreases gradually with increasing scan rates, which can be attributed to diffusion limitation of ions into the porous of active materials at high scan rates. The negative effect is more pronounced in the case of Pica SC as reported elsewhere ⁴⁷. This can be attributed to the different textural properties of these two carbons. Vulcan with low specific surface area but open porosity offers an easily accessible electrode area for ions and quinone molecules. Even at high scan rates the ions and redox molecules might reach the electrode surface very rapidly. However, the presence of micropores in Pica carbon produces diffusion limitation of ions and quinone molecules causing slow kinetics of the electrochemical response of Pica SC. This slower kinetics is reflected in the significant capacitance fading at higher scan rates in comparison with Vulcan SC.

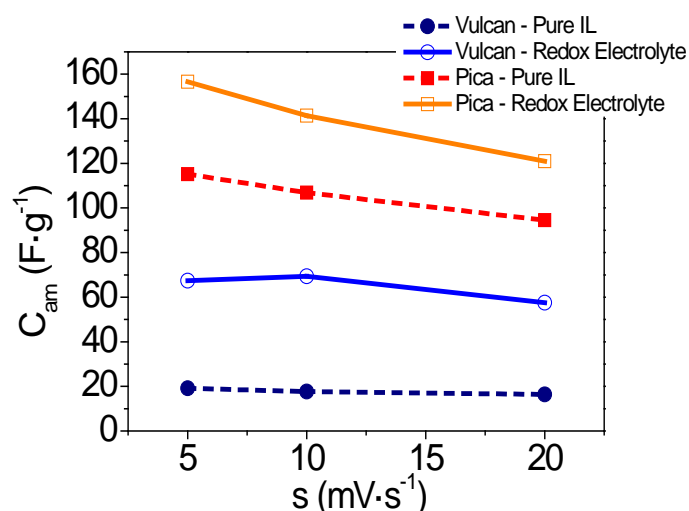


Figure 3.6. Specific capacitance (C_s) versus scan rate for SCs with different electrodes (Pica and Vulcan) and electrolytes (0.4 M pBQ in $\text{PYR}_{14}\text{TFSI}$ and pure $\text{PYR}_{14}\text{TFSI}$). $T=60^\circ\text{C}$.

3.2.2.2 *Galvanostatic Charge-Discharge Experiments*

In order to complete the electrochemical characterization, galvanostatic charge-discharge (CD) experiments were performed from 0 V to 2.0 V, 3.0 V and 3.5 V at different current densities. As an example, Figure 3.7 shows the CD profiles of SCs based on Pica and Vulcan ranging from 0 V to 3 V at $10 \text{ mA}\cdot\text{cm}^{-2}$. The linear voltage profile that is commonly obtained for electric double layer capacitors (EDLCs) is observed when pure $\text{PYR}_{14}\text{TFSI}$ is used. Similarly to CV, addition of the redox pBQ into $\text{PYR}_{14}\text{TFSI}$ causes a large distortion in the shape of the charge-discharge profiles and a flattening at around 1.2 V is observed for both carbonaceous materials. This plateau at intermediate voltages might be attributed to the reversible redox reaction of pBQ observed by CV in 3-electrode cell and reported by Compton et al. in similar aprotic ionic liquids⁴⁸. Figure 3.7 also shows that addition of redox pBQ provokes longer response times due to the faradaic contribution. The discharging times for hybrid SCs ranged from 15 to 75 seconds for Vulcan and from 45 to 270 seconds for Pica (depending on the current densities). This response is slower than the response of Vulcan and Pica SCs with pure IL (2-17 seconds and 30-200 seconds, respectively) but still quite quick and clearly more similar to a hybrid supercapacitor than a battery, with common charging times in the range of several hours.

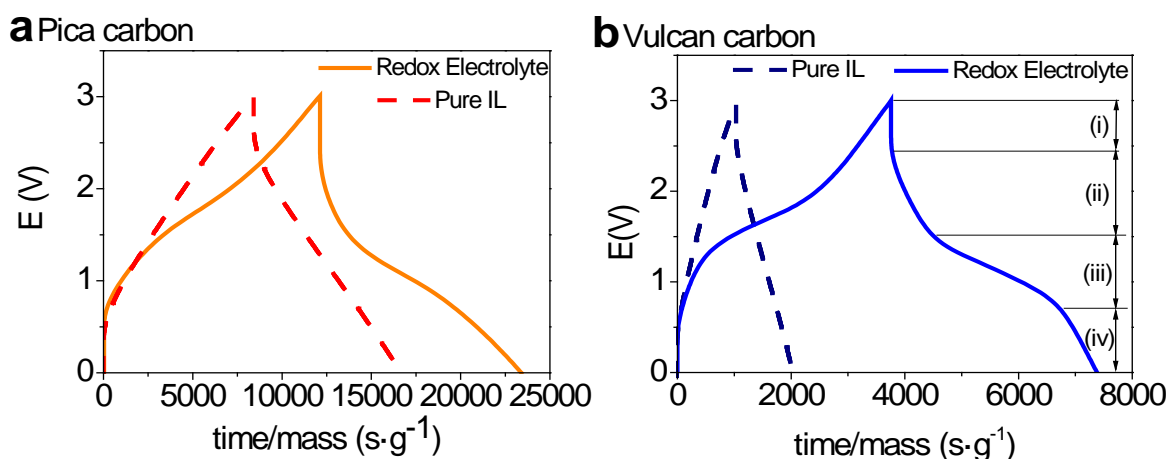


Figure 3.7. Voltage profiles plot up to 3 V at 60 °C and current density 10 mA·cm⁻²: (a) Pica carbon (b) Vulcan carbon. Electrolytes: Pure PYR₁₄TFSI and 0.4 M pBQ in PYR₁₄TFSI

In electric double layer capacitors, the slope of the discharge profile is used to calculate capacitance ($C \sim 1/\text{slope}$) that is constant along the voltage. However, according to Figure 3.7, in SCs with redox electrolytes the discharge slope is not constant meaning that the capacitance is changing with the voltage. In such cases, the accuracy of the linear regression is not as good as it should be and it is preferred to calculate the capacitance by integration of the current from cyclic voltammetry (Eq. 3.6).

Still, interesting information can be extracted from the slope of these discharge curves. For instance, Figure 3.7b shows that hybrid SCs with Vulcan carbon and redox electrolyte exhibits a discharge voltage profile having four different regions; (i) the ohmic drop at the beginning of the discharge (from 3 V to 2.5 V), (ii) the plateau region typical of faradaic contribution (from 1.5 V to 0.8 V), and two linear segments (iii) from 2.5 V to 1.5 V and (iv) from 0.8 V to 0 V. It is worth mentioning that the slopes of these two linear segments are the same as those in discharge profile of Vulcan SC with pure PYR₁₄TFSI. Apparently, at those voltages in which the pBQ redox reaction is not taking place, the formation of electric double layer is occurring to the same extent than for Vulcan SC with pure PYR₁₄TFSI, meaning that the capacitance in these voltage ranges is associated exclusively to the formation of the double layer. This is a very interesting finding since it could be stated that the storage mechanism for redox-electrolyte systems depends on the voltage range according to the extension of the faradaic reactions. At those voltages

where the redox reaction does not occur the storage mechanism is mainly electrostatic and the capacitance will be due only to the double layer formation.

Besides previous qualitative interpretations, charge-discharge experiments were used to quantify the effect of pBQ in terms of specific real energy (E_{real}) of hybrid SCs by following Eq. 3.9. The specific real energy (E_{real}) of SCs operating at different working conditions (2 V, 3 V and 3.5 V) is represented in Figure 3.8.

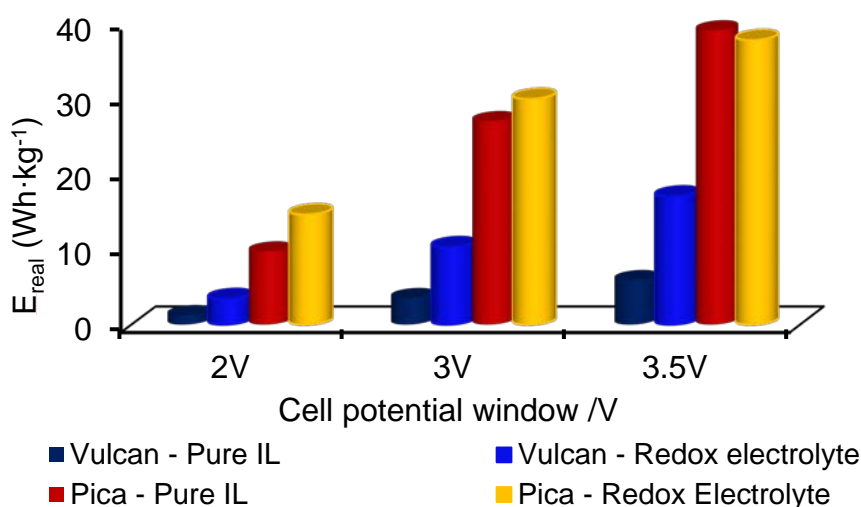


Figure 3.8. Real energy density (E_{real}) versus operating voltage of the SCs obtained from CD experiments: current density $5 \text{ mA}\cdot\text{cm}^{-2}$. $T^{\text{a}}=60 \text{ }^{\circ}\text{C}$.

As expected, E_{real} increases with the maximum operating voltage in all the cases. If pure $\text{PYR}_{14}\text{TFSI}$ is used as electrolyte there is no faradaic contribution and only electrostatic interaction at electrode/electrolyte interface is involved in the energy storage mechanism. Since specific surface area of Pica activated carbon is much higher than Vulcan, both the double layer capacitance and real energy density associated to Pica SCs with pure $\text{PYR}_{14}\text{TFSI}$ are significantly higher than for Vulcan SCs. It is observed that for SCs based on Vulcan, the addition of pBQ to $\text{PYR}_{14}\text{TFSI}$ electrolyte results in increasing values of E_{real} at the three operating voltages. At 2 V, 3 V and 3.5 V the E_{real} of Vulcan SC with redox electrolyte is 3 times the E_{real} of SC with pure $\text{PYR}_{14}\text{TFSI}$. According to Figure 3.8, in the case of SCs based on Pica, the beneficial effect of pBQ addition is very significant at 2 V with 52 % increment (from 9.6 to $14.7 \text{ Wh}\cdot\text{kg}^{-1}$). However, this increment is only about 10 % when Pica hybrid SCs are charged to 3 V and the use of a redox electrolyte becomes slightly detrimental if the operating voltage is increased up

to 3.5 V. This performance might be explained by the physical adsorption of some quinoyl species that can clog the micropores structure of Pica hindering the diffusion of ions to the surface of electrodes. As a consequence, as observed in Figure 3.7a the equivalent series resistance (ESR) increases and the contribution of the double layer to the total capacitance decreases in Pica hybrid SCs with p-BQ redox electrolyte. This effect is negligible in Vulcan electrodes, characterized by a non-porous but easy accessible surface.

It is worth mentioning that if the system would behave as a battery, one should relate the faradaic contribution to the concentration and volume of electrolyte in the cell. However, since we are investigating this redox electrolyte in hybrid SCs the systems were evaluated at high rates in which only a small percentage of available quinone molecules will have time to react. In fact, even at the lower current density of $5 \text{ mA}\cdot\text{cm}^{-2}$ only 32 % and 2.6 % of available quinone molecules react in Vulcan and Pica SCs, respectively. Those values were estimated having into account the different total pore volume of Pica and Vulcan ($1.58 \text{ cm}^3\cdot\text{g}^{-1}$ and $0.33 \text{ cm}^3\cdot\text{g}^{-1}$) and comparing the measured capacity with the maximum capacity assuming that all available redox molecules react. The different “usable” quinone percentage is related with the small pore size of Pica carbon that makes more difficult the diffusion of quinone molecules into their small pores, so less quinones react in the surface of Pica in comparison with Vulcan.

The effect of current density in SCs performance could be observed in Figure 3.9 that shows the evolution of E_{real} with current density when the SCs are charged from 0 V to 3 V. In the case of Vulcan SCs, there is a reduction of E_{real} with increasing current going from 3.5 to 1.7 $\text{Wh}\cdot\text{kg}^{-1}$ whereas for Pica SCs the E_{real} values decrease from 27 $\text{Wh}\cdot\text{kg}^{-1}$ at $5 \text{ mA}\cdot\text{cm}^{-2}$ to 11.3 $\text{Wh}\cdot\text{kg}^{-1}$ at $20 \text{ mA}\cdot\text{cm}^{-2}$. This trend is typically observed in microporous materials, especially with electrolytes containing bulky ions such as ionic liquids, due to the increasing ion diffusion resistance inside micropores. This effect is less important for Vulcan carbon black, having open porosity that facilitates ion mobility. Since mass loading is different for Pica and Vulcan SCs, energy density was also analyzed as a function of the current normalized by the mass instead of by the geometrical area and same trend was observed.

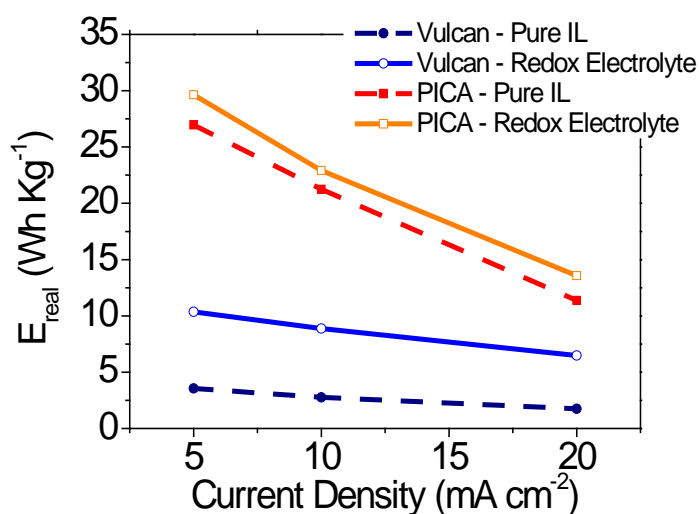


Figure 3.9. Real energy density (E_{real}) versus current density for different SCs. Obtained from CD experiments over a range in voltage from 0 V to 3 V. $T=60\text{ }^{\circ}\text{C}$

According to Figure 3.9, the use of redox electrolyte (0.4 M pBQ in $\text{PYR}_{14}\text{TFSI}$) in hybrid SCs results in an enhancement of E_{real} in both carbonaceous materials. The E_{real} increment obtained in SCs based on Vulcan is about 300 % going from $3.5\text{ Wh}\cdot\text{kg}^{-1}$ to $10.3\text{ Wh}\cdot\text{kg}^{-1}$ at $5\text{ mA}\cdot\text{cm}^{-2}$ which is significantly higher than the 10 % increase observed in hybrid SCs based on Pica, in the same experimental conditions. The different faradaic contribution of the redox electrolyte for Vulcan and Pica might be attributed to the different textural properties of these two carbonaceous materials as reported by Isikli et al.⁴⁹ due to the high specific surface area of Pica carbon ($2400\text{ m}^2\cdot\text{g}^{-1}$) the contribution of the double layer to the capacitance in this carbon is very significant and might be somewhat masking the faradaic contribution of the redox electrolyte. Moreover, the diffusion of quinone species into the microporous structure of Pica is more difficult than in the open structure of Vulcan carbon.

The values of specific real energy (E_{real}) and specific real power (P_{real}) associated with these SCs are represented in a Ragone plot in Figure 3.10. The higher intrinsic electrical conductivity of Vulcan carbon ($\sigma=1.45\text{ S}\cdot\text{cm}^{-1}$) and the less restricted mobility of the ions in their open porosity turn into higher values of P_{real} when compared with Pica carbon ($\sigma=0.25\text{ S}\cdot\text{cm}^{-1}$). It is observed that the use of redox electrolyte results in higher values of E_{real} , especially in Vulcan hybrid SCs, but causes a decrease in P_{real} probably due to the higher equivalent series resistance (ESR) and the slower response associated with the

existence of slower faradaic transfer processes. Still, those P_{real} values are in the common range for hybrid SCs and are much higher than those for batteries.

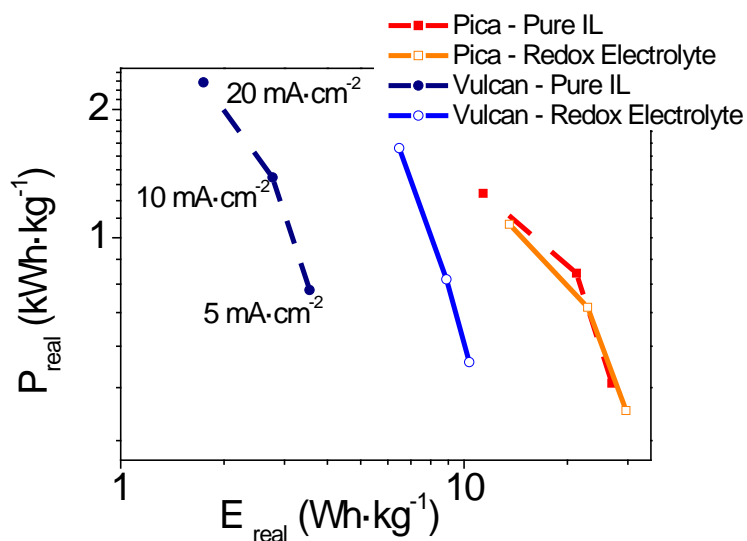


Figure 3.10. Ragone plot of the SCs obtained from CD experiments over a voltage range from 0 to 3 V. $T^{\text{a}}=60^{\circ}\text{C}$.

3.2.2.3 Cycling experiments

Long-term cycling stability experiments were performed in Vulcan hybrid SCs by charging-discharging the SCs up to 3 V at $10\text{ mA}\cdot\text{cm}^{-2}$ (see Figure 3.11). The specific real energy of Vulcan hybrid SCs operating with redox electrolyte is higher than for pure ionic liquid for 1000 cycles. Energy delivered by Vulcan hybrid SC with redox electrolyte goes from $8\text{ Wh}\cdot\text{kg}^{-1}$ to $4\text{ Wh}\cdot\text{kg}^{-1}$ during the cycling while SC containing pure IL exhibit lower but constant energy values of $2.8\text{ Wh}\cdot\text{kg}^{-1}$.

This performance fading with cycles has been observed in other hybrid systems and more in particular in those hybrid SCs using redox electrolytes. In fact, most of those publications does not include cyclability experiment for the full device but only for half-cell system ⁴³. In those articles that show a considerable number of cycles, the capacitance retention is lower than 50 % after 1000 cycles ²⁵. In this sense, we consider that despite not being good results if we compare them with pure EDLC, the hybrid SCs reported here exhibit similar or even better cycling behavior than similar hybrid SCs reported in literature. Moreover, the obtained values of energy density are much higher than those in previous works due to the appropriate electrolyte composition and their

dual effect; high capacitance due to the redox couple and high operating voltage due to the ionic liquid. In summary, the advantages of this system are that keeping high power density values (in the range of some commercial supercapacitors and higher than those obtained with batteries) we achieve a huge increase in the energy density values, until three times higher with respect to those obtained with the same systems using pure ionic liquid electrolyte.

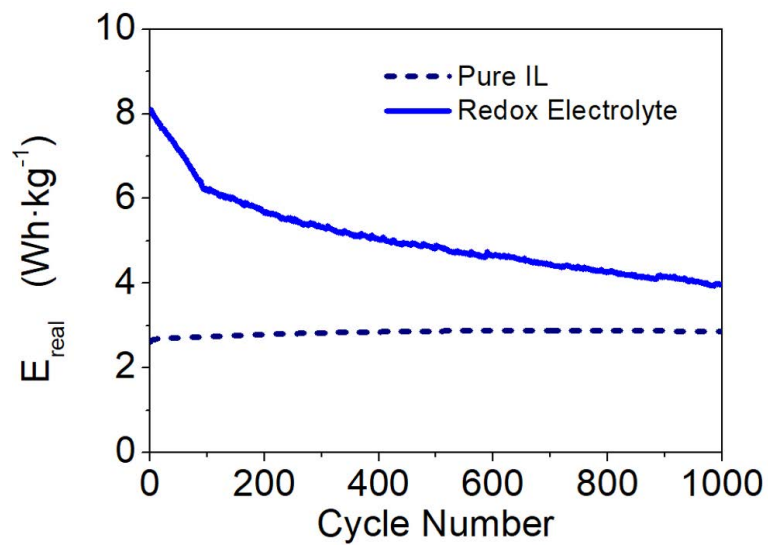


Figure 3.11. Cycling stability of Vulcan SCs obtained from CD experiments from 0 to 3 V at $10 \text{ mA}\cdot\text{cm}^{-2}$. $T^{\text{a}}=60 \text{ }^{\circ}\text{C}$.

3.2.3 Insights into the Energy Storage Mechanism by Electrochemical Impedance Spectroscopy Study

In order to complete the electrochemical characterization of these hybrid SCs, and for a better understanding of their performance and their energy storage mechanism, Electrochemical Impedance Spectroscopy (EIS) technique was employed. In this part of the study only SCs based on Vulcan electrodes were analyzed, keeping the same composition of redox electrolyte (0.4 M pBQ in IL) and Pure IL for comparison (for more experimental details see section 3.4).

EIS is a very powerful technique to characterize electrochemical phenomena occurring at different frequencies in supercapacitors. The EIS allows an overview of the whole frequency behavior of these systems and provides information about their resistive and capacitive behavior and the identification of diffusion-limited processes. In addition, EIS is well-suited for studying separately the contribution of the double layer capacitance and the contribution of the faradaic reaction of redox-active molecules to the charge storage since these two processes occur at different frequencies⁵⁰.

- *Complex plane plots*

The typical Nyquist plot for a real electric double layer capacitor (EDLC) based on carbon electrodes exhibits three distinct parts: a semi-circle at high frequency, a tilted linear variation of the impedance in the middle frequency range and a vertical tail at low frequency. In the very high frequency domain, ions do not have enough time to penetrate inside pores and only the external surface is accessible, so the resistive components have more influence^{51,52}. On the contrary, at very low frequencies, complete penetration of ions inside the porous structure of the activated carbon occurs, charge saturation dominates and the electrode behaves as an ideally polarizable porous interface, yielding a vertical line in the Nyquist representation. In the intermediate frequency range, the resistance and capacitance are frequency dependent and the diffusion processes have a strong influence. Between intermediate and low frequency domains, the impedance response shows a characteristic frequency (f_0) which separates two different dominant behaviors from resistive to capacitive, as will be discussed later.

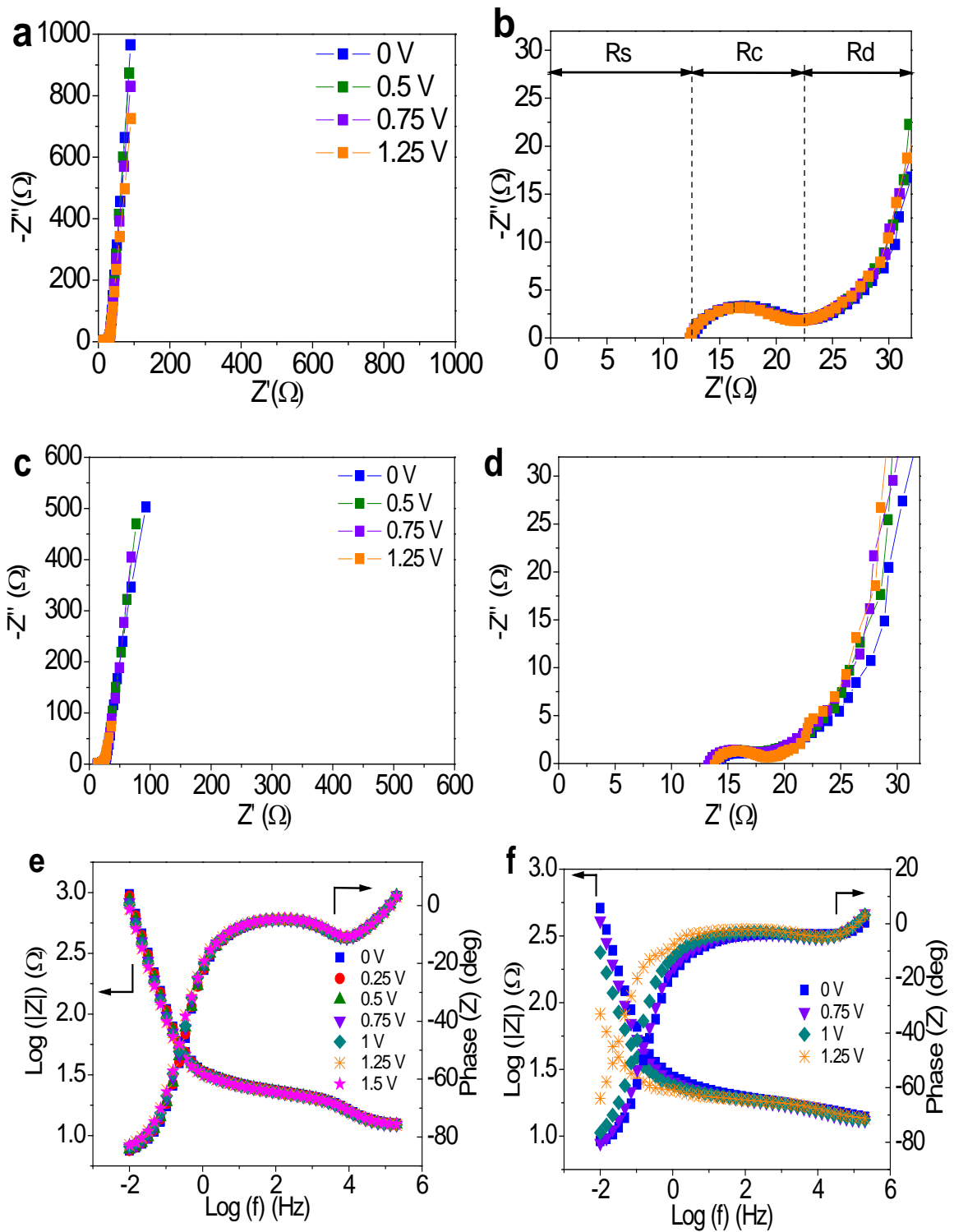


Figure 3.12. Nyquist plot at different bias voltage for the SCs a) Pure IL. b) Pure IL-enlarged. Resistance contributions are labeled. c) Redox electrolyte. d) Redox electrolyte-enlarged. e) Bode plot at different bias voltage of Pure IL Electrolyte-SCs. f) Bode plot at different bias voltage of Redox Electrolyte – SCs

Figure. 3.12 compares the Nyquist plot of SCs with pure IL as electrolyte and the hybrid SCs with redox electrolyte at different bias voltage. It is clear that bias voltages do not

have an important effect on Nyquist plot for conventional SC. However, Nyquist plot of SC using redox electrolyte is strongly affected by bias voltage due to the occurrence of faradaic reaction at a certain voltage, this can also be clearly observed in Bode plots (Figure 3.12e and f.). Moreover, the magnitude of different resistive processes (electric resistance R_s , resistance at the electrode/electrolyte interface R_c and diffusion resistance R_d) occurring in the SCs can be extracted from Nyquist plot analyzing separately three frequency zones (Figure. 3.12 b).

The first intersection with the x-axis at the highest frequency (R_s) is mainly attributed to the electric resistance due to all the connections, particularly the measurement connections, the contact resistance between the activated carbon and the current collector as well as the resistance of the bulk electrolyte ⁵³.

At higher frequencies, the diameter of the semicircle (R_c) has been attributed to the resistance at the interface between porous surface of the electrode and the electrolyte. This complex structure had been extensively studied and modeled as a transmission line model (ladder network) in the 60's by de Levie ⁵⁴. For the hybrid SCs this resistance also includes the charge transfer resistance associated to the faradaic contribution, which occurs almost in the same frequency domain. In this case, this parameter is related with two different processes, the formation of the double layer in the EDLC and the charge transfer in the hybrid devices. It is important to remark that in the SC with redox electrolyte the semicircle is not as well-defined as the obtained with pure IL probably due to the more dispersive charge processes involved ⁵⁵. In this work we attribute the cause of the distortion to the difference in frequency at which the formation of the double layer and the faradaic process take place, as will be discussed in the next section. However, the frequency change is not large enough to produce two differentiated semicircles and an overlap between them is obtained, causing a distorted semicircle.

At low frequencies, the contribution of the diffusion of the ions (R_d) can be obtained as the real value of the impedance ($R_d = Z'(0.01 \text{ Hz}) - R_s - R_c$). In this frequency range, the ions

are able to reach electrode area deeper into the pores of the carbonaceous material, with the consequence of a longer path for the ions in the electrolyte.

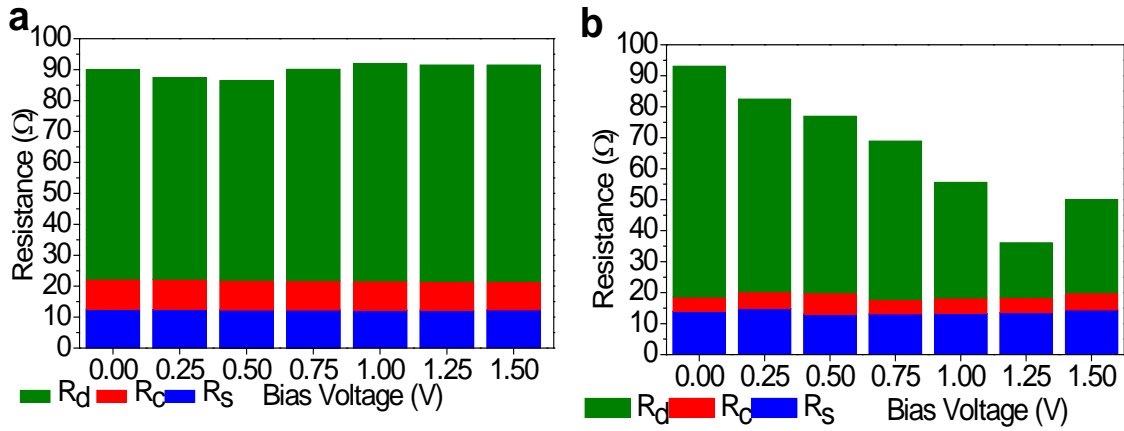


Figure 3.13. Resistance contributions and its dependence with bias voltage. a) Pure IL Electrolyte b) Redox Electrolyte.

Figure 3.13 shows the dependence of the whole resistance and their single mentioned contributions at different bias voltages for both SCs. It is observed that there is no dependency of the resistance on the bias voltage in the EDLC with pure IL. The total resistance and each contribution keep constant with the bias voltage only very slight and not significant changes are observed. However, a totally different tendency is observed for the hybrid devices. In these redox-SCs R_d suffers important changes with the bias voltage. In the case of R_d the polarization causes a noteworthy decrease (about 60 %) in the diffusion resistance which reaches a minimum value at quinone reaction potential (1.25 V). Further discussion of these changes will be explained together with the equivalent circuit in the last part of this section.

- *Complex Capacitance*

With the aim of taking the deviation from the ideal behavior of a pure capacitor into consideration, the impedance of the whole system can be defined by using a capacitance $C(\omega)$ that is frequency dependent:

$$Z(\omega) = \frac{1}{j2\pi f C(2\pi f)} \quad (3.4)$$

$$C(\omega) = C'(\omega) - j C''(\omega) = \frac{-Z''(2\pi f)}{2\pi f |Z(2\pi f)|^2} - j \frac{Z'(2\pi f)}{2\pi f |Z(2\pi f)|^2} \quad (3.5)$$

Where $C'(\omega)$ and $C''(\omega)$ are the real part and the imaginary part of $C(\omega)$, as well as $Z'(\omega)$ and $Z''(\omega)$ are the real part and the imaginary part of the impedance, respectively; ω is angular frequency defined as $\omega=2\pi f$; and f is the lineal frequency.

The frequency dependence of complex capacitance might be used to study the energy storage mechanism. At high frequencies, both the imaginary and the real part of the capacitance are negligible, since the resistive processes dominate. At low frequencies the capacitive processes are dominant. $C'(\omega)$ gives information about the capacitance value of the whole system and tends to the capacitance value extracted from the cyclic voltammetry or current charge/discharge curves, while C'' quantifies the losses of energy. Specifically, the relaxation time (τ_R) that represents how fast a SC can be cycled can be expressed as the inverse of the characteristic frequency (f_0) ($\tau_R = 1/f_0$). This is the frequency at which the resistive and capacitive components of the system are the same ($C'(2\pi f_0)=C''(2\pi f_0)$) (corresponding to a phase angle (Φ) -45° for an ideal behavior). This value can be easily obtained from the maximum of $C''(\omega)$ corresponding to the maximum loss of energy by ohmic dissipation⁵⁵⁻⁵⁷ The higher these values are, the higher the rate cyclability of the supercapacitor, as will be discussed later in this section.

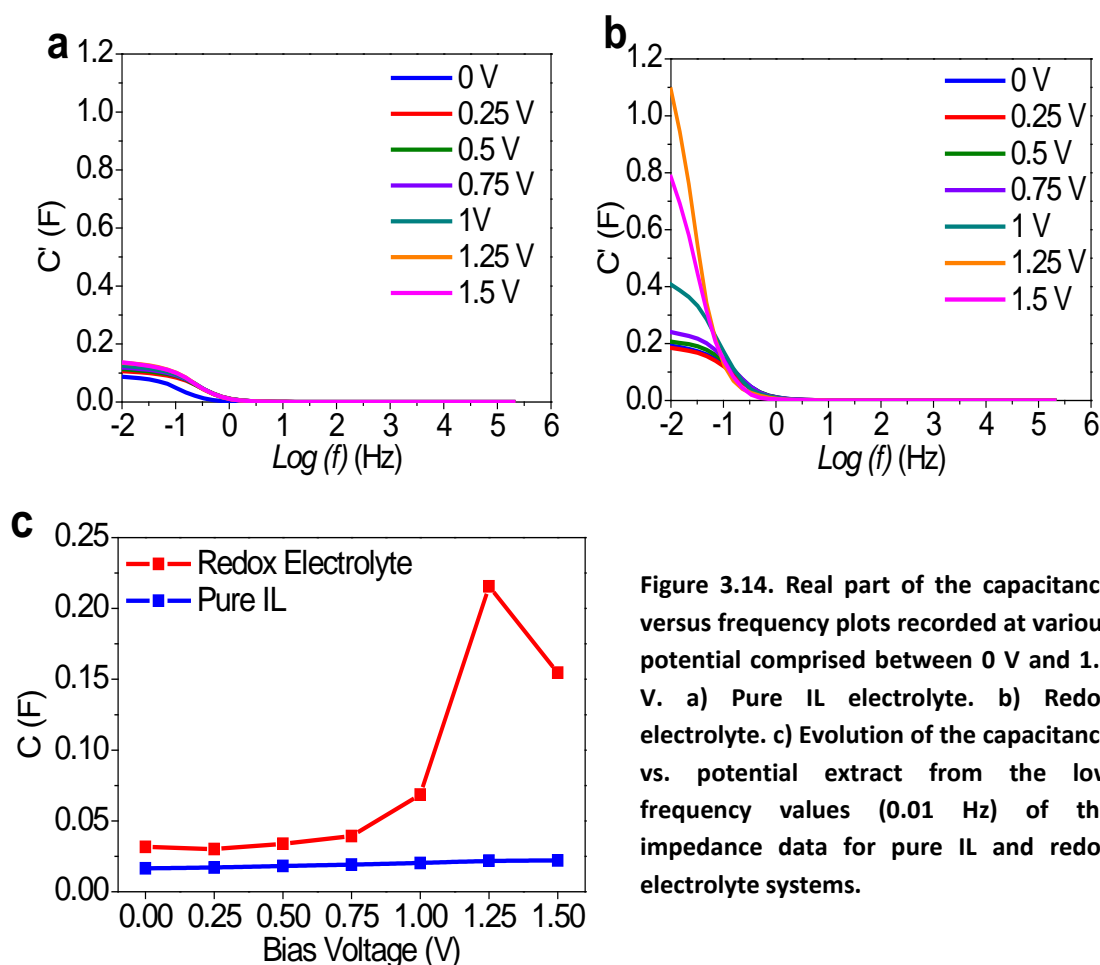


Figure 3.14. Real part of the capacitance versus frequency plots recorded at various potential comprised between 0 V and 1.5 V. a) Pure IL electrolyte. b) Redox electrolyte. c) Evolution of the capacitance vs. potential extract from the low frequency values (0.01 Hz) of the impedance data for pure IL and redox electrolyte systems.

The maximum value of real capacitance is evaluated at low frequency, under these conditions the ions have enough time to reach the electrode surface which is hidden deep in the carbon pores. At these frequencies a major fraction of the porosity of the electrode is accessible to the electrolyte. As the frequency increases, the ions cannot follow the applied electric field anymore and do not reach the depth of the electrode pores and a sharp decrease of C' is obtained. This tendency can be seen in Figure 3.14a and Figure 3.14b, both curves show a typical drop of capacity when frequency increases, and finally the capacity keeps constant at a very low value. Nevertheless, Figure 3.14 reveals differences in the shapes of C' versus frequency when going from pure IL electrolyte (Figure 3.14a) to redox electrolyte (Figure 3.14b) as well as, with the bias voltage applied. The capacitance values obtained are higher for systems with redox electrolytes in comparison with the SCs with pure IL as electrolyte. This difference becomes especially significant when the DC potential applied is close to the potential at

which the pBQ reaction takes place (≈ 1.25 V). In the systems in which the redox electrolyte is used the sharp drop in C' occurs with an onset frequency shifted towards the lower frequencies in comparison with those SCs with pure IL. This demonstrates the redox reaction is a slower process and occurs at slightly different frequencies than the double layer formation. In the case of SCs based on pure IL, the onset frequency is shifted towards higher values when a bias voltage is applied; this means that the penetration of the ions inside the pores is easier when a polarization is made, thus enhancing ionic transportation within the pores.

In Figure 3.14c the capacitance evolution measured at low frequency (10 mHz) is plotted as a function of the bias voltage. These experimental results show that the capacitance is not linear with the voltage when redox electrolyte is used. However, the tendency can be considered as linear when the supercapacitor uses pure ionic liquid as electrolyte. In this case, the slight variations in the values can be explained by the reduction of the distance separating the charge at the electrode/electrolyte interface with the increasing polarization. Another explanation is to consider the series connected capacitance inside the electrode, due to the space charge created by the displacement of charge in the conductor^{58,59}. In the case of SCs with redox electrolyte a large increase in the capacitance at 1.25 V (ten times higher) can be observed as can be expected due to the redox reaction of the quinone.

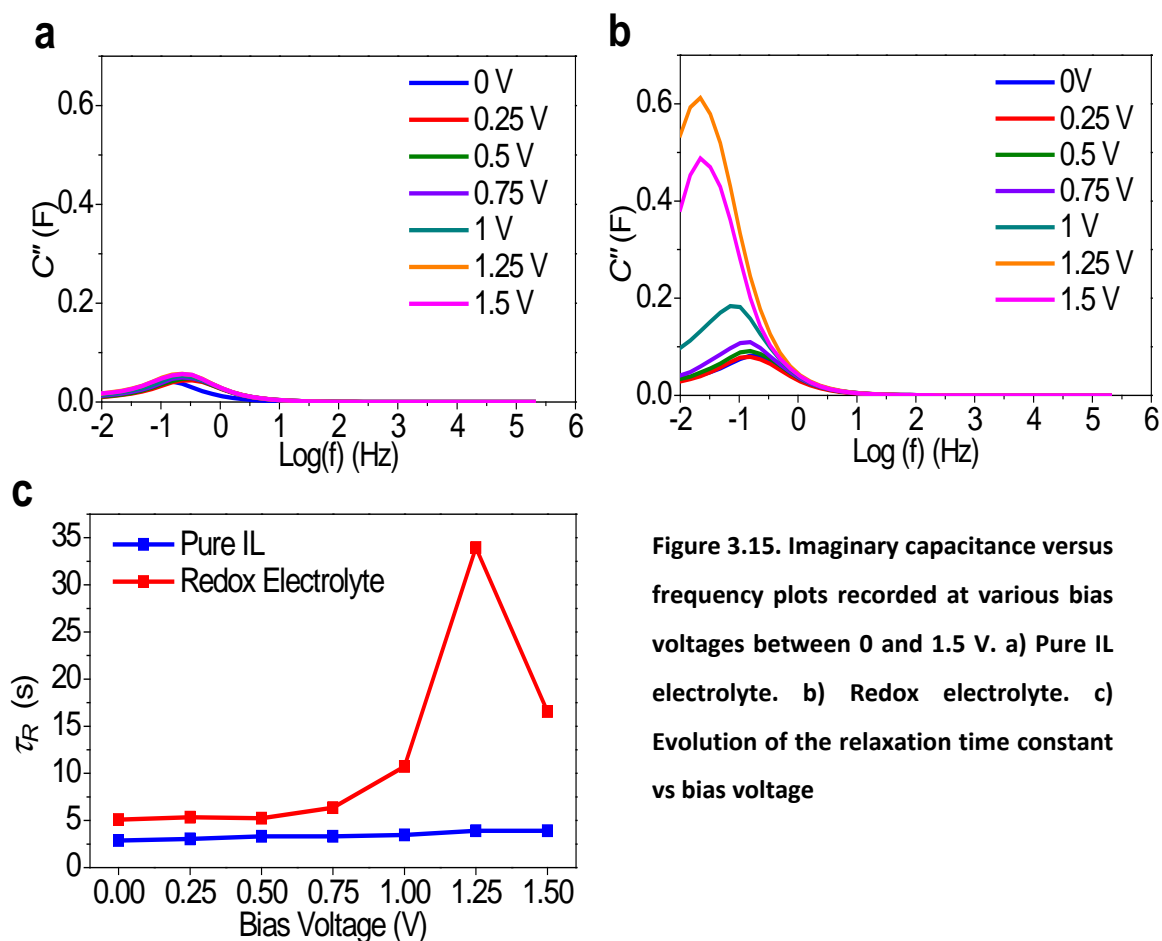


Figure 3.15. Imaginary capacitance versus frequency plots recorded at various bias voltages between 0 and 1.5 V. a) Pure IL electrolyte. b) Redox electrolyte. c) Evolution of the relaxation time constant vs bias voltage

As it was mentioned before, the energy dissipation in the system can be evaluated from the imaginary part of the capacitance $C''(\omega)$. The influence of the bias voltage in $C''(\omega)$ can be extracted from Figure 3.15. As can be observed $C''(\omega)$ reaches a maximum at a characteristic frequency (f_0), due to the dual effect of resistive components which dissipate energy through ohmic loss and capacitive components which store electric energy, simultaneously. The dispersed energy radically increases when approaching f_0 , since only few electric charges are stored at the electrode surface and a resistive behavior dominates. After reaching the maximum, these losses decrease rapidly with the frequency diminution and the system becomes more capacitive. For those systems with pure IL as electrolyte the $C''(\omega)$ maximum is obtained at the same frequency without voltage dependency. However, the use of redox electrolyte causes an increment of dispersed energy and shows bias voltage dependence. The $C''(\omega)$ maximum is achieved at lower frequency and it is higher when the DC potential applied is the one at which the quinone molecules are electroactive due to the supplementary charge stored.

This result clearly shows and confirms the double layer formation and the redox processes take place at different frequencies.

As it was aforementioned $C''(\omega)$ reaches a maximum at the characteristic frequency (f_0) which corresponds with an angle very close to -45° (-48° for pure IL-SC and -52° for hybrid SC) in the Bode plot of the system (see Figure 3.12e and f). This f_0 can be used as a figure of merit to compare the performances of SCs describing how fast a SC can be cycled. The inverse of this remarkable frequency corresponds to a relaxation time ($\tau_R = 1/f_0$) at which the whole system changes from a resistive to a capacitive behavior. At f_0 , the system is as much capacitive as resistive and corresponds to a maximum loss in energy by ohmic dissipation. In other words, τ_R represents the minimum time needed to efficiently discharge 63 % the energy accumulated in the device⁵⁵. In the present study, f_0 for pure IL electrolyte systems is about 0.3 Hz and it keeps constant with the bias voltage. However, hybrid SCs rely on kinetically limited faradic reactions hence, the characteristic frequency f_0 obtained for SC with redox electrolyte becomes lower and shows dependence with the applied bias voltage. For bias voltage below 1V the value is constant about 0.2 Hz, very close to those ones obtained with pure IL electrolyte (0.3 Hz). If bias voltage goes above 1 V and faradaic reaction starts, f_0 decreases down to 0.03 Hz. As consequence, the time constant is higher for the SC with redox electrolyte, as expected since the redox reaction is a slower process in comparison with the formation of the electrostatic double layer and it is turned into longer discharge times for those devices (Figure 3.15c).

It is worth noting that only experimental impedance data were evaluated for the preceding discussion, it was not based on any assumption or supposition of electrical models.

- *Equivalent Electrical Circuit Fitting*

For further understanding the behavior of the hybrid SCs studied, models can be proposed to describe the electric behavior of supercapacitor with a good approximation^{43,60,61}. In this study, an equivalent electric circuit was developed, based only on the experimental data and the analysis of the results discussed previously.

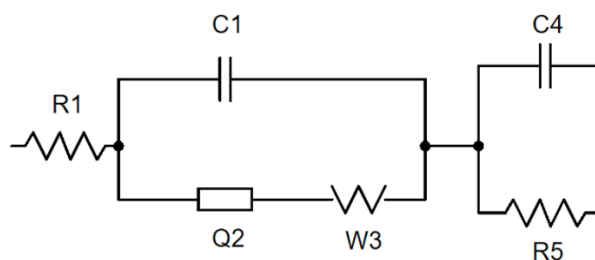


Figure 3.16. Equivalent electrical circuit proposed for the devices under study.

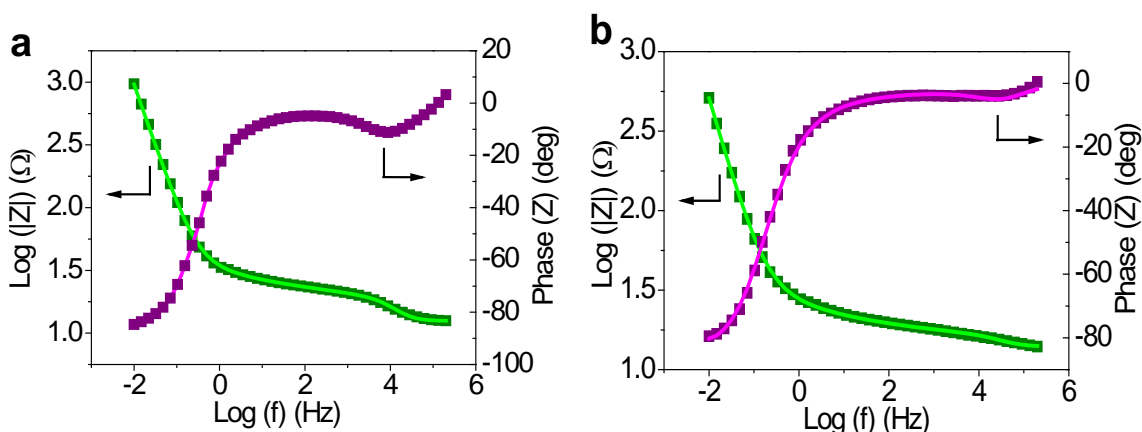


Figure 3.17. Bode Plot model fitting validation at 0 V bias voltage. Fitting (Continuous line); Experimental data (dots). a) Pure IL SCs. b) Redox Electrolyte

Hence, the circuit model takes into consideration the electrochemical and kinetic characteristics of the double layer and the phenomena which take place at the electrode-electrolyte interface region such as faradaic reactions. The proposed model is represented in Figure 3.16, the originality of this model resides in the limited number of components required to consider frequency and voltage dependencies of capacitance, series resistance, redistribution of electrical charges on the electrode surface and the contribution of faradaic reactions. As can be seen in Figure 3.17 the selected model fitted suitably with the experimental data and the elements are related with the main

parameters discussed in the previous section: electrolyte resistance, faradaic charge transfer resistance, Warburg impedance, double layer capacitance and self-discharge.

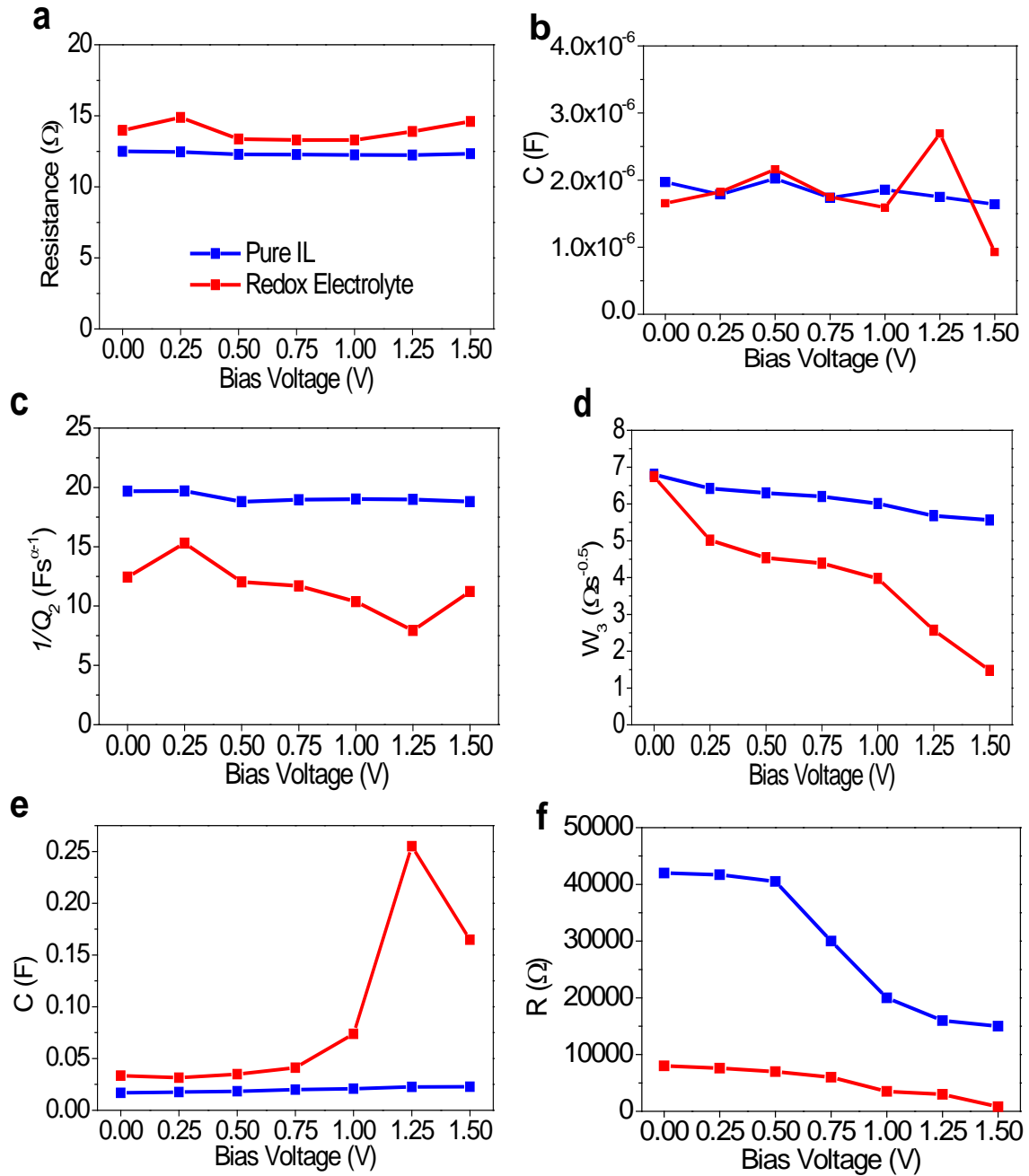


Figure 3.18. Dependence on bias voltage of equivalent electrical circuit elements: a) resistance R_1 . b) capacitor C_1 . c) constant phase element $1/Q_2$. d) Warburg impedance W_3 . e) capacitor C_4 . f) resistance R_5 .

The first element of the equivalent circuit is resistance R_1 which represents the bulk electrolyte and the electrical connections resistance and corresponds with R_s in the

Nyquist plot previously discussed in Figure 3.12. The capacitor $C1$ is related with the distribution of the charge in the frequency domain. The obtained values are small and different reasons have been discussed on literature about the origin of the capacitance distribution such as electrode surface roughness and heterogeneities⁶²⁻⁶⁴, electrode porosity⁶⁵, variation of coating composition⁶⁶, slow adsorption reactions⁶⁷, and non-uniform potential and current distribution⁶⁸⁻⁷¹. $C1$ together with $Q2$ correspond with the semicircle observed in the Nyquist plot. $Q2$ is a constant phase element (CPE) whose impedance can be defined through the following equation $Z_{CPE} = \frac{1}{Q_{CPE}(j2\pi f)^\alpha}$ (accordingly $Z_{Q2} = \frac{1}{Q_2(j2\pi f)^\alpha}$) where Q_{CPE} and α refer to the CPE coefficient and exponent, respectively, while f represents the frequency. The α exponent ranges from -1 to 1. For $\alpha = -1, 0, 1$ the CPE is equivalent to pure inductor, pure resistor and pure capacitor, respectively⁷². The next element is $W3$ and represents the Warburg impedance that shows at middle frequency range in the complex plot. $C4$ is a capacitor which refers to the absolute capacitance of the system and is located in parallel to the resistance $R5$ which is related with the self-discharge and can be observed as a tilted straight line at low frequencies in Nyquist plot. The tendency of each element of the circuit with the bias voltage is represented in Figure 3.19.

The values obtained for the resistance as function of bias voltage for the systems with redox electrolyte are slightly higher than for pure IL based SCs because the redox molecules dissolved into the electrolyte decrease its conductivity. For both systems, the $R1$ value keeps constant over the bias voltage. These values perfectly fit with the R_s contributions represented in Figure 3.13.

The next elements in the electric circuit are the capacitor $C1$ and the constant phase element $Q2$ which are related with the charge distribution and the semicircle resistance in the Nyquist plot (R_c) respectively. In the case of SC with redox electrolytes, the exponents (α) of $Q2$ were estimated through fitting results to vary between 0.08 and 0.13. These values are close to 0 and indicate the behavior of this element is close to a pure resistor. It is not a simple resistor because factors mentioned above, such as the electrode porosity and the charge transfer, are involved. It is worthy to mention R_c has two different contributions; On one hand, it is related to the resistance at the porous

structure of the electrode material (R_p). On the other hand, a resistance associated with the charge transfer process (R_{ct}) in parallel with R_p , can be also considered. The values obtained for the systems with redox electrolyte are lower than SC with pure IL as electrolyte and in particular when the redox reaction occurs (1.25 V). This variation can be attributed to favored charge transfer process inside the porous structure of the carbon electrode. For systems with pure IL the value of this element keeps constant as it was expected since in this SC there are not charge transfer processes involved. This tendency can be also observed in Figure 3.14 in which R_c is represented together with the resistance contributions.

The Warburg impedance is represented by the next element in the circuit model ($W3$). The $W3$ values obtained for the SC with redox electrolyte are lower than those shown by SC with pure IL and they change with bias voltage applied. The lowest values are achieved at 1.25-1.5 V, the potential at which the quinone redox reaction takes place. This is in good agreement with the results shown in Figure 3.13. This tendency can be explained due to the diffusion process of the generated charged species is favored since the potential applied increases and the electromotive force boots too and as result, the diffusion impedance decreases.

The absolute capacitance of the system, capacitor $C4$ in the circuit model, keeps constant over the bias voltage applied for SC with pure IL as electrolyte. However, SCs with redox electrolyte show a strong dependence of $C4$ with bias voltage. Two domains can be distinguished, up to 0.75 V the value keeps constant. Beyond this potential value, the capacitance increases and reaches a maximum at the redox reaction potential (1.25 V). This value (0.25 F) is ten times higher than the displayed by pure IL-SC (0.02 F). This result clearly indicates improved capacitive performance when the redox reaction takes places. It should be noticed that this results presents the same tendency than the capacitance results obtained from low frequency impedance data presented previously in Figure 3.14c.

The last element in the electrical circuit model is the resistance $R5$. This element is associated with self-discharge process. As it was mentioned before, for a non-ideal supercapacitor a non-straight line (slope $\neq 1$) is found at low frequency due to parasitic

currents, the higher deviation in the slope the higher influence of self-discharge. The values of $R5$ obtained for SC with pure IL as electrolyte are higher than those for systems with redox electrolyte implying lower self-discharge as it was expected due to the different energy storage mechanisms involved. Furthermore, in the hybrid devices the redox molecules dissolved into the electrolyte can undergo shuttle process. This shuttle effect is commonly observed in devices with redox electrolytes when a non-selective membrane is used as separator as some Redox Flow Batteries. These movements of the redox molecules through the separator become in an easier self-discharge and lower efficiencies. A decreasing tendency in the value of $R5$ with the bias voltage can be also observed in both devices. This means that the self-discharge phenomena are facilitated by increasing the applied bias potential.

The developed equivalent electrical circuit provides results in good agreement with the information extracted from the analysis of experimental data. Therefore, this model can be used to predict the behavior of SCs with this kind of redox non-conventional electrolytes and points out the importance of a deeper knowledge in their energy storage mechanism. As it has been demonstrated the EIS is a useful tool that takes on importance in the study of these new hybrid devices.

3.3 Conclusions

In this chapter a redox non-conventional electrolyte for increasing hybrid supercapacitors performance has been investigated for the first time. This is an innovative hybrid system that combines two energy-storage processes: the double-layer formation characteristic of carbon-based SCs and the faradaic reactions characteristic of batteries. Moreover, the use of electrochemically stable ionic liquid electrolytes endows a voltage increase that triggers the specific power and energy of SCs.

A redox type electrolyte based on para-Benzoquinone (pBQ) dissolved in the ionic liquid N-butyl-N-methylpyrrolidinium bis(trifluoromethanesulfonyl) imide (PYR₁₄TFSI) was used in carbon-carbon supercapacitors. It has been evidenced that the pBQ redox molecules dissolved in the ionic liquid electrolyte provides a significant enhancement in the electrochemical properties of hybrid SCs in terms of specific capacitance (C_s) and specific real energy (E_{real}). The optimized concentration of pBQ that caused higher improvement was found to be 0.4M. This increment is due to the faradaic redox reaction of pBQ in PYR₁₄TFSI that undergoes a two-step reaction mechanism in aprotic ionic liquids. It has been also demonstrated that the faradaic contribution of the redox electrolyte depends on the type of carbon in the electrode. For instance, the faradaic contribution of the redox electrolyte in microporous Pica- based SC is less significant under high polarization (52 % increase of E_{real} at 2 V, while 1 0% at 3 V) This is possibly due to clogging and higher diffusion limitations in the predominant microporous structure of Pica activated carbon under high polarization. On the other hand, the beneficial effect of p-BQ was found to remarkably increase capacitance in carbons having open porosity with low to medium specific surface areas such as Vulcan. Vulcan SCs results in a 3-fold increase of C_s and 3-fold increase of E_{real} operating at voltages as high as 3.0 V or 3.5 V.

In order to better understanding their energy storage mechanism, the SC performance was further studied by Electrochemical Impedance Spectroscopy. EIS is a powerful technique to evaluate the behavior and the effect of the addition of redox active species into the electrolyte and allows an overview of the whole frequency performance of these systems. Studying the frequency dependence of the resistance, the different

contributions to the total cell resistance can be distinguished. It has been demonstrated the diffusion-related component of the resistance has a strong dependence on the bias voltage in the hybrid SCs, being reduced by 60 % at the faradaic reaction potential of 1.25 V, while other components of the total resistance remain almost constant.

In addition, the evolution of the capacitance with the frequency has also been investigated. The capacitance obtained is ten times higher when the redox electrolyte is used, but the onset frequency to achieve the maximum capacitance is shifted to lower frequencies, implying the kinetics of the redox reactions is slower than of pure capacitive phenomena. This also points out that the formation of the double layer and the redox processes occur at different frequencies and the performance of the SC is highly influenced by this difference. The study of the time constant shows an increase for the hybrid devices if the polarization applied reaches the reaction potential. The capacitance tendency is not linear with the voltage for the devices with quinoid-electrolyte; a 7-fold increase in the value of the capacitance is obtained at 1.25 V bias voltage because of the different storage mechanisms.

Additionally, an equivalent electrical circuit was proposed. Despite its simplicity due to the limited number of components, it fits suitably with the experimental data both in pure IL and in presence of redox molecules. It provides results in good agreement with the conclusions extracted from the analysis of experimental data. Therefore, it can be used to predict the behavior of SCs with this kind of non-conventional electrolytes. The results show that EIS is a method to evaluate SC parameters such as self-discharge, time constant, resistance and capacitance components as function of bias voltage and frequency, more precisely than other usual electrochemical techniques like galvanostatic charge-discharge or cyclic voltammetry that, in the best case, can provide just average values, causing an overestimation/underestimation of the device performance.

3.4 Experimental

3.4.1 Electrode and Electrolyte Preparation

Commercial activated carbon Picatif BP 10 (Pica) and carbon black Vulcan XC72R (Vulcan) provided by PICA and CABOT Corporation respectively were used as active materials. N₂ adsorption-desorption isotherms revealed a main microporous structure with a high specific surface area for Pica (S_{BET} about 2400 m²·g⁻¹) while in the case of Vulcan no microporosity was detected and the specific surface area was much lower, typical from carbon blacks (S_{BET} 240 m²·g⁻¹). Table 3.2 including the textural properties, also shows that the total pore volume for Pica carbon is much higher than in the case of Vulcan (1.58 cm³·g⁻¹ and 0.33 cm³·g⁻¹, respectively) ⁴⁷.

Table 3.2. Textural properties of Pica and Vulcan carbons⁴⁷.

Carbon	S_{BET} (m ² ·g ⁻¹)	Total Pore Volume (cm ³ ·g ⁻¹)	V_{micro}	V_{micro} (%)	Pore length (nm)
Pica	2400	1.58	0.85	48	1.4
Vulcan	240	0.33	0	0	-

Polytetrafluoroethylene (PTFE 60 wt.% dispersion in water, Sigma Aldrich) was employed as a binder and acetylene black (Sigma Aldrich) used as a conductive agent for electrode preparation. As a standard procedure, a paste was prepared by vigorous mixing the activated carbon (80 wt.%), acetylene black (10 wt.%) and PTFE (10 wt.%) in 2-propanol. The paste was rolled onto a coin-shaped stainless steel mesh current collector (d = 1 cm). The electrodes were then pressed with a uniaxial press (CARVER model 3853-0) applying a pressure of 19 metric tonnes cm⁻² and dried at 130 °C under vacuum overnight (Figure 3.19). The mass-loading of the dried electrodes was about 5 mg cm⁻² and 3 mg cm⁻² for Pica and Vulcan electrodes, respectively.



Figure 3.19. Picture of the electrodes after the preparation process.

N-butyl-N-methylpyrrolidinium bis(trifluoromethanesulfonyl) imide (PYR₁₄TFSI) 99.5 % purity purchased from Solvionic and p-Benzoquinone (pBQ) > 99.5 % purity from Fluka Analytical were used as received for electrolyte preparation. Pure PYR₁₄TFSI and a solutions 0.1 M, 0.4 M and 0.8 M of p-Benzoquinone in PYR₁₄TFSI were used as electrolytes. Preparation of electrolytes was performed inside a MBraun glove box (O₂ and H₂O ≤ 0.1 ppm) (Figure 3.20).



Figure 3.20. MBraun glove box

3.4.2 Assembly of Supercapacitors

Supercapacitors (SCs) were built by placing a cellulosic filter paper (100 μm) soaked with the electrolyte, pure PYR₁₄TFSI or 0.4 M p-BQ in PYR₁₄TFSI, between two carbon electrodes in a two electrode Swagelok cell (Figure 3.21). In order to avoid the short-circuit an insulating plastic (Maylar) is placed inside the cell. Pairs of electrodes with similar mass were selected for each SC. Before assembling the SC, the electrodes were impregnated with the electrolyte under vacuum at least for 1 h. Impregnation and assembling of the cell were performed inside the glove box.

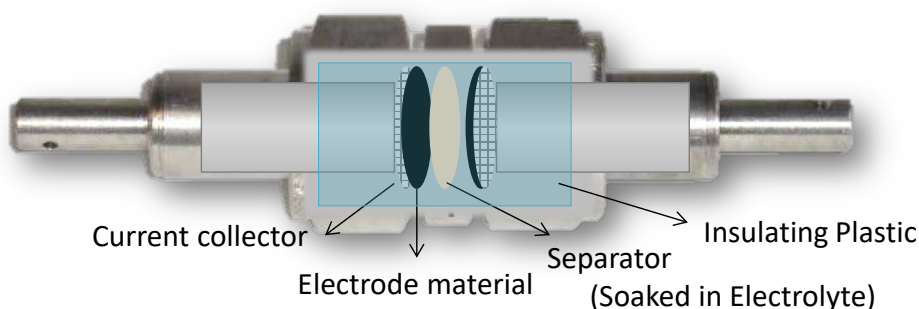


Figure 3.21. Two electrodes configuration in a Swagelok® cell

3.4.3 Electrochemical Characterization of Supercapacitors

Cyclic voltammetry (CV) and galvanostatic charge–discharge (CD) testing was performed using Biologic VMP multichannel potentiostatic–galvanostatic system. All experiments were performed at 60 °C.

3.4.3.1 *Cyclic voltammetry experiments*

Cyclic voltammetry is a method for investigating the electrochemical behavior of a system and is the most widely used technique for acquiring qualitative information about electrochemical reactions. Their advantages are considerable information on the thermodynamics of redox processes, on the kinetics of heterogeneous electron-transfer reactions, and on coupled chemical reactions or adsorption processes can be obtained very quickly.

In this technique, the voltage is swept between two values at a constant rate and when the voltage reaches the limit values the scan is reversed and the voltage is swept back to the initial point. Then the usual representation of the data is current density vs voltage and is called voltammogram. The shape of the voltammogram gives information about the energy storage mechanism: for an ideal capacitive material a rectangular shape will be obtained, in the contrary if the material investigated is non-capacitive faradaic, intense peaks will appear. The typical voltammograms obtained for a capacitive material and a reversible single electron transfer reaction are represented in Figure 3.22.

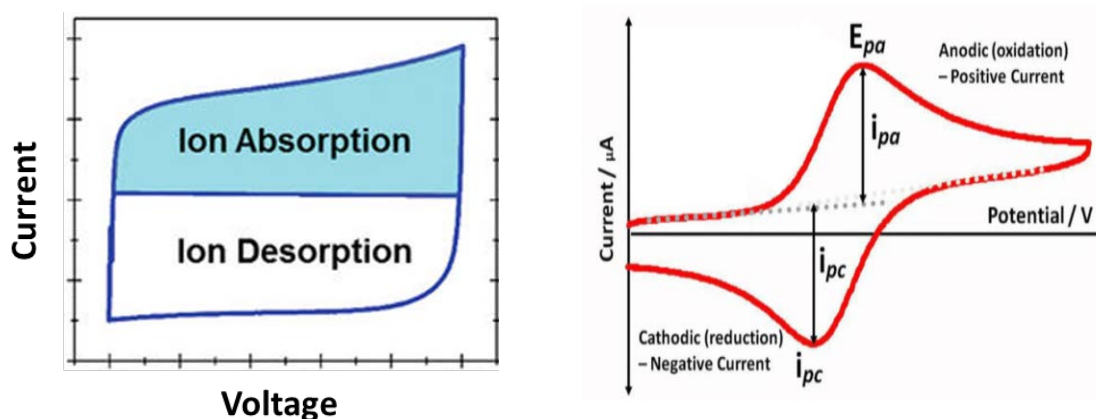


Figure 3.22. Scheme of a cyclic voltammetry for: (right) Capacitive material; (left) Faradaic material.

Therefore, as the voltage is swept from V_1 to V_2 the equilibrium position shifts from no conversion of the electroactive species to full conversion at the electrode surface. Then, the current rises as the voltage is swept and the conversion takes place. The peak occurs, since at some point the diffusion layer is sufficiently large above the electrode that the flux of reactant to the electrode is not fast enough to continue converting species and at this point the current begins to drop. Then, during the inverse scan the current flows in the opposite sense (from the solution to the electrode). For a reversible electrochemical reaction the voltage separation between the current peaks is $59/n$ (mV). The position of the peaks does not depend on the scan rate and the ratio of the peaks current is equal to 1.

In order to characterize the hybrid SCs studied in this chapter, cyclic voltammetry was performed from 0 V to 3 V at different scan rates (5, 10 and 20 $\text{mV}\cdot\text{s}^{-1}$) and galvanostatic charge-discharge experiments from 0 V to different voltages (2 V, 3 V and 3.5 V) and conducted at various current densities (5, 10 and 20 $\text{mA}\cdot\text{cm}^{-2}$).

The specific capacitance of the electrodes (C_{am}) was calculated from the integral of the CV curves as expressed by Eqs. (3.6) and (3.7).

$$C_{SC} (\text{Fg}^{-1}) = \frac{Q}{\Delta V} = \frac{\int I dV}{s \cdot \Delta V \cdot m_t} \quad (3.6)$$

$$C_{am} (\text{Fg}^{-1}) = 4C_{SC} \quad (3.7)$$

Where: Q is the charge stored; ΔV is the applied potential window; I is the applied current; s is the scan rate and m_t is the total mass of activated carbon.

3.4.3.2 Galvanostatic Charge-Discharge experiments

The galvanostatic charge discharge technique consists in applying a constant current density and measuring the voltage signal of the device. Specifically, for charging the device a positive current is applied and for discharging a negative current should be applied. Thus the potential between the two electrodes of the device is recorded. Usually in this type of experiments the maximum and minimum voltage is fixed. The typical representation of these experiments is potential vs time graph (Figure 3.23).

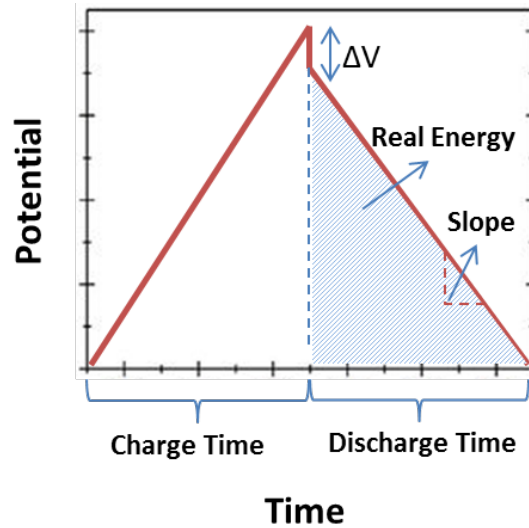


Figure 3.23. Schematic illustration of a galvanostatic charge discharge curve of a supecapacitor

Equivalent Series Resistance (ESR) is a parameter that can be obtained from the ohmic drop (ΔV) found in the charge-discharge curves applying the eq (3.8) and represents the total resistance of the cell. Specific real energy (E_{real}) was obtained from galvanostatic CD measurements by applying Eq. (3.9) to the discharge voltage profiles. Specific real power (P_{real}) was calculated from Eq. (3.10).

$$ESR = \frac{\Delta V}{2I} A \quad (3.8)$$

$$E_{real} = \frac{1}{m_t} \int_{t_i}^{t_f} I \cdot V \cdot dt = \frac{I}{m_t} \int_{t_i}^{t_f} V dt \quad (3.9)$$

$$P_{real} = \frac{E_{real}}{t_{discharge}} \quad (3.10)$$

Where: ΔV is the ohmic drop; A is the geometrical area of the electrode; I is the current applied; m_t is the total mass of the electrodes; V is the maximum voltage; $t_{discharge}$ is the discharge time at that current density ($t = t_f - t_i$).

In many papers authors refer to specific energy as that calculated with the well-known equation $E_{max}=1/2CV^2$. This equation refers to the maximum energy of the supercapacitor considering an “ideal electrical double layer supercapacitor” without faradaic contribution or ohmic drop”. However, we prefer to use the “real energy”, calculated directly from the integration of the discharge curve. Although E_{real} values are lower than E_{max} they better represent the energy delivered by a hybrid supercapacitor having important contribution of faradaic reactions.

3.4.3.3 *Electrochemical Impedance Spectroscopy Experiments*

Electrochemical Impedance Spectroscopy is a powerful technique that allows for studying the different resistive and capacitive contributions in the behavior of the device in a wide range of frequency. In this technique a sinusoidal voltage perturbation with small amplitude is applied meanwhile the frequency is swept from high values to small ones. Thus, the response of the device is recorded. The impedance (Z) is defined by the relation between the voltage applied and the current response of the system. It is usually represented by complex mathematical expression (Eq. 3.11).

$$Z(\omega) = \frac{1}{jf C(2\pi f)} \quad (3.11)$$

Where ω is the angular frequency $\omega = 2\pi f$; f is the frequency and C is the capacitance.

The usual representations of the impedance results are called Nyquist plot and Bode plot (Figure 3.24). In the first one, the imaginary part of the impedance (Z'') is plotted versus the real part of the impedance (Z'). In the Bode plot the phase angle (θ) and the modulus ($|Z|$) of the impedance are represented versus the frequency range. To perform an impedance experiment, the system must be causal, stable, linear and invariant in time and any external disturbances such as electrical noise must be avoided.

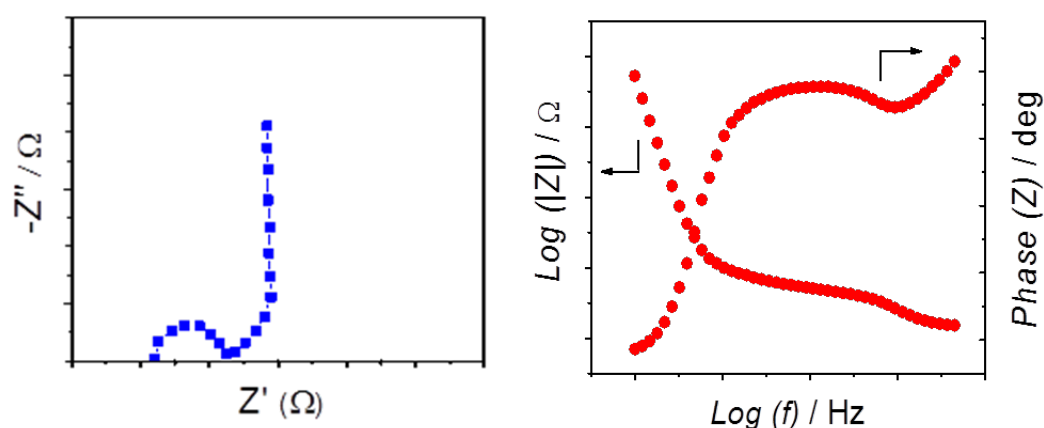


Figure 3.24. Schematic representation of Nyquist diagram (right) and Bode plot (left) for a supercapacitor.

For EIS experiments the supercapacitor was polarized at different fixed bias potentials between 0 V and 1.5 V and a small ripple of 10 mV was overlaid on the DC component. The ripple frequency was swept between 10 mHz and 100 kHz. In order to ensure the

accuracy of the measurements Kramers-Kronig transformation analysis was performed. In this analysis the error of each recorded data was calculated. As criteria to validate the measurements an error < 5% was established.

For impedance data fittings, the tool Zfit from EC-Lab® software was employed to adjust the electrical equivalent circuit. A low standard deviation of the overall fit ($\chi^2 < 10^{-3}$) was settled as mathematical criteria for a suitable fitting.

3.5 References

- 1 M. Conte, *Fuel Cells*, 2010, **10**, 806–818.
- 2 A. Burke, *J. Power Sources*, 2000, **91**, 37–50.
- 3 E. Frackowiak and F. Béguin, *Carbon N. Y.*, 2001, **39**, 937–950.
- 4 Y. Zhai, Y. Dou, D. Zhao, P. F. Fulvio, R. T. Mayes and S. Dai, *Adv. Mater.*, 2011, **23**, 4828–4850.
- 5 M. Pandurangappa, N. S. Lawrence and R. G. Compton, *Analyst*, 2002, **127**, 1568–1571.
- 6 G. Pognon, T. Brousse, L. Demarconnay and D. Bélanger, *J. Power Sources*, 2011, **196**, 4117–4122.
- 7 M. Weissmann, O. Crosnier, T. Brousse and D. Bélanger, *Electrochim. Acta*, 2012, **82**, 250–256.
- 8 K. Kalinathan, D. P. DesRoches, X. Liu and P. G. Pickup, *J. Power Sources*, 2008, **181**, 182–185.
- 9 A. Le Comte, T. Brousse and D. Bélanger, *Electrochim. Acta*, 2014, **137**, 447–453.
- 10 R. D. L. Smith and P. G. Pickup, *Electrochim. Acta*, 2009, **54**, 2305–2311.
- 11 G. Wang, R. Liang, L. Liu and B. Zhong, *Electrochim. Acta*, 2014, **115**, 183–188.
- 12 Q. Abbas, P. Ratajczak, P. Babuchowska, A. L. Comte, D. Belanger, T. Brousse and F. Beguin, *J. Electrochem. Soc.*, 2015, **162**, A5148–A5157.
- 13 G. Pognon, T. Brousse and D. Bélanger, *Carbon N. Y.*, 2011, **49**, 1340–1348.
- 14 B. Akinwolemiwa, C. Peng and G. Z. Chen, *J. Electrochem. Soc.*, 2015, **162**, A5054–A5059.
- 15 B. Akinwolemiwa, C. Wei and G. Z. Chen, *Electrochim. Acta*, 2017, **247**, 344–357.
- 16 S. T. Senthilkumar, R. K. Selvan and J. S. Melo, *J. Mater. Chem. A*, 2013, **1**, 12386–12394.
- 17 S. Yamazaki, T. Ito, M. Yamagata and M. Ishikawa, *Electrochim. Acta*, 2012, **86**, 294–297.
- 18 S. T. Senthilkumar, R. K. Selvan, Y. S. Lee and J. S. Melo, *J. Mater. Chem. A*, 2013, **1**, 1086–1095.
- 19 G. Lota, K. Fic and E. Frackowiak, *Electrochem. commun.*, 2011, **13**, 38–41.
- 20 G. Lota and E. Frackowiak, *Electrochem. commun.*, 2009, **11**, 87–90.
- 21 E. Frackowiak, K. Fic, M. Meller and G. Lota, *ChemSusChem*, 2012, **5**, 1181–1185.
- 22 K. Fic, E. Frackowiak and F. Béguin, *J. Mater. Chem.*, 2012, **22**, 24213–24223.
- 23 B. Huskinson, M. P. Marshak, C. Suh, S. Er, M. R. Gerhardt, C. J. Galvin, X. Chen, A. Aspuru-Guzik, R. G. Gordon and M. J. Aziz, *Nature*, 2014, **505**, 195–198.
- 24 B. Yang, L. Hooper-Burkhardt, F. Wang, G. K. Surya Prakash and S. R. Narayanan, *J. Electrochem. Soc.*, 2014, **161**, A1371–A1380.

- 25 S. Roldan, C. Blanco, M. Granda, R. Menendez and R. Santamaria, *Angew. Chem. Int. Ed. Engl.*, 2011, **50**, 1699–1701.
- 26 S. Roldán, M. Granda, R. Menéndez, R. Santamaría and C. Blanco, *J. Phys. Chem. C*, 2011, **115**, 17606–17611.
- 27 S. Roldán, Z. González, C. Blanco, M. Granda, R. Menéndez and R. Santamaría, *Electrochim. Acta*, 2011, **56**, 3401–3405.
- 28 S. Roldán, M. Granda, R. Menéndez, R. Santamaría and C. Blanco, *Electrochim. Acta*, 2012, **83**, 241–246.
- 29 H. Yu, L. Fan, J. Wu, Y. Lin, M. Huang, J. Lin and Z. Lan, *RSC Adv.*, 2012, **2**, 6736–6740.
- 30 H. J. Yu, J. H. Wu, L. Q. Fan, Y. Z. Lin, S. H. Chen, Y. Chen, J. L. Wang, M. L. Huang, J. M. Lin, Z. Lan and Y. F. Huang, *Sci. China Chem.*, 2012, **55**, 1319–1324.
- 31 K. B. Hatzell, M. Beidaghi, J. W. Campos, C. R. Dennison, E. C. Kumbur and Y. Gogotsi, *Electrochim. Acta*, 2013, **111**, 888–897.
- 32 L. Su, L. Gong, H. Lü and Q. Xü, *J. Power Sources*, 2014, **248**, 212–217.
- 33 H. Xie, Y. Zhu, Y. Wu, Z. Wu and E. Liu, *Mater. Res. Bull.*, 2014, **50**, 303–306.
- 34 S.-E. Chun, B. Evanko, X. Wang, D. Vonlanthen, X. Ji, G. D. Stucky and S. W. Boettcher, *Nat. Commun.*, 2015, **6**, 7818.
- 35 D. P. Dubal, O. Ayyad and V. Ruiz, *Chem. Soc. Rev.*, 2015, **44**, 1777–1790.
- 36 N. Fechler, G. A. Tiruye, R. Marcilla and M. Antonietti, *RSC Adv.*, 2014, **4**, 26981–26989.
- 37 A. Balducci, R. Dugas, P. L. Taberna, P. Simon, D. Plée, M. Mastragostino and S. Passerini, *J. Power Sources*, 2007, **165**, 922–927.
- 38 M. M. Jaramillo, A. Mendoza, S. Vaquero, M. Anderson, J. Palma and R. Marcilla, *RSC Adv.*, 2012, **2**, 8439–8446.
- 39 A. J. Bard and L. R. Faulkner, *Electrochemical Methods: Fundamentals and Applications*, Department of Chemistry and Biochemistry University of Texas at Austin, 2nd edn., 2001.
- 40 H. D. Yoo, J. H. Jang, J. H. Ryu, Y. Park and S. M. Oh, *J. Power Sources*, 2014, **267**, 411–420.
- 41 E. Frackowiak, M. Meller, J. Menzel, D. Gastol and K. Fic, *Faraday Discuss.*, 2014, **172**, 179–198.
- 42 K. M. Košiček, K. Kvastek and V. Horvat-Radošević, *Electrochim. Acta*, 2016, **195**, 77–84.
- 43 L.-Q. Mai, A. Minhas-Khan, X. Tian, K. M. Hercule, Y.-L. Zhao, X. Lin and X. Xu, *Nat. Commun.*, 2013, **4**, 2923.
- 44 H. S. Kim, T. D. Chung and H. Kim, *J. Electroanal. Chem.*, 2001, **498**, 209–215.
- 45 M. A. Bhat, *Electrochim. Acta*, 2012, **81**, 275–282.
- 46 P. S. Guin, S. Das and P. C. Mandal, *Int. J. Electrochem.*, 2011, **2011**, 1–22.

- 47 S. Vaquero, R. Díaz, M. A. Anderson, J. Palma and R. Marcilla, *Electrochim. Acta*, 2012, **86**, 241–247.
- 48 Y. Wang, E. I. Rogers, S. R. Belding and R. G. Compton, *J. Electroanal. Chem.*, 2010, **648**, 134–142.
- 49 S. Isikli and R. Diaz, *J. Power Sources*, 2012, **206**, 53–58.
- 50 K. W. Leitner, B. Gollas, M. Winter, *Electrochim. Acta*, 2004, **50**, 199–204.
- 51 J. Gamby, P. L. Taberna, P. Simon, J. F. Fauvarque and M. Chesneau, *J. Power Sources*, 2001, **101**, 109–116.
- 52 J. Chmiola, G. Yushin, R. Dash and Y. Gogotsi, *J. Power Sources*, 2006, **158**, 765–772.
- 53 R. Kötz, R. Kötz, M. Carlen and M. Carlen, *Electrochim. Acta*, 2000, **45**, 2483–2498.
- 54 R. De Levie, *Electrochim. Acta*, 1964, **9**, 1231–1245.
- 55 C. Cougnon, E. Lebègue and G. Pognon, *J. Power Sources*, 2015, **274**, 551–559.
- 56 P. L. Taberna, P. Simon and J. F. Fauvarque, *J. Electrochem. Soc.*, 2003, **150**, A292–A300.
- 57 J. Miller, *Proc. Eighth Semin. Double Layer Capacit. Similar Energy Storage Devices*, 1998, 21–35.
- 58 A. G. Pandolfo and A. F. Hollenkamp, *J. Power Sources*, 2006, **157**, 11–27.
- 59 F. Rafik, H. Gualous, R. Gallay, A. Crausaz and A. Berthon, *J. Power Sources*, 2007, **165**, 928–934.
- 60 S. Fletcher, V. J. Black and I. Kirkpatrick, *J. Solid State Electrochem.*, 2014, **18**, 1377–1387.
- 61 P. A. Basnayaka, M. K. Ram, L. Stefanakos and A. Kumar, *Graphene*, 2013, **2**, 81–87.
- 62 L. Nyikos and T. Pajkossy, *Electrochim. Acta*, 1985, **30**, 1533–1540.
- 63 Z. Kerner, *J. Electroanal. Chem.*, 1998, **448**, 139–142.
- 64 C. H. Kim, S. I. Pyun and J. H. Kim, *Electrochim. Acta*, 2003, **48**, 3455–3463.
- 65 H.-K. Song, H.-Y. Hwang, K.-H. Lee and L. H. Dao, *Electrochim. Acta*, 2000, **45**, 2241–2257.
- 66 J. Vogelsang and W. Strunz, *Electrochim. Acta*, 2001, **46**, 3619–3625.
- 67 T. Pajkossy, T. Wandlowski and M. Kolb, *J. Electroanal. Chem.*, 1996, **414**, 209–220.
- 68 J. Newman, *J. Electrochem. Soc.*, 1966, **113**, 1235–1241.
- 69 J. Newman, *J. Electrochem. Soc.*, 1970, **117**, 507–508.
- 70 J. A. Trainham and J. Newman, *J. Electrochem. Soc.*, 1977, **124**, 1528–1540.
- 71 D. B. Bonham and M. E. Orazem, *J. Electrochem. Soc.*, 1999, **146**, 2199–2208.
- 72 J.-P. Diard, B. Le Gorrec and C. Montella, *Handbook of Electrochemical Impedance Spectroscopy-Electrical circuits containing CPEs*, Bio-Logic, 2013.

Chapter 4. Membrane-Free
Redox Flow Batteries
by Using Two Immiscible
Redox Electrolytes

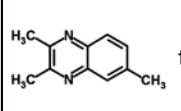
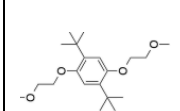
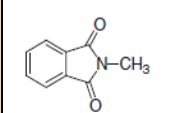
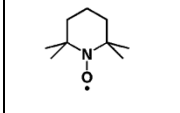
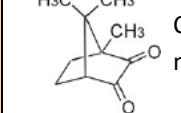
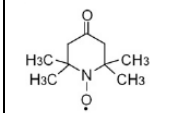
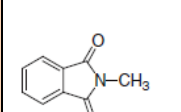
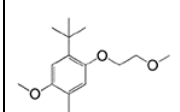
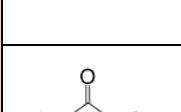
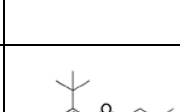
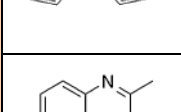
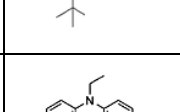
4.1 Introduction

As it was mentioned in the Chapter 1 of this PhD thesis, Redox Flow Batteries (RFBs) utilize electroactive species that are dissolved into the electrolytes and are stored in two external tanks, making it possible to decouple power and energy ^{1,2}. The most developed RFB technology involves the aqueous All-Vanadium system, discovered in the 1980s ³, whose major issues are the limited performance, short lifetime and high cost of the ion-selective membranes and the high price, toxicity and scarcity of vanadium compounds ⁴. Moreover, the aqueous nature of the current vanadium electrolytes limit the operating voltage and consequently the energy density of RFBs⁵.

Therefore, one of the most promising research topics has been the substitution of aqueous electrolytes by nonaqueous electrolytes ⁶ or even ionic liquids ⁷, which are more electrochemically stable and would allow achieving higher cell voltages and energy densities ⁸.

Another encouraging research line is the replacement of expensive, toxic and scarce vanadium compounds by organic redox molecules both in aqueous and nonaqueous RFBs. Most of these organic compounds are abundant, low cost, environmentally friendly and offer countless possibilities through synthetic strategies ⁹. In the last few years, organic redox flow batteries (ORFBs) based on organic redox molecules such as quinones ^{10,11}, phthalimide ¹², methoxyethoxybenzene ¹³, phenothiazine ¹⁴, nitroxides ¹⁵, viologens ¹⁶ and pyridines ¹⁷ have experienced a great deal of interest, becoming one of the hottest topics in electrochemical energy storage ¹⁸. Most representative examples of ORFBs, using both aqueous and nonaqueous electrolytes, and their reported characteristics are gathered in Table 4.1.

Table 4.1. Comparison of technical parameters and key factors of reported aqueous and nonaqueous ORFBs

	Anolyte	Catholyte	Separator	Media	V (V)	CE (%)	EE (%)	Cycles	Q retention	P(W·cm ⁻²)	Highlights	Ref
Non Aqueous Organic RFB	 2,3,6-trimethylquinoxaline	 DBBB	Nafion 117	LiBF ₄ in PC	1.3	70	37	30	100 (non-Flow)	8·10 ⁻⁵	Coin cell configuration. Low CE and EE	19
	 MPh	 TEMPO	Nepem 117	NaClO ₄ in ACN	1.36	90	74	20	-	4.7·10 ⁻⁴	First example of “all organic RFB”	20
	 Camphorquinone	 4-Oxo TEMPO	Fuma Tech	TEABF ₄ in PC	2.03	80	71	3	(95) (non-Flow)	0.002	Novel organic molecules providing higher operating voltages. Only 3 cycles of charge-discharge.	17
	 MePh	 DBMMB	Daramic /Celgard	LiTFSI in DME	1.9	90	69	50	100	0.066	Using porous separators results in high current densities. Mixed reactant electrolytes are necessary to mitigate crossover.	12
	 FL	 DBMMB	Daramic	TEA-TFSI in DME	2.2	95	82	50	85	0.022	High OCV. Stability study of radical species in different supporting electrolytes.	13
	 TMeQ	 BCF3EPT	Nafion 117	LiBF ₄ in PC	1.3	85	42	50	0(non-Flow)	2·10 ⁻⁴	Swagelok cell configuration. Huge capacity loss over time.	14

4. Membrane-Free Redox Flow Batteries by Using Two Immiscible Redox Electrolytes

Table 4.1. Continuation

	Anolyte	Catholyte	Separator	Media	V (V)	CE (%)	EE (%)	Cycles	Q retention	P ($W \cdot cm^{-2}$)	Highlights	Ref
Aqueous Organic RFB	AQS	BQDS	Nafion 112	H ₂ SO ₄	0.45	90	40	12	90	0.0036	First example of all-organic aqueous RFB.	10
	2,6-DHAQ	[Fe(CN) ₆] ⁴⁻ Ferrocyanide	Nafion 212	KOH	1.1	99	84	100	90	0.45	Alkaline Flow Battery	11
	Methyl-Viologen	4-OH-TEMPO	AEM	NaCl	1.05	100	72	100	99	0.042	Neutral pH. High OCV and current densities	16
	AQDS	Br	Nafion 212	H ₂ SO ₄	0.65	95	55	15	99.2	0.6	Increasing in the OCV about 11% by adding -OH groups in AQDS	21
	Methyl-Viologen	TEMPTMA	Fumasep FAA3PE30	NaCl	1.15	100	70	100	100	0.088	Novel organic molecule. Neutral pH. High OCV.	22
	[(NPr) ₂ TTZ]	N ^{Me} -TEMPO	AMV	NaCl	1.1	100	73	300	90	0.044	Novel two-electron anolyte	23

Regardless of the chemical nature of the electroactive species and the type of electrolytes, most RFBs rely on ion-selective membranes to separate the two redox electrolytes and to prevent the crossover of active compounds while allowing the migration of charge carriers. Therefore, ion-selective membranes still remain one of the severe obstacles for the massive commercialization of RFBs because they are expensive (approaching 40% of the total cost)²⁴ and limit the performance and lifetimes of RFBs^{25,26}. In order to avoid the use of ion-selective membrane and minimize the effect of the crossover, some new approaches are being investigated such as: hybrid RFBs, semisolid RFBs, the use of size-exclusion/porous separators, and microfluidic designs (Figure 4.1).

- Hybrid RFBs. It is worth mentioning that ion-selective membranes are not strictly necessary in this type of RFBs where at least one chemical species is plated as a solid in the electrochemical cells during charge^{27,28}. Redox chemistry of active species with formation of electrodeposits leads to another type of cell configuration without membranes and with only one electrolyte reservoir as represented in Figure 4.1a. Some selected membrane-free redox flow batteries include Zn^{29,30}, Cd³¹ or lithium³². However, in this hybrid RFB technology is not possible to fully decouple power and energy, being probably the most important advantage of redox flow batteries over conventional ones.
- Semisolid RFBs. In this approach, the electrolytes are solid suspensions of active materials with high capacity and a conductive additive dispersed in the solvent (See Figure 4.1b). Due to the large size of the particles, these suspensions enable the use of cheap and enduring microporous separators instead of ion-exchange membranes^{33,34}.
- Polymer RFBs. Some research groups have introduced a novel strategy of separating the catholyte and anolyte by size-exclusion separators that are cheaper than ion-selective membranes. In such batteries, the use of active polymer-based system³⁵ or other macromolecules³⁶ with large size allows the use of size-exclusion separators avoiding the crossmixing of active materials (see Figure 4.1c).

4. Membrane-Free Redox Flow Batteries by Using Two Immiscible Redox Electrolytes

- Symmetric RFBs: Two categories can be distinguished i) those in which the active species have multiple oxidation states and the same electrolyte can be used as catholyte and anolyte^{36–39}; and (ii) those that use already mixed-electrolytes^{12,13,40}. In both cases the mixture of electrolytes is not an issue and the use of a common porous separator is possible although they have the disadvantage of requiring idle active material (see Figure 4.1d).
- Microfluidic RFB. The only way to completely eliminate membranes or separators in RFBs so far has been through the development of fluidodynamic engineering solutions to maintain a laminar flow minimizing the mixture of the electrolytes as represented in Figure 4.1e^{41–44}. Most of these batteries exploit the laminar flow of electrolytes through parallel micro-channels and thus their real applications are limited to power small micro-devices.

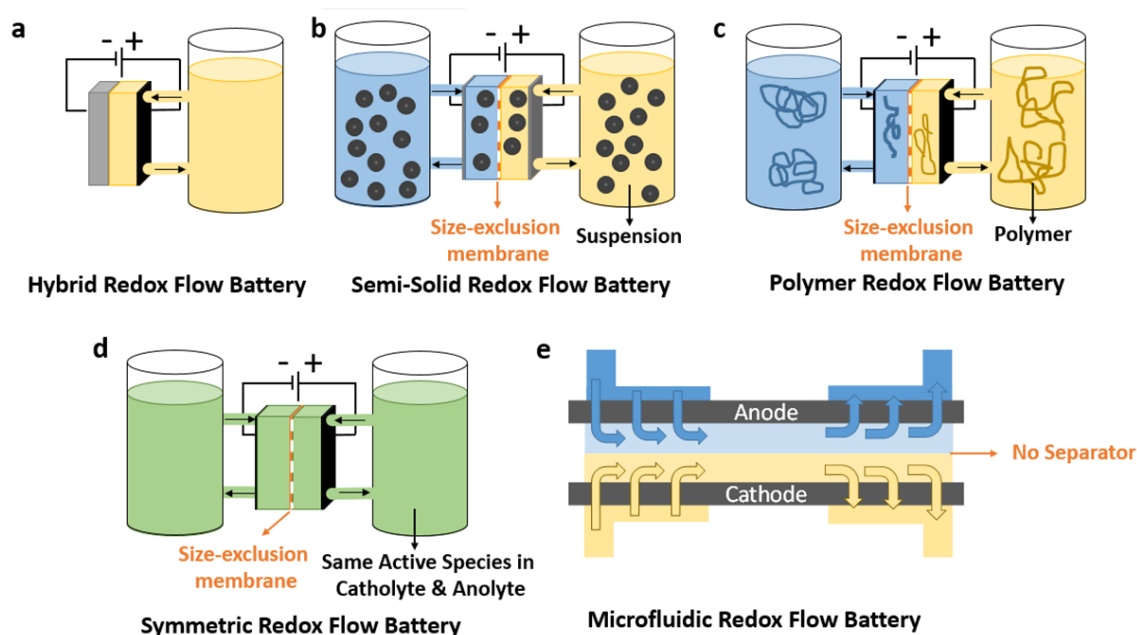


Figure 4.1. Schematic illustration of different approaches to avoid the use of ion-exchange membrane. a) Hybrid RFB. b) Semi-solid RFB. c) Polymer RFB. d) Symmetric RFB. e) Microfluidic RFB.

As demonstrated in chapter 3, the use of redox electrolytes (typically used in RFBs) in supercapacitors (SC) has given rise to new hybrid configurations and designs with enhanced performance. In fact, the combination of different aspects typical from supercapacitors and redox flow batteries into novel hybrid devices brings additional

4. Membrane-Free Redox Flow Batteries by Using Two Immiscible Redox Electrolytes

features/advantages singular from each technology. One example is the so-called “flow-capacitor” introduced by Hatzell et al.⁴⁵ in which the carbon material (typically used in SCs) is dispersed into the electrolyte and pumped into the reactor of a RFB (Figure 4.2a). Other example was proposed by Chun et al.⁴⁶ and consisted on using two dissolved redox species (Figure 4.2b), previously used in RFB and separated by an ion-exchanged membrane, in a hybrid SC with enhanced energy density.

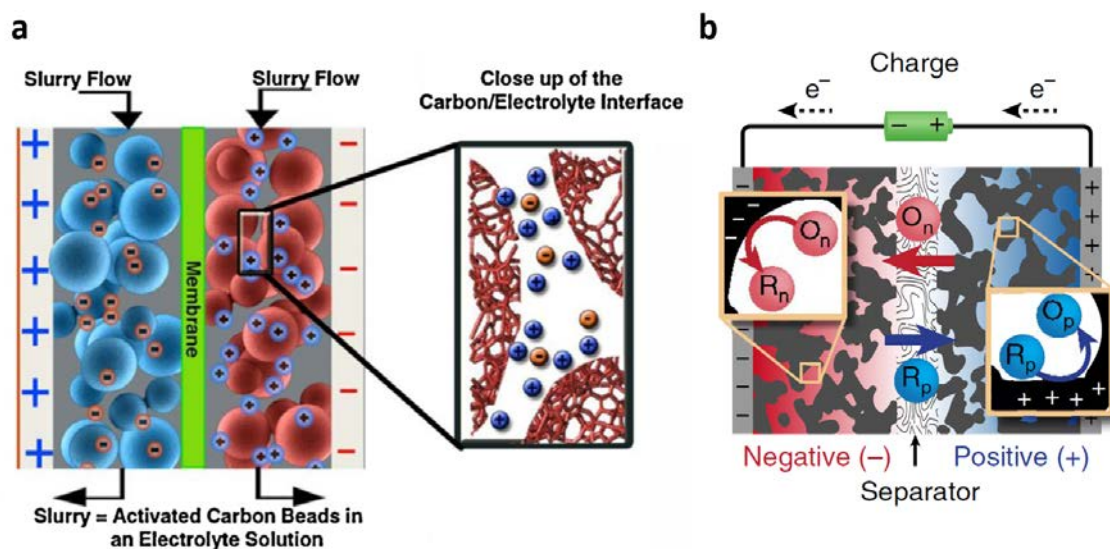


Figure 4.2. a) Illustration of a “flow-capacitor”. Adapted from⁴⁵. b) Description of design of a hybrid SC with two redox molecules. Adapted from⁴⁶.

In line with these new capacitors designs, in the first part of this chapter, a simple and original idea which combines two redox electrolytes is reported. This idea consists in combining the IL redox electrolyte used in hybrid SCs in chapter 3 with an immiscible aqueous redox electrolyte, with the aim of developing an innovative concept of Membrane-Free RFB. Both redox electrolytes, based on quinones, have been successfully proven to enhance the energy density of hybrid SC^{47,48}. This improvement is due to the faradaic contribution of the quinone reaction which takes place in the positive electrode of the aqueous SC^{47,48} and in the negative electrode of the IL-based SC (see chapter 3). In this chapter, it is described how by combining these two immiscible redox electrolytes is possible to assemble a battery. The selection of immiscible electrolytes is a key aspect of this idea because it allows to develop a battery in which neither ion-exchange membrane nor separator are necessary. In this concept the interface functions as a “natural” barrier making the use of any membrane

4. Membrane-Free Redox Flow Batteries by Using Two Immiscible Redox Electrolytes

superfluous. A schematic representation of this Membrane-Free concept based on the mutual immiscibility of redox electrolytes containing organic molecules is shown in Figure 4.3.

As illustrated in Figure 4.3 this Membrane-Free RFB concept might overcome many of the current limitations of RFBs since vanadium compounds will be substituted by organic molecules and ion-exchange membranes will be totally removed. Moreover, this concept presents advantages over abovementioned strategies to remove the membrane. For instance, it might be easily scalable since their fluid dynamics is less restricted than in microfluidic designs in which it is limited to laminar-flow regimes. Additionally, unlike hybrid RFBs, in this Membrane-Free RFB both active species are liquid electrolytes so that power and energy is totally decoupled.

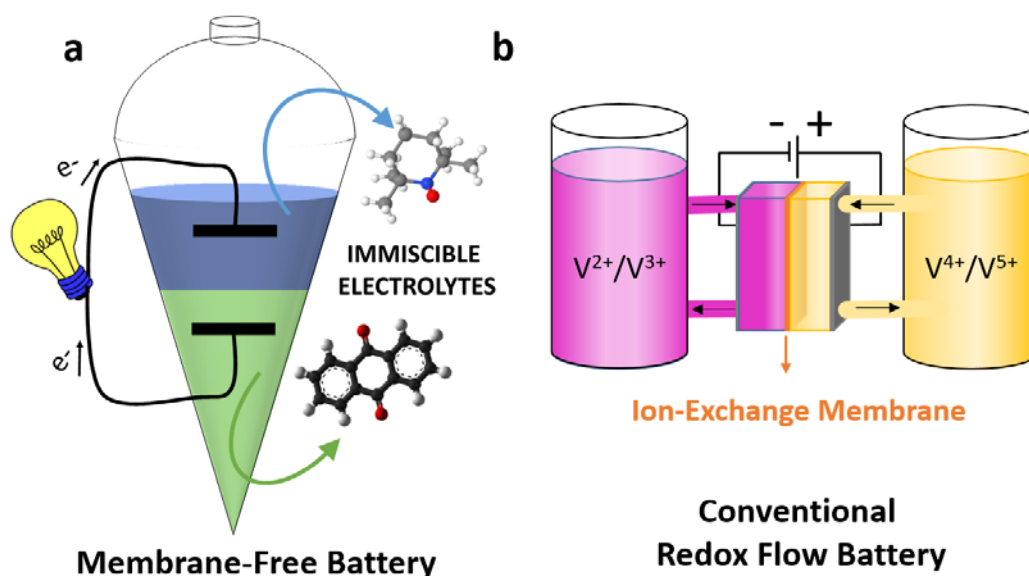


Figure 4.3. a) Schematic representation of the Membrane-Free Battery concept based on immiscible organic redox electrolytes. b) Illustration of a conventional Redox Flow Battery based on vanadium active species and having an ion-exchange membrane.

In the first part of this chapter, we will investigate the feasibility of this Membrane-Free RFB concept by developing the “proof-of-concept”. The second part of this chapter will be addressed to the versatility of this concept and the possibility of being implemented using different immiscible systems (aqueous or nonaqueous solvents) and different redox compounds.

4.2 Results and Discussion

4.2.1 Proof-of-concept of Membrane-Free Battery

The first example of Membrane-Free Battery consisted on combining the IL redox electrolyte described in previous chapter with an immiscible aqueous redox electrolyte, both containing dissolved quinoyl species. Both electrolytes were previously used in hybrid SCs separately to enhance the storage capacity of those devices. Here, these two organic redox electrolytes will be used together in a new configuration of Membrane-Free Battery which is based on the mutual immiscibility of the electrolytes. In particular, the proof-of-concept battery represented in Figure 4.4, is based on a solution of pBQ in hydrophobic ionic liquid, 1-butyl-1-methylpyrrolidinium bis(trifluoromethanesulfonyl)imide (PYR₁₄TFSI) and an acidic solution of hydroquinone (H₂Q). Both redox electrolytes spontaneously form a liquid-liquid biphasic system that was investigated as a battery without adding any membrane or physical separator.

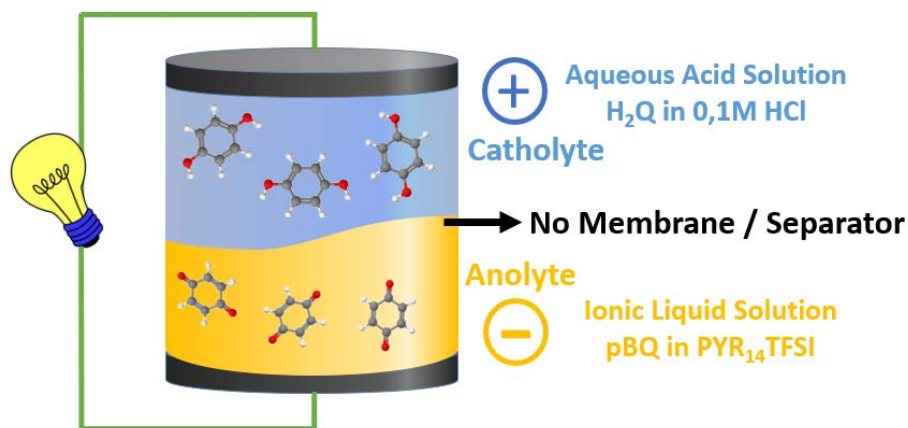


Figure 4.4. Proof-of Concept of Membrane-Free Battery

The choice of pBQ and H₂Q as redox-active organic molecules is motivated by their simplicity, relatively high solubility in the electrolytes (~ 0.7 M for aqueous and IL electrolyte) and their theoretical capacity; $495 \text{ mAh}\cdot\text{g}^{-1}$ and $486 \text{ mAh}\cdot\text{g}^{-1}$ for pBQ and H₂Q, respectively. It is remarkable that, by taking advantage of the different redox mechanism underwent by quinones in different electrolytes, the same molecule was

4. Membrane-Free Redox Flow Batteries by Using Two Immiscible Redox Electrolytes

used as active species in both electrolytes. Moreover, similar to all-vanadium RFB technology, in this particular example pBQ and H₂Q constitute different oxidation states of the same molecule meaning that the eventual cross-over would provoke certain loss of efficiency but not irreversible contamination. Finally, both compounds have a low molecular weight-to-charge ratio of 54 g·(mol·e⁻)⁻¹ and 55 g·(mol·e⁻)⁻¹, respectively. This is substantially less than 150 g·(mol·e⁻)⁻¹ proposed by Sandford and colleagues for achieving grid-cost parity⁴⁹.

4.2.1.1 *Electrochemical Characterization of Redox Electrolytes*

The immiscible electrolytes forming the biphasic system (acidic solution of hydroquinone (H₂Q) and parabenzoquinone (pBQ) dissolved in PYR₁₄TFSI) were subjected to cyclic voltammetry (CV) in 3 electrode electrochemical cells, separately. The shape of the CVs in Figure 4.5 denotes a quasi-reversible redox behavior for both electrolytes.

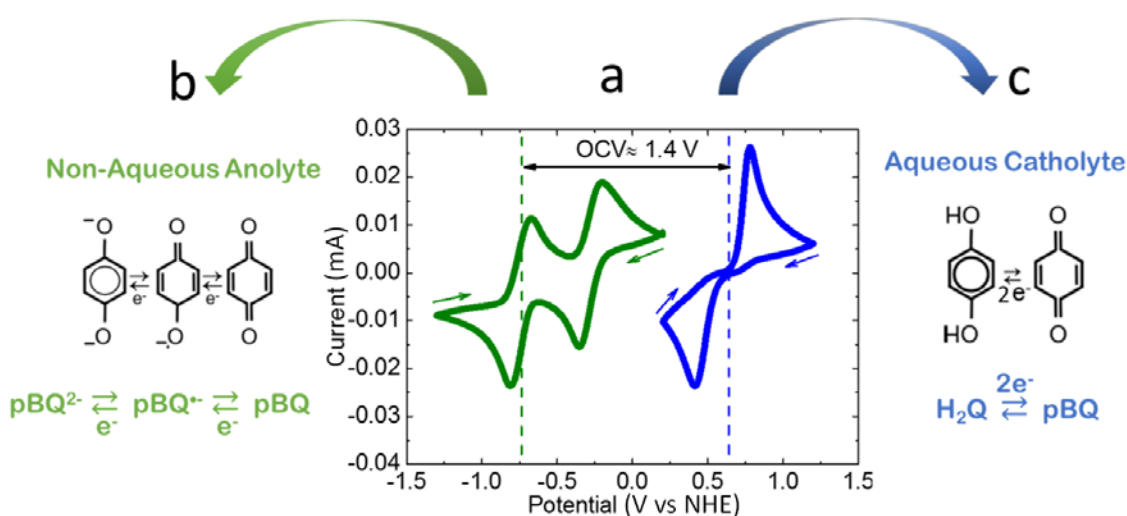


Figure 4.5. Electrochemical characterization of immiscible redox electrolytes. a) Cyclic voltammetry experiments of 20 mM pBQ in PYR₁₄TFSI (green) and 20 mM H₂Q in 0.1 M HCl (blue) performed in 3-electrode electrochemical cells (scan rate= 10 mV·s⁻¹). b) and c) Redox-active organic species in both electrolytes and their corresponding redox mechanisms depending on the nature of the electrolyte.

As reported elsewhere, hydroquinone (H₂Q) in acidic media suffers a reversible oxidation to parabenzoquinone (pBQ) in one step (blue curve), involving the exchange of 2 electrons and 2 protons⁵⁰. On the other hand, the parabenzoquinone (pBQ) in

aprotic electrolyte undergoes a two consecutive reversible reduction reactions to radical anion ($\text{pBQ}^{\bullet-}$) and dianion (pBQ^{2-}), exchanging 2 electrons in total (green curve)⁵¹. According to the redox potential of each reaction, acidic solution of H_2Q will act as the catholyte and the pBQ solution in the IL will be the anolyte. The position of CVs in Figure 4.5 anticipates an open circuit voltage (OCV) of about 1.4 V for the battery assembled by combining these two immiscible electrolytes (calculated as the difference between the redox potential of catholyte and anolyte). This OCV is higher than previous examples of RFBs based on quinoyl species^{10,11,52}. This is likely due to the ionic liquid, which is electrochemically more stable than former aqueous electrolytes and allows the reduction of pBQ at more negative voltages.

It should be highlighted that, the same simple molecule follows different redox reaction pathways occurring at different redox potentials, depending on the protic/aprotic nature of the electrolyte. Although this has been reported before⁵¹, this is the first time in which this voltage difference is exploited to develop a symmetric battery. This “symmetric design” offers advantages such as mitigating chemical contamination associated with crossover of the electrolytes. Until now, these benefits have been limited to complex redox molecules having multiple oxidation states^{37–39} but with the development of this Membrane-Free concept the opportunities boost greatly.

The redox mechanisms described above and represented in Figure 4.5b,c were confirmed by rotating disk electrode (RDE) experiments depicted in Figure 4.6. In these experiments the electrode rotates inducing a perpendicular flow of electrolyte to the electrode surface. Thus, the mass transport of reactants close to the surface of the electrode is controlled by diffusion since it is assumed that there is a totally stagnant layer. The electrochemical technique employed is Linear Sweep Voltammetry (LSV) whereby the current is measured during the oxidation/reduction reaction of the active species (see Experimental section 4.4.3). These experiments were used to calculate the diffusion coefficients (D) and reaction rate constants (K^0) for both redox electrolytes using the Koutecky-Levich equation (4.1). The results are gathered in Table 4.2.

4. Membrane-Free Redox Flow Batteries by Using Two Immiscible Redox Electrolytes

Table 4.2. Diffusion Coefficients, kinetic rate constants, conductivity and viscosity of the anolyte and catholyte

	Electrolyte	Reaction	D ($\text{cm}^2\cdot\text{s}^{-1}$)	K^0 ($\text{cm}\cdot\text{s}^{-1}$)	Conductivity ($\text{mS}\cdot\text{cm}^{-1}$) ⁵³	Viscosity (cP) ⁵³
Anolyte	pBQ in $\text{PYR}_{14}\text{TFSI}$	$\text{pBQ} \rightarrow \text{pBQ}^{\bullet-}$	$5.8 \cdot 10^{-5}$	$1.2 \cdot 10^{-3}$	2.2	84.3
		$\text{pBQ}^{\bullet-} \rightarrow \text{pBQ}^{2-}$	$8.6 \cdot 10^{-5}$	$7.7 \cdot 10^{-3}$		
Catholyte	H_2Q in 0.1 M HCl	$\text{H}_2\text{Q} \rightarrow \text{pBQ}$	$4.1 \cdot 10^{-4}$	$3.8 \cdot 10^{-1}$	392.0	0.9

The diffusion coefficient calculated for H_2Q in 0.1 M HCl was higher than for the same molecule in sulfuric acid ($D \sim 10^{-6} \text{ cm}^2\cdot\text{s}^{-1}$)⁵², organic ($D \sim 10^{-5}\text{-}10^{-6} \text{ cm}^2\cdot\text{s}^{-1}$)^{54,55} or neutral electrolytes ($D = 10^{-4}\text{-}10^{-5} \text{ cm}^2\cdot\text{s}^{-1}$)^{56,57}. Moreover, the fast kinetics of H_2Q was corroborated with the high rate constant (see Table 4.2) that is in the same range of recent published results⁵⁸. For the ionic liquid redox electrolyte, two diffusion coefficients (D) can be calculated, since two horizontal plateaus are observed corresponding to the two steps of the reduction reaction of pBQ in the IL (Figure 4.6a). The resulting D and rate constants for both steps of the reaction (see Table 4.2) are similar to those reported by other groups in aprotic electrolytes^{50,59,60}. As expected, the lower conductivity and higher viscosity of the ionic liquid electrolyte leads to more significant mass transport and kinetic limitations that are evidenced by the lower diffusion coefficient (D) and rate constants (K^0) compared to the aqueous electrolyte.

4. Membrane-Free Redox Flow Batteries by Using Two Immiscible Redox Electrolytes

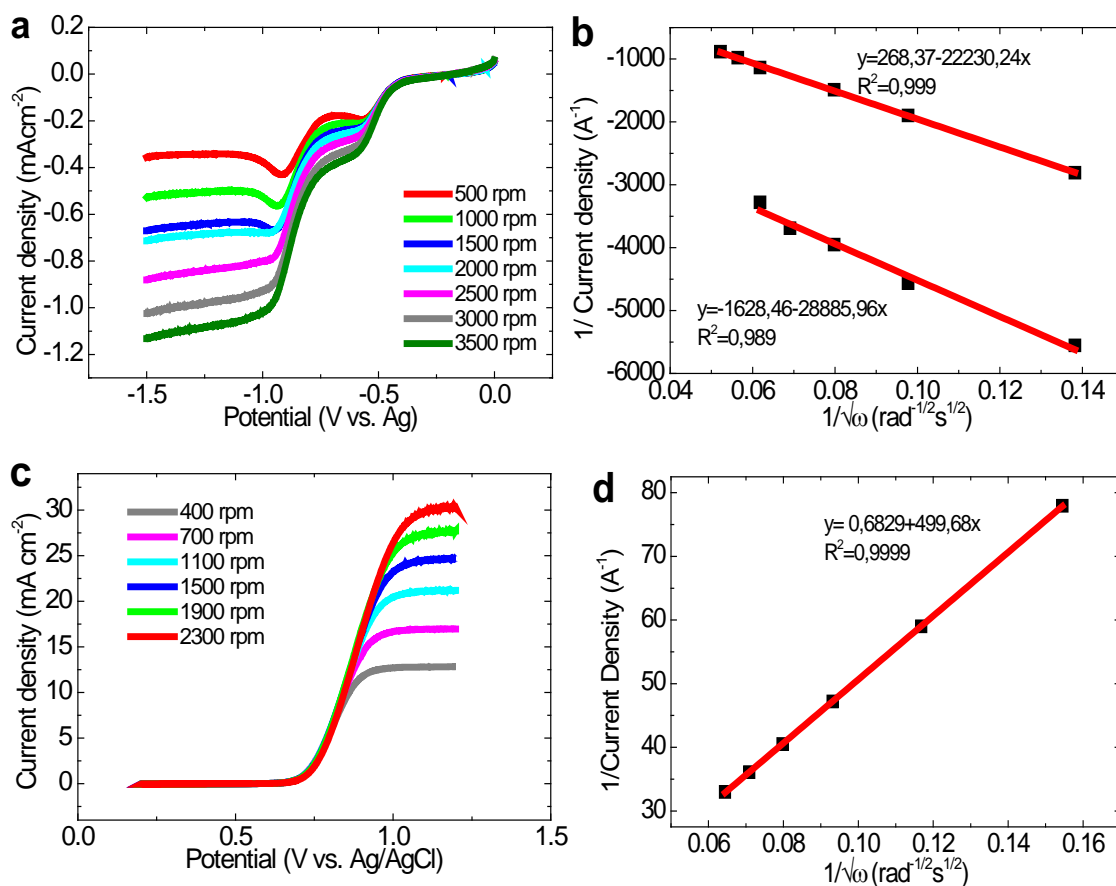


Figure 4.6. Electrochemical investigation of redox electrolytes using a Rotating Disk Electrode (RDE). a) RDE experiments (LSV at $10 \text{ mV}\cdot\text{s}^{-1}$) of 5 mM pBQ in $\text{PYR}_{14}\text{TFSI}$. b) Levich plot of 5 mM pBQ in $\text{PYR}_{14}\text{TFSI}$ and the line fit (red line) with its mathematical expression. c) RDE experiments (LSV at $10 \text{ mV}\cdot\text{s}^{-1}$) of 5 mM H_2Q in 0.1 M HCl. d) Levich plot of 5 mM H_2Q in 0.1 M HCl.

4.2.1.2 Assembly and Electrochemical Characterization of Membrane-Free Battery

A static Membrane-Free Battery was “assembled” simply by mixing similar volumes of both electrolytes and immersing one carbon electrode in each immiscible phase (at this point, the battery is totally discharged). A photograph of the experimental set-up is shown in Figure 4.7. It is worth to remark that neither physical separator nor ion-exchange membrane was used because catholyte and

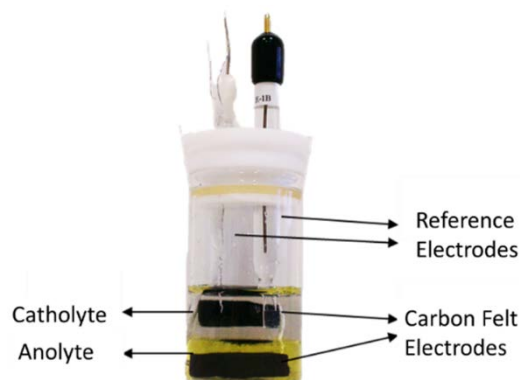


Figure 4.7. Experimental set-up of the Membrane-Free Battery.

anolyte are immiscible and spontaneously form two separate phases (see Experimental section 4.4.4).

This battery was charged to different States of Charge (SOC) from 5 % to 90 % and the potential-current response and current-power relationships were determined in discharge (see Figure 4.8). The battery shows very promising behavior especially at 35% of SOC, with an initial discharge voltage of approximately 1.2 V at low currents. This voltage remains above 0.60 V after increasing the current. At this SOC, a power density of $1.85 \text{ mW}\cdot\text{cm}^{-2}$ can be achieved, being similar to those reported in literature for organic RFBs operating with nonaqueous electrolytes^{14,19,20} (see Table 4.1).

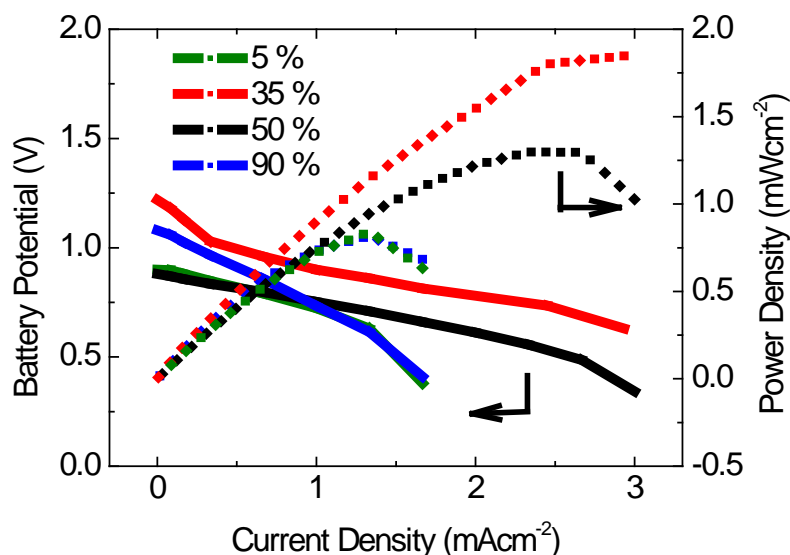


Figure 4.8. Polarization curves of the Membrane-Free Battery at four different states of charge (SOC). All data were collected at room temperature using a 20 mM pBQ in $\text{PYR}_{14}\text{TFSI}$ solution as the anolyte and 20 mM H_2Q in 0.1 M HCl as the catholyte.

Figure 4.9a shows the charge-discharge profile of the battery and the individual voltage profiles of each phase when charged to 35 % of SOC at low current density. As anticipated by CVs, during the charging stage, H_2Q is oxidized to pBQ at a constant voltage of 0.45 V (vs Ag/AgCl) in the aqueous catholyte. Meanwhile, the voltage profile of the anolyte displayed the reduction of pBQ to the radical anion ($\text{pBQ}^{\cdot-}$) and to the dianion (pBQ^{2-}). During discharge, the immiscible biphasic system behaves as a common battery with a discharge voltage reaching a plateau of 0.8 V demonstrating the practical feasibility of the Membrane-Free system. The coulombic efficiency of this

4. Membrane-Free Redox Flow Batteries by Using Two Immiscible Redox Electrolytes

battery was close to 100 % demonstrating that this first example of a Membrane-Free Battery, although far from being optimized, already behaves similar to common RFBs employing expensive ion-exchange membranes¹⁹.

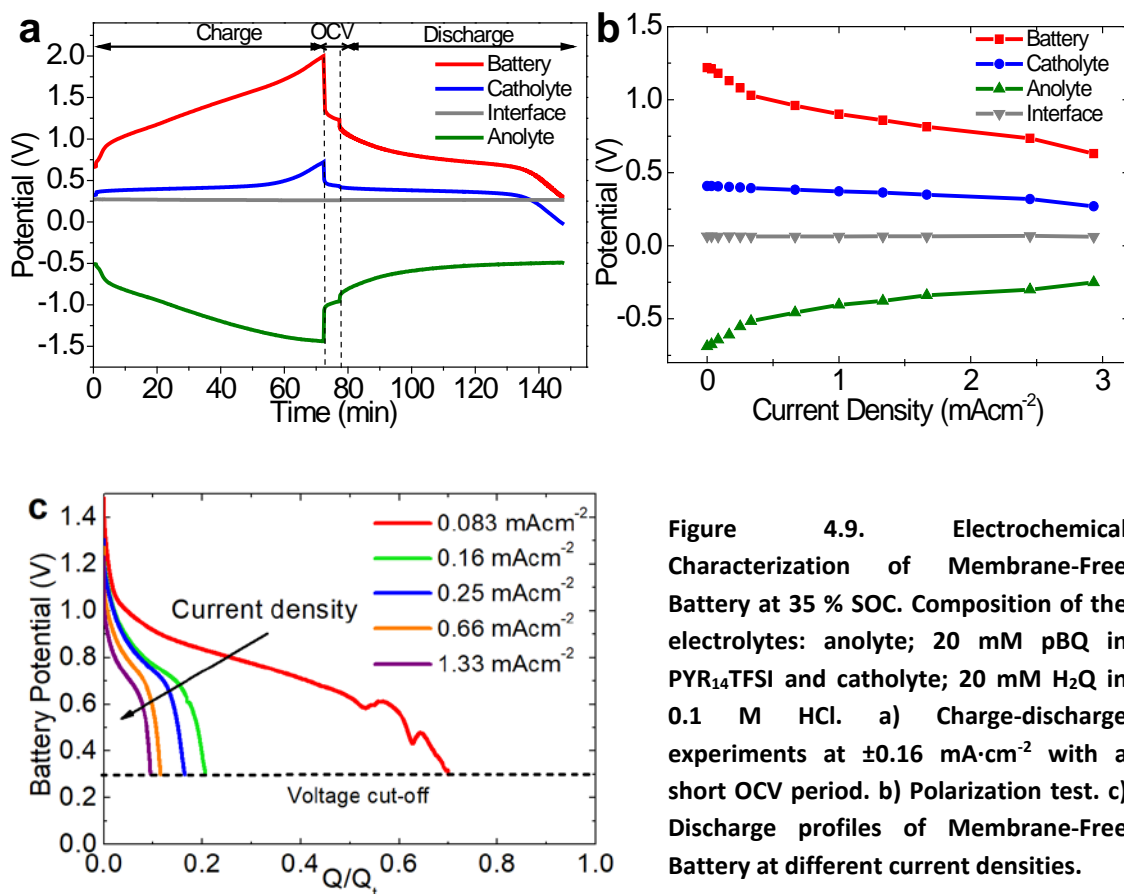


Figure 4.9. Electrochemical Characterization of Membrane-Free Battery at 35 % SOC. Composition of the electrolytes: anolyte; 20 mM pBQ in $\text{PYR}_{14}\text{TFSI}$ and catholyte; 20 mM H_2Q in 0.1 M HCl. a) Charge-discharge experiments at $\pm 0.16 \text{ mA}\cdot\text{cm}^{-2}$ with a short OCV period. b) Polarization test. c) Discharge profiles of Membrane-Free Battery at different current densities.

As expected, the ionic liquid anolyte (green curve in Figure 4.9a) contributes with a larger polarization to the battery overpotential due to its higher viscosity, lower ionic conductivity, smaller diffusion coefficients and slower kinetics of the active species in comparison with aqueous catholyte. Remarkably, during the OCV step the voltage drop at the interface, which is one of the key issues of this innovative concept, was found to be negligible revealing the high mobility of charge carriers, probably protons, through the interface. Those results are corroborated in the Figure 4.9b that shows the polarization curve of the battery. The catholyte potential decreases very slightly from 0.4 V to 0.3 V while the anolyte suffers from higher polarizations, from -0.69 V to -0.25 V with increasing currents. Interestingly, the overpotential across the interface, is

constant and very low which illustrates its stability and its minor contribution to the total resistance of the battery (about 2 %, calculated from the linear part of the curve).

Figure 4.9c displays the full discharging behavior of the battery at different current densities (voltage cut-off 0.3 V). The Membrane-Free Battery exhibits a constant plateau at about 0.8 V and capacity utilization close to 70 %, when discharged at low current densities. Similar to any other type of battery, increasing discharge currents leads to lower capacities due to higher overpotentials, especially in the anolyte.

The reversibility of the battery was investigated through profound charge-discharge cycles (from 35 % to 0 % SOC). Figure 4.10a shows that during the first 10 cycles, the voltage of the battery was constant and only a minor decrease in capacity was observed probably due to the crossover of active species. After 20 cycles a significant reduction in battery voltage caused by the increasing overpotential of the anolyte, was observed. Figure 4.10b shows that the capacity retention remains above 50 % after 30 cycles, confirming the moderate reversibility of the battery. Additionally to the crossover or poor electrochemical stability of redox species, the efficiency during the cycling might be decreased due to the self-discharge. This phenomenon occurs in this Membrane-Free concept by the direct chemical reaction between the generated species at the interface. Although this effect can be important in other batteries as it will be discussed in next chapter, in this proof-of-concept battery the high viscosity of the anolyte hinders the diffusion of reduced species to the interphase and consequently reduces the self-discharge.

4. Membrane-Free Redox Flow Batteries by Using Two Immiscible Redox Electrolytes

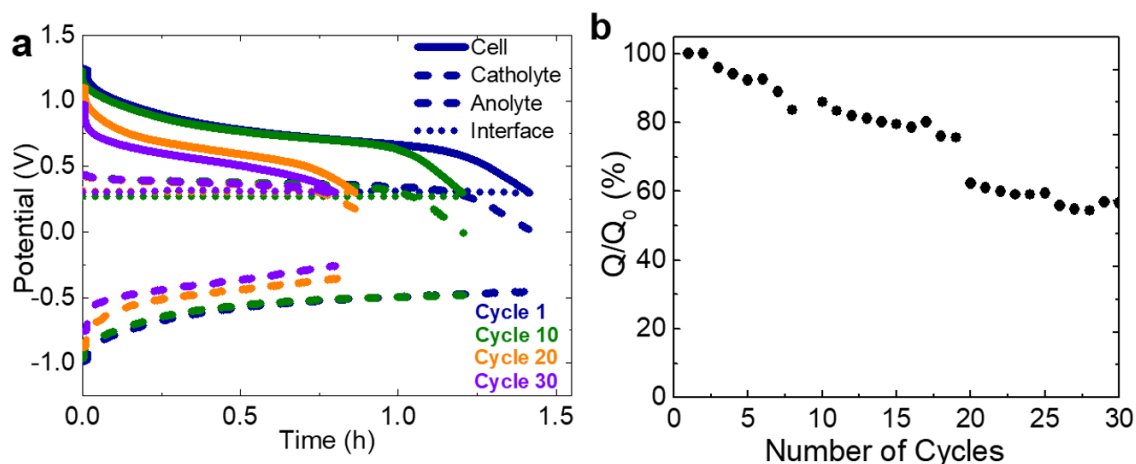


Figure 4.10. Membrane-Free Battery performance at 35 % SOC. Composition of the electrolytes: 20 mM pBQ in PYR₁₄TFSI and 20 mM H₂Q in 0.1 M HCl. a) Cyclability test at $\pm 0.16 \text{ mA}\cdot\text{cm}^{-2}$ using voltage cut-offs of 0.3 V in discharge and 2 V in charge (profound discharge). Discharge curves of 1st, 10th, 20th and 30th cycles with their individual profiles: Voltage of the full battery (continuous line), catholyte and anolyte individual voltages (dashed lines) and voltage drop at the interface (dotted line). b) Capacity retention vs. cycle number.

Before analyzing more deeply the origin of battery fading, we assembled a more practical battery employing more concentrated redox electrolytes; 0.1 M H₂Q in 0.1 M HCl for the catholyte and 0.1 M pBQ in PYR₁₄TFSI for the anolyte. The polarization curve of this battery (see Figure 4.11a) shows a slightly higher OCV than the diluted example (1.4 V vs. 1.2 V). Once the current density is applied, a voltage drop is observed due to activation losses likely triggered by the saturation of the electrode surface owing to the higher amount of available active species. Then, increasing the current density a linear voltage/current relationship and a power density close to $1.85 \text{ mW}\cdot\text{cm}^{-2}$ is obtained, similar to the example with diluted electrolytes. Figure 4.11b shows the discharge profile of the concentrated battery with a discharge voltage plateau of 0.9 V and the individual profiles of each electrolyte and the interface exhibiting very stable profiles during 8 h. The higher concentration of the active species causes an improvement in the discharge capacity reaching 90 % of the theoretical one at the lowest current density (Figure 4.11c). This enhancement is probably resulting from a reduction in the crossover due to the higher amount of active species decreases the concentration gradient. As in any type of battery, a diminution in the discharge capacity is obtained when the current density increases due to the higher overpotential.

4. Membrane-Free Redox Flow Batteries by Using Two Immiscible Redox Electrolytes

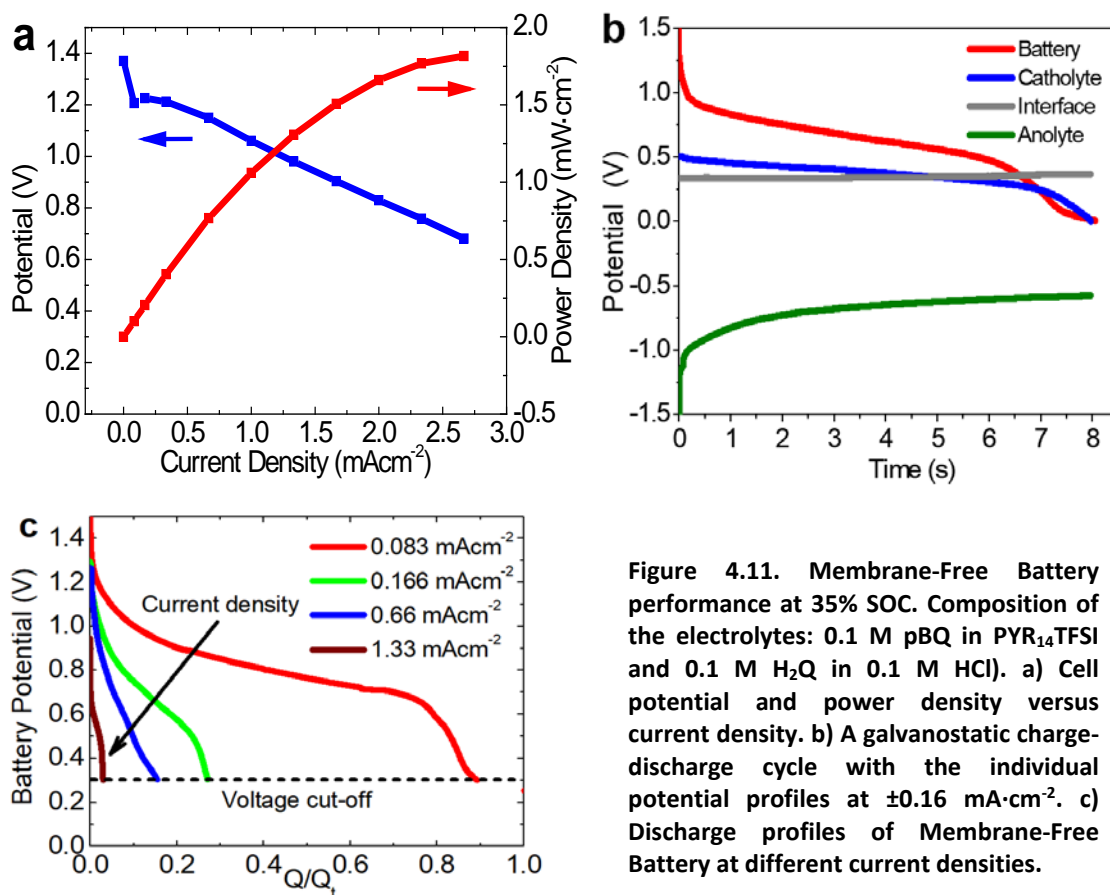


Figure 4.11. Membrane-Free Battery performance at 35% SOC. Composition of the electrolytes: 0.1 M pBQ in $\text{PYR}_{14}\text{TFSI}$ and 0.1 M H_2Q in 0.1 M HCl). a) Cell potential and power density versus current density. b) A galvanostatic charge-discharge cycle with the individual potential profiles at $\pm 0.16 \text{ mA}\cdot\text{cm}^{-2}$. c) Discharge profiles of Membrane-Free Battery at different current densities.

In order to investigate the long term performance of this new battery concept, the Membrane-Free Battery was charged/discharged at $\pm 0.66 \text{ mA}\cdot\text{cm}^{-2}$ during 75 cycles. Under these experimental conditions in which short cycles are employed (low variation of state of charge (SOC)) the crossover of active species and the effect of the self-discharge are probably minimized. Figure 4.12 shows the excellent capacity retention of the system that operates with coulombic efficiencies (CE) exceeding 99 % along cycling and with energy efficiencies (EE) of about 70 % (the energy efficiency (EE) was calculated as; coulombic efficiency (CE) \times voltage efficiency (VE)). This behavior compares very positively with other organic redox flow batteries reported in literature (see Table 4.1), confirming the excellent performance of the battery over cycling.

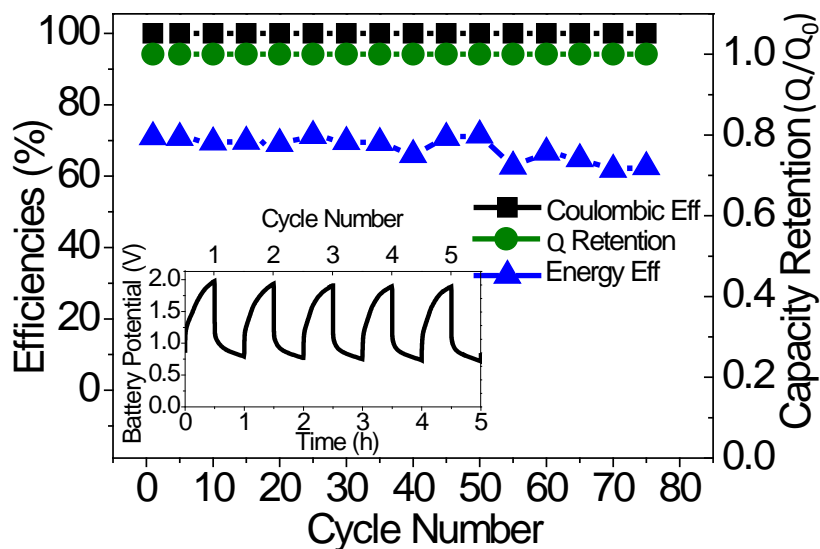


Figure 4.12. Electrochemical Characterization of Membrane-Free Battery at 35 % SOC. Composition of the electrolytes: anolyte; 0.1 M pBQ in PYR₁₄TFSI and catholyte; 0.1 M H₂Q in 0.1 M HCl. Cyclability study at $\pm 0.66 \text{ mA}\cdot\text{cm}^{-2}$. Coulombic efficiency, energy efficiency and capacity retention versus cycles. Inset: Voltage profile of the battery for the first 5 cycles

The substitution of the ion-selective membrane by a liquid/liquid interface raises many questions that makes this simple battery concept very intriguing and fascinating. One interesting issue is related to the crossover of active species through the interface which is governed by equilibrium thermodynamics through partition coefficients. The partitioning of the active species is mainly influenced by the polarity and nature of the solvent. Although these thermodynamic aspects will be investigated in next chapter, CVs of each phase were performed before and after cycling in order to shed light on the changes experienced by the electrolytes (Figure 4.13a, b). CV curves of catholyte present similar shape but lower peak currents after cycling. This is probably due to crossover of active species (H₂Q or pBQ) from the catholyte to the anolyte.

4. Membrane-Free Redox Flow Batteries by Using Two Immiscible Redox Electrolytes

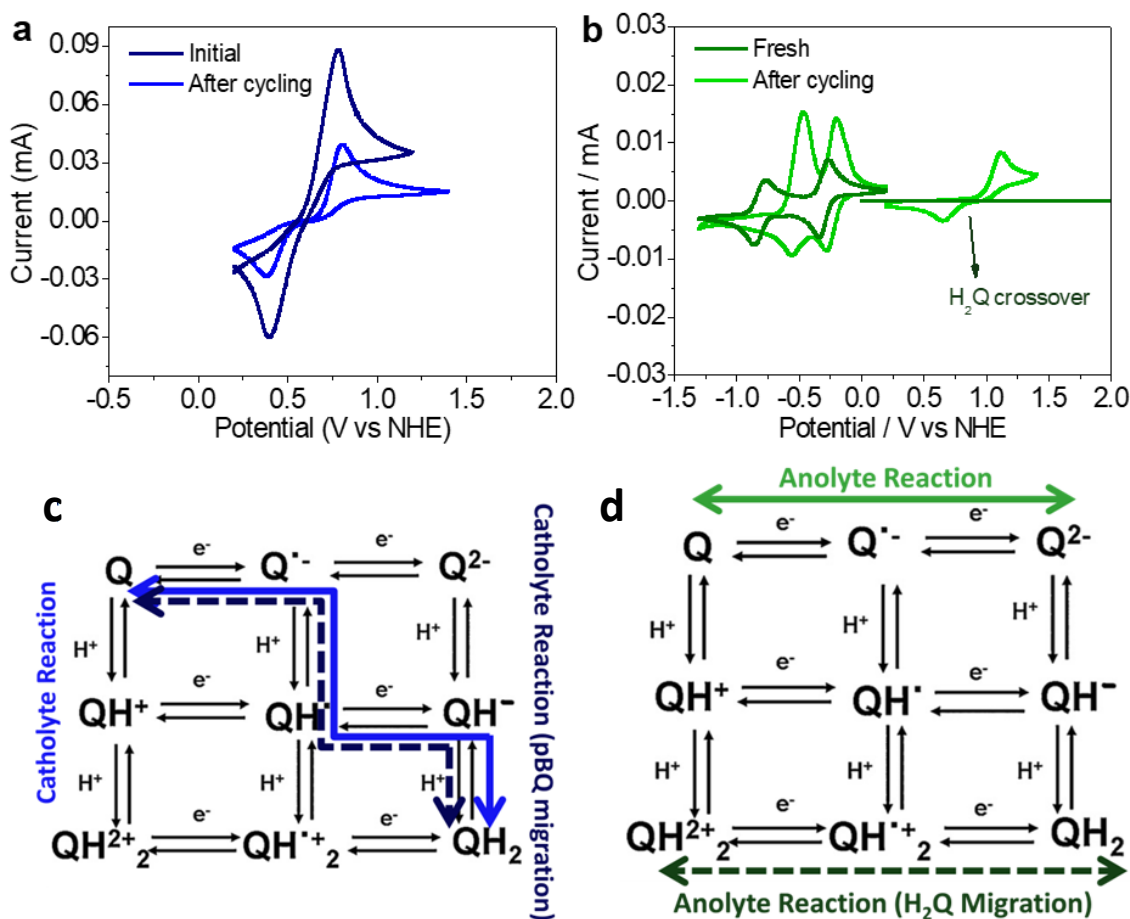


Figure 4.13. Electrochemical investigation of the two immiscible electrolytes before and after cycling. Electrolyte active species concentration: 20 mM. a) CVs of catholyte. b) CVs of anolyte. c) Reaction mechanism and pathways for catholyte: Dissolved species (continuous line) and species coming from anolyte (dotted line). d) Reaction mechanism and pathways for anolyte: Dissolved species (continuous line) and species coming from catholyte (dotted line)

The CV of the anolyte (Figure 4.13b) shows a new peak at positive potentials attributed to the redox reaction of H_2Q in ionic liquid. This demonstrates the crossover of H_2Q from the catholyte to the anolyte. The CV at negative potentials shows higher peak currents after cycling, confirming the crossover of pBQ from the catholyte. Interestingly, the redox peaks were shifted towards more positive potentials probably due to the presence of protons that most likely act as the charge carriers and lead to different reaction pathways (Figure 4.13c and d). The evolution of redox peaks to more positive potential will lead to lower battery OCV as confirmed during cycling in Figure 4.10. It should be highlighted that, in this specific example of Membrane-Free Battery in which pBQ and H_2Q represent different oxidation states of the same redox-active molecule, the migration of the species through the interface does not cause

irreversible electrolyte contamination but only a certain capacity loss due to electrolyte imbalance. This imbalance explains the origin of the battery failure at the end of the discharge. As shown in Figure 4.9a and Figure 4.11b, the drop of the battery voltage is triggered by the catholyte probably due to the depletion of active species that migrate to the anolyte.

The results demonstrate the feasibility of this innovative Membrane-Free Battery concept, which relies on immiscible redox electrolytes. The electrochemical performance of the proof-of-concept battery does not significantly differ from a conventional one since it maintains a stable discharge voltage profile, high capacity and good reversibility. The theoretical charge capacity of this Membrane-Free Battery is $5.36 \text{ Ah}\cdot\text{L}^{-1}$ and the theoretical energy density is $2.4 \text{ Wh}\cdot\text{L}^{-1}$, for an estimated operating voltage of 0.9 V. In fact, using saturated electrolytes with approximately 0.7 M of active species in each electrolyte, the energy density and the theoretical capacity became as high as $22.5 \text{ Wh}\cdot\text{L}^{-1}$ and $18.76 \text{ Ah}\cdot\text{L}^{-1}$, respectively. It is worth mentioning that these high values, which have been obtained from a proof-of-concept cell that is not optimized in any respect, are already comparable with recent examples of organic RFBs using membranes⁶¹.

Although the concept has been validated for one biphasic system in particular, this disruptive technology is very versatile and can be applied to other pairs of redox molecules and immiscible solvents. Therefore, a further study using different electrolytes to exemplify and corroborate its versatility is carried out in next section.

4.2.2 Versatility of Membrane-Free Redox Flow Battery Concept

In order to explore the versatility of this Membrane-Free Redox Flow Battery concept, we have first investigated the electrochemical properties of a variety of immiscible redox electrolytes, including aqueous and nonaqueous, in 3-electrode electrochemical cells. In a further step, based on their mutual immiscibility and their individual redox potentials, different pairs of immiscible redox electrolytes were assembled and tested

in a full battery arrangement. The versatility of Membrane-Free Redox Flow Battery concept is represented in Figure 4.14.

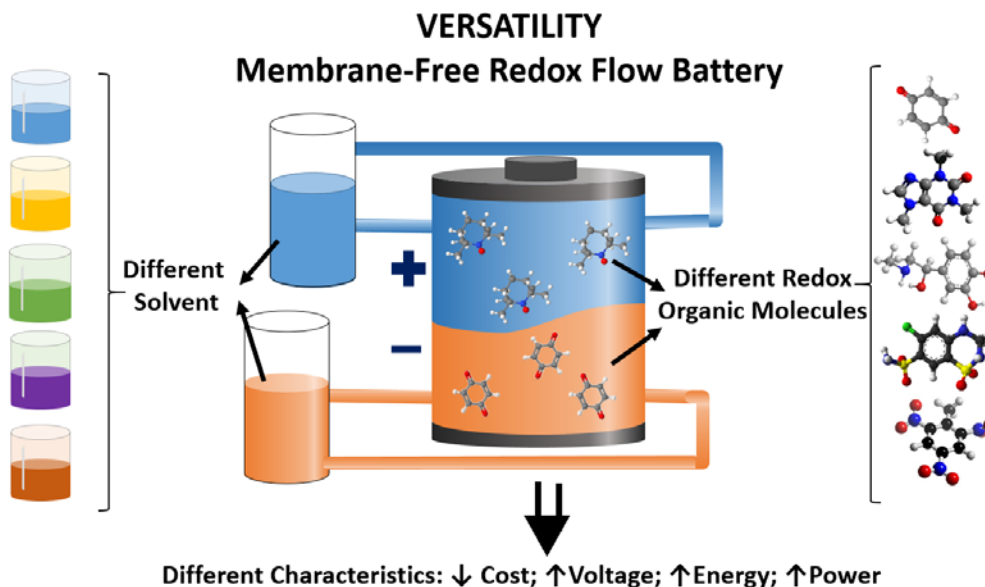


Figure 4.14. Schematic representation of the versatility of Membrane-Free RFB concept

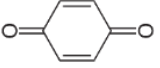
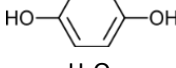
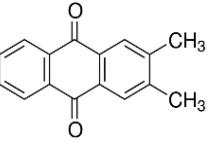
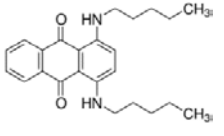
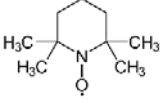
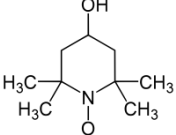
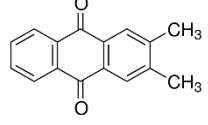
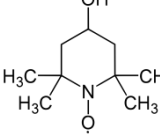
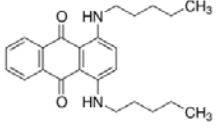
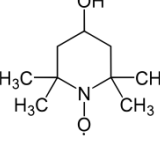
With the double aim of increasing the voltage of the battery and demonstrating the validity of the concept with asymmetric chemistries, we have tested other redox compounds besides hydroquinone (H₂Q) and parabenzoquinone (pBQ) used in the proof-of concept battery. Thus, here it has also been investigated 2,2,6,6-tetramethylpiperidine-1-oxyl (TEMPO), 4-Hydroxy-2,2,6,6-tetramethylpiperidine-1-oxyl (OH-TEMPO), 2,3-dimethylantraquinone (2,3DMAQ) and 1,4-Bis(pentylamino)anthraquinone (OilBlue N) as redox-active species.

Regarding the nature of the immiscible electrolytes, neutral-pH aqueous solutions and common organic solvents such as 2-butanone and propylene carbonate (PC) were employed to replace the PYR₁₄TFSI anolyte and the acidic catholyte present in the proof-of-concept battery.

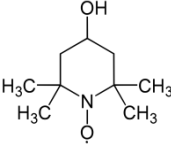
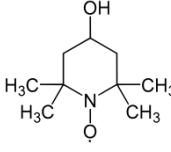
Table 4.3 shows the composition of the different electrolytes and all possible combinations to assemble Membrane-Free RFBs. The proof-of-concept Membrane-Free Battery reported in section 4.2.1 was also included to easily identify the main compositional changes adopted in the proposed electrolytes and the presumable innovation of the batteries.

4. Membrane-Free Redox Flow Batteries by Using Two Immiscible Redox Electrolytes

Table 4.3. Different combination of immiscible anolyte and catholyte and theoretical OCV of the corresponding Membrane-Free RFBs.

Battery	Anolyte (-)		Catholyte (+)		OCV	Main changes/ Main innovation
	Electrolyte media	Redox Compound	Electrolyte media	Redox Compound		
Previous Example	PYR ₁₄ TFSI	 pBQ	0.1 M HCl (aq)	 H ₂ Q	1.4	Proof- of concept
A	=	 2,3DMAQ	=	=	1.95	Different redox organic molecule in the anolyte/ Higher battery voltage and power density
B	=	 OilBlue N	=	=	2.1	
C	=	=	0.1 M NaCl (aq)	 TEMPO	1.5	Different redox organic molecule and neutral media/ Higher battery voltage and less-corrosive catholyte
D	2-Butanone (0.1 M TBAPF ₆)	=	=	=	1.1	Common and cheaper solvent in the anolyte/ Less-expensive battery
E	PC (0.1 M TBAPF ₆)	=	=	=	1.0	
F	PC +PYR ₁₄ TFSI (75+25 %w)	=	0.5 M NaCl (aq)	 OH-TEMPO	1.0	Cheaper anolyte and more soluble redox compound in the neutral catholyte/ Less-corrosive and more concentrated catholyte/ Less-expensive battery
G	=	 2,3DMAQ	0.5 M NaCl (aq)	 OH-TEMPO	2.05	Different redox organic molecules in both catholyte and anolyte, neutral catholyte/ Higher battery voltage and less-corrosive catholyte
H	=	 OilBlue N	0.5 M NaCl (aq)	 OH-TEMPO	2.2	

4. Membrane-Free Redox Flow Batteries by Using Two Immiscible Redox Electrolytes

I	2-Butanone (0.1 M TBAPF ₆)	=	0.5 M NaCl (aq)	 OH-TEMPO	1.2	Common and cheaper solvent in the anolyte and neutral media in the catholyte. Different redox-organic molecule in the catholyte / Less-expensive battery / Less-corrosive catholyte
J	PC (0.1 M TBAPF ₆)	=	0.5 M NaCl (aq)	 OH-TEMPO	1.45	

= same composition that in the proof-of-concept Membrane-Free Battery

* theoretical OCV was calculated as the difference between the redox potentials of catholyte and anolyte

4.2.2.1 Electrochemical Characterization of Immiscible Electrolytes

The electrochemical behavior of each electrolyte was studied separately by cyclic voltammetry (CV) in 3-electrode electrochemical cells. CVs of 10 pairs of immiscible redox electrolytes described in Table 4.3 are represented in Figure 4.15-4.21. The theoretical open circuit voltage (OCV) for each anolyte-catholyte combination was calculated as the difference between their redox potentials and included in Table 4.2.

Effect of active species in the anolyte:

The catholyte of Batteries A, B, D and E is composed of hydroquinone (H₂Q) dissolved in acidic media as in the proof-of-concept battery. The CVs of H₂Q in Figure 4.15 shows, as it was described previously, that at this acidic pH the redox reaction of the H₂Q involves two electrons and two protons (see Scheme in Figure 4.13c) that are exchanged in only one step at a redox potential of 0.6 V vs. NHE^{51,62}. The only difference of Batteries A and B with respect to the proof-of-concept battery was the active redox molecule in the anolyte. It is well known that increasing the number of aromatic rings in quinoyl-based molecules favors the delocalization of electrons resulting in more negative redox potentials (E⁰) as follows; E⁰_{antraquinones} < E⁰_{naphthoquinone} < E⁰_{benzoquinones}. Moreover, the functionalization with electron-donating groups such as -CH₃ also lowers the E⁰. Therefore, the parabenzoquinone (pBQ) employed in the PYR₁₄TFSI anolyte of the proof-of-concept battery was replaced by anthraquinone derivatives; 2,3-DMAQ in Battery A, and Oilblue N in Battery B (Figure 4.15c and d)

4. Membrane-Free Redox Flow Batteries by Using Two Immiscible Redox Electrolytes

with the final goal of increasing the OCV of the battery. In Figure 4.15b, c and d it is observed that, as it was commented before, in aprotic electrolytes quinone compounds (Q) undergoes two consecutive reversible reduction reactions to radical anion ($Q^{\cdot-}$) and dianion (Q^{2-}), exchanging 2 electrons in total (see Figure 4.16) ⁶³. As expected, the redox potentials of substituted anthraquinones were shifted towards more negative potential and the theoretical OCV of Batteries A and B increased around 40-50 % with respect to the proof-of-concept example just by changing the redox molecule dissolved in the anolyte.

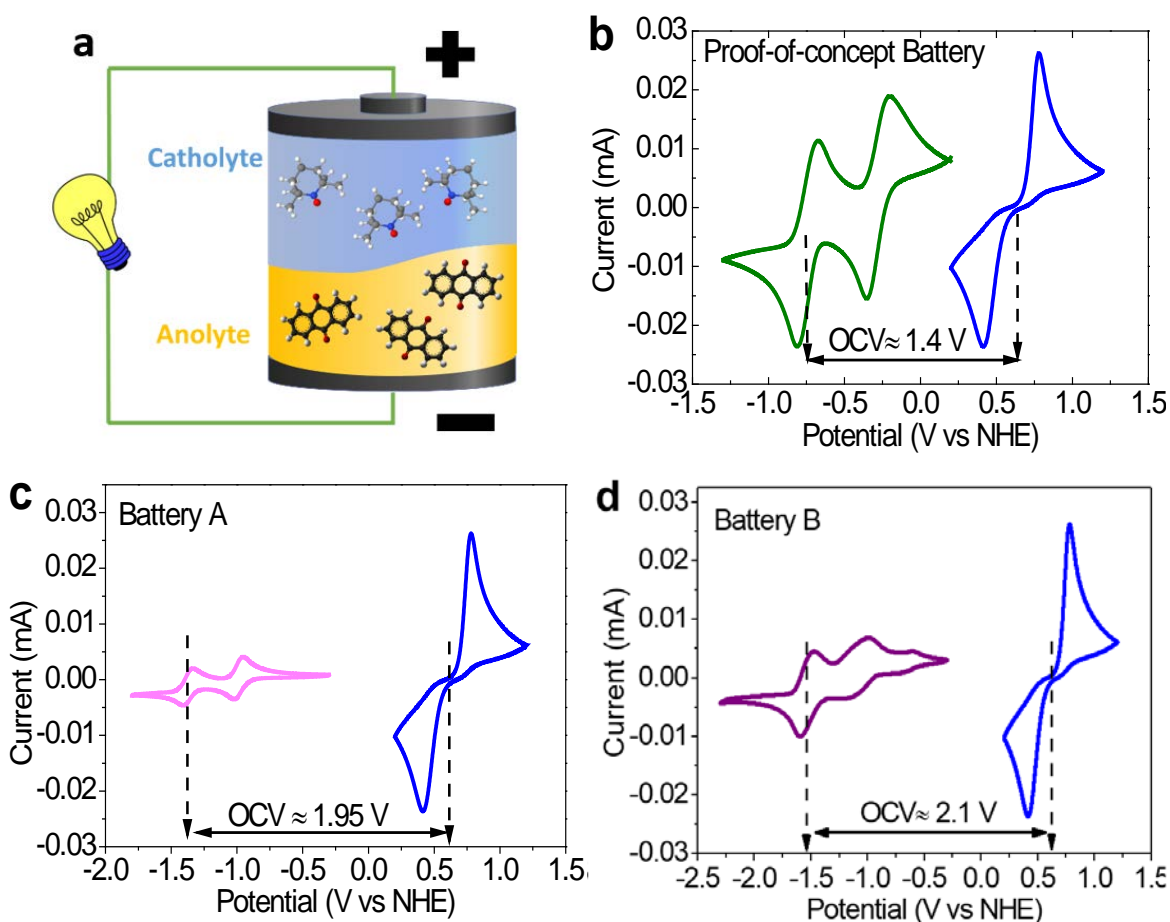


Figure 4.15. a) Schematic illustration of Membrane-Free Battery based on immiscible electrolytes. b), c), d) CVs of pairs of immiscible anolyte and catholyte (pBQ in green, H₂Q in blue, 2,3-DMAQ in pink, OilBlue N in purple). The composition of electrolytes is 20 mM of redox active specie. Scan rate: 10 mV·s⁻¹.

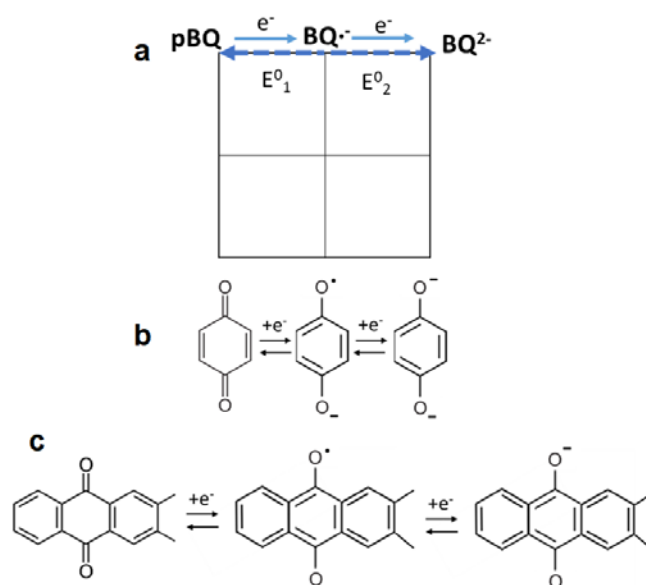


Figure 4.16. a) Scheme-of-squares for redox reaction of quinones in aprotic electrolyte. b) Reaction mechanism for pBQ (Proof-of-concept). c) Reaction mechanism for 2,3-DMAQ (Battery A).

Effect of active species in the catholyte:

Battery C is composed by the same anolyte that the proof-of-concept battery but the acidic catholyte was substituted by TEMPO dissolved in neutral-pH electrolyte (0.1 M NaCl). It should be noticed that besides the safety advantages, neutral pH prevents undesired reactions such as comproportionation or disproportionation of TEMPO-based molecule in acid media^{64,65}. Figure 4.17a shows that TEMPO undergoes a reversible redox reaction at 0.75 V vs. NHE turning into its oxoammonium cation form during oxidation (see Scheme in Figure 4.17b). Therefore, a gain of 100 mV (OCV 1.5 V) is expected for this battery compared with the proof-of-concept one.

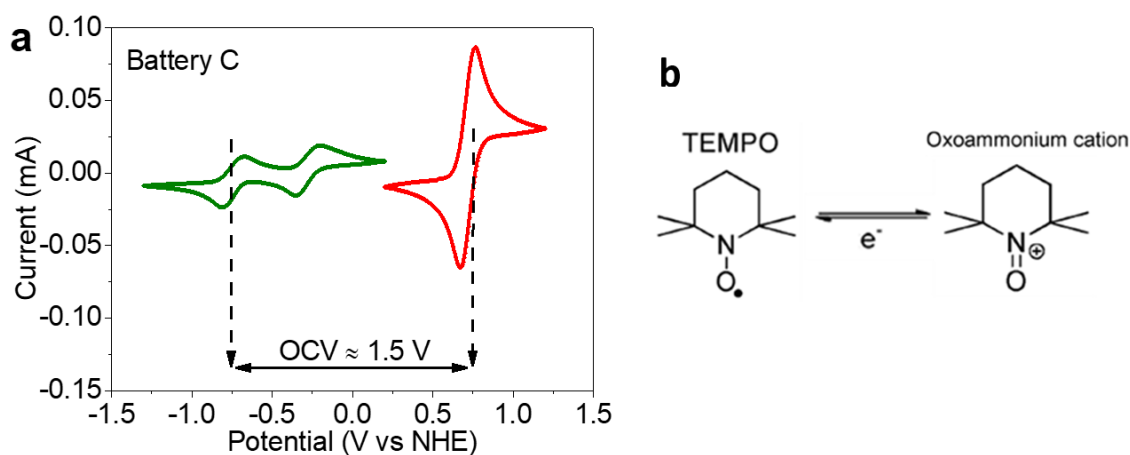


Figure 4.17. a) CVs of pairs of immiscible anolyte and catholyte (pBQ in green, TEMPO in red). Active species concentration: 20mM pBQ in the anolyte and 40mM TEMPO in the catholyte. Scan rate: 10 mV·s⁻¹. b) Scheme of Redox reaction mechanism for TEMPO in 0.1 M NaCl

Effect of solvent in the anolyte

Batteries D and E (Figure 4.18a and b) use the same redox species than in the proof-of-concept battery but the ionic liquid of the anolyte was changed by 2-butanone and propylene carbonate (PC), respectively. The use of these inexpensive solvents would reduce the battery cost, which is an important current goal for RFB technology. In Battery D, only a pair of peaks is observed at -0.5 V (vs NHE) which is attributable to the first step of the pBQ reaction. The second step does not occur, likely due to a degradation reaction between the radical anion ($BQ^{\cdot-}$) and the 2-butanone electrolyte. On the other hand, in Battery E the two steps of reduction reaction of the pBQ are clearly observed. However, the intensity of the oxidation peak of BQ^{2-} decreases probably due to the comproportionation reaction between the pBQ and the dianion that compromises the reversibility of the reaction in PC (see Figure 4.19)^{55,66}.

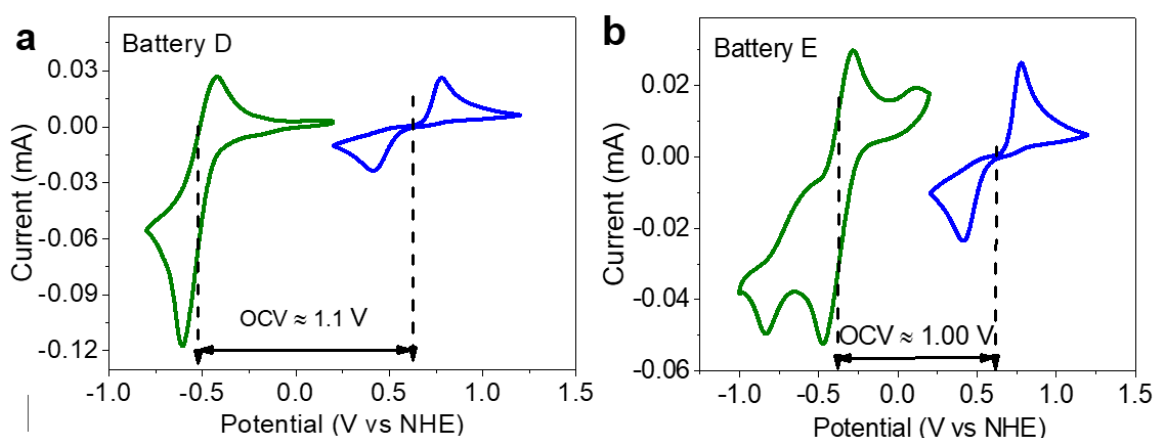


Figure 4.18. a), b) CVs of pairs of immiscible anolyte and catholyte (pBQ in green, H_2Q in blue). The composition of electrolytes is 20 mM of redox active specie. Scan rate: $10 \text{ mV}\cdot\text{s}^{-1}$.

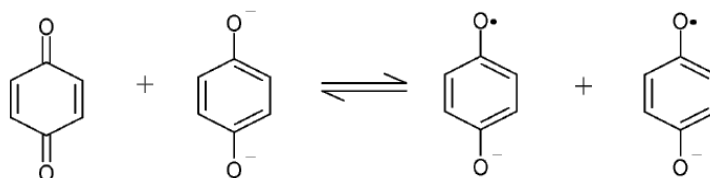


Figure 4.19. Comproportionation process mechanism suggested by some authors for pBQ^{55,66}.

Effect of the supporting salt in the anolyte

In an attempt to improve the reversibility of pBQ in PC, the supporting salt (TBAPF₆) used in Battery E was substituted by PYR₁₄TFSI in Battery F since this ionic liquid already demonstrated good performance in combination with pBQ in the proof-of-concept battery. Thus, the supporting electrolyte of anolyte in Battery F was composed by a mixture of PYR₁₄TFSI and PC (25-75 %wt, equivalent to 0.7 M of PYR₁₄TFSI). As can be seen in Figure 4.20, the large ions of PYR₁₄TFSI improve the stabilization of the BQ^{•-} making the first step of the reaction more reversible (similar peak current for oxidation and reduction). However, the distorted second peak of the CV indicates that the comproportionation reaction is still taking place. In Battery F, the active species in the catholyte is the OH-TEMPO that presents higher solubility in aqueous media than non-functionalized TEMPO and similar reversible redox reaction at 0.75 V (vs NHE) as observed in Figure 4.20.

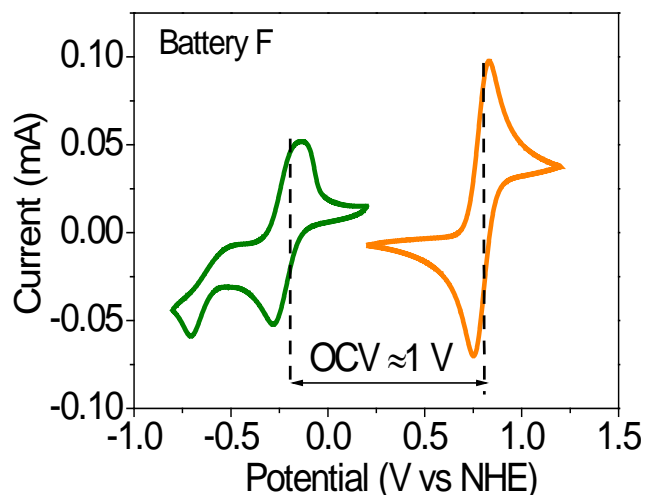


Figure 4.20. CVs of pairs of immiscible anolyte and catholyte (pBQ in green, OH-TEMPO in orange). The composition of electrolytes is 20 mM of redox active specie. Scan rate: 10 mVs⁻¹.

Due to the high reversibility of OH-TEMPO in the catholyte of Battery F, Batteries G-J, similar to Batteries A, B, D and E but with OH-TEMPO-based catholyte were also proposed and their corresponding CVs represented in Figure 4.21a-d. The OCV values

4. Membrane-Free Redox Flow Batteries by Using Two Immiscible Redox Electrolytes

are slightly higher (≈ 100 mV) than in the case of Batteries A, B, D and E due to the higher redox potential of OH-TEMPO.

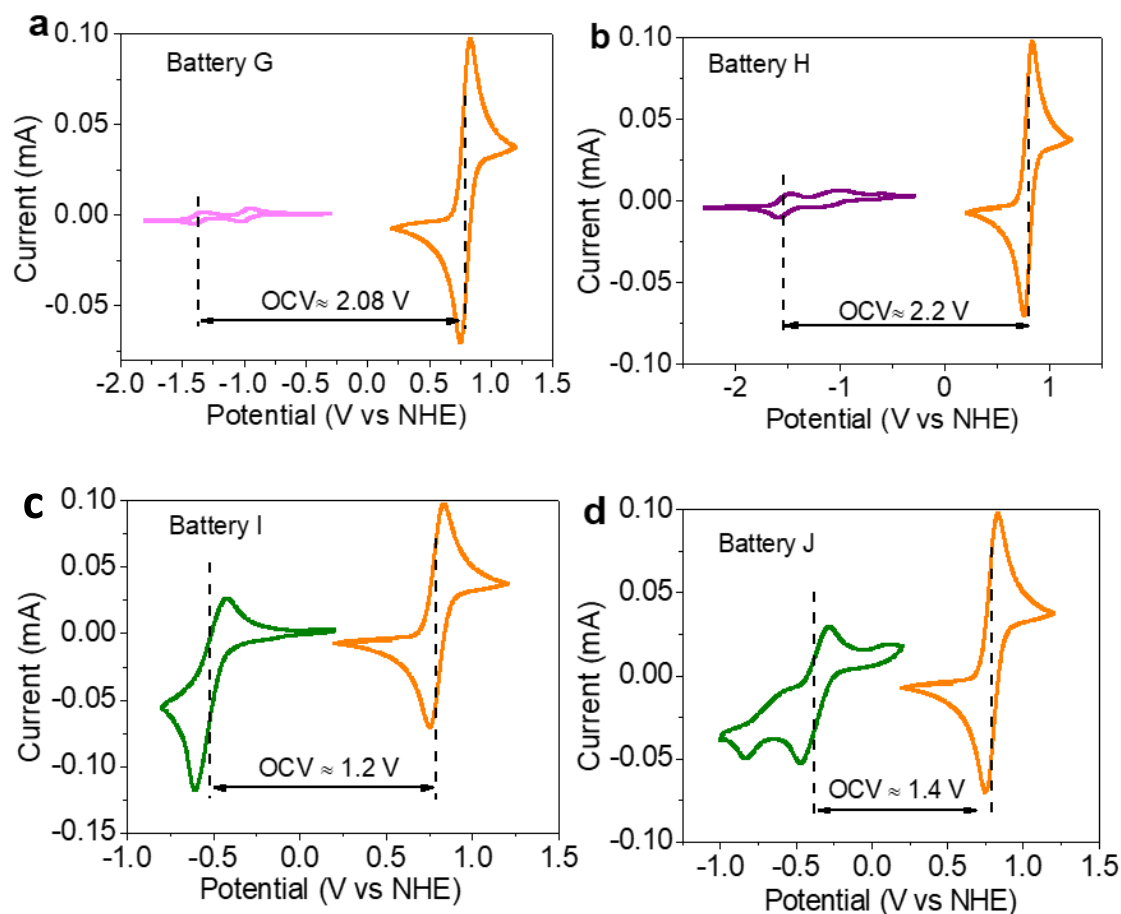


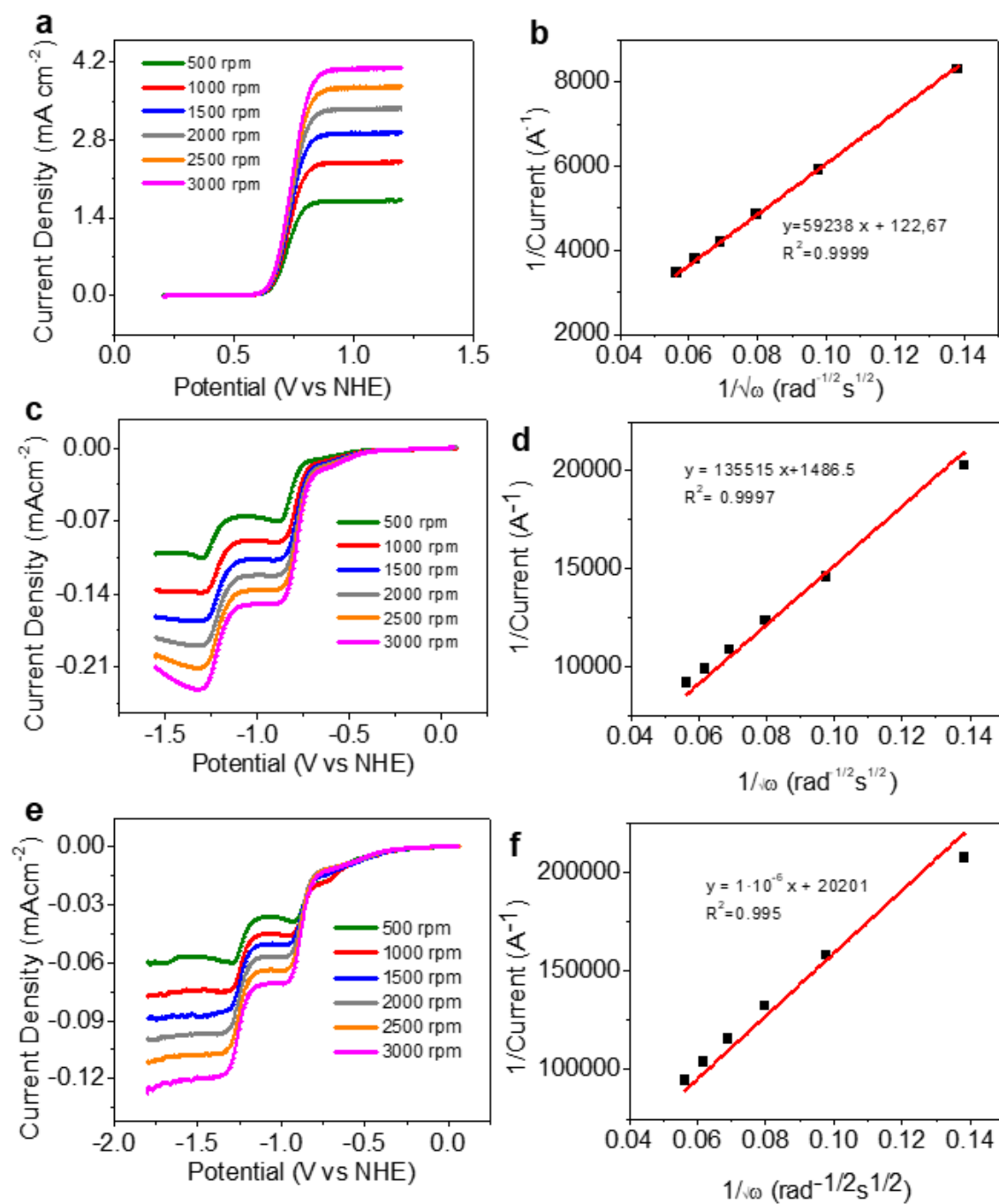
Figure 4.21. a), b), c), d) CVs of pairs of immiscible anolyte and catholyte (pBQ in green, 2,3-DMAQ in pink, OilBlue N in purple, OH-TEMPO in orange). The composition of electrolytes is 20 mM of redox active specie. Scan rate: $10 \text{ mV}\cdot\text{s}^{-1}$.

Rotating Disc Electrode (RDE) experiments

In order to shed some light into the kinetics of the attainable Membrane-Free Batteries, RDE experiments were performed to determine the diffusion coefficients (D) and the rate constants (k^0) in all electrolytes (see Figure 4.22 and Table 4.4). Among the formulated anolytes, OilBlue N and 2,3-DMAQ in $\text{PYR}_{14}\text{TFSI}$ present the lower diffusion coefficients likely motivated by the high viscosity and low conductivity of the ionic liquid and the large size of anthraquinones in comparison with pBQ. Among the studied catholytes, the one based on H_2Q in acidic media exhibit higher D and k^0 than those based on TEMPO molecule in neutral-pH media. It is worth to remark that the

4. Membrane-Free Redox Flow Batteries by Using Two Immiscible Redox Electrolytes

obtained D and K^0 values are comparable to similar redox compounds employed in ORFB^{10,12,22}. Since the electrolytes demonstrated fast electrode kinetics, the losses due to activation polarization are not expected to be very relevant in the battery arrangement.



4. Membrane-Free Redox Flow Batteries by Using Two Immiscible Redox Electrolytes

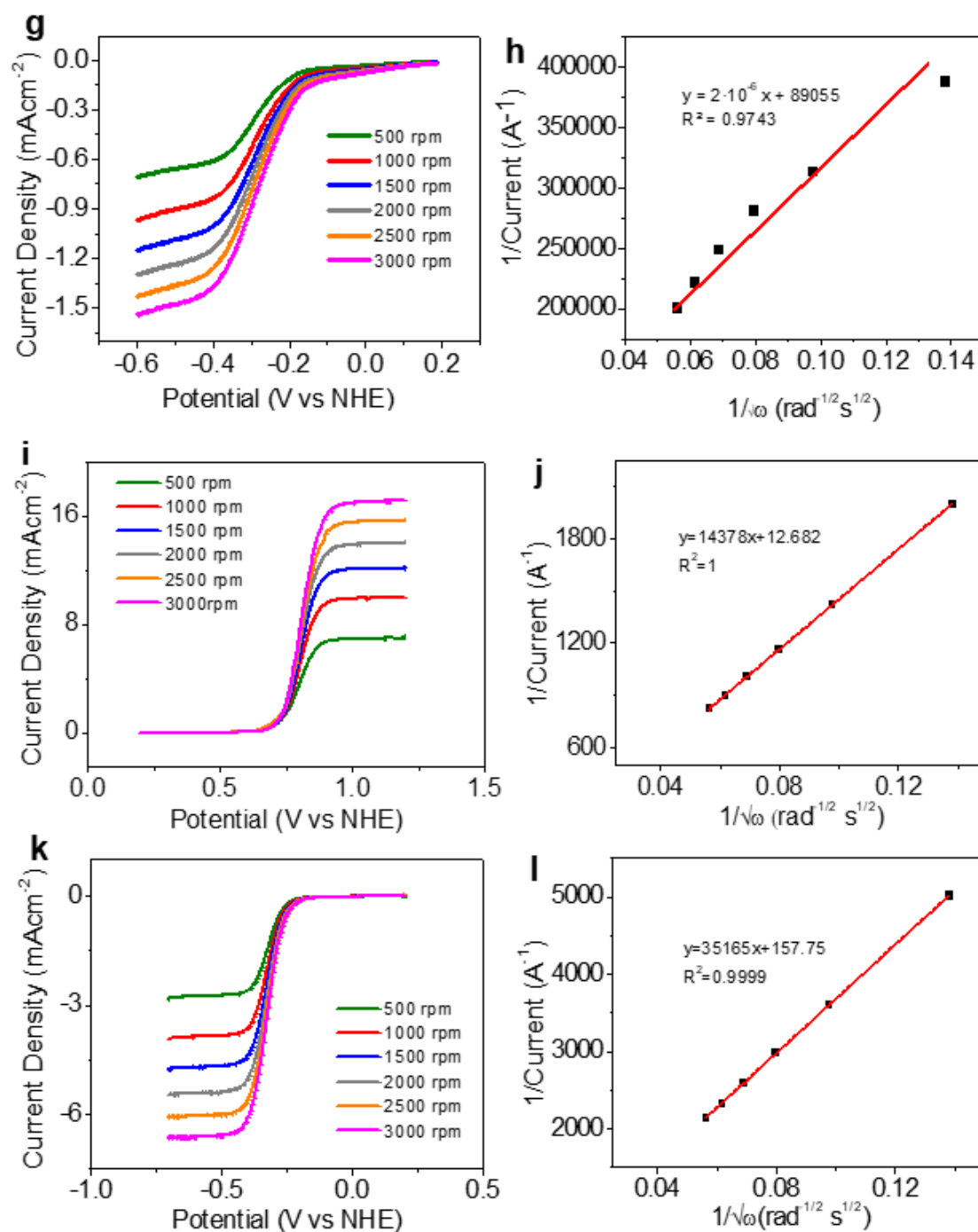


Figure 4.22. Rotating Disk Electrode experiments. Electrolytes concentration: 5mM. Figures on the Left: LSV at 10 mV·s⁻¹; Right: Levich plot (the mass-transport limited current vs. the square root of the rotation rate and the line fit (red line) with its mathematical expression. a and b) TEMPO in 0.1M NaCl. c and d) 2,3-Dimethylantraquinone in PYR₁₄TFSI. e and f) OilBlue N in PYR₁₄TFSI. g and h) pBQ in PC (0.1 M TBAPF₆). i and j) OH-TEMPO (0.5 M NaCl). k and l) pBQ in PC + PYR₁₄TFSI (75:25 %wt).

Table 4.4. Diffusion Coefficients and kinetic rate constants of the different electrolytes

	Electrolyte	Battery	D (cm²s⁻¹)	K^0 (cms⁻¹)
Anolytes	pBQ in PYR ₁₄ TFSI	Proof-of-concept Battery C	$5.8 \cdot 10^{-5}$	$1.2 \cdot 10^{-3}$
	2,3DMAQ in PYR ₁₄ TFSI	Battery A, G	$1.5 \cdot 10^{-7}$	$2.9 \cdot 10^{-4}$
	OilBlueN in PYR ₁₄ TFSI	Battery B, H	$5.1 \cdot 10^{-8}$	$1.1 \cdot 10^{-4}$
	pBQ in 0.1 M TBAPF ₆ – PC	Battery E, J	$2.1 \cdot 10^{-6}$	$3.2 \cdot 10^{-3}$
	pBQ in PC+PYR ₁₄ TFSI	Battery F	$3.9 \cdot 10^{-6}$	$1.5 \cdot 10^{-3}$
Catholytes	H ₂ Q in 0.1 M HCl	Proof-of-concept Battery A, B, D and E	$4.1 \cdot 10^{-4}$	$3.8 \cdot 10^{-1}$
	TEMPO in 0.1 M NaCl	Battery C	$6.6 \cdot 10^{-6}$	$3.8 \cdot 10^{-4}$
	OH-TEMPO in 0.5 M NaCl	Battery F-J	$7.1 \cdot 10^{-6}$	$5.2 \cdot 10^{-4}$

4.2.2.2 Electrochemical Performance of Membrane-Free Redox Flow Batteries

In order to demonstrate the versatility of the Membrane-Free Redox Flow Battery concept and considering the electrochemical performance of the electrolytes, the most representative pairs of immiscible electrolytes were selected to assemble and characterize 5 different Membrane-Free Batteries; Battery A, B, C, E and F. The purpose was to demonstrate at least one example of every main allure of this battery concept which rely on the possibility of modifying either the active molecules or the electrolyte solvent giving rise to Membrane-Free Redox Flow Batteries with different characteristics. The batteries were assembled in a static configuration by mixing the same volume of redox electrolytes forming a biphasic system, which obviates the need of any physical separator. The static configuration allows for doing a more simplified analysis of the performance of the batteries without considering the fluid dynamics thus reducing the number of variables and facilitating the comparison of different electrolytes. The electric connection was done by introducing a carbon electrode in each phase (see more experimental details in section 4.4.4). All the batteries are at fully discharge state when assembled so, first the batteries were galvanostatically charged up to a certain state of charge (SOC). The electrochemical performance of each different battery is detailed below.

- **Battery A and Battery B**

In Battery A, due to the more negative redox potential of 2,3-DMAQ compared with pBQ, the CV curves of catholyte and anolyte in Figure 4.15c anticipate an OCV of 1.95 V, which is 40 % higher than in the proof-of-concept battery (see section 4.2.1).

Figure 4.23a shows the voltage of the battery and the individual potential profiles of the electrolytes during charge-discharge. The voltage of the battery exhibits a clear plateau at 1.4 V during the charging process and a stable discharge plateau at 1.35 V. This high discharge voltage represents an increase of 50 % in comparison to the operating voltage of the proof-of-concept battery. The difference between the theoretical OCV and the operating voltage is motivated by the less negative potential in the anolyte which indicates that the second step of the 2,3-DMAQ reaction was not reached at this SOC. Thus, the theoretical OCV is reduced and becomes 1.58 V which is very close to the observed OCV. The low overpotential at the interface (~ 100 mV) and the good reversibility of the two redox reactions contribute to obtain very high coulombic efficiency (99.9 %), voltage efficiency (> 90 %) and energy efficiency (90 %).

Figure 4.23b shows that, similar to any type of battery, increasing the current density causes a decrease in the discharge voltage. In this case, it can be attributed mostly to the higher ohmic polarization exhibited by the anolyte at higher currents whereas the potential of the catholyte keeps constant (Figure 4.23c). This behavior might be caused by the higher viscosity and lower conductivity of the ionic liquid anolyte, and to the lower diffusion coefficient of 2,3-DMAQ compared to the one of H₂Q in the catholyte. It should be noticed that the voltage drop of the battery at the end of the discharge is driven by the sudden potential drop of the catholyte. This is probably due to active species depletion associated with some cross-migration of the H₂Q towards the anolyte. Figure 4.23d and e show how the voltage remains above 1 V during the discharge after increasing the current up to 2.3 mA·cm⁻² with no noticeable kinetic or mass transport limitations. A power density value about 3 mW·cm⁻² can be achieved, which is quite promising in comparison with other values for nonaqueous ORFB reported in literature^{14,19,20} and about 62 % higher than the proof-of concept battery. This improvement is attributable to the higher voltage achieved by changing the pBQ by 2,3-DMAQ in the anolyte.

4. Membrane-Free Redox Flow Batteries by Using Two Immiscible Redox Electrolytes

In Figure 4.23f and g the polarization test during charge is depicted together with the individual profiles of each electrolyte. As can be seen, at current density higher than $2 \text{ mA}\cdot\text{cm}^{-2}$ the polarization of the battery is moderate and is caused by the polarization of the anolyte.

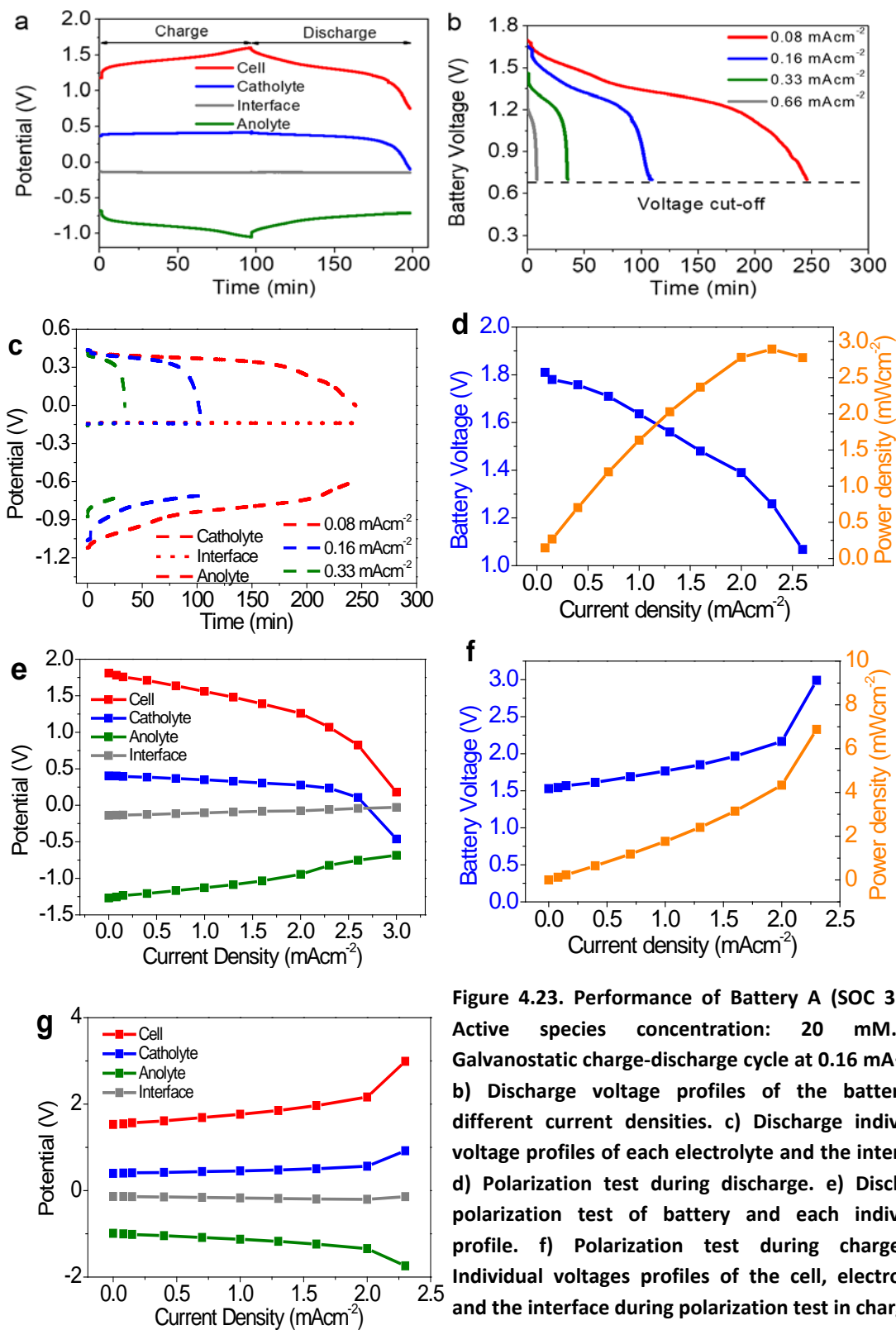


Figure 4.23. Performance of Battery A (SOC 35 %). Active species concentration: 20 mM. a) Galvanostatic charge-discharge cycle at $0.16 \text{ mA}\cdot\text{cm}^{-2}$. b) Discharge voltage profiles of the battery at different current densities. c) Discharge individual voltage profiles of each electrolyte and the interface. d) Polarization test during discharge. e) Discharge polarization test of battery and each individual profile. f) Polarization test during charge. g) Individual voltages profiles of the cell, electrolytes and the interface during polarization test in charge.

4. Membrane-Free Redox Flow Batteries by Using Two Immiscible Redox Electrolytes

Figure 4.24a shows the discharge voltage profiles of Battery B in which pBQ was substituted by OilBlue N as active species in the $\text{PYR}_{14}\text{TFSI}$ anolyte, keeping the same catholyte. As mentioned before, such combination of immiscible electrolytes will lead to a battery with a theoretical OCV as high as 2.1 V (Figure 4.15d). As shown in Figure 4.24a, this large OCV leads to a battery discharge voltage of 1.75 V, which is one of the highest operating voltages reported in nonaqueous ORFB^{12–14,20}.

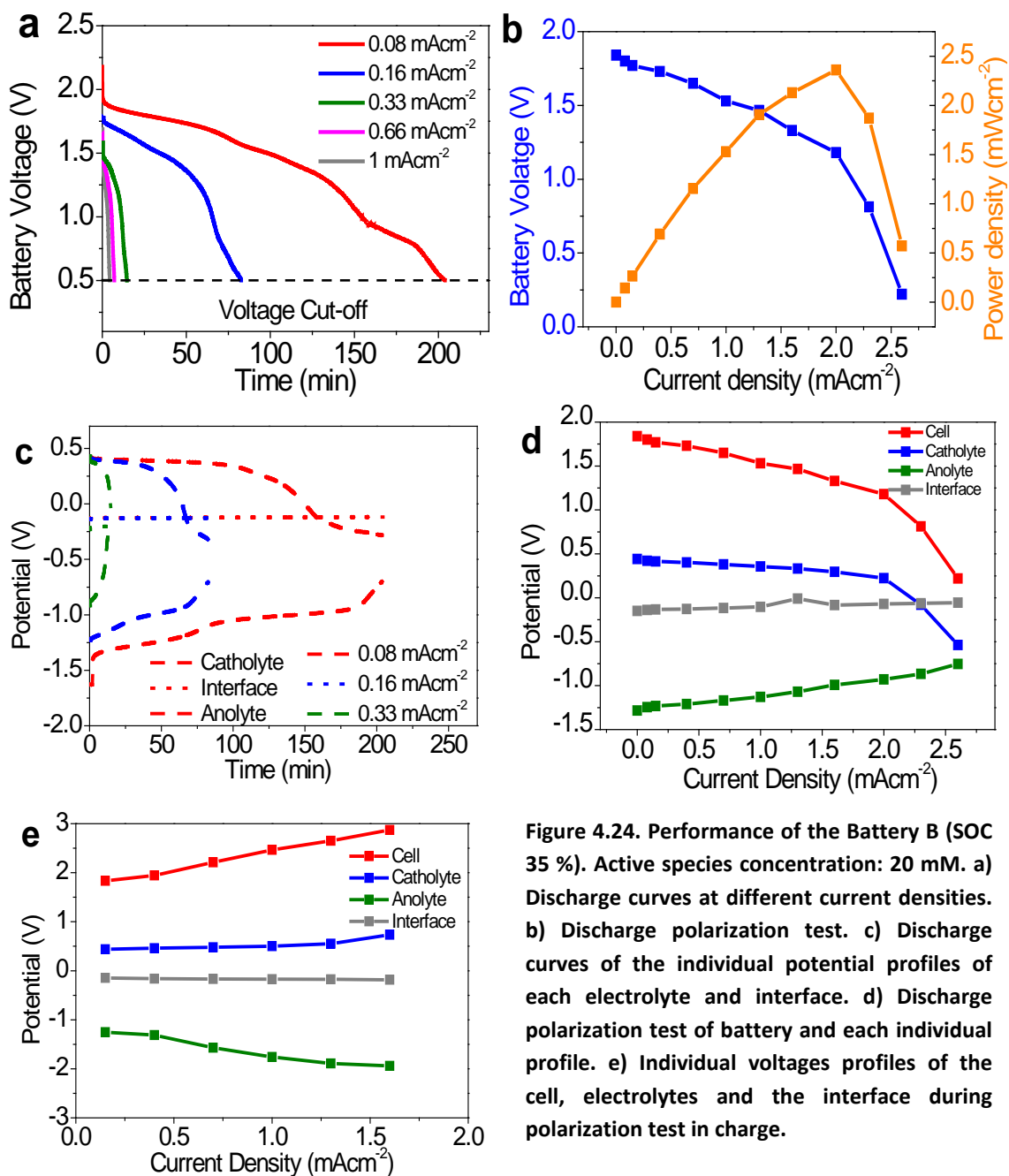


Figure 4.24. Performance of the Battery B (SOC 35 %). Active species concentration: 20 mM. **a)** Discharge curves at different current densities. **b)** Discharge polarization test. **c)** Discharge curves of the individual potential profiles of each electrolyte and interface. **d)** Discharge polarization test of battery and each individual profile. **e)** Individual voltages profiles of the cell, electrolytes and the interface during polarization test in charge.

4. Membrane-Free Redox Flow Batteries by Using Two Immiscible Redox Electrolytes

The behavior of Battery B is similar to the one revealed by Battery A, although the physicochemical properties of the anolyte in Battery B causes higher ohmic polarizations in its potential profile (Figure 4.24c). On the other hand, Figure 4.24b, d and e show the battery capacity is limited by the catholyte, possibly due to the cross-migration of the H₂Q towards the anolyte. Despite the lower D and K^0 of OilBlue N compared to pBQ (see Table 4.4), the Battery B delivered 35 % higher power density (2.5 mW·cm⁻²) than the proof-of-concept battery, likely due to the double operating voltage attained for this battery. The improvement in the OCV, the operating voltage, as well as the power density achieved in Batteries A and B in comparison with the proof-of-concept battery are due to the different active species used in the anolyte. In Figure 4.25 both the CVs of immiscible electrolytes and discharge profiles of such batteries are represented together for easier analysis. As it was commented before, the theoretical OCV is increased by changing the pBQ dissolved in the anolyte, in the proof-of-concept battery, by substituted anthraquinones in Batteries A and B. Accordingly, the discharge voltage of these batteries is higher (1.5 times in Battery A and almost 2 times in Battery B) than the one obtained in the proof-of-concept battery.

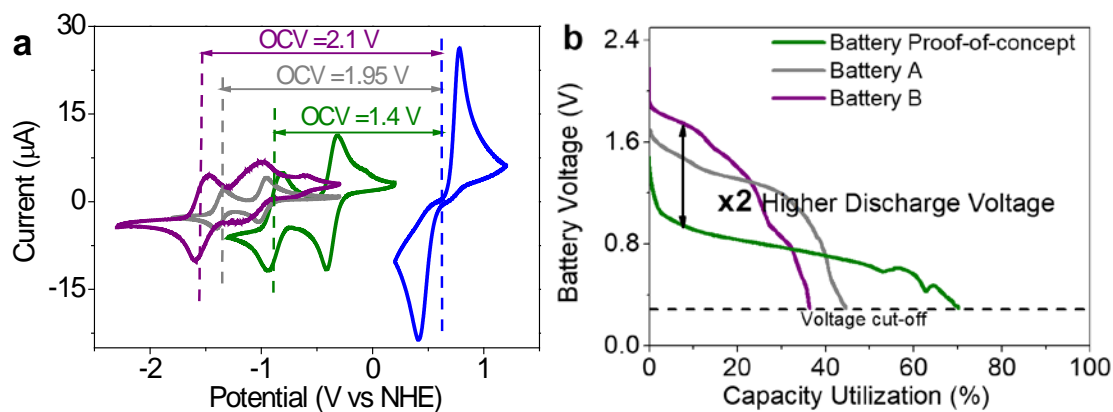


Figure 4.25. a) Comparison of CV for the anolytes and the catholyte used in the Batteries A, B and Proof-of-concept (H₂Q in 0.1 M HCl in blue, 2,3-DMAQ in PYR₁₄TFSI in grey, OilBlue N in PYR₁₄TFSI in purple and pBQ in PYR₁₄TFSI in green). b) Comparison between potential-capacity discharge profile at 0.08 mA·cm⁻² (35 %SOC) for Batteries A, B and Proof-of-concept.

- **Battery C**

The effect of replacing the active species in the catholyte was explored in Battery C. In this case, the acidic catholyte containing H₂Q utilized in the proof-of concept-battery was replaced by neutral solution of TEMPO whereas the same anolyte was used (pBQ in PYR₁₄TFSI). According to Figure 4.17a, the theoretical OCV of this battery will increase 100 mV with respect to the proof-of-concept battery reaching up to 1.5 V.

Figure 4.26a shows that during charge, the voltage profile of Battery C exhibits two plateaus at about 1.0 V and 1.4 V corresponding to the two reduction steps of pBQ in the anolyte. During the discharge, the initial battery voltage is close to 1.5 V but decreases gradually, induced by the high ohmic overpotential of the ionic liquid anolyte that presents much higher viscosity and lower conductivity than the aqueous catholyte. The catholyte potential remains very stable at 0.5 V (redox potential of TEMPO) evidencing negligible overpotential. However, after several minutes of discharge, the potential of the catholyte decays, probably due to the cross-migration of TEMPO from catholyte to anolyte causing the prompt drop of the battery voltage.

As expected, increasing the current density provokes a drop in the battery voltage that is again triggered by the overpotential of the anolyte (see Figure 4.26b and c). Concerning to the interface, it should be stressed that it displays an extremely flat potential close to 0 V at all current densities. In fact, the resistance at the interface only represents about 5 % of the overall internal resistance of the cell during the discharge. This low contribution contrasts with the high resistances associated with ion-exchange membranes employed in conventional RFB¹¹ and supposes a clear advantage of this Membrane-Free concept. The polarization test of the battery in Figure 4.26d displays a quite linear response without any evidence of kinetic losses at low current densities, denoting a quite fast electrode kinetics (see also Figure 4.26e) and a peak power density of 0.8 mW·cm⁻² which is comparable with other reported nonaqueous ORFB^{14,20,67}.

4. Membrane-Free Redox Flow Batteries by Using Two Immiscible Redox Electrolytes

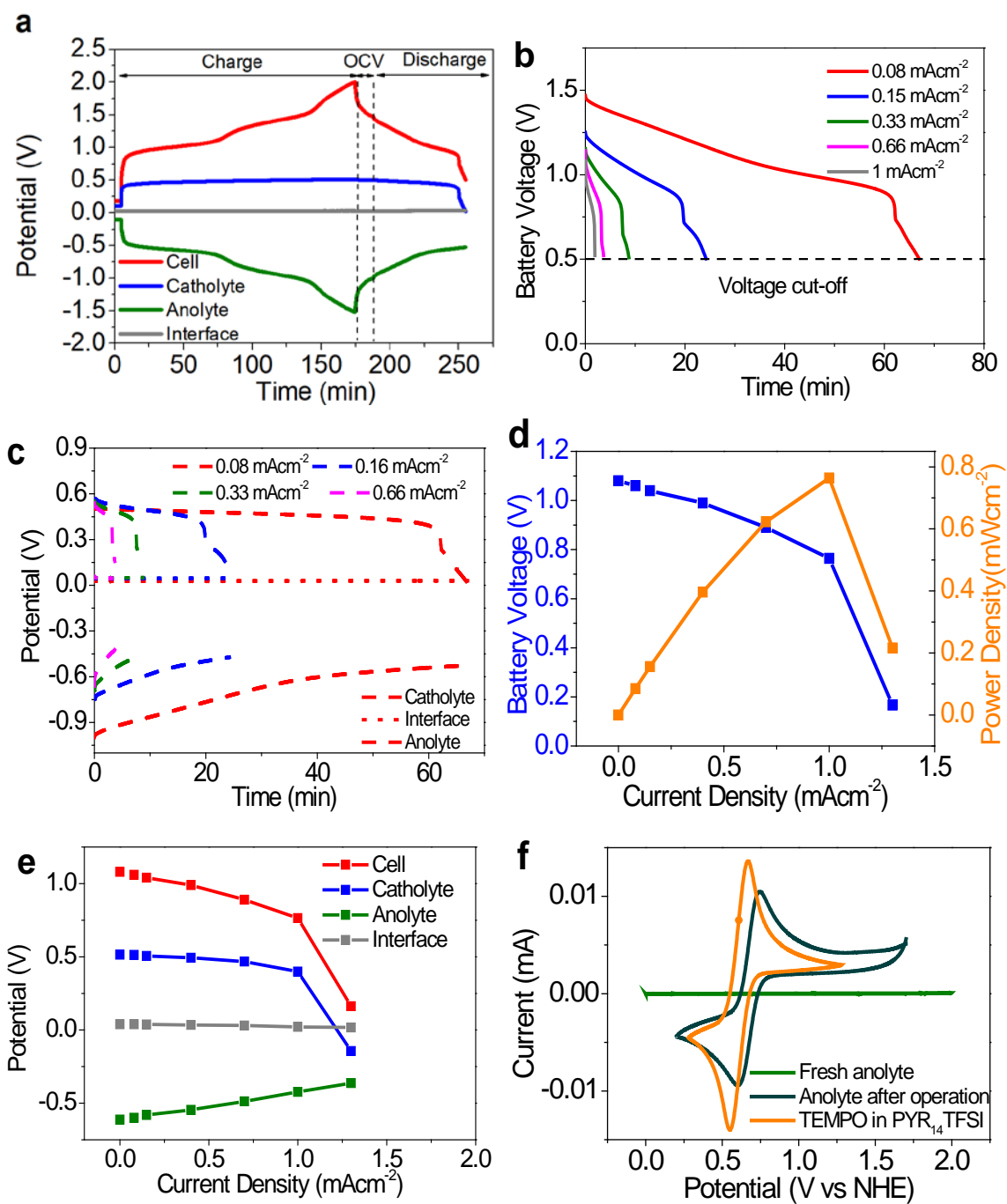


Figure 4.26. Performance of the Battery C (SOC 35%). Active species concentration: 40 mM in catholyte and 20 mM in anolyte. a) Galvanostatic charge-discharge cycle at $0.08 \text{ mA}\cdot\text{cm}^{-2}$. b) Discharge voltage profiles of the battery at different current densities. c) Discharge individual voltage profiles of each electrolyte and the interface. d) Polarization test during discharge. e) Discharge polarization test of battery and each individual phase at 35 % SOC. f) CV of the anolyte at positive potential range before operating (light green) and after battery operation (dark green), for comparison CV of TEMPO in $\text{PYR}_{14}\text{TFSI}$ at 20 mM concentration was also included (orange).

As mentioned before, the premature failure of the battery is driven by the sudden potential drop of the catholyte (see Figure 4.26a and c). This is probably due to the migration of TEMPO molecules from catholyte to anolyte leading to a misbalance of active species in the battery. This crossover of TEMPO through the interface was evidenced by recording the CV of the anolyte before and after battery operation. Figure 4.26f shows that the CV of fresh anolyte does not show any redox peak in the positive range whereas the CV of the anolyte after battery operation shows a redox peak at 0.6 V attributable to TEMPO. This crossover is an important drawback in conventional RFBs, especially in those cases in which the ion-selective membranes are substituted by cheap size-exclusion separators to reduce the resistance of the battery. In such cases, a recent strategy consisting of using mixed-reactant electrolytes in the two battery compartments is being explored by several groups^{12,13,40,68}. Thus, although an important part of the active material is unusable, the low concentration gradient through the separator mitigates the crossover during battery operation. It is worth to remark that in this novel concept of Membrane-Free RFB the crossover of active species will be exclusively governed by thermodynamic aspects such as partition coefficients. Therefore, it would be possible to avoid completely the crossover by selecting pairs of redox molecules that do not migrate to opposite phases spontaneously. These valuable thermodynamic aspects will be addressed in the next chapter of this thesis.

- **Battery E**

In an attempt to expand the application of Membrane-Free RFB concept to conventional solvents, the $\text{PYR}_{14}\text{TFSI}$ ionic liquid used as anolyte in the proof-of-concept battery was replaced by propylene carbonate (PC) in Battery E. According to the CV studies, the theoretical OCV of Battery E is 1.00 V (see Figure 4.18b). As it was mentioned before, the parasitic reaction of comproportionation among the pBQ and its dianion takes place in PC media, so the potential of the anolyte was limited at -0.5 V during charge to hinder the formation of the dianion.

4. Membrane-Free Redox Flow Batteries by Using Two Immiscible Redox Electrolytes

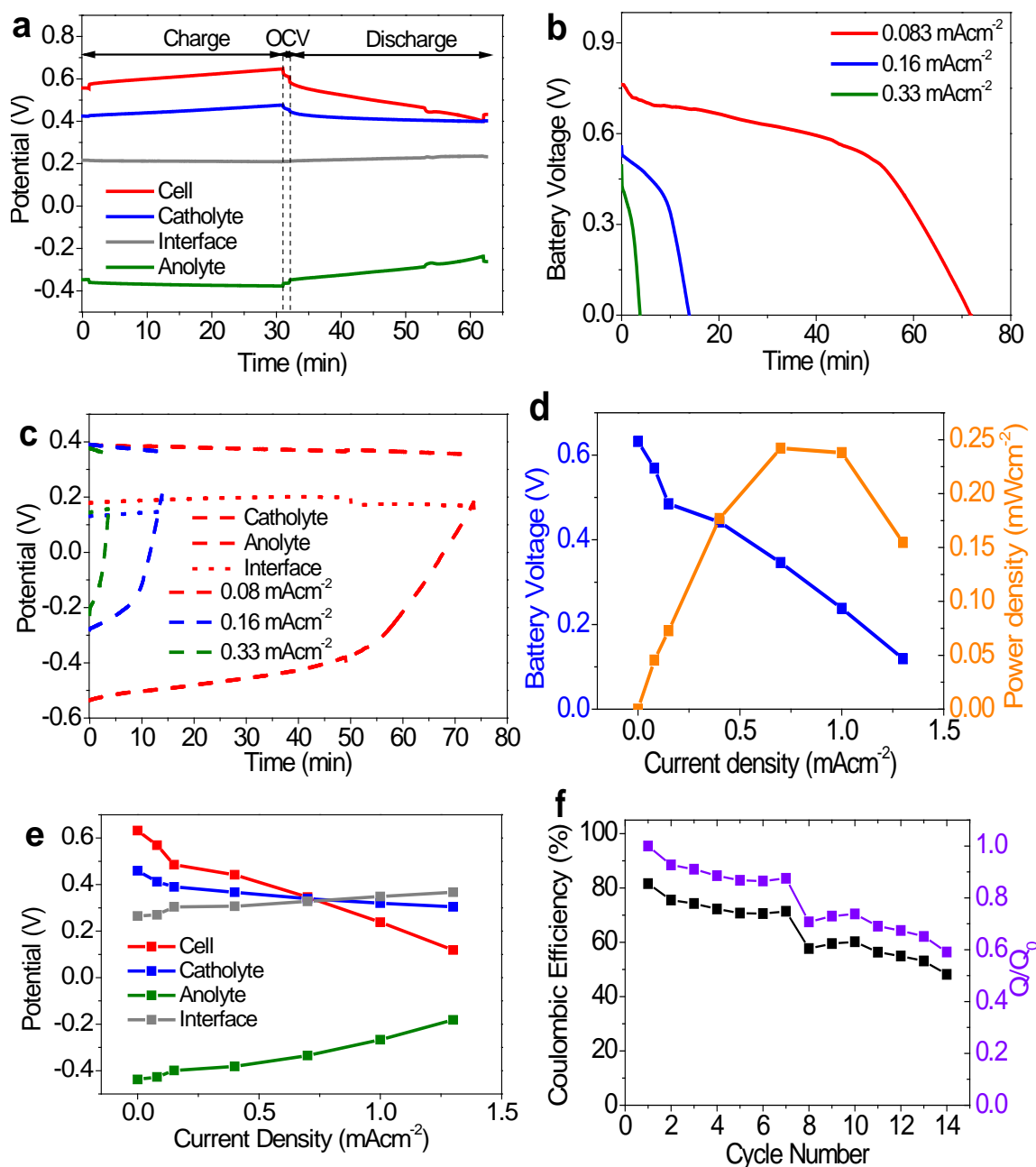


Figure 4.27. Performance of the Battery E (SOC 25 %). Active species concentration: 20 mM in catholyte and anolyte. a) Galvanostatic charge-discharge cycle at 0.16 mA·cm⁻². b) Discharge voltage profiles of the battery at different current densities. c) Discharge individual voltage profiles of each electrolyte and the interface at different current densities. d) Polarization test during discharge. e) Discharge polarization test of battery and each individual profile (catholyte, anolyte and interface). f) Cycling stability (5 %SOC) at 0.16 mA·cm⁻²

Figure 4.27a shows that during the charge both catholyte, interface and anolyte exhibit quite stable potentials. As a consequence, the battery voltage is stable at around 0.6 V. Throughout the discharge, the potential of the catholyte continues completely flat at 0.4 V while the potential of the anolyte slowly decreases leading to a slow decrease in

the battery potential at about 0.55 V. Profound discharge experiments at different current densities (Figure 4.27b and c) demonstrated that the performance of the battery is influenced mostly by the anolyte that is less conductive and more viscous ($1.2 \text{ kg}\cdot\text{cm}^{-3}$ and 2.50 cP) than the aqueous catholyte. Moreover, the D and K^0 exhibited by pBQ in PC are lower than the one revealed by H₂Q in the aqueous media affecting the battery performance (See Table 4.4).

The potential-current response of the battery during discharging (Figure 4.27d) is also controlled by high ohmic polarization revealed by the anolyte (see Figure 4.27e). It is worthy to remark that the battery failure at the end of the discharge is due to the sudden drop of anolyte potential. This high concentration polarization might be attributed to the poor redox reversibility of pBQ in PC evidenced by the CV curve in Figure 4.18b, where the anodic peak current was much larger than the cathodic one, meaning that only some of the species reduced during charge were able to be re-oxidized during discharge. This poor reversibility of pBQ in PC is reflected in the long-term battery performance that losses about 40% of initial capacity in less than 15 cycles (see Figure 4.27f).

- **Battery F**

With the aim of improving the electrochemical performance of the system, in Battery F TBAPF₆ was substituted by PYR₁₄TFSI as supporting salt in the anolyte. Thus, the anolyte was composed by pBQ dissolved in a mixture of PC and PYR₁₄TFSI (75-25 wt%). This redox electrolyte has lower viscosity and much lower cost than the pure PYR₁₄TFSI used in Batteries A, B and C. Moreover, the CV of this anolyte shows similar values for anodic and cathodic peak currents demonstrating that the redox reaction of pBQ is more reversible in this electrolyte than in the electrolyte employed in Battery E.

Besides the anolyte, in Battery F the catholyte was also changed with respect to the proof-of-concept battery. Here, the catholyte was composed by TEMPO functionalized with a hydroxyl group (OH-TEMPO) in neutral media (0.5 M NaCl). The OH-TEMPO exhibits electrochemical performance, diffusion coefficient (D) and kinetic constant (K^0) similar to TEMPO (see Table 4.4), but presents some additional advantages such as

4. Membrane-Free Redox Flow Batteries by Using Two Immiscible Redox Electrolytes

its higher solubility and diminished hydrophobicity²². Higher solubility will allow to assemble batteries with higher concentration of active species and the reduced hydrophobicity will mitigate the cross-migration of active species through the interface as observed in Battery C.

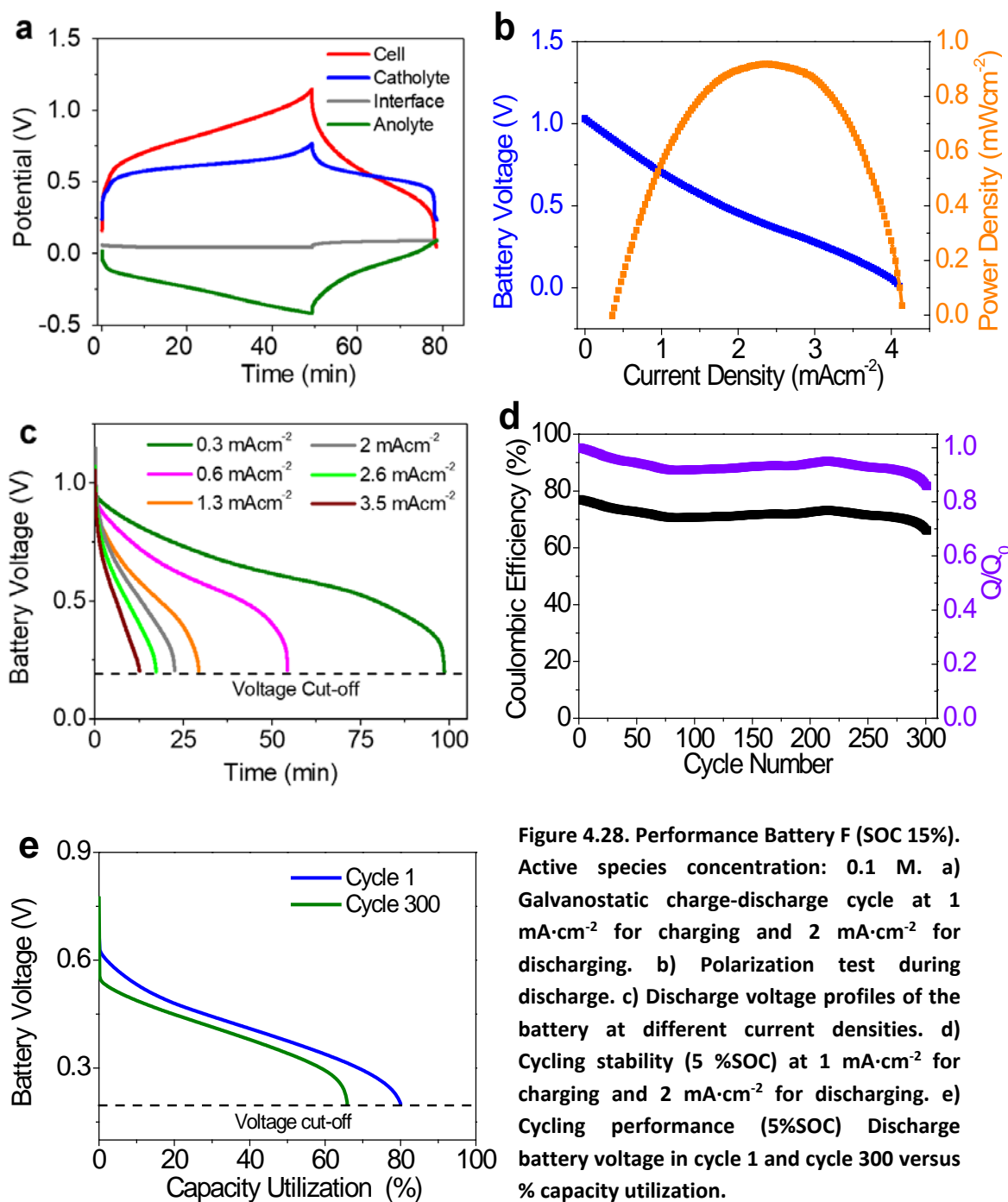


Figure 4.28. Performance Battery F (SOC 15%). Active species concentration: 0.1 M. a) Galvanostatic charge-discharge cycle at 1 mA·cm⁻² for charging and 2 mA·cm⁻² for discharging. b) Polarization test during discharge. c) Discharge voltage profiles of the battery at different current densities. d) Cycling stability (5 %SOC) at 1 mA·cm⁻² for charging and 2 mA·cm⁻² for discharging. e) Cycling performance (5%SOC) Discharge battery voltage in cycle 1 and cycle 300 versus % capacity utilization.

As it is observed in Figure 4.28a, the individual potentials of each electrolyte during the battery operation are in good agreement with the CV experiments (Figure 4.20). Similar to the previous batteries, the anolyte showed higher overpotential than the catholyte due to different factors such as its lower conductivity and higher viscosity and the higher diffusion limitations of pBQ in the nonaqueous anolyte (see Table 4.4). It should be noted that the overpotential of the interface is very small (≈ 40 mV), with very low contribution to the internal resistance of the battery. In the discharge polarization test (Figure 4.28b), a peak power density of $0.9 \text{ mW}\cdot\text{cm}^{-2}$ was reached which is 4 times higher than the power density obtained in the Battery E. This significant increase in the power density, associated with the higher current density reached in this battery, is probably due to the higher concentration of the electrolytes and to the higher reversibility of the pBQ in Battery F.

In addition, profound discharge capacity tests were carried out at different current densities from 0.3 to $3.5 \text{ mA}\cdot\text{cm}^{-2}$ (Figure 4.28c). Increasing the current density causes a decrease in the battery voltage, as in any other type of battery, due to the higher overpotentials as can be also observed in the polarization experiment. The cycling life of this battery was evaluated over 300 cycles and very stable performance was revealed (Figure 4.28d). The battery voltage during cycling only undergoes slight variations due to a small increase in the overpotential (Figure 4.28e). Hence, a high capacity retention (Q/Q_0) of 85 % was attained which highlights the higher reversibility of the pBQ reaction in this anolyte (PC-PYR₁₄TFSI 75-25 %wt) in comparison with the anolyte of Battery E. These results point out the relevance of the compatibility and affinity between the active species and the supporting electrolyte for having a stable performance. It is worthy to highlight here that the coulombic efficiency is less than 100% in this long cycling experiment (about 80 % during all cycling). This is probably due to the self-discharge process taking place at the interface via electron exchange reaction between the generated species. More details about this phenomenon that is inherent to the Membrane-Free concept will be investigated deeply in the next chapter.

4.3 Conclusions

In this chapter, a Membrane-Free Redox Flow Battery that relies on the immiscibility of redox electrolytes and where the vanadium species are replaced by organic redox molecules was reported. Specifically, it was confirmed that an acidic solution of hydroquinone (H_2Q) and an hydrophobic ionic liquid, 1-Butyl-1-methylpyrrolidinium bis(trifluoromethanesulfonyl)imide ($PYR_{14}TFSI$) containing dissolved parabenzoquinone (pBQ), spontaneously forms a biphasic system that behaves as a battery without the need of any membrane or physical separator. This proof-of-concept of Membrane-Free Battery exhibits an open circuit voltage of 1.4 V, maintains a stable discharge voltage at 0.9 V and presents high capacity and good reversibility.

Moreover, it was demonstrated that this disruptive technology is very versatile and can be applied to other pairs of redox molecules and immiscible (aqueous-nonaqueous) solvents. Thus, besides the ones used in the proof-of-concept battery, different pairs of immiscible electrolyte were formulated based on commercial available organic redox materials, common inexpensive organic solvents and non-corrosive aqueous media. In addition to the proof-of-concept battery, 5 batteries were assembled with the most promising electrolytes, revealing that this Membrane-Free Battery concept can be applied to different pairs of immiscible electrolytes containing different redox pairs and leading to batteries with different properties. As an indication of the performance of the studied batteries, changing the active species dissolved in the anolyte from pBQ to anthraquinones (examples Battery A and B) a theoretical cell voltage as high as 2 V was achieved. This OCV is one of the highest reported and means a 50 % enhancement in comparison with the pioneering example. Furthermore, a two times increased operating voltage (from 0.9 to 1.8 V) and 35 % superior power density was attained. On the other hand, changing the solvent and the supporting electrolyte (Battery E and F) reduced the battery cost. Moreover, the results underlined the seminal importance of an adequate compatibility and affinity among redox species and supporting electrolytes.

It has been revealed that some thermodynamic aspects such as partition coefficients are crucial factors for achieving a stable long-cycling performance. Definitely, further

4. Membrane-Free Redox Flow Batteries by Using Two Immiscible Redox Electrolytes

improvements will be achieved by investigating deeply thermodynamic aspects to reduce the crossover contamination, selecting judiciously the redox species and the electrolyte (increasing organic molecules solubility and enhancing cell voltages via molecular design and electrolyte choice), as well as working on the engineering aspects of the cell design.

4.4 Experimental

4.4.1 Reagents

N-butyl-N-methylpyrrolidinium bis(trifluoromethanesulfonyl) imide (PYR₁₄TFSI) having a 99.5 % purity was purchased from Solvionic. Propylene Carbonate (anhydrous 99.7 % purity) and 2-Butanone (ACS reagent \geq 99.0 % purity) were purchased from Sigma Aldrich. P-Benzoquinone (pBQ) ($>$ 99.5 % purity) was obtained from Fluka Analytical; Hydroquinone (H₂Q) reagent ($>$ 99% purity), Bis(pentylamino)anthraquinone (OilBlue N) (dye content 96 %), 2,3-dimethylantraquinone (assay 98 %), 2,2,6,6-Tetramethyl-1-piperidinyloxy (TEMPO) (98 % purity), 4-Hydroxy-2,2,6,6-tetramethylpiperidine 1-oxyl (OH-TEMPO) (97 % purity), Sodium Chloride (ACS reagent \geq 99.8 %), were purchased from Sigma Aldrich. Tetra-n-butylammonium hexafluorophosphate (TBAPF₆) (assay 98 %) was obtained from Acros Organic. All of the reagents were used as received for electrolyte preparation.

4.4.2 Preparation of Electrolytes

Catholytes and anolytes were prepared by dissolving organic compounds in the corresponding solvent after addition of supporting electrolyte when necessary. In section 4.2.1, the proof of concept battery was demonstrated by using two different concentrations of active species, a 20 mM solution of pBQ in PYR₁₄TFSI and a 20 mM solution of H₂Q in 0.1 M HCl were used in a diluted battery and the active specie concentration was increased up to 0.1 M in a more concentrated proof-of concept battery.

In section 4.2.2 the composition of electrolytes is as follows: for Battery A a solution 20 mM of 2,3-dimethylantraquinone in PYR₁₄TFSI was used as anolyte and 20 mM of H₂Q in 0.1 M HCl as catholyte, for Battery B a solution 20 mM of OilBlue N in PYR₁₄TFSI was used as anolyte and 20 mM of H₂Q in 0.1 M HCl as catholyte, for Battery C a solution 20 mM of pBQ in PYR₁₄TFSI was used as anolyte and 40 mM of TEMPO in 0.1 M NaCl as catholyte, for Battery D a solution 20 mM of pBQ in (0.1 M TBAPF₆) 2-Butanone was used as anolyte and 20 mM of H₂Q in 0.1 M HCl as catholyte, for Battery E a solution

4. Membrane-Free Redox Flow Batteries by Using Two Immiscible Redox Electrolytes

20 mM of pBQ in (0.1 M TBAPF₆) PC as anolyte and 20 mM of H₂Q (0.1 M HCl) as catholyte and for Battery F a solution 0.1 M of pBQ in PC+ PYR₁₄TFSI (75:25 %wt) was used as anolyte and a solution 0.1 M of OH-TEMPO in 0.5 M NaCl was used as catholyte. For RDE experiments, the same procedure was followed to obtain solutions of 5 mM concentration in all the electrolytes.

4.4.3 Electrochemical characterization of redox electrolytes

All electrochemical tests were conducted using a Biologic VMP multichannel potentiostat. A glassy carbon electrode (ID: 3 mm) and a platinum mesh were used as working and counter-electrodes respectively for three-electrode cyclic voltammetry (CV) tests. Ag/AgCl was used as reference electrode in the aqueous electrolyte and an Ag wire was used as pseudo-reference electrode in nonaqueous electrolytes.

Rotating-disk electrode (RDE) experiments were performed using a BASi RDE-2 rotating-disk electrode system. All tests were obtained using a three-electrode cell with a glassy carbon rotating electrode (ALS Co., Ltd). Counter and reference electrodes were the same as those for the three-electrode CV test.

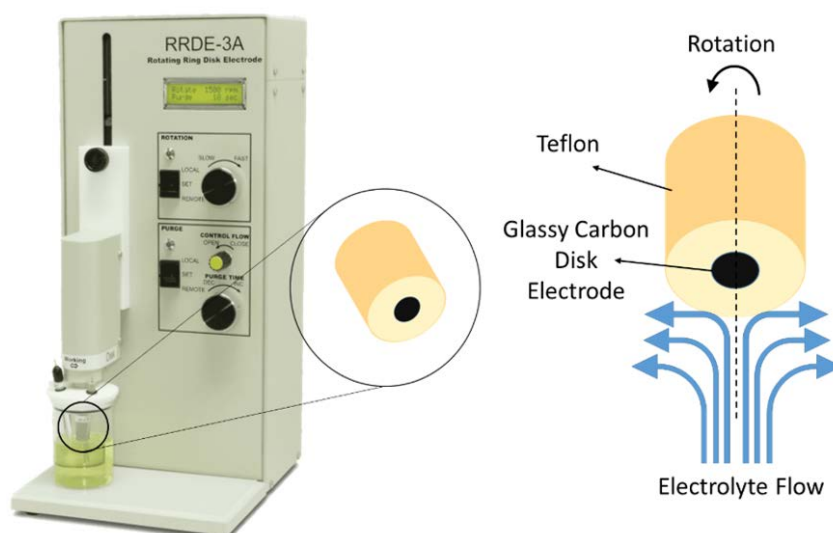


Figure 4.29. Rotating disk electrode setup and schematic representation of the working.

4. Membrane-Free Redox Flow Batteries by Using Two Immiscible Redox Electrolytes

As it is shown in Figure 4.29, RDE creates a totally defined electrolyte flow pattern in which the mass transport of the dissolved species is almost completely due to convection. The polished disk electrode is embedded in an insulating plastic and the structure is rotated about a perpendicular axis to the surface of the disk. Then the electrolyte is pulled upward and derived outward.

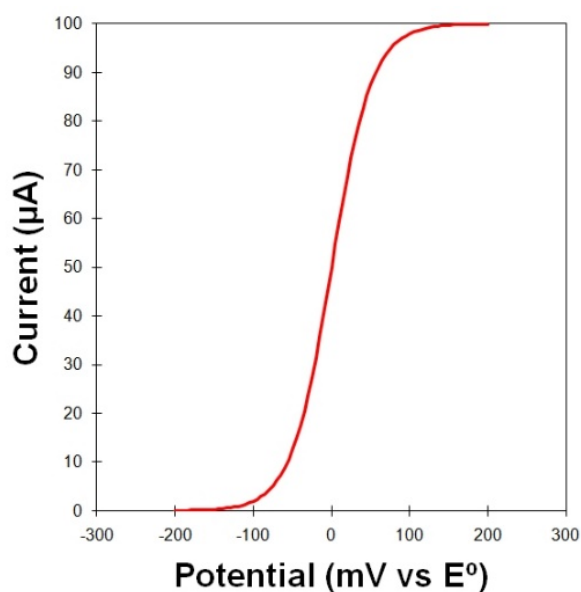


Figure 4.30. Schematic representation of the linear sweep voltammetry experiment result

Linear sweep voltammetry (LSV) is an electrochemical method which measures the current at a working electrode whereas the potential is linearly swept in time between the working electrode and the reference one. Thus, oxidation or reduction reaction of species dissolved into the electrolyte is detected through the variation in the current signal at the potential at which the reaction is undertaken (Figure 4.30). Since these experiments were performed using a rotating disk electrode the diffusion and kinetics parameters were allowed to be calculated.

LSV measurements were conducted at a scan rate of $10 \text{ mV}\cdot\text{s}^{-1}$ over a range of rotation rates (400 rpm to 3000 rpm). Before and during testing, the electrolytes were purged with ultra-high purity Argon to ensure adequate deaeration. Diffusion coefficients (D) and heterogeneous rate constants (k^0) were calculated using the Koutecky-Levich equation (4.1).

$$\frac{1}{i} = \frac{1}{i_K} + \frac{1}{i_l} \quad (4.1)$$

Where: $i_l = 0.62 e^- F A D^{2/3} \omega^{1/2} \vartheta^{-1/6} C_n$; and $i_K = e^- F A K^0 C_n$

and e^- is the number of electrons transferred, F the Faraday constant, A the disc area, D the diffusion coefficient, θ the kinematic viscosity, C_n the electroactive species concentration and K^0 the heterogeneous rate constant. A Levich plot was constructed from the RDE data by plotting the mass-transport limited current vs. the square root of the rotation rate (Figure 4.6b and d Figure 4.22b, d, f, h, j and l).

4.4.4 Battery Assembly

Due to the immiscibility of the two electrolytes, biphasic liquid-liquid system were formed spontaneously when 4 ml of the aqueous electrolyte (catholyte) was mixed with 4 ml of nonaqueous electrolyte (anolyte) in a cylindrical electrochemical cell of 2.5 cm diameter. The aqueous electrolytes occupied the upper phase and the nonaqueous electrolytes formed the lower phase of these systems. One carbon felt electrode (squared shape of 1.5 cm²) was immersed in each phase forming the positive and negative terminals. Permeable carbon felts provided by SGL CARBON GmbH (grade GFD4.6 EA) (4.6 mm thickness) (Figure 4.31) were pretreated by immersion in 1 M NaOH solution at 80 °C during 1 h to improve the wettability of the electrolytes.



Figure 4.31 Carbon Felt material used as electrodes

4. Membrane-Free Redox Flow Batteries by Using Two Immiscible Redox Electrolytes

The distance between two carbon electrodes was approximately 2 cm. No ion-exchange membrane or physical separator was used to separate the two redox electrolytes. In order to follow the voltage evolution of the individual electrolyte and the voltage difference through the interface, two reference electrodes were immersed into each electrolyte; Ag/AgCl in the aqueous phases and a silver wire that will act as a pseudoreference in the nonaqueous phases. A photograph of a Membrane-Free Battery set-up is shown in Figure 4.32.

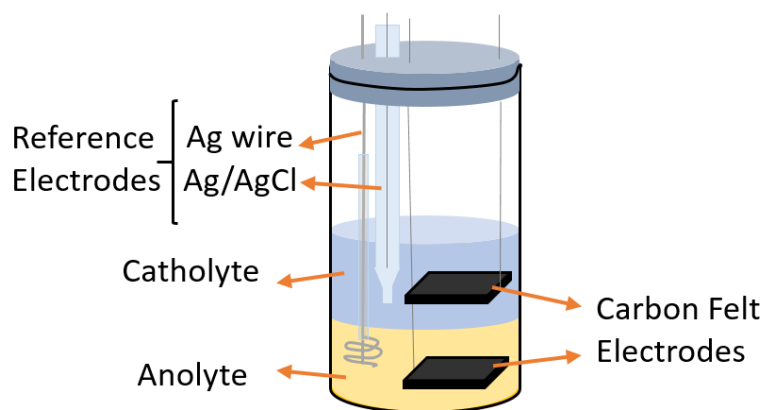


Figure 4.32. Schematic illustration of an assembled Membrane-Free Battery.

4.4.5 Electrochemical Characterization of Membrane-Free RFB.

All investigated Membrane-Free Redox Flow Batteries were initially assembled in a fully discharged state. To obtain polarization curves, the Membrane-Free batteries were first charged to the desired SOC and then polarized by point-by-point galvanostatic holds from 0 to $4 \text{ mA}\cdot\text{cm}^{-2}$ (maximum).

To conduct galvanostatic discharge experiments, the Membrane-Free RFB were first galvanostatically charged to the desired SOC and subsequently discharged at different current densities (in a range from $-0.083 \text{ mA}\cdot\text{cm}^{-2}$ to $-3.5 \text{ mA}\cdot\text{cm}^{-2}$), with voltage limits of 0.3 and 2.0 V for the proof-of-concept battery and with voltage cut-off of 0.5 V-0.7 V and 2.0 V for Batteries A-F.

4. Membrane-Free Redox Flow Batteries by Using Two Immiscible Redox Electrolytes

The maximum theoretical capacity of the battery (Q_t) was calculated by Eq (4.2), where n is the amount of active species (mol), e^- is the number of electron exchanged and F is the Faraday constant ($96500 \text{ s}\cdot\text{A}\cdot\text{mol}^{-1}$).

$$Q_t = n e^- F \quad (4.2)$$

Capacity utilization (%) was calculated as the ratio between the discharge capacity and the maximum theoretical capacity (Q_t) at one specific state of charge (SOC). It was calculated by Eq (4.3), where SOC refers to battery state of charge and Q is the discharge capacity delivered by the battery.

$$\text{Capacity utilization (\%)} = \frac{Q}{Q_t \cdot \text{SOC}} \cdot 100 \quad (4.3)$$

The cycle life experiments consisted in charging and discharging continuously at constant current. For the diluted proof-of-concept battery the current density was $\pm 0.16 \text{ mA}\cdot\text{cm}^{-2}$ using voltage cut-offs of 0.3 V in discharge and 2 V in charge. For the proof-of-concept battery with concentrated electrolytes the current density applied was $\pm 0.66 \text{ mA}\cdot\text{cm}^{-2}$ and the charging and discharging times were fixed to 30 minutes each (short charge-discharge cycles). For Battery E the cycles were performed at $\pm 0.16 \text{ mA}\cdot\text{cm}^{-2}$ and for Battery F the current densities applied were $1 \text{ mA}\cdot\text{cm}^{-2}$ for charging and $2 \text{ mA}\cdot\text{cm}^{-2}$ for with a voltage cut-off of 1.3 and 0.2 V. The capacity retention was calculated by dividing the number of discharged coulombs during the n^{th} cycle by the discharged coulombs occurring during the first cycle (Eq. 4.4).

$$\text{Capacity retention} = Q/Q_0 \quad (4.4)$$

Coulombic efficiency (CE) is the ratio between the charge delivered during discharge and the charge applied during charge (See Eq 4.5). Voltage efficiency (VE) is defined as the relation between the averaged discharge voltage and the averaged charge voltage (See Eq. 4.6). The energy efficiency (EE) was calculated as; coulombic efficiency (CE) \times voltage efficiency (VE) (See Eq. 4.7).

$$CE = \frac{Q_d}{Q_c} \quad (4.5)$$

$$VE = \frac{V_d}{V_c} \quad (4.6)$$

$$EE = CE \cdot VE \quad (4.7)$$

4.5 References

- 1 G. L. Soloveichik, *Chem. Rev.*, 2015, **115**, 11533–11558.
- 2 P. Leung, X. Li, C. P. de León, L. Berlouis, C. T. J. Low and F. C. Walsh, *RSC Adv.*, 2012, **2**, 10125–10156.
- 3 M. Skyllas-Kazacos, M. Rychcik, R. G. Robins and A. G. Fane, *J. Electrochem. Soc.*, 1986, **133**, 1057–1058.
- 4 M. Park, J. Ryu, W. Wang and J. Cho, *Nat. Rev. Mater.*, 2016, **2**, 16080.
- 5 B. Li and J. Liu, *Natl. Sci. Rev.*, 2017, **4**, 91–105.
- 6 R. M. Darling, K. G. Gallagher, J. A. Kowalski, S. Ha and F. R. Brushett, *Energy Environ. Sci.*, 2014, **7**, 3459–3477.
- 7 A. Ejigu, P. A. Greatorex-Davies and D. A. Walsh, *Electrochem. commun.*, 2015, **54**, 55–59.
- 8 K. Gong, Q. Fang, S. Gu, S. F. Y. Li and Y. Yan, *Energy Environ. Sci.*, 2015, **8**, 3515–3530.
- 9 J. Winsberg, T. Hagemann, T. Janoschka, M. D. Hager and U. S. Schubert, *Angew. Chemie - Int. Ed.*, 2016, **55**, 2–28.
- 10 B. Yang, L. Hooper-Burkhardt, F. Wang, G. K. Surya Prakash and S. R. Narayanan, *J. Electrochem. Soc.*, 2014, **161**, A1371–A1380.
- 11 K. Lin, Q. Chen, M. R. Gerhardt, L. Tong, S. B. Kim, L. Eisenach, A. W. Valle, D. Hardee, R. G. Gordon, M. J. Aziz and M. P. Marshak, *Science (80-.)*, 2015, **349**, 1529–1532.
- 12 X. Wei, W. Duan, J. Huang, L. Zhang, B. Li, D. Reed, W. Xu, V. Sprenkle and W. Wang, *ACS Energy Lett.*, 2016, **1**, 705–711.
- 13 X. Wei, W. Xu, J. Huang, L. Zhang, E. Walter, C. Lawrence, M. Vijayakumar, W. A. Henderson, T. Liu, L. Cosimbescu, B. Li, V. Sprenkle and W. Wang, *Angew. Chemie - Int. Ed.*, 2015, **54**, 8684–8687.
- 14 A. P. Kaur, N. E. Holubowitch, S. Ergun, C. F. Elliott and S. A. Odom, *Energy Technol.*, 2015, **3**, 476–480.
- 15 T. Janoschka, N. Martin, M. D. Hager and U. S. Schubert, *Angew. Chemie - Int. Ed.*, 2016, **55**, 14427–14430.
- 16 T. Liu, X. Wei, Z. Nie, V. Sprenkle and W. Wang, *Adv. Energy Mater.*, 2016, **6**, 1501449.
- 17 S. K. Park, J. Shim, J. Yang, K. H. Shin, C. S. Jin, B. S. Lee, Y. S. Lee and J. D. Jeon, *Electrochem. commun.*, 2015, **59**, 68–71.
- 18 W. Wang and V. Sprenkle, *Nat. Chem.*, 2016, **8**, 204–206.
- 19 F. R. Brushett, J. T. Vaughey and A. N. Jansen, *Adv. Energy Mater.*, 2012, **2**, 1390–1396.
- 20 Z. Li, S. Li, S. Liu, K. Huang, D. Fang, F. Wang and S. Peng, *Electrochem. Solid-State Lett.*, 2011, **14**, A171–A173.

4. Membrane-Free Redox Flow Batteries by Using Two Immiscible Redox Electrolytes

- 21 B. Huskinson, M. P. Marshak, C. Suh, S. Er, M. R. Gerhardt, C. J. Galvin, X. Chen, A. Aspuru-Guzik, R. G. Gordon and M. J. Aziz, *Nature*, 2014, **505**, 195–198.
- 22 T. Janoschka, N. Martin, M. D. Hager and U. S. Schubert, *Angew. Chemie - Int. Ed.*, 2016, **55**, 14427–14430.
- 23 J. Luo, B. Hu, C. Debruler and T. L. Liu, *Angew. Chemie Int. Ed.*, 2018, **57**, 231–235.
- 24 V. Viswanathan, A. Crawford, D. Stephenson, S. Kim, W. Wang, B. Li, G. Coffey, E. Thomsen, G. Graff, P. Balducci, M. Kintner-Meyer and V. Sprenkle, *J. Power Sources*, 2014, **247**, 1040–1051.
- 25 L. Joerissen, J. Garche, C. Fabjan and G. Tomazic, *J. Power Sources*, 2004, **127**, 98–104.
- 26 M. Moore, J. Watson, T. A. Zawodzinski Jr., M. Zhang and R. M. Counce, *ECS Trans.*, 2012, **41**, 1–19.
- 27 A. A. Chilenskas, E. C. Gay, R. K. Steunenber, H. S. Lim, A. M. Lackner and R. C. Knechtli, 1978, 1154–1157.
- 28 B. Li, Z. Nie, M. Vijayakumar, G. Li, J. Liu, V. Sprenkle and W. Wang, *Nat. Commun.*, 2015, **6**, 1–8.
- 29 P. K. Leung, T. Martin, A. A. Shah, M. R. Mohamed, M. A. Anderson and J. Palma, *J. Power Sources*, 2017, **341**, 36–45.
- 30 P. K. Leung, T. Martin, A. A. Shah, M. A. Anderson and J. Palma, *Chem. Commun.*, 2016, **52**, 14270–14273.
- 31 Y. Xu, Y. Wen, J. Cheng, G. Cao and Y. Yang, *Electrochem. commun.*, 2009, **11**, 1422–1424.
- 32 Yuan Yanga, Guangyuan Zhengb and Yi Cuia, *Energy Environ. Sci.*, 2013, **6**, 1552.
- 33 M. Duduta, B. Ho, V. C. Wood, P. Limthongkul, V. E. Brunini, W. C. Carter and Y. M. Chiang, *Adv. Energy Mater.*, 2011, **1**, 511–516.
- 34 E. Ventosa, M. Skoumal, F. J. Vazquez, C. Flox, J. Arbiol and J. R. Morante, *ChemSusChem*, 2015, **8**, 1737–1744.
- 35 T. Janoschka, N. Martin, U. Martin, C. Friebe, S. Morgenstern, H. Hiller, M. D. Hager and U. S. Schubert, *Nature*, 2015, **527**, 78–81.
- 36 J. Friedl, M. A. Lebedeva, K. Porfyrakis, U. Stimming and T. W. Chamberlain, *J. Am. Chem. Soc.*, 2018, **140**, 401–405.
- 37 W. Duan, R. S. Vemuri, J. D. Milshtein, S. Laramie, R. D. Dmello, J. Huang, L. Zhang, D. Hu, M. Vijayakumar, W. Wang, J. Liu, R. M. Darling, L. Thompson, K. Smith, J. S. Moore, F. R. Brushett and X. Wei, *J. Mater. Chem. A*, 2016, **4**, 5448–5456.
- 38 J. Carretero-Gonzalez, E. Castillo-Martinez and M. Armand, *Energy Environ. Sci.*, 2016, **9**, 3521–3530.
- 39 R. A. Potash, J. R. McKone, S. Conte and H. D. Abruña, *J. Electrochem. Soc.*, 2016, **163**, A338–A344.
- 40 Y. K. Zeng, X. L. Zhou, L. An, L. Wei and T. S. Zhao, *J. Power Sources*, 2016, **324**,

- 738–744.
- 41 W. A. Braff, M. Z. Bazant and C. R. Buie, *Nat. Commun.*, 2013, **4**, 2346.
- 42 R. Ferrigno, A. D. Stroock, T. D. Clark, M. Mayer and G. M. Whitesides, *J. Am. Chem. Soc.*, 2002, **2**, 12930–12931.
- 43 E. Kjeang, R. Michel, D. a. Harrington, N. Djilali and D. Sinton, *J. Am. Chem. Soc.*, 2008, **130**, 4000–4006.
- 44 J. W. Lee, M.-A. Goulet and E. Kjeang, *Lab Chip*, 2013, **13**, 2504–2507.
- 45 J. W. Campos, M. Beidaghi, K. B. Hatzell, C. R. Dennison, B. Musci, V. Presser, E. C. Kumbur and Y. Gogotsi, *Electrochim. Acta*, 2013, **98**, 123–130.
- 46 S.-E. Chun, B. Evanko, X. Wang, D. Vonlanthen, X. Ji, G. D. Stucky and S. W. Boettcher, *Nat. Commun.*, 2015, **6**, 7818.
- 47 S. Roldán, C. Blanco, M. Granda, R. Menéndez and R. Santamaría, *Angew. Chemie Int. Ed.*, 2011, **50**, 1699–1701.
- 48 S. Roldán, M. Granda, R. Menéndez, R. Santamaría and C. Blanco, *J. Phys. Chem. C*, 2011, **115**, 17606–17611.
- 49 C. S. Sevov, R. E. M. Brooner, E. Chénard, R. S. Assary, J. S. Moore, J. Rodríguez-López and M. S. Sanford, *J. Am. Chem. Soc.*, 2015, **137**, 14465–14472.
- 50 M. A. Bhat, *Electrochim. Acta*, 2012, **81**, 275–282.
- 51 P. S. Guin, S. Das and P. C. Mandal, *Int. J. Electrochem.*, 2011, **2011**, 1–22.
- 52 B. Huskinson, M. P. Marshak, C. Suh, S. Er, M. R. Gerhardt, C. J. Galvin, X. Chen, A. Aspuru-Guzik, R. G. Gordon and M. J. Aziz, *Nature*, 2014, **505**, 195–198.
- 53 M. Galiński, A. Lewandowski and I. Stępnia, *Electrochim. Acta*, 2006, **51**, 5567–5580.
- 54 R. Salazar, J. Vidal, M. Martínez-Cifuentes, R. Araya-Maturana and O. Ramírez-Rodríguez, *New J. Chem.*, 2015, **39**, 1237–1246.
- 55 X. Ji, C. E. Banks, D. S. Silvester, A. J. Wain and R. G. Compton, *J. Phys. Chem. C*, 2007, **111**, 1496–1504.
- 56 W. Sun, Q. Jiang, M. Yang and K. Jiao, *Bull. Korean Chem. Soc.*, 2008, **29**, 915–920.
- 57 Y. She, Y. Tang, H. Liu and P. He, *Chem. Cent. J.*, 2010, **4**, 17.
- 58 E. Laviron, *J. Electroanal. Chem. Interfacial Electrochem.*, 1984, **164**, 213–227.
- 59 C. Rüssel and W. Jaenicke, *J. Electroanal. Chem.*, 1984, **180**, 205–217.
- 60 T. Nagaoka and S. Okazaki, *J. Phys. Chem.*, 1985, **89**, 2340–2344.
- 61 J. D. Millshtein, A. P. Kaur, M. D. Casselman, J. A. Kowalski, S. Modekrutti, P. L. Zhang, N. Harsha Attanayake, C. F. Elliott, S. R. Parkin, C. Risko, F. R. Brushett and S. A. Odom, *Energy Environ. Sci.*, 2016, **9**, 3531–3543.
- 62 M. Quan, D. Sanchez, M. F. Wasylkiw and D. K. Smith, *J. Am. Chem. Soc.*, 2007, **129**, 12847–12856.
- 63 M. A. Bhat, *Electrochim. Acta*, 2012, **81**, 275–282.

4. Membrane-Free Redox Flow Batteries by Using Two Immiscible Redox Electrolytes

- 64 V. D. Sen and V. A. Golubev, *J. Phys. Org. Chem.*, 2009, **22**, 138–143.
- 65 Q. Zhang, J. Rong, D. Ma and B. Wei, *Energy Environ. Sci.*, 2011, **4**, 2152.
- 66 C. Rüssel and W. Janicke, *J. Electroanal. Chem.*, 1986, **199**, 139–151.
- 67 X. Xing, Y. Huo, X. Wang, Y. Zhao and Y. Li, *Int. J. Hydrogen Energy*, 2017, **42**, 17488–17494.
- 68 S. M. Laramie, J. D. Milshtein, T. M. Breault, F. R. Brushett and L. T. Thompson, *J. Power Sources*, 2016, **327**, 681–692.

Chapter 5 . Membrane-Free
Redox Flow Batteries
based on Aqueous
Biphasic Systems

5.1 Introduction

In chapter 4 a novel concept of Membrane-Free RFB based on the immiscibility of two electrolytes (aqueous/nonaqueous) and in which the metallic active compounds were substituted by organic redox molecules was studied. The results obtained highlighted two aspects: (i) the versatility of the Membrane-Free Concept; (ii) the seminal importance of the cross-migration of the active species through the interface.

The versatility of the Membrane-Free concept was demonstrated in chapter 4, since it might be applied to different combinations of immiscible electrolytes containing a huge variety of redox organic molecules but only biphasic systems based on aqueous/nonaqueous phases were investigated. However, in this chapter systems formed by two aqueous phases will be studied, since they are particularly interesting in terms of sustainability, cost and environmental impact.

Aqueous Biphasic Systems (ABS) are systems in which the addition of two water soluble compounds (two polymers¹, one polymer-one salt², one ionic liquid-one salt³) above certain concentrations causes the spontaneous separation of the system into two liquid (aqueous-rich) phases. The ABS have been intensively studied in separation, purification and extraction processes^{3,4}, as an environmental friendly, low cost and scalable method in comparison with the conventional ones based on volatile organic solvents. They have been widely investigated in the last decade, in particular, the selective separation of a large number of compounds such as biomolecules⁵⁻⁸, metals⁹⁻¹¹ and drugs residues^{12,13}. In addition, the nature of the phase-forming components, as well as the operating conditions such as pH and temperature, upon the partition of the target compounds have been evaluated^{4,6}. The main advantages of these systems rely on a low interfacial tension, fast phase separation, easy scale-up, and high water content, providing favorable conditions to the design of extraction/separation processes for target molecules or products.

In this chapter, we aim to expand the range of applications of IL-based ABS to a new field: the electrochemical energy storage. Besides the immiscibility of the two electrolytes, in the previous chapter it was explained that the selective solubility of each target redox molecule in the two liquid phases will be of paramount importance

to develop batteries with minimized crossover. The crossover or cross-contamination of active species from catholyte to anolyte and vice versa reduces the battery performance decreasing its efficiency and provoking a misbalance of active species in the two battery compartments. Differently from conventional RFB in which the crossover typically occurs through the ineffective membranes, in this Membrane-Free RFB concept, the cross-contamination will be determined by the partition coefficients of the positive and negative redox organic molecules between the two coexisting phases.

There are different strategies to manipulate the partition and/or selectivity of the dissolved compounds between the coexisting phases of an ABS: i) by changing the nature of the phase-forming components (e.g., polymers, salts or ILs) and/or by using additives; ii) by changing the composition of the phase-forming components; iii) by manipulation of other conditions, such as pH and temperature ³. The introduction of ionic liquids (ILs) in ABS brought additional advantages to these extraction systems in terms of performance and selectivity, mainly due to the wide range of available ILs and the possibility of tailoring the coexisting phases polarities and affinities for target compounds ¹⁴. On the other hand, the ABS based on polymers have also several advantages since some polymers such as poly(ethylene glycol) (PEG) are widely used in our daily products and approved by REACH. These polymers are environmentally friendly, have low cost and are produced at large scale.

In this chapter, we will investigate different ABS as promising platforms for developing Total Aqueous Membrane-Free RFB with appropriate electrochemical performance and minimal cross-contamination. To do that, we will examine some thermodynamic properties such as the biphasic formation and the partition coefficients of several redox-active organic molecules. Moreover, we will also determine the electrochemical behavior of such immiscible phases. All these properties together are extremely relevant for the final application as a battery since they will determine the chemical and electrochemical stability of the redox molecules and the cross-over of active species through the interface, which will eventually affect the efficiency of the battery.

5.2 Results and Discussion

5.2.1 Partitioning Characterization and Design of Aqueous Biphasic System (ABS) as Suitable Immiscible Electrolytes for Membrane-Free RFB

5.2.1.1 *Phase Diagrams of ABS*

In order to study the viability of the application of ABS as the basis for a Membrane-Free RFB, the main requirement of this battery concept, the immiscibility of the electrolytes, was first investigated. To do that, the phase diagrams of several ABS were determined. ABS are ternary mixtures composed of two solutes/phase-forming components and water that above certain concentrations, described by the respective binodal curve, undergo phase separation leading to the formation of two aqueous-rich phases, each one enriched in one of the solutes. ABS phase diagrams are usually represented in orthogonal axis, in which only the concentration of the two solutes is displayed (water composition is omitted and corresponds to the difference required to reach 100 wt%) (Figure 5.1). The binodal curve of each phase diagram separates the monophasic and biphasic regions, whereas the respective tie-lines (black line in Figure 5.1; see experimental details in section 5.4.2) give the composition of each phase (black dots labeled as T and B in Figure 5.1) for a given initial mixture composition (green dot labeled as M in Figure 5.1).

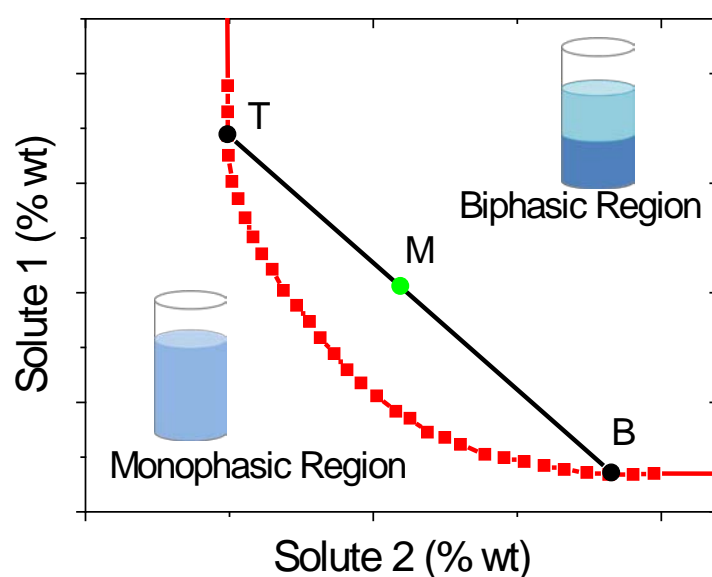
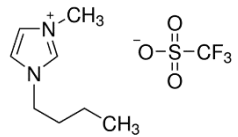
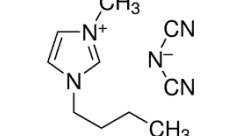
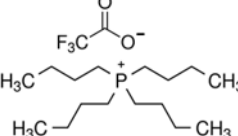
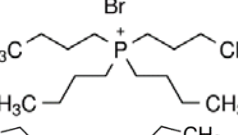
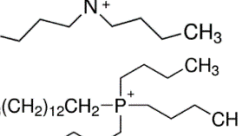
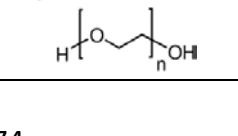



Figure 5.1. Illustrated representation of a phase diagram.

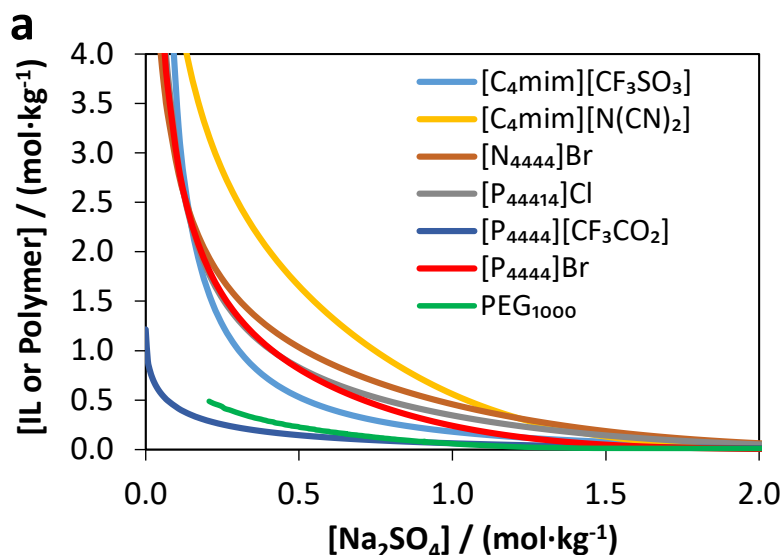
Some novel phase diagrams were determined in this work, whereas others were taken from the literature ¹⁵. In this chapter, the solutes selected to form the ABS are sodium sulfate on one hand and a set of IL/polymer on the other hand. The inorganic salt Na₂SO₄ was selected due to its high charge density and moderate ability to form hydration complexes, and thus to act as suitable salting-out agent for the ILs/polymer leading to the formation of ABS. Moreover, the acidic-neutral pH of most of ABS obtained with this salt brings additional advantages such as the higher chemical and electrochemical stability of some organic molecules, the low corrosive character of the media, and the lower environmental impact in case of electrolyte leak in the battery.

Table 5.1 depicts the chemical structure of the different ILs and polymer investigated to prepare ABS. Since the formation of Na₂SO₄-based ABS is promoted by the hydrophobic character of IL/polymer ^{16–18} most of the candidates were highly hydrophobic having anions with weaker interactions with water (*i.e.* with low hydrogen bond basicity) ¹⁹ or cations with low hydrogen-bond acidity ²⁰.

Table 5.1. Chemical structure of ionic liquids used to form ABS

Ionic Liquid	Chemical Structure
[C ₄ mim][CF ₃ SO ₃]	
[C ₄ mim][N(CN) ₂]	
[P ₄₄₄₄][CF ₃ CO ₂]	
[P ₄₄₄₄]Br	
[N ₄₄₄₄]Br	
[P ₄₄₄₁₄]Cl	
PEG ₁₀₀₀	

The binodal curves in molality units (mole of IL or Polymer or salt *per* kg of the other two species) and percentage by weight for the different ILs/polymer are given in Figure 5.2a and b, respectively. They were determined through the cloud point titration method at 25 °C and atmospheric pressure. These experimental data were correlated according to the equation proposed by Merchuck et al.²¹ (Eq. 5.1), and the correlation parameters are gathered in Table 5.2 (see Experimental section 5.4.2). Figure 5.2a shows that the ability to form ABS, when $[IL \text{ or Polymer}] = [salt]$ in molality, follows the order: $[P_{4444}][CF_3CO_2] > PEG_{1000} > [C_4mim][CF_3SO_3] > [P_{4444}Br] \approx [P_{44414}Cl] > [N_{4444}Br] > [C_4mim][N(CN)_2]$. The trend to biphasic formation is influenced by the affinity of the IL cation and anion for water (the higher it is, the more difficult it is to salt-out the IL and create an ABS). However, the influence of the cation is not clearly observed due to the mixed effect attributed to the presence of different anions. On the other hand, the effect of the IL anion on the ABS formation can be appraised with the $[C_4mim]$ -based series of ILs. It should be stressed that the anion influence in the hydrophobicity of the IL is more relevant due to the more significant anion-water interactions. The lower the hydrogen bond basicity of the anion, the lower its coordination with water molecules and thus more easily the IL is salted-out and undergoes phase separation^{22–24}.



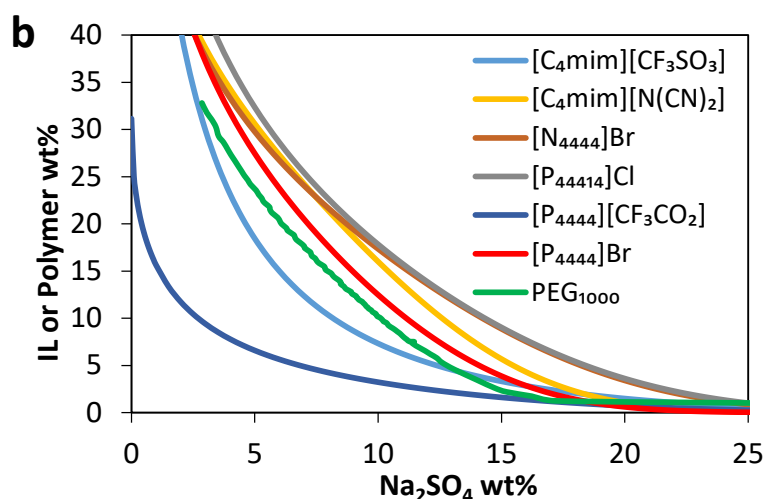


Figure 5.2. Phase diagrams according to the fitting of equation (5.1) to the experimental data obtained at 25°C and atmospheric pressure: a) in molality units; b) percentage by weight. Phase diagrams for $[C_4mim][CF_3SO_3]$, and $[C_4mim][N(CN)_2]$ were taken from literature¹⁵.

Table 5.2. Parameters A, B and C obtained from Merchuk fitting²¹ (equation 5.1) for each ABS tested

IL or Polymer	$A \pm \sigma$	$B \pm \sigma$	$10^5 C \pm \sigma$
$[C_4C_{1im}][CF_3SO_3]$	155.2 ± 8.3	-0.950 ± 0.033	4.97 ± 0.10
$[C_4C_{1im}][N(CN)_2]$	78.2 ± 1.7	-0.402 ± 0.015	31.56 ± 5.24
$[P_{44414}]Cl$	105.0 ± 2.9	-0.520 ± 0.014	13.10 ± 2.07
$[P_{4444}]Br$	95.2 ± 1.0	-0.538 ± 0.006	33.18 ± 1.21
$[N_{4444}]Br$	81.3 ± 1.7	-0.441 ± 0.010	15.00 ± 8.56
$[P_{4444}][CF_3CO_2]$	31.1 ± 0.9	-0.690 ± 0.022	8.55 ± 12.78
PEG_{1000}	94.9 ± 0.8	-0.599 ± 0.017	32.98 ± 2.13

Among all the investigated ILs, $[P_{4444}][CF_3CO_2]$ presents the largest biphasic region, thus requiring lower amounts of salt to be salted-out from aqueous media. In fact, this IL was synthesized in this work to prepare a water soluble ionic liquid of high hydrophobicity by combining a cation with low charge density and strong steric shielding with an anion with low hydrogen bond basicity according to the discussion above on the mechanism of IL-ABS formation. In the case of polymer PEG, its high hydrophobicity facilitates also the biphasic formation becoming an interesting alternative to develop inexpensive batteries.

In RFBs, the redox active molecules should be highly soluble in the electrolyte, chemical and electrochemical stable, and should exhibit fast and reversible

electrochemical activity. As mentioned in the introduction, it must be stressed that the crossover of one redox molecule from one electrolyte to the opposite one (through the membrane in conventional RFB) causes its contamination, and as consequence decreases the battery performance. Therefore, besides the imperative formation of the two immiscible phases, the transformation of an ABS to a Membrane-Free RFB requires a highly selective separation of two different redox molecules, one in each phase.

5.2.1.2 Partition Coefficients of Organic Molecules in the ABS

The specific solubility of a certain molecule in each phase of an ABS, directly related with the partition coefficients, relies on the physicochemical properties of these phases. Factors such as nature of IL/polymer and salt, pH or temperature affect the partition coefficients in ABS^{4,6}. Here, we analyze the effect of different ILs/polymer on the partition coefficients of five organic redox molecules widely investigated in RFB: methyl viologen (MV), hydroquinone (H₂Q), athraquinone-2-sulfonic acid (AQ2S), quinoxaline (QUI) and 2,2,6,6-tetramethyl-1-piperidinyloxy (TEMPO).

Figure 5.3 represents the partition coefficients (K) calculated as the ratio of concentrations of each compound in the two immiscible phases of all the studied IL-based ABS. The chemical structures of the redox molecules and their octanol-water partition coefficients (K_{ow})²⁵ are also given in Figure 5.3. Table 5.3 includes the numerical values of partition coefficients (K). Values of K higher than 1 mean that the target molecule is dissolved preferably in the top phase and values lower than 1 indicate that the target molecule partitions to the bottom phase.

As can be seen in Figure 5.3, a selective separation enabling a top-phase rich in one redox molecule and a bottom phase rich in other molecule was attained in all systems. The bottom phase is the salt-rich phase in all cases excepting for the ABS containing [C₄mim][CF₃SO₃]. It is observed that most of the molecules exhibit higher affinity to the top phase whereas MV is selectively partitioned into the salt-rich phase (bottom phase). This means that MV has lower affinity to hydrophobic phase that in this system is the IL-rich/ polymer-rich phase. This trend is in close agreement with their octanol-

5. Membrane-Free Redox Flow Batteries based on Aqueous Biphasic Systems

water partition coefficients, in which only MV has K_{ow} values < 1 , and thus preferentially partitions to hydrophilic phases, in this work the salt-rich phase. In the case of systems based on more hydrophobic ILs, such as those containing ILs with phosphonium cations, and in particular when combined with the fluorinated anion ($[P_{4444}][CF_3CO_2]$), a large increase in the partition coefficients of MV to the salt-rich phase was observed.

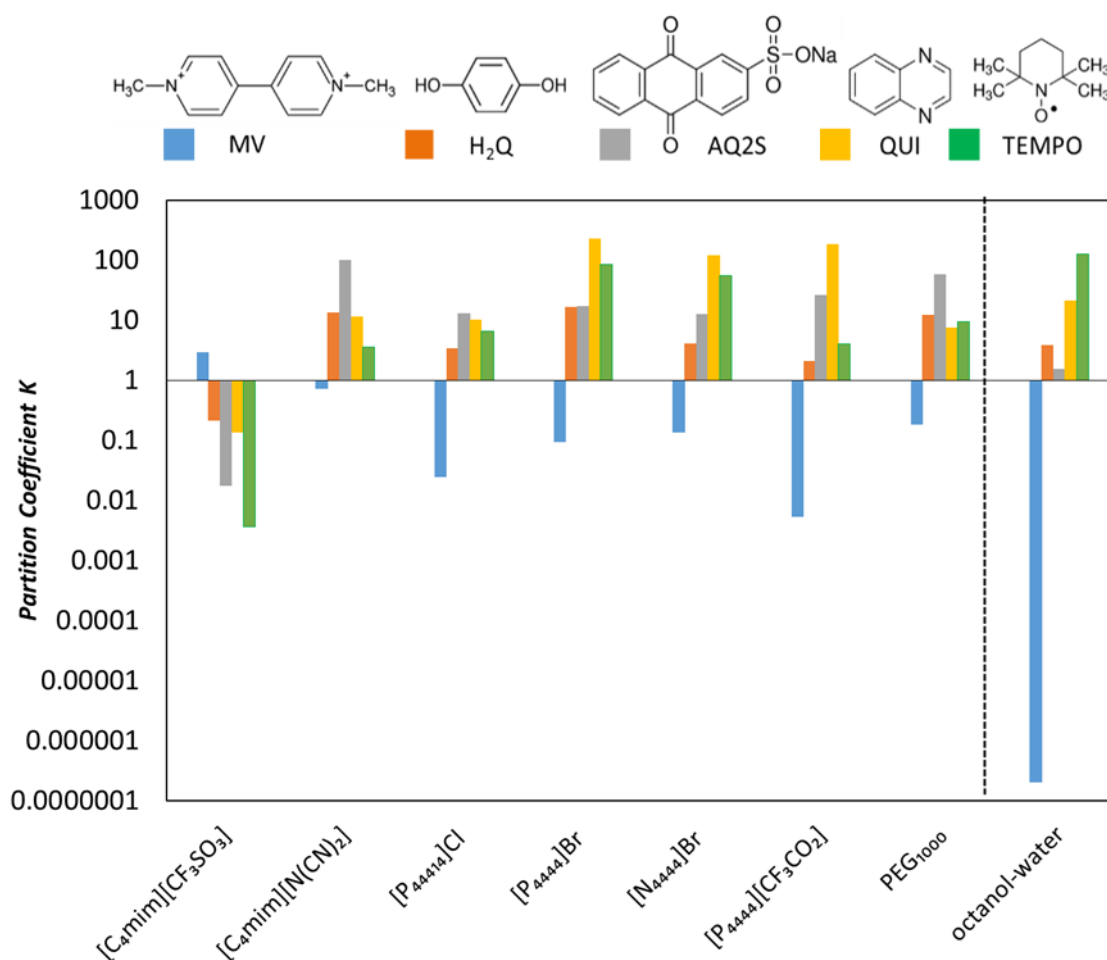


Figure 5.3. Partition coefficients (K) of the target molecules in ABS based on different ionic liquids or PEG₁₀₀₀ and the partition coefficients in octanol water (K_{ow}) taken from ²⁵.

Table 5.3. Partition coefficients (*K*) calculated as the ratio of concentrations of each compound in the two immiscible phases of all the studied ABS and octanol-water system.

IL+ Na₂SO₄ + H₂O	TEMPO	H₂Q	AQ2S	QUI	MV
[C ₄ mim][CF ₃ SO ₃]	3.6·10 ⁻³	0.21	0.02	0.14	2.89
[C ₄ mim][N(CN) ₂]	3.56	13.53	98.86	11.49	0.72
[P ₄₄₄₁₄]Cl	6.55	3.39	13.15	10.31	0.02
[P ₄₄₄₄]Br	84.19	16.47	16.95	226.66	0.09
[N ₄₄₄₄]Br	55.86	4.05	12.43	120	0.13
[P ₄₄₄₄][CF ₃ CO ₂]	3.96	2.08	25.89	185.22	5.3·10 ⁻³
PEG ₁₀₀₀	9.46	12.38	58.27	7.61	0.18
octanol + water	125.89	3.89	1.55	20.89	1.99·10 ⁻⁷

The separation of the target molecules can be evaluated by selectivity (*S*), defined as the ratio of partition coefficients of two target molecules, which describes their equilibrium distribution between the two immiscible phases. The more different from 1 the selectivity values are, the greater separation between those molecules is achieved. From the partition coefficient determination it was observed that MV is the only molecule that preferentially partitions into the salt-rich phase. The selectivity values (*S*) of the different molecules with respect to MV are included in Table 5.4 and represented in Figure 5.4.

The selectivity values are higher (>100) for all the molecules in those systems in which the ILs are based on the phosphonium cation. For TEMPO and AQ2S especially large *S* are also observed when fluorinated anions are involved, such as in the case of [C₄mim][CF₃SO₃] and [P₄₄₄₄][CF₃CO₂]. Higher *S* values are obtained with more hydrophobic IL, closely correlating with their ability to form ABS with Na₂SO₄ – a trend that results from the higher polarity difference between the coexisting phases and the partition being dominated by the hydrophobic interactions as suggested by the dominating role that the log *K_{ow}* has on the partition of the molecules. In summary, with the exception of [C₄mim][N(CN)₂], the ABS studied present large selectivity values which indicate that all ABS selected are able to separate MV from the remaining organic molecules with a significant difference in concentration. This difference is important since the lower is the concentration of the target molecule in the opposite phase, the lower will be the amount of idle active specie in a battery.

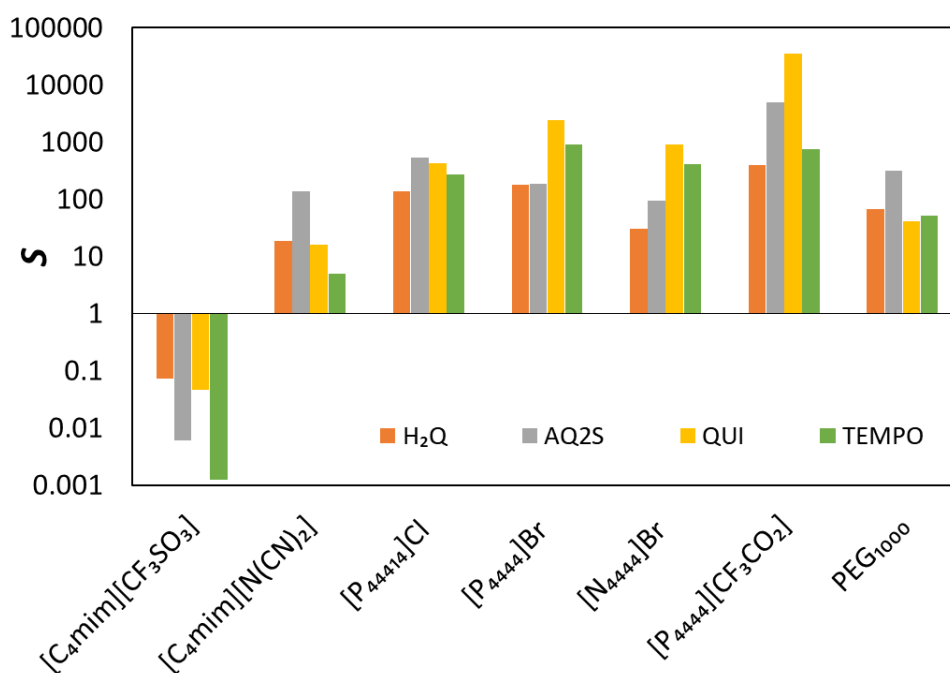


Figure 5.4. Selectivity of the target molecules with respect to MV

Table 5.4. Selectivity (*S*) calculated as the ratio of partition coefficient of the target molecule and MV ($K_{molecule}/K_{MV}$) in each ABS.

IL+ Na ₂ SO ₄ + H ₂ O	H ₂ Q	AQ2S	QUI	TEMPO
[C ₄ mim][CF ₃ SO ₃]	$7.41 \cdot 10^{-2}$	$0.60 \cdot 10^{-2}$	$4.67 \cdot 10^{-2}$	$0.12 \cdot 10^{-2}$
[C ₄ mim][N(CN) ₂]	18.89	138.07	16.05	4.97
[P ₄₄₄₁₄]Cl	138.26	536.80	420.91	267.35
[P ₄₄₄₄]Br	178.44	183.57	2455.69	912.13
[N ₄₄₄₄]Br	30.45	93.46	902.25	420.00
[P ₄₄₄₄][CF ₃ CO ₂]	391.70	4884.91	34947.16	747.55
PEG ₁₀₀₀	67.66	318.59	41.58	51.72

5.2.2 Electrochemical characterization of redox-active ABS

The theoretical voltage of an ABS operating as a Membrane-Free RFB will be determined by the difference between the redox potentials of the two organic molecules selectively dissolved in each phase. Among the tested redox organic molecules, MV was the only one which was selectively separated from the others. This implies that MV should be necessarily one of the two redox molecules incorporated in the ABS. The most suitable candidate for the opposite phase should exhibit high partition coefficient in that phase as well as a separated redox potential with respect

to MV. Therefore, the electrochemical properties of ABS containing pairs of redox molecules that selectively migrate to opposite phases were investigated.

The ABS composed by $[P_{44414}]\text{Cl}$ and Na_2SO_4 was selected as case study to investigate the electrochemistry of all possible combination of redox couples. Four different redox ABS formed by $[P_{44414}]\text{Cl}$ were prepared by adding together 20 mM solutions of MV and AQ2S, MV and QUI, MV and H_2Q and MV and TEMPO. Then, the electrochemical performance of each phase was separately tested by cyclic voltammetry (CV) in 3-electrode electrochemical cells and the results are gathered in Figure 5.5.

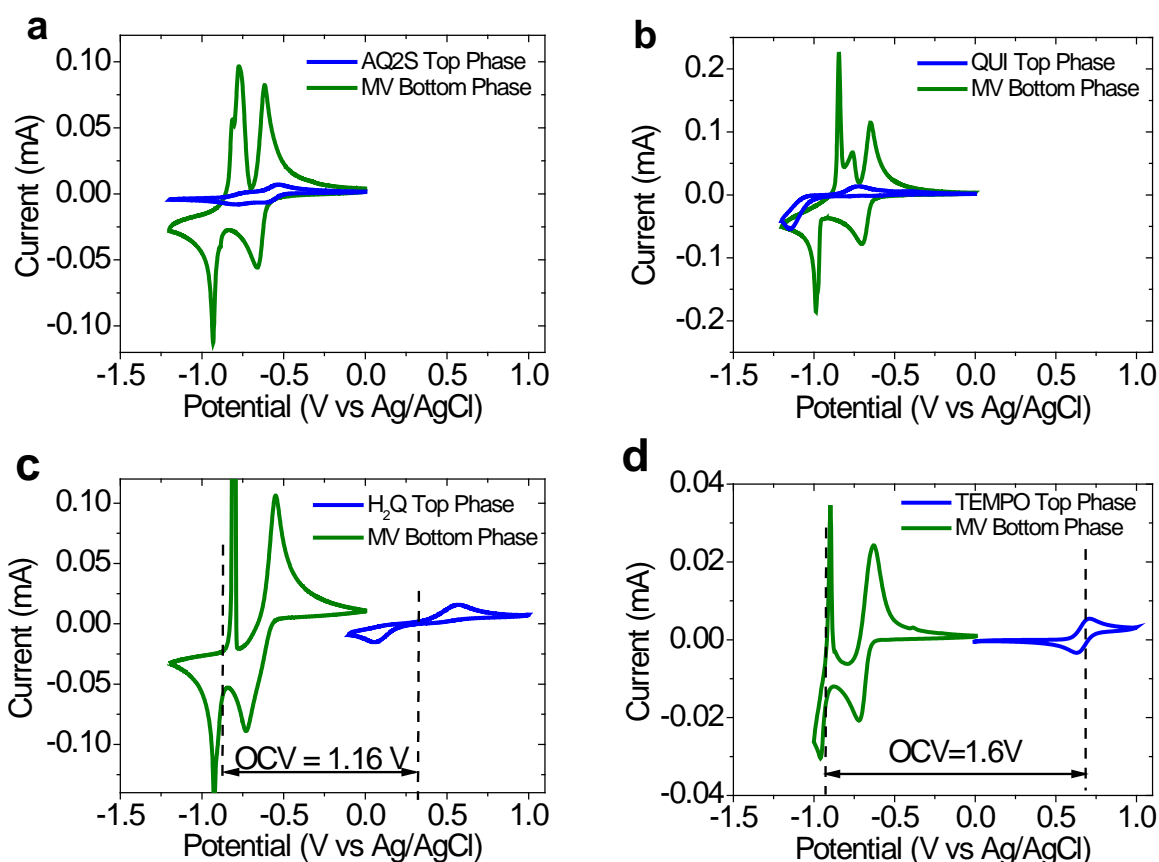


Figure 5.5. CV of each phase for the system based on $[P_{44414}]\text{Cl} + \text{Na}_2\text{SO}_4$ with different active species at 20 mM concentration in the initial mixture; a) MV+AQ2S, b) MV+QUI, c) MV+ H_2Q and d) MV+TEMPO

As it can be observed, the bottom phase being rich in MV in the four systems, displays a CV curve with two intense redox peaks at negative potentials which corresponds to the reduction-oxidation of MV molecule. This reaction occurs in two steps exchanging 2 electrons in total. The first step corresponds to the formation of the radical cation

and the second one corresponds to the formation of the neutral form (see Figure 5.6b). Therefore, the bottom phase rich in MV would act necessarily as the anolyte or negative electrolyte of the battery. The top phases rich in AQ2S (Figure 5.5a) and QUI (Figure 5.5b) also show reduction and oxidation peaks in the CVs but they appear at similar redox potential than for MV meaning that the resultant battery would have a very low voltage. In addition, although according to the partition coefficients the presence of AQ2S or QUI in the bottom phase is relatively small, it still causes some distortions in the redox signal of MV-rich bottom phase. Contrary to AQ2S and QUI, top phases rich in H₂Q and TEMPO exhibit reversible redox behavior at positive voltages (Figure 5.5c and d). Both systems offer a redox potential sufficiently different from MV for being considered as catholyte or positive electrolyte when combined with MV. Table 5.5 shows a detailed analysis of electrochemical characterization of the different redox ABS. It is worth to remark that the theoretical voltages of Membrane-Free RFBs formed by MV/H₂Q and by MV/TEMPO would be as high as 1.16 V and 1.6 V, respectively. On account of the higher redox potential, partition coefficients and selectivity of TEMPO compared with H₂Q, TEMPO was selected as redox pair for the catholyte. It is worth mentioning that the combination of MV and TEMPO has been recently explored for aqueous redox flow batteries with organic redox compounds^{26,27}.

Table 5.5. Potential redox reaction of majority species in each phase of a system based on [P₄₄₄₁₄]Cl

Combination	TOP Phase					BOTTOM Phase					OCV (V)		
	A.S. Majority	E ⁰ (V*)	E _{pa} (V*)	E _{pc} (V*)	ΔE _p (V)	A. S. Majority	E ⁰ (V*)	E _{pa} (V*)	E _{pc} (V*)	ΔE _p (V)			
MV-AQ2S	AQ2S	1 st step	-0.57	-0.53	-0.61	0.08	MV	1 st step	-0.64	-0.62	-0.66	0.04	-
		2 nd step	-0.76	-0.73	-0.79	0.06		2 nd step	-0.85	-0.77	-0.93	0.16	
MV-QUI	QUI	1 st step	-0.94	-0.72	-1.15	0.43	MV	1 st step	-0.68	-0.65	-0.71	0.05	-
		2 nd step						2 nd step	-0.91	-0.76	-0.99	0.15	
MV-H ₂ Q	H ₂ Q	1 st step	0.31	0.56	0.06	0.50	MV	1 st step	-0.64	-0.55	-0.73	0.18	1.16
		2 nd step						2 nd step	-0.86	-0.8	-0.92	0.12	
MV-TEMPO	TEMPO	1 st step	0.66	0.7	0.63	0.07	MV	1 st step	-0.67	-0.63	-0.72	0.09	1.33
		2 nd step						2 nd step	-0.93	-0.9	-0.97	0.07	

*Potential vs Ag/AgCl reference electrode

In order to evaluate the effect of composition of ABS in the electrochemical performance of the system, different Redox-active ABS containing different ionic liquids/polymer were prepared by adding TEMPO and MV (20 mM concentration) as active species within the mixture. After formation of the biphasic system and succeeding migration of TEMPO and MV to the top and bottom phase, respectively, the immiscible redox phases of all ABS studied, were electrochemically characterized in 3-electrode electrochemical cells (Figure 5.6).

CVs of [P₄₄₄₄]Br-based ABS represented in Figure 5.6c are very distorted and did not display a reversible electrochemical activity in any of the two phases. At negative potentials the anolyte exhibits an intense reduction peak (-0.85 V vs Ag/AgCl) which is likely due to an overlap between the reduction reaction of MV and the electrolysis of water producing hydrogen. This water degradation occurs at this potential in acidic electrolytes such as this ABS with pH of 3.1 (see Table 5.6). Concerning to the catholyte behavior, a large and irreversible oxidation peak appears at 0.8 V vs Ag/AgCl, being likely associated with the oxidation of Br⁻ anion from the ionic liquid to Br₂. Therefore, although partition coefficients and selectivity of MV and TEMPO redox molecules are appropriate, this ABS would not be a good candidate as Membrane-Free RFB due to the parasitic reactions occurring in both catholyte (top phase) and anolyte (bottom phase).

Figure 5.6d shows the CVs of the [N₄₄₄₄]Br-based ABS with two reversible redox peaks at negative potentials (-0.67 V and -0.91 V) related with the two step MV redox reaction depicted in Figure 5.6b. The higher pH of [N₄₄₄₄]Br-based ABS in comparison with the ABS containing [P₄₄₄₄]Br (pH 4.9 vs. pH 3.1) hinders the parasitic hydrogen evolution due to water electrolysis. However, the CV of the IL-rich top phase shows that the oxidation of Br⁻ to Br₂ still occurs at positive potentials due to the presence of Br⁻ anion in the IL. As a result, this system is not either suitable for being used as a Membrane-Free RFB and IL having different counter-anion should be employed to form redox active ABS.

The electrochemical performance of [P₄₄₄₄][CF₃CO₂]-based ABS in which the [Br] anion of the IL was substituted for [CF₃CO₂] is depicted in Figure 5.6e. CV shows a quite reversible response associated with the two steps redox reaction of MV in the anolyte

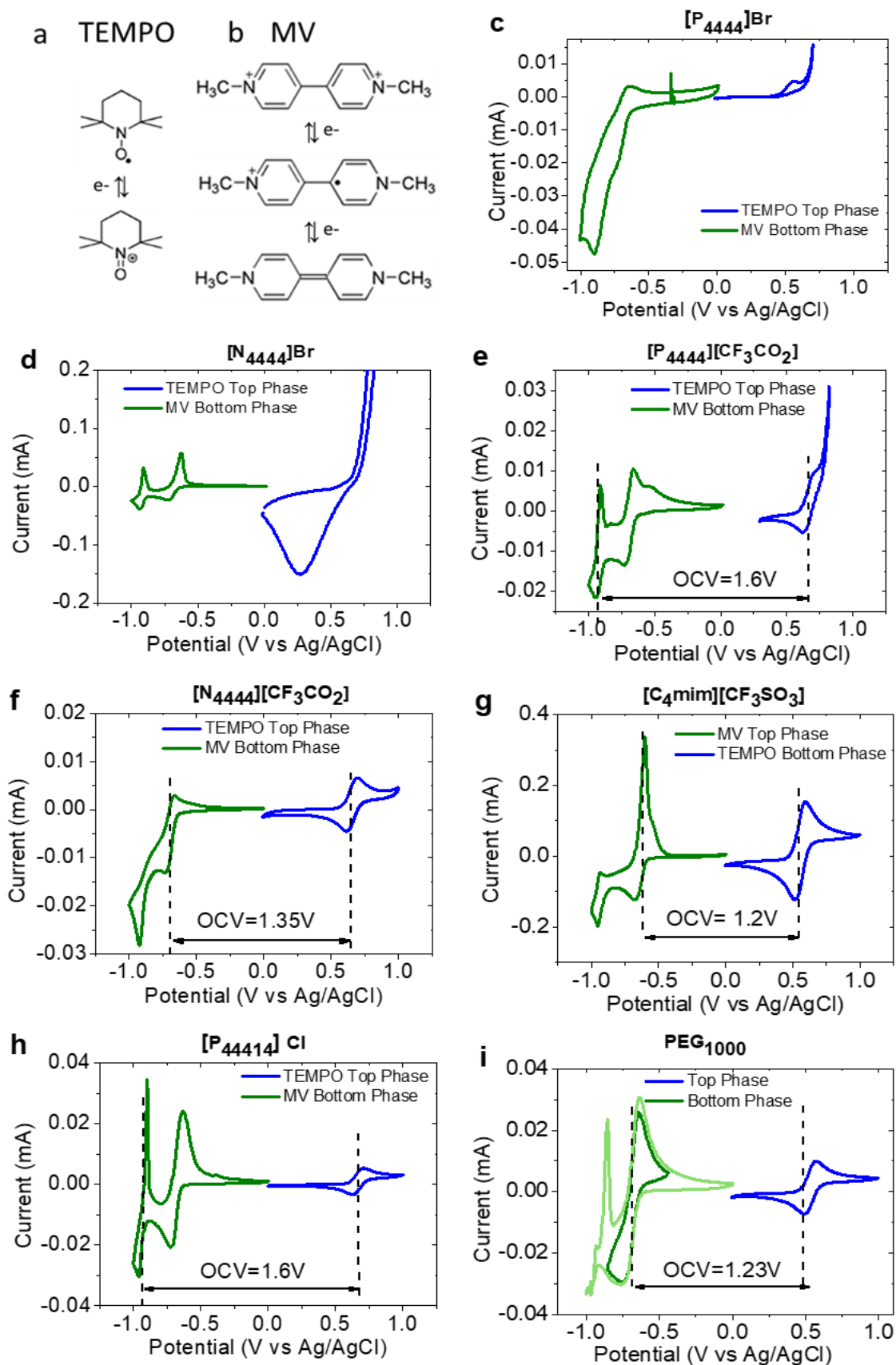


Figure 5.6. Redox reactions of the active species: a) TEMPO. b) Methyl viologen. Cyclic voltammetry of the phases separately of the systems based on IL+ Na₂SO₄+ 20mM TEMPO-20mM MV. c) [P₄₄₄₄]Br. d) [N₄₄₄₄]Br. e) [P₄₄₄₄][CF₃CO₂]. f) [N₄₄₄₄][CF₃CO₂]. g) [C₄mim][CF₃SO₃]. h) [P₄₄₄₁₄]Cl. i) PEG₁₀₀₀. Scan rate 10 mV·s⁻¹. MV (in green) TEMPO (in blue).

In Figure 5.6h the CVs of the biphasic system based on [P₄₄₄₁₄]Cl are plotted. A reversible redox peak at 0.67 V was observed corresponding to the reaction of TEMPO in the IL-rich top phase. In this system, the two steps associated with MV redox reaction in the salt-rich bottom phase appear at -0.68V and -0.93V with quite reversible redox behavior although very close to the stability limits of the electrolyte, which requires a careful control of the voltage during the battery operation to avoid the degradation of the electrolyte. The CVs of the PEG₁₀₀₀-based system are represented in Figure 5.6i. The bottom phase containing MV shows the two steps reduction reaction clearly defined by the appearance of two pairs of redox peaks. The first step of the redox reaction at -0.68 V is very reversible however, the second step shows low reversibility due to the insolubility of neutral species of MV²⁸. Thus, in this system, only the first reversible MV²⁺/MV⁺ redox reaction can be effectively used. It is worth mentioning that this behavior is intrinsic to the MV molecule and most examples of RFB with this molecule in literature describe the use of a cut-off voltage²⁷. In the CV of the top phase (polymer-rich) TEMPO exhibits two well-defined peaks, corresponding to the reversible redox reaction in which the oxoammonium cation is formed.

According to the thermodynamic and electrochemical properties of the investigated ABS, those containing [N₄₄₄₄][CF₃CO₂], [C₄mim][CF₃SO₃], [P₄₄₄₁₄]Cl and PEG₁₀₀₀ fulfill all the requirements to be transformed in Membrane-Free RFBs. Those requirements include appropriate partition coefficients for MV and TEMPO, high selectivity, good electrochemical stability of both top and bottom phases and reversible electrochemistry of MV and TEMPO active molecules resulting in a high theoretical open circuit voltage. As mentioned above, the theoretical open circuit voltage (OCV) of a battery can be estimated as the difference between the two redox potential at which each reaction take place in each immiscible phase. Therefore, in the four mentioned ABS the OCVs values are between 1.2 V and 1.6 V, the latter being, to the best of our knowledge, one of the highest OCV ever reported for an Aqueous Organic Redox Flow Battery^{26,27,29-32}.

Among the four different Redox-active ABS that fulfill the requirements to become Membrane-Free RFB, we have selected the one composed of PEG₁₀₀₀ to assemble a

Total Aqueous Membrane-Free Battery. This PEG₁₀₀₀-based ABS has several advantages respect to the ones based on ILs such us higher eco-friendly properties (this polymer is used in our daily products and approved by REACH*), lower cost and large scale production. These aspects need to be considered since the cost and environmental issues can limit the technology development.

5.2.3 Electrochemical Characterization of Total Aqueous Membrane-Free Battery based on an ABS

The results presented in the previous section confirm that PEG-based ABS containing MV and TEMPO represent a promising approach for developing a Membrane-Free RFB. On account of this, this system was investigated in more detail. Figure 5.7 depicts the phase diagram for the ABS formed by poly(ethylene glycol) (PEG₁₀₀₀) and Na₂SO₄. The ABS was prepared with the following mixture composition: 25 wt% PEG₁₀₀₀ + 6 wt% Na₂SO₄ + 69 wt% H₂O as pointed out with a red dot in Figure 5.7. The composition of each phase or respective tie-line for this initial mixture composition, i.e. the composition of the PEG-rich phase (top phase) and salt-rich phase (bottom phase), is also given in Figure 5.7.

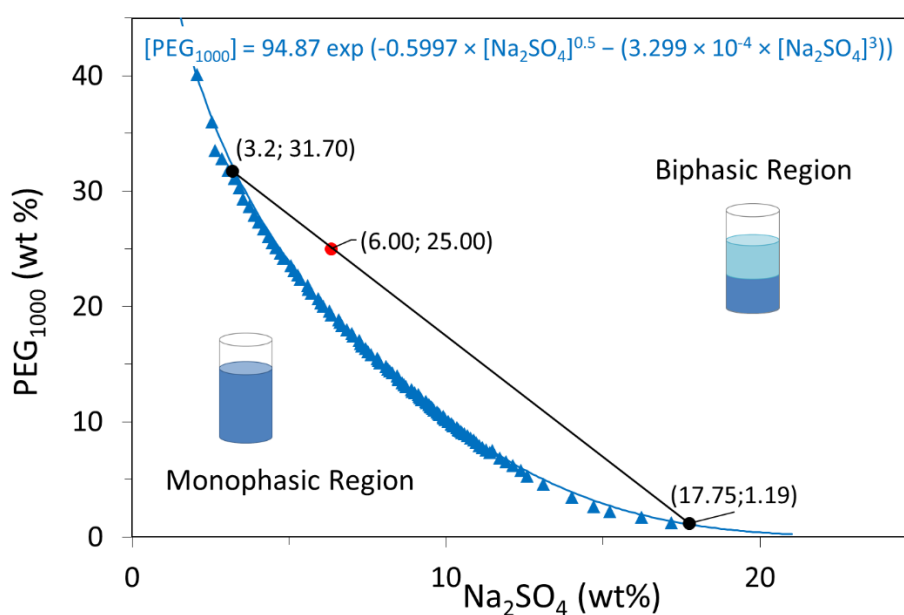


Figure 5.7. Binodal curve of the phase diagram of the ABS composed of PEG₁₀₀₀ + Na₂SO₄ + H₂O (blue dots + blue line), initial mixture composition (red dot) and composition of each phase (black dots and black line representing the respective tie-line, TLL = 33.85; $\alpha=0.769$)

5. Membrane-Free Redox Flow Batteries based on Aqueous Biphasic Systems

As shown in Figure 5.8, among the redox-molecule tested, only MV preferentially partitions to the bottom phase of the ABS, whereas the remaining molecules partition preferentially to the top phase (PEG-rich).

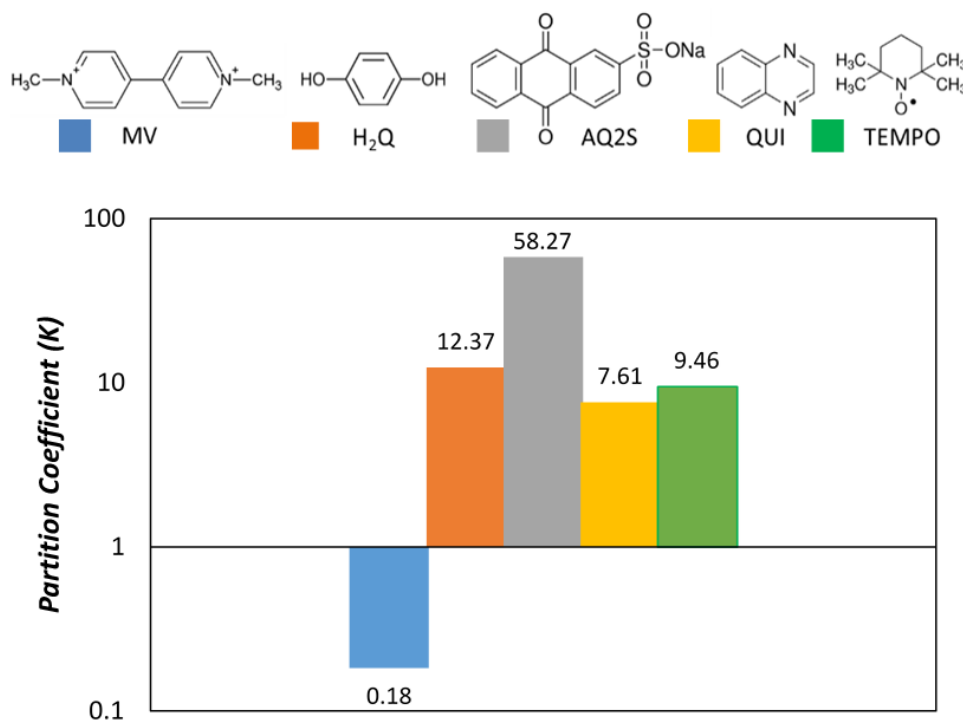


Figure 5.8. Partition coefficients of redox organic molecules between the PEG and salt-rich phases in the studied ABS. Chemical structures and abbreviations for the organic redox molecules are also given.

Among them, TEMPO was selected due to its electrochemical behavior as the most appropriate compound. Thus, the system based on PEG₁₀₀₀ containing MV and TEMPO as active species exhibited an OCV of 1.23 V as was shown in Figure 5.9.

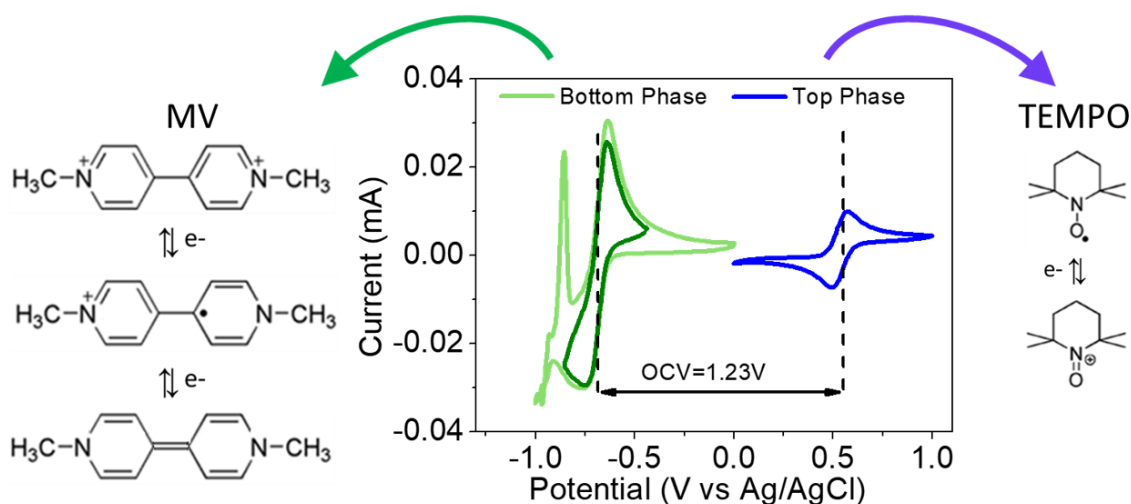


Figure 5.9. CV of the immiscible phases of PEG-based ABS containing TEMPO (blue) and MV (light and dark green depending on the voltage limits) at 20 mM concentration. Reaction mechanism of MV and TEMPO.

Besides partition coefficients and redox potentials, other physicochemical properties, such as ionic conductivity, pH and density were determined for the investigated PEG-based ABS containing 0.1 M of TEMPO and MV in the initial mixture (Table 5.7). As expected, the conductivity of the bottom phase is ten times higher than the one obtained for the top phase, due to the higher salt concentration. It is however important to remark that the presence of a salt is necessary in both phases since it will act as a supporting electrolyte providing ionic conductivity and counter-ions during the battery operation. The pH is close to neutrality in the two phases guaranteeing low corrosive and safer electrolytes in comparison with the acidic/alkaline solutions used in conventional aqueous RFB^{29,30}.

Table 5.7. Physicochemical properties of each phase of PEG-based ABS containing 0.1 M of TEMPO and MV in the initial mixture. Calculated Diffusion Coefficient (D) and Rate Constant (k^0) for MV and TEMPO in bottom and top phases, respectively

	Composition (wt%)	Density ($\text{g}\cdot\text{L}^{-1}$)	pH	Conductivity ($\text{mS}\cdot\text{cm}^{-1}$)	Diffusion Coefficient (D) ($\text{cm}^2\cdot\text{s}^{-1}$)	Rate Constant (k^0) ($\text{cm}\cdot\text{s}^{-1}$)
Top Phase	31.7 % PEG 3.2 % salt (~ 0.23 M)	1068	6.28	8.55	$9.09\cdot 10^{-7}$	$2.53\cdot 10^{-3}$
Bottom Phase	1.19 % PEG 17.75 % salt (~ 1.4 M)	1145	5.04	85.7	$5.01\cdot 10^{-6}$	$3.41\cdot 10^{-3}$

Table 5.7 also includes the diffusion coefficients (D) and the heterogeneous rate constants (K^0) determined by using Rotating Disk Electrode (RDE) for MV in the bottom (salt-rich) phase and TEMPO in the top (PEG-rich) phase (see Figure 5.10). It can be observed that the diffusion of active species is hampered in the top phase with D of TEMPO being one order of magnitude lower than for MV. This can be attributed to the lower salt concentration and lower conductivity of this phase. However, this difference in conductivity and salt concentration is not a hurdle for having fast charge transfer reactions in both phases, according to the high K^0 values obtained. Thus, the charge transfer resistance at the electrode surface will be low in both catholyte and anolyte anticipating good energy efficiency and power performance in a battery configuration.

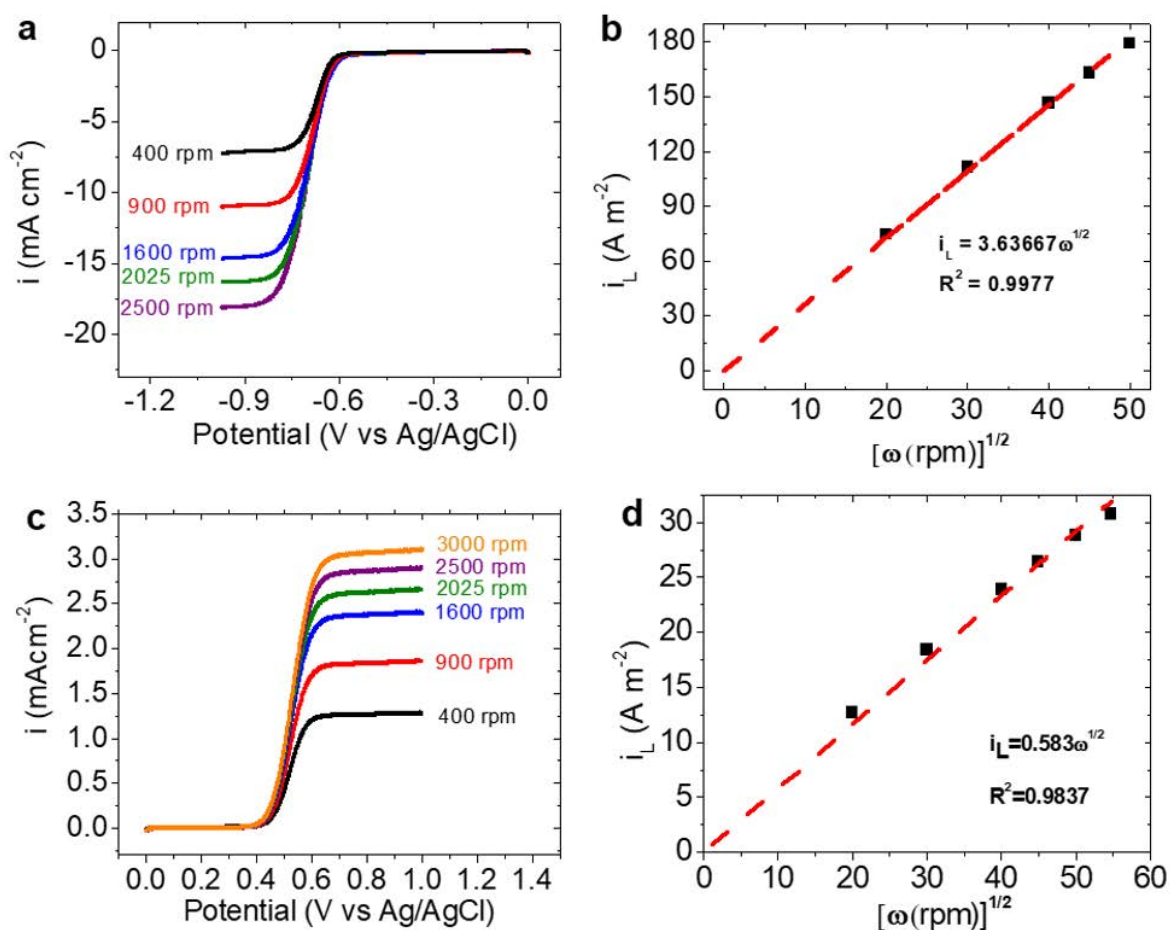


Figure 5.10. Rotating Disk Electrode Experiments. a), b) Linear Sweep Voltammetry (LSV) and Levich plot at $10 \text{ mV}\cdot\text{s}^{-1}$ of 5 mM MV in bottom phase. c), d) LSV and Levich plot at $10 \text{ mV}\cdot\text{s}^{-1}$ of 5 mM TEMPO in top phase.

5. Membrane-Free Redox Flow Batteries based on Aqueous Biphasic Systems

The reliability of ABS application as a Membrane-Free RFB was demonstrated by assembling a full battery just by introducing one carbon felt electrode in each phase. In order to test this new concept of battery in practical conditions, the concentration of active species in the initial mixture was as high as 0.1 M for both TEMPO and MV. The demonstration of the cell was conducted in a static cell in which the same volume of the two phases was added. As illustrated in Figure 5.11a, the top-phase (TEMPO-rich) constitutes the catholyte and the bottom phase (MV-rich) corresponds to the anolyte of this Membrane-Free Battery. It should be mentioned that this system offers several economic, environmental and safety advantages: i) PEG-based ABS are nontoxic and non-flammable with all components being inexpensive and commercially available in bulk quantities; ii) the two immiscible electrolytes are based on non-corrosive, neutral-pH aqueous solutions; iii) the active species are tunable and commercially available organic molecules; iv) the battery operates without any separator which reduces significantly the battery cost.

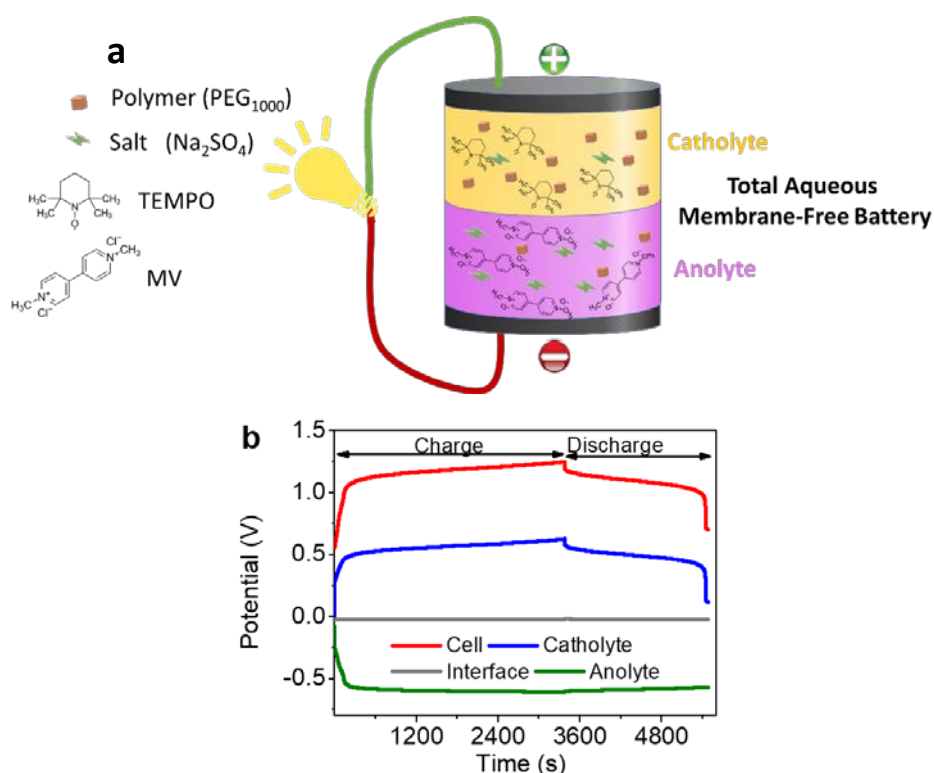


Figure 5.11. a) Schematic illustration of the Total Aqueous Membrane-Free Battery, b) Galvanostatic charge-discharge of the battery (20 %SOC) and individual potential profiles of each electrolyte and the interface; charge at C/4 and discharge at C/5.

Figure 5.11b shows the voltage profile of the full battery, as well as the potential profiles of the individual electrolytes and the interface. The battery voltage exhibits

clear and very stable plateaus during charging and discharging at 1.15 V and 1.05 V, respectively, which are very close to the theoretical voltage calculated from the CV (1.23 V, Figure 5.9). The individual profiles of the catholyte and anolyte display very small overpotentials and flat and constant plateaus at 0.5 V for the catholyte and -0.6 V for the anolyte, being in good agreement with CV experiments. The overpotential of the catholyte is higher than for the anolyte probably due to the lower conductivity and diffusion coefficient of the active species in this phase. It should be noticed that the interface overpotential is negligible establishing a clear advantage of this Membrane-Free configuration compared to conventional RFB in which the membrane overpotential contributes significantly to enhance the battery resistance. In fact, the overall resistance of this Membrane-Free RFB is very small which can enhance greatly the voltage efficiency in comparison with conventional RFB.

5.2.3.1 Polarization Experiments

Figure 5.12 show the polarization curve of the battery and the evolution of the individual potentials of the two electrolytes and the interface at 20 % of state of charge (SOC). As can be seen in Figure 5.12, the catholyte suffers from higher polarization than the anolyte during the experiment. As mentioned before, this behavior is due to the lower conductivity and diffusion coefficient shown by the catholyte, which is caused by the higher content of polymer in this phase. The influence of the polymer-rich phase in the battery performance is stronger in charge because of the higher restricted diffusion of the active species to the electrode surface during charging. As mentioned before, the interface barely shows polarization, which is a good advantage in comparison to the conventional batteries in which the membrane increases greatly the overall internal resistance of the battery. The polarization response demonstrates a maximum power density output of $23 \text{ mW}\cdot\text{cm}^{-2}$ at $30 \text{ mA}\cdot\text{cm}^{-2}$ (Figure 5.12a, orange trace). It is worth to remark that this value of power density is more than 12 times higher than the pioneering example of Membrane-Free RFB described in Chapter 4. This significant increase can be attributed to the replacement

of the ionic liquid anolyte which exhibited low conductivity and high viscosity by an aqueous electrolyte.

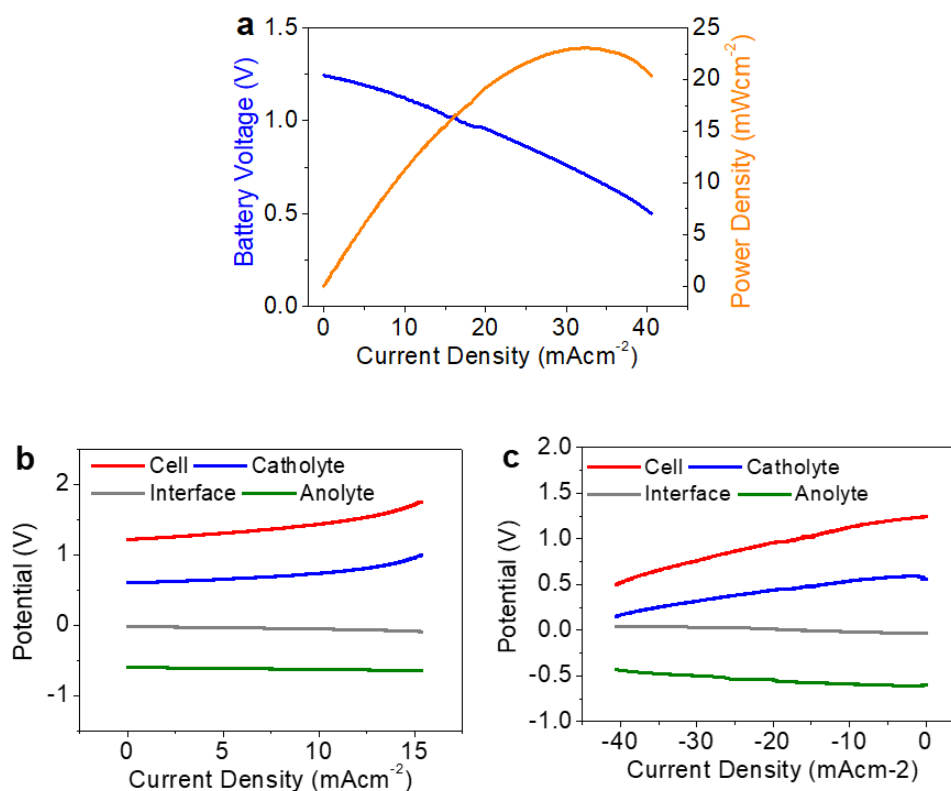


Figure 5.12. a) Polarization curve of the battery (20 %SOC) during discharge. b) Polarization curves including catholyte, anolyte and interface potential profiles during charge and c) discharge polarization.

5.2.3.2 Charge-Discharge Experiments

Figure 5.13a shows the discharge profiles of the battery at different C-rates. It should be noticed that considering that the theoretical voltage is 1.23 V, the discharge profile exhibits an ohmic drop as small as 40 mV at C/7 and it increases only up to 330 mV when high current density (2C) is applied. As expected in any type of battery, increasing the current density causes a drop in the discharge voltage motivated by a higher overpotential as a consequence of the diffusion limitations. It is important to remark that even at moderate to high C-rates the battery shows a voltage close to 1 V.

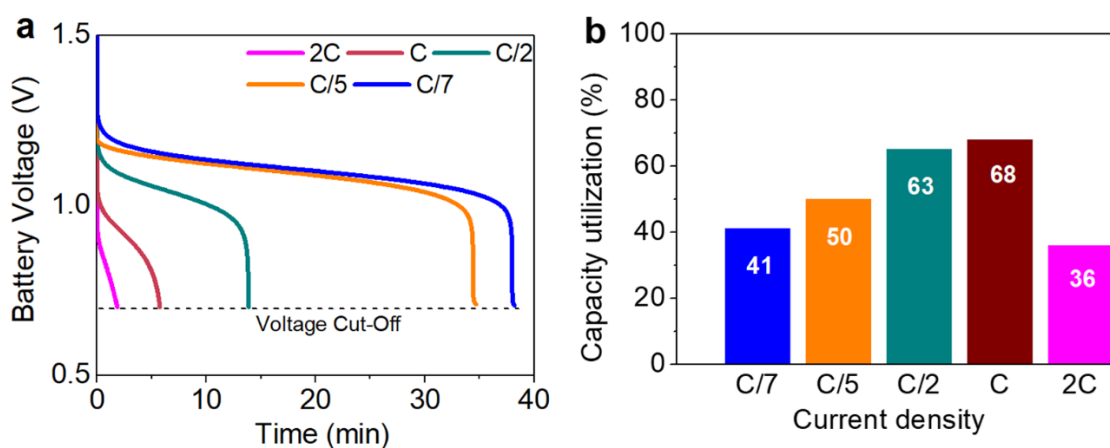
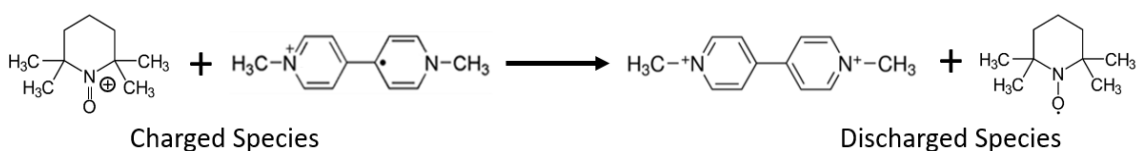


Figure 5.13. a) Discharge battery voltage profile at different current densities (20 %SOC). b) Capacity test at different current densities (20 %SOC).

Figure 5.13b shows the percentage of capacity utilization, defined as the ratio between the discharge capacity and the theoretical capacity at specific SOC, at different discharge rates. The highest capacity utilization is attained at 1C with a discharge capacity close to the 70 % of the theoretical one. Contrarily to typical battery behavior, decreasing the current density leads to lower capacity. This non-conventional trend might be attributed to the self-discharge phenomenon that in this system is due to the direct chemical reaction leading to a direct electron exchange at the interface (see Figure 5.14 and Scheme 5.1). This interesting phenomenon that is inherent to the Membrane-Free configuration is also very important for microfluidic membrane-less batteries but, to the best of our knowledge, it has not been investigated in detail.

5.2.3.3 Self-discharge Phenomenon



Scheme 5.1. Self-discharge reaction mechanism.

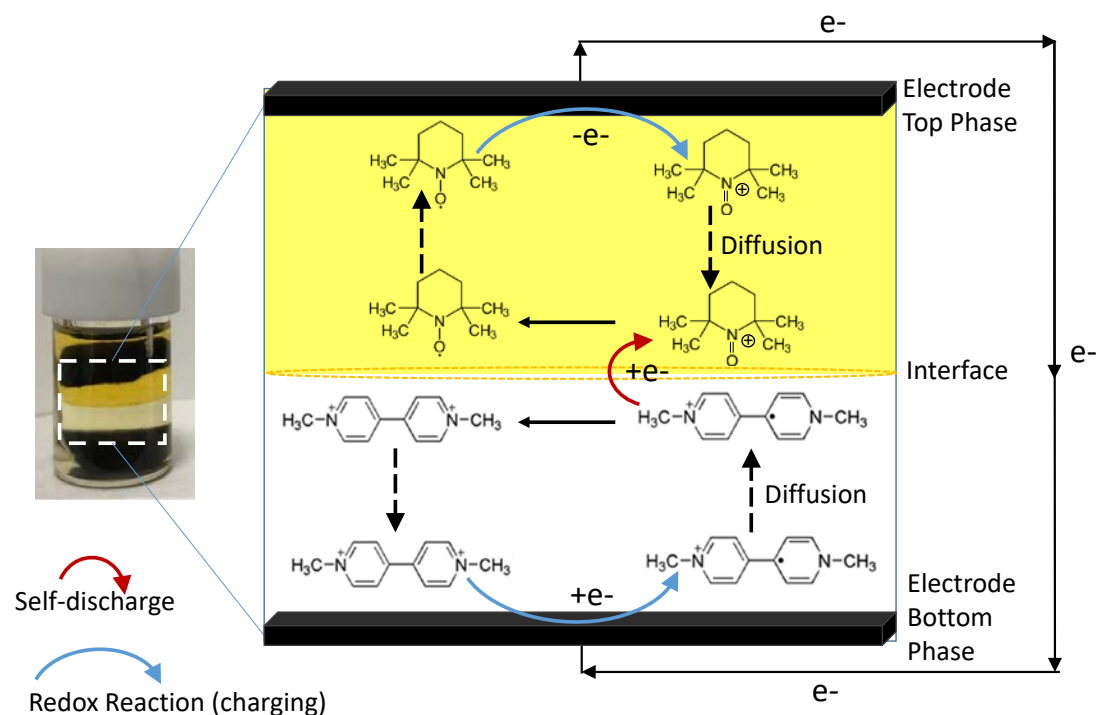


Figure 5.14. Schematic illustration of the self-discharge process

Although a thorough investigation is out of the scope of this thesis, the self-discharge was analyzed by monitoring the evolution of the battery open circuit voltage (OCV) over time (starting at 20% SOC). Figure 5.15 shows that the initial OCV coincides with the theoretically calculated but it slowly decreases during the experiment (at $1 \text{ mV}\cdot\text{min}^{-1}$, calculated from the lineal part of the curve). In fact, after 260 min, the battery was fully discharged due to the abovementioned self-discharge process. This means that during this time, the generated species during the charge (TEMPO $^+$ and MV $^+$ (in top and bottom phase, respectively) have met each other at the interface and have undergone an electron exchange. Thus, the charge stored during the charging process has been “consumed” in this recombination and it is not available in the battery anymore.

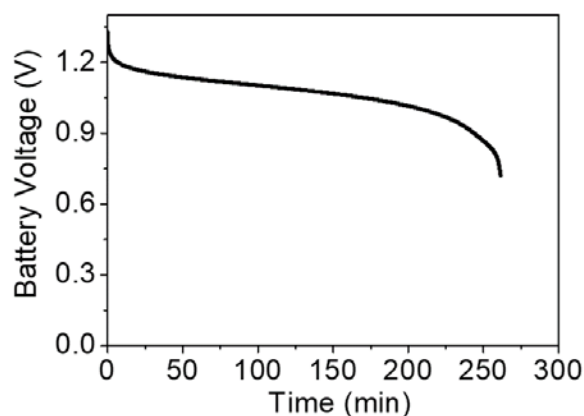


Figure 5.15. Self-discharge experiment (starting at 20 %SOC) consisting of monitoring the evolution of the OCV of the battery over time.

As evidenced by the experiments performed at different current densities (Figure 5.13), the loss of capacity due to the self-discharge is more relevant in experiments performed at C-rates lower than 1C, since the effective residence time (time needed to discharge completely) is longer. This was demonstrated through experiments in which the discharge current was decreased right after having discharged the battery completely at a certain C-rate. Figure 5.16a shows that if the initial discharge was performed at low currents (<1 C), the battery was not able to deliver additional capacity in the subsequent discharge at lower currents. This indicates that there are not active species available in the electrolyte, probably due to the direct electron exchange occurring at the interface.

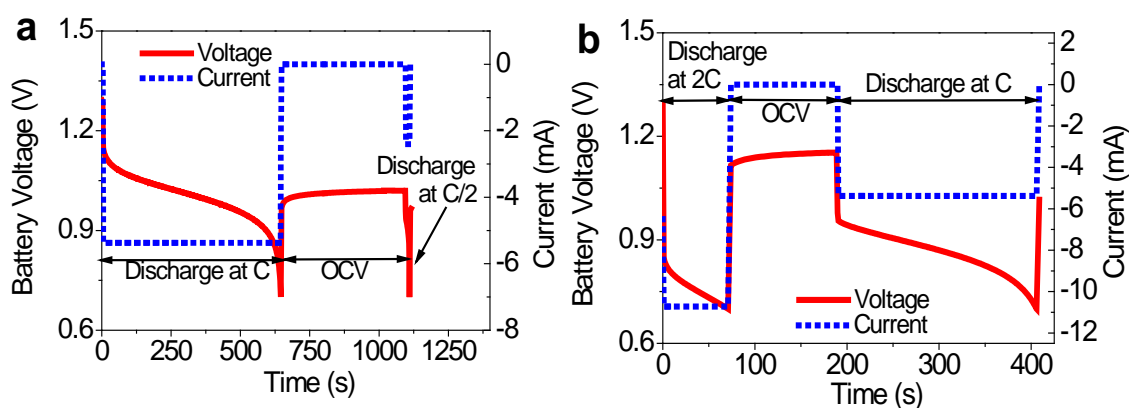


Figure 5.16. Discharge battery voltage (20% SOC): a) Consecutive discharge experiments at C and C/2; b) Consecutive discharge experiments at 2C and C.

On the contrary, if the battery is initially discharged at 2C, in the subsequent discharge at 1C, additional capacity is delivered denoting that there are still active species available in the electrolyte (see Figure 5.16b). Therefore, it was demonstrated that the self-discharge becomes irrelevant (contributes < 2 % to the discharge) when the effective residence time is short as occurs at 2C where the low capacity utilization (36 %) is exclusively attributed to diffusion limitations as in any other battery technology.

According to these results, the self-discharge depends on the residence time of the active species within the cell and thus becomes more relevant in a static configuration (where the residence time is infinite). Therefore, the residence time of the active species and consequently the self-discharge might be minimized in a flow configuration.

5.2.3.4 *Cycling Experiments*

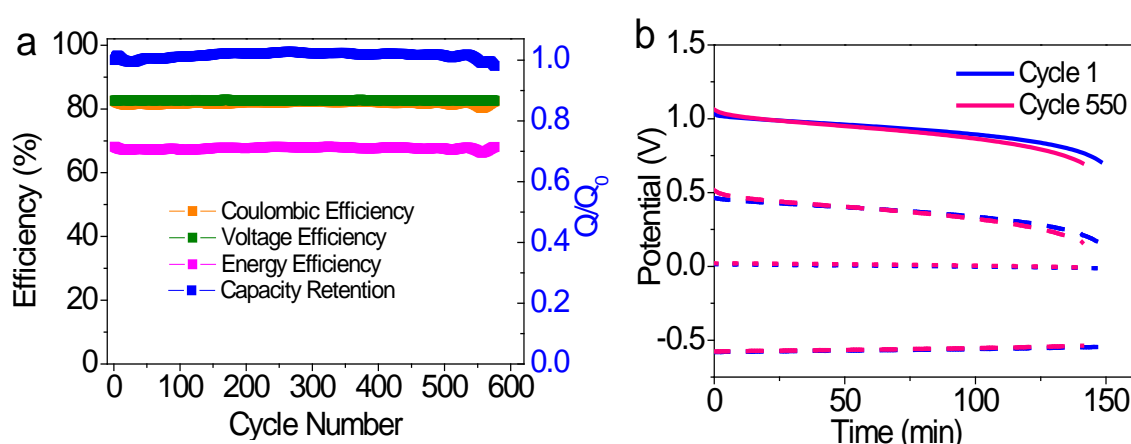


Figure 5.17. Cyclability test of the battery (5 %SOC), charging at C/2 and discharging at C. a) Efficiency and capacity retention vs cycle number. b) Individual potential profiles during cycling.

An extended charge-discharge experiment was performed to analyze the long-term battery behavior over 550 cycles. The evaluation of the capacity retention over cycles (Figure 5.17a) highlights the stable cycling performance of the battery. After 550 cycles the battery exhibited more than 99.99 % capacity retention per cycle. The trend of coulombic, voltage and energy efficiencies are displayed in Figure 5.17a. The coulombic efficiency remains constant around 82 % over the cycling test as well as the voltage efficiency which is one of the highest reported^{27,33–37}, and ascribed to the fast kinetics and remarkable low overpotentials exhibited by the battery. On account of

this, the averaged energy efficiency of the battery is 67 % which is comparable and even higher than the one obtained in conventional neutral aqueous RFB^{33–35}. The stability was also confirmed by the potential profiles of the individual electrolytes and the interface which remain stable over cycling (Figure 5.17b). Likely, the excellent long-term stability of the battery is credited due to the absence of crossover during the battery operation. As mentioned before, the crossover/cross-contamination of the active species in this battery concept was appraised by the determined partition coefficients. Once the equilibrium is established, there is no significant diffusive migration of the active species between the phases through the interface. Thus, the study of partition affinity offers the possibility to control the composition and to avoid the crossover during operation, which guarantees a stable and reliable cycling battery performance.

5.3 Conclusions

The concept of Membrane-Free RFB, applied to aqueous/non-aqueous system in chapter 4, was expanded here to biphasic systems in which the two phases are aqueous. This brings some advantages in terms of price, environmental issues and battery performance. The feasibility of aqueous biphasic systems (ABS) as immiscible redox electrolytes for a Membrane-Free RFB, was demonstrated in this chapter. The selective partition of two different redox molecules between the phases is crucial for the effective performance of the electrochemical device. Thus, the effect of the composition of the ABS on the partition coefficient of 5 organic redox molecules from different families has been tested. An increase in the hydrophobicity of the components used enhanced the partition of the redox molecules, allowing for achieving high partition coefficients and selectivity (>100). In addition, the electrochemical behavior of 7 systems based on Na₂SO₄ was evaluated. Through this study of the partitioning and electrochemical behavior TEMPO and MV were found to be the most suitable species for the catholyte (top phase) and anolyte (bottom phase), respectively. Among the different systems, those containing [N₄₄₄₄][CF₃CO₂], [C₄mim][CF₃SO₃], [P₄₄₄₁₄]Cl and PEG₁₀₀₀ fulfill all the thermodynamic and electrochemical requirements to be transformed in Membrane-Free RFBs. In addition, some of the theoretical battery voltages obtained are higher than those reported in aqueous ORFBs.

Considering the results obtained, the ABS based on PEG₁₀₀₀ was selected to become a Total Aqueous Membrane-Free RFB, containing MV and TEMPO as active species. Besides the complete removal of the membrane, the developed battery offers additional advantages since the electrolytes employed are based on non-corrosive, non-flammable and sustainable neutral-pH aqueous solutions of abundant redox-active organic molecules. Moreover, the system based on PEG₁₀₀₀ has several advantages respect to those based on ILs such as environmental-friendly properties, this polymer is used in daily common products, has low cost and is produced at large scale. Analyzing the battery behavior, the composition of the phases of this system demonstrated to have a significant influence on the battery performance since the polymer-rich phase (acting as the catholyte) showed lower conductivity and smaller

diffusion coefficient. However, both electrolytes, as well as the interface, displayed low overpotentials during the charge-discharge tests, favorably comparing with conventional RFB where the membrane contributes greatly to increase the internal resistance.

The open circuit voltage of the battery coincides with the theoretical one (1.23 V) and the capacity utilization was as high as 68 % at high current density (20 % SOC). The maximum power density was as high as $23 \text{ mW}\cdot\text{cm}^{-2}$ at $30 \text{ mA}\cdot\text{cm}^{-2}$, being more than 12 times higher than our pioneering example of Membrane-Free Battery described in chapter 4. In addition, the battery showed an excellent long-term cycling with a capacity retention 99.9 % over 550 cycles and an exceptional round-trip efficiency (70 %). This excellent long-term performance of the battery confirms the thermodynamic study of the partition of the active species as a good strategy to avoid the crossover during battery operation. These results highlight the potential of the Membrane-Free RFB based on ABS as a new energy storage technology by overcoming some technical hurdles of the conventional RFB related to membrane issues, corrosive electrolytes or expensive and limited metallic reactants.

As an inherent aspect of Membrane-Free RFB technology, we anticipated that the self-discharge phenomena is one of the most important challenges that this new technology should address in near future. Some aspects such as cell design, operation conditions and fluidodynamics, and their effect on the battery performance, including self-discharge processes, should be investigated as part of the future work in this field.

5.4 Experimental

5.4.1 Reagents.

The following chemicals were used in the determination of the phase diagrams and partition coefficients: 1-butyl-3-methylimidazolium dicyanamide ($[\text{C}_4\text{mim}][\text{N}(\text{CN})_2]$) 98%, 1-butyl-3-methylimidazolium triflate ($[\text{C}_4\text{mim}][\text{CF}_3\text{SO}_3]$) 99%, and tributyltetradecylphosphonium chloride ($[\text{P}_{44414}]\text{Cl}$) >95% were supplied by Iolitec, Tetrabutylammonium bromide ($[\text{N}_{4444}]\text{Br}$) 98% was obtained from Fluka. Poly(ethylene glycol) MW average 950-1050 (PEG_{1000}) was purchased from Sigma Aldrich. Tetrabutylphosphonium bromide ($[\text{P}_{4444}]\text{Br}$) Cyphos IL163 were supplied by Cytec Industries Inc.

In addition to commercial ILs, the IL tetrabutylphosphonium trifluoroacetate ($[\text{P}_{4444}][\text{CF}_3\text{CO}_2]$) was also investigated and synthesized by us. The reagents used in the synthesis of this IL were a tetrabutylphosphonium hydroxide ($[\text{P}_{4444}]\text{OH}$) solution (40 wt% in water), purchased from Sigma Aldrich, and Trifluoroacetic acid (TFA acid) 99% supplied by Acros Organics. The synthesis procedure involves three steps. Firstly, an acid-base reaction was carried out between $[\text{P}_{4444}]\text{OH}$ and TFA acid at 60 °C for 2 h. Then, to remove the solvent excess, the sample was subjected to evaporation on a rotary evaporator under vacuum. Finally, the obtained IL was dried at 50 °C under vacuum (0.1 Pa) during 72 h. The purity of the IL was then checked by ^1H , ^{13}C , ^{31}P and ^{19}F NMR spectra and found to be >99 wt%.

The inorganic salt sodium sulfate anhydrous (Na_2SO_4) ACS reagent $\geq 99\%$ was purchased from Sigma Aldrich. The organic molecules 2,2,6,6-tetramethyl-1-piperidinyloxy (TEMPO) 98%, anthraquinone 2-sulfonic acid sodium salt monohydrate 97% (AQ2S), quinoxaline (QUI) 99%, methyl viologen dichloride hydrate 98% (MV), and hydroquinone (H_2Q) reagent plus >99% were supplied by Sigma Aldrich and used as received.

5.4.2 ABS Phase diagrams

In this work, novel ternary systems composed of $\text{Na}_2\text{SO}_4 + \text{H}_2\text{O}$ and the following ionic liquids: $[\text{N}_{4444}]\text{Br}$, $[\text{P}_{4444}]\text{Br}$, $[\text{P}_{4444}][\text{CF}_3\text{CO}_2]$, PEG_{1000} and $[\text{P}_{44414}]\text{Cl}$, were determined at $25\text{ }^\circ\text{C}$ ($\pm 1\text{ }^\circ\text{C}$). The remaining phase diagrams were taken from the literature^{15,38,39}. All phase diagrams were determined at $25\text{ }^\circ\text{C}$ and atmospheric pressure using the cloud point titration method^{40,41}. A salt aqueous solution ($\approx 25\text{ wt}\%$ for Na_2SO_4) and aqueous solutions of the different hydrophilic ILs/polymer (ranging from 60-80 wt%) were prepared. Then, repetitive drop-wise addition of the salt solution was added to the IL solution until a cloud solution was detected (biphasic solution), followed by the addition of ultrapure water until a limpud monophasic solution was attained. This procedure was performed under constant stirring. The composition of the ternary systems was determined by weight quantification ($\pm 10^{-4}\text{ g}$) of all components. All phase diagrams were correlated using equation (5.1), proposed by Merchuk et al.²¹.

$$[\text{IL or Polymer}] = A \exp[(B[\text{Salt}]^{0.5}) - (C[\text{Salt}]^3)] \quad (5.1)$$

where $[\text{IL or Polymer}]$ and $[\text{Salt}]$ are the IL or polymer and salt weight percentages (wt%), respectively, and A , B and C are parameters obtained by regression of the experimental data.

For the determination of the tie-line, a ternary mixture composed of PEG_{1000} , Na_2SO_4 and H_2O (25, 6, 69 wt%, respectively) was gravimetrically prepared. After the complete separation of the phases, each phase was individually weighted. Then the TL was calculated by the resolution of the following 4 equation system (eqs. 5.2-5.5)²¹. The compositions of the top and bottom phase are determined by the lever-arm rule.

$$[\text{Polymer}]_T = A \exp[(B \times [\text{Salt}]_T^{0.5}) - (C \times [\text{Salt}]_T^3)] \quad (5.2)$$

$$[\text{Polymer}]_B = A \exp[(B \times [\text{Salt}]_B^{0.5}) - (C \times [\text{Salt}]_B^3)] \quad (5.3)$$

$$[\text{Polymer}]_T = \frac{[\text{Polymer}]_M}{\alpha} - \frac{1-\alpha}{\alpha} \times [\text{Polymer}]_B \quad (5.4)$$

$$[\text{Salt}]_T = \frac{[\text{Salt}]_M}{\alpha} - \frac{1-\alpha}{\alpha} \times [\text{Salt}]_B \quad (5.5)$$

where T , B , and M designate the top phase, the bottom phase and the initial mixture, respectively. $[\text{Polymer}]$ and $[\text{Salt}]$ are PEG₁₀₀₀ and Na₂SO₄ weight fraction. The parameter α is the ratio between the top phase weight and the total mixture weight.

The solution of the referred system gives the concentration of IL/polymer and inorganic salt in the top and bottom phases.

The tie-line length (TLL) denotes the distance, i.e., the difference in composition between the top phase and the bottom phase and was calculated according to equation (5.6):

$$TLL = \sqrt{([\text{Salt}]_T - [\text{Salt}]_B)^2 + ([\text{IL}]_T - [\text{IL}]_B)^2} \quad (5.6)$$

5.4.3 Partition coefficients determination

The partition coefficient (K) represents the equilibrium distribution ratio of the target molecule between the top and the bottom phase and is defined by equation (5.7).

$$K = \frac{[\text{target molecule}]_{\text{Top Phase}}}{[\text{target molecule}]_{\text{Bottom Phase}}} \quad (5.7)$$

In order to determine the partition coefficients of each organic molecule, ternary mixtures were prepared in the biphasic region with the following composition Na₂SO₄ salt (10 wt%) + IL (35 wt%) + aqueous solution containing 20 mM of the target molecule (55 wt%). In the case of the system based on polymer the initial mixture had this composition: salt (6 wt%) + polymer (25 wt%) + aqueous solution containing 20 mM of the target molecule (69 wt%). Then, the systems were allowed to equilibrate for at least 12h. After that, each phase was carefully separated and subjected to UV analysis (using a synergy/HTX microplate reader at a wavelength of 240 nm for TEMPO, 314 nm for QUI, 329 nm for AQ2S, 258 nm for MV and 290 nm for H₂Q) for further calculation of each molecule concentration, using calibration curves previously established (Figure 5.18).

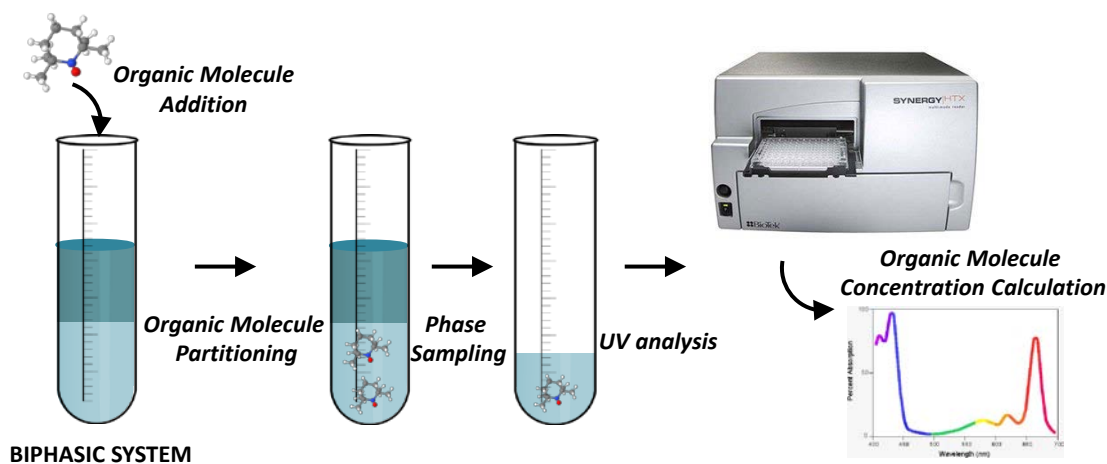


Figure 5.18. Schematic representation of partition coefficient determination method

5.4.4 Preparation of Redox-active ABS

Redox-active ABS is defined as a biphasic system containing two redox active molecules, each of them dissolved selectively in one of the phases to form the catholyte and anolyte of a battery. Redox-active ABS composed of Na_2SO_4 , IL, and water (10, 35 and 55 wt%, respectively) and Na_2SO_4 , PEG₁₀₀₀, and water (6, 25 and 69 wt%, respectively) were prepared adding two redox molecules with suitable partition coefficients at 20 mM concentration each. Once the equilibrium between the two phases was established, their electrochemical properties as redox electrolytes were evaluated separately by means of electrochemical methods.

5.4.5 Electrochemical characterization

Electrochemical characterization of the electrolytes. The CV experiments were conducted in a Biologic VMP multichannel potentiostat at $10 \text{ mV}\cdot\text{s}^{-1}$ and room temperature using as reference electrode Ag/AgCl and a Pt mesh as counter electrode. Ionic conductivity of the phases of the ABS was measured with Conducell 4UxF Arc sensor from Hamilton Bonaduz AG.

Rotating-disk electrode (RDE) experiments were performed using a BASi RDE-2 rotating-disk electrode system. All tests were obtained using a three-electrode cell with a glassy carbon rotating electrode (ALS Co., Ltd). Counter and reference

electrodes were the same as those for the three-electrode CV test. Linear Sweep Voltammetry measurements were conducted at a scan rate of $10 \text{ mV}\cdot\text{s}^{-1}$ over a range of rotation rates (400 rpm to 3000 rpm). Before and during testing, the electrolytes were purged with ultra-high purity Argon to ensure adequate deaeration. Diffusion coefficients (D) and heterogeneous rate constants (k^0) were calculated using the Koutecky-Levich equation (5.8).

$$\frac{1}{i} = \frac{1}{i_K} + \frac{1}{i_l} \quad (5.8)$$

Where: $i_l = 0.62 e^- F A D^{2/3} \omega^{1/2} \nu^{-1/6} C_n$; and $i_K = e^- F A K^0 C_n$

and e^- is the number of electrons transferred, F the Faraday constant, A the disc area, D the diffusion coefficient, ν the kinematic viscosity, C_n the electroactive species concentration and k^0 the heterogeneous rate constant. A Levich plot was constructed from the RDE data by plotting the mass-transport limited current vs. the square root of the rotation rate.

Assembly and Electrochemical characterization of the battery. The battery was built in a glass cell by adding the same volume of each phase of the ABS (3.5 mL) and introducing one carbon felt electrode (SGL CARBON GmbH) in each one. Carbon felts (grade GFD 4.6 EA, 4.6 mm thickness) purchased from SGL CARBON GmbH were used as electrode material. In order to make them hydrophilic they were cut with rectangular shape (geometric surface area $\sim 1.5 \text{ cm}^2$) and merged in 1 M NaOH solution at $80 \text{ }^\circ\text{C}$ during 1 h. Then they were washed up to pH=7 with ultrapure water and dried at $100 \text{ }^\circ\text{C}$ overnight. The cell was galvanostatically charge-discharged on a Biologic VMP multichannel potentiostat with voltage safety limits of 1.5 and 0.7 V at current densities from C/7 to 2C. The polarization curve was obtained in a current density range of -40 to $15 \text{ mA}\cdot\text{cm}^{-2}$ and voltage limits of 1.7 V and 0.5 V.

The capacity of the battery (Q_t) was calculated by eq (5.9), where n is the amount of active species (mol), e^- is the number of electron exchanged and F is the Faraday constant ($96485 \text{ A}\cdot\text{s}\cdot\text{mol}^{-1}$).

$$Q_t = n e^- F \quad (5.9)$$

5. Membrane-Free Redox Flow Batteries based on Aqueous Biphasic Systems

Capacity utilization (%) is defined as the ratio between the discharge capacity and the theoretical capacity at one specific state of charge. It was calculated by eq (5.10), where SOC refers to battery state of charge and Q is the discharge capacity delivered by the battery.

$$\text{Capacity utilization (\%)} = \frac{Q}{Q_{t.SOC}} \cdot 100 \quad (5.10)$$

5.5 References

- 1 S. Bamberger, E. D. Brooks, K. A. Sharp, J. M. V. Alstine and T. J. Webber, *Partitioning in Aqueous Two-Phase Systems Theory, Methods, Uses and Applications to Biotechnology*, Academic Press, INC, London, 1985.
- 2 B. Y. Zaslavsky, *Aqueous Two-Phase Partitioning Physical Chemistry and Bioanalytical Applications*, Marcel Dekker, INC, New York, 1995.
- 3 M. G. Freire, A. F. M. Cláudio, J. M. M. Araújo, J. a. P. Coutinho, I. M. Marrucho, J. N. C. Lopes and L. P. N. Rebelo, *Chem. Soc. Rev.*, 2012, **41**, 4966.
- 4 M. G. Freire, Ed., *Ionic-Liquid- Based Aqueous Biphasic Systems Fundamentals and Applications*, Springer Berlin Heidelberg, Green Chem., 2016.
- 5 E. V. Capela, M. V. Quental, P. Domingues, J. A. P. Coutinho and M. G. Freire, *Green Chem.*, 2017, **19**, 1850–1854.
- 6 S. P. M. Ventura, F. A. e Silva, M. V. Quental, D. Mondal, M. G. Freire and J. A. P. Coutinho, *Chem. Rev.*, 2017, **117**, 6984–7052.
- 7 D. Mondal, M. Sharma, M. V. Quental, A. P. M. Tavares, K. Prasad and M. G. . Freire, *Green Chem.*, 2016, **18**, 6071–6081.
- 8 M. V. Quental, M. Caban, M. M. Pereira, P. Stepnowski, J. A. P. Coutinho and M. G. Freire, *Biotechnol. J.*, 2015, **10**, 1457–1466.
- 9 D. Depuydt, W. Dehaen and K. Binnemans, *Ind. Eng. Chem. Res.*, 2015, **54**, 8988
- 10 K. Ghosh, M. Maiti, S. Lahiri and V. Afzal Hussain, *J. Radioanal. Nucl. Chem.*, 2014, **302**, 925–930.
- 11 B. Onghena, T. Opsomer and K. Binnemans, *Chem. Commun.*, 2015, **51**, 15932–15935.
- 12 H. F. D. Almeida, I. M. Marrucho and M. G. Freire, *ACS Sustain. Chem. Eng.*, 2017, **5**, 2428–2436.
- 13 H. F. Almeida, M. G. Freire and I. M. Marrucho, *Green Chem.*, 2017, **19**, 4651–4659.
- 14 J. F. B. Pereira, L. P. N. Rebelo, R. D. Rogers, J. A. P. Coutinho and M. G. Freire, *Phys. Chem. Chem. Phys.*, 2013, **15**, 19580.
- 15 H. Passos, University of Aveiro, 2017.
- 16 M. G. Freire, C. L. S. Louros, L. P. N. Rebelo and J. A. P. Coutinho, *Green Chem.*, 2011, **13**, 1536.
- 17 M. Domínguez-Pérez, L. I. N. Tomé, M. G. Freire, I. M. Marrucho, O. Cabeza and J. A. P. Coutinho, *Sep. Purif. Technol.*, 2010, **72**, 85–91.
- 18 A. F. M. Cláudio, A. M. Ferreira, S. Shahriari, M. G. Freire and J. A. P. Coutinho, *J. Phys. Chem. B*, 2011, **115**, 11145–11153.
- 19 A. F. M. Cláudio, L. Swift, J. P. Hallett, T. Welton and M. G. Coutinho, João A. P. Freire, *Phys. Chem. Chem. Phys.*, 2014, **16**, 6593–6601.
- 20 K. A. Kurnia, F. Lima, A. F. M. Cláudio, J. A. P. Coutinho and M. G. Freire, *Phys.*

- Chem. Chem. Phys.*, 2015, **17**, 18980–18990.
- 21 J. C. Merchuk, B. A. Andrews and J. A. Asenjo, *J. Chromatogr. B Biomed. Sci. Appl.*, 1998, **711**, 285–293.
- 22 L. I. N. Tomé, F. R. Varanda, M. G. Freire, I. M. Marrucho and J. A. P. Coutinho, *J. Phys. Chem. B*, 2009, **113**, 2815–2825.
- 23 S. P. M. Ventura, M. G. Freire, M. G. Freire, I. M. Marrucho and I. M. Marrucho, *J. Phys. Chem. B*, 2009, **113**, 5194–5199.
- 24 S. P. M. Ventura, S. G. Sousa, L. S. Serafim, A. S. Lima, M. G. Freire and J. A. P. Coutinho, *J. Chem. Eng. Data*, 2012, **57**, 507–512.
- 25 R. S. of Chemistry, <http://www.chemspider.com>.
- 26 T. Janoschka, N. Martin, M. D. Hager and U. S. Schubert, *Angew. Chemie - Int. Ed.*, 2016, **55**, 14427–14430.
- 27 T. Liu, X. Wei, Z. Nie, V. Sprenkle and W. Wang, *Adv. Energy Mater.*, 2016, **6**, 1501449.
- 28 C. L. Bird and a. T. Kuhn, *Chem. Soc. Rev.*, 1981, **10**, 49–82.
- 29 B. Yang, L. Hooper-Burkhardt, F. Wang, G. K. Surya Prakash and S. R. Narayanan, *J. Electrochem. Soc.*, 2014, **161**, A1371–A1380.
- 30 K. Lin, Q. Chen, M. R. Gerhardt, L. Tong, S. B. Kim, L. Eisenach, A. W. Valle, D. Hardee, R. G. Gordon, M. J. Aziz and M. P. Marshak, *Science (80-.)*, 2015, **349**, 1529–1532.
- 31 B. Huskinson, M. P. Marshak, C. Suh, S. Er, M. R. Gerhardt, C. J. Galvin, X. Chen, A. Aspuru-Guzik, R. G. Gordon and M. J. Aziz, *Nature*, 2014, **505**, 195–198.
- 32 B. Hu, C. Debruler, Z. Rhodes and T. Liu, *J. Am. Chem. Soc.*, 2016, **139**, 1207–1214.
- 33 T. Janoschka, N. Martin, M. D. Hager and U. S. Schubert, *Angew. Chemie - Int. Ed.*, 2016, **55**, 14427–14430.
- 34 B. Hu, C. DeBruler, Z. Rhodes and T. L. Liu, *J. Am. Chem. Soc.*, 2017, **139**, 1207–1214.
- 35 E. S. Beh, D. De Porcellinis, R. L. Gracia, K. T. Xia, R. G. Gordon and M. J. Aziz, *ACS Energy Lett.*, 2017, **2**, 639–644.
- 36 J. Luo, B. Hu, C. Debruler and T. L. Liu, *Angew. Chemie Int. Ed.*, 2018, **57**, 231–235.
- 37 B. Hu, C. Seefeldt, C. DeBruler and T. L. Liu, *J. Mater. Chem. A*, 2017, **5**, 22137
- 38 T. E. Sintra, R. Cruz, S. P. M. Ventura and J. A. P. Coutinho, *J. Chem. Thermodyn.*, 2014, **77**, 206–213.
- 39 Y. Deng, J. Chen and D. Zhang, *J. Chem. Eng. Data*, 2007, **52**, 1332–1335.
- 40 C. M. S. S. Neves, S. P. M. Ventura, M. G. Freire, I. M. Marrucho and J. A. P. Coutinho, *J. Phys. Chem. B*, 2009, **113**, 5194–5199.
- 41 S. P. M. Ventura, C. M. S. S. Neves, M. G. Freire, I. M. Marrucho, J. Oliveira and J. A. P. Coutinho, *J. Phys. Chem. B*, 2009, **113**, 9304–9310.

Chapter 6. Final Conclusions and Recommendations

This doctoral thesis has studied deeply the development of new redox electrolytes and their application in different electrochemical energy storage devices. This work has demonstrated the successful application of redox electrolytes based on organic redox molecules in hybrid SCs and in a new concept of Membrane-Free Redox Flow Battery. In each chapter, specific conclusions have been included according to the discussed results. Thus, in this last chapter, general conclusions have been extracted for each technology:

Redox electrolytes in hybrid SCs

1) The performance of hybrid supercapacitors containing redox electrolytes based on organic redox molecules dissolved into an ionic liquid exhibit two energy-storage mechanisms: the double-layer formation characteristic of carbon-based SCs and the faradaic reactions characteristic of batteries. It has been evidenced that the pBQ redox molecules dissolved in the IL (PYR₁₄TFSI) electrolyte provide a significant enhancement in the electrochemical properties of hybrid SCs in terms of specific capacitance (C_s) and specific real energy (E_{real}). In addition, it has been demonstrated that the use of an ionic liquid, as electrolyte, improved the operating voltage of the device and thus the E_{real} .

2) The analysis of the influence of the textural properties of carbonaceous electrode material on the performance of hybrid supercapacitors evidenced that the faradaic contribution of the redox electrolyte depends on the type of carbon in the electrode. Specifically, the textural properties of the electrode material, particularly the porosity, have a relevant influence on the electrochemical performance of the hybrid SC, especially when a redox electrolyte is used. The beneficial effect of pBQ was found to remarkably increase the capacitance in carbons having open porosity with low to medium specific surface areas such as Vulcan. In the case of microporous carbonaceous materials such as Pica, the faradaic contribution of the redox electrolyte was shown to be less significant under high polarization. This behavior is possibly due to clogging and higher diffusion limitations in the predominant microporous structure of this type of carbonaceous material.

3) In-depth analysis using Electrochemical Impedance Spectroscopy demonstrated that the diffusion-related component of the resistance has a strong dependence on the bias voltage in the hybrid SCs, while other components of the total resistance remain almost constant. In addition, the results point out that the formation of the double layer and the redox processes occur at different frequencies and the performance of the SC is highly influenced by this difference. The capacitance tendency is not linear with the voltage for the devices with quinoid-electrolyte; a 7-fold increase in the value of the capacitance is obtained at 1.25 V bias voltage because of the different storage mechanisms. Additionally, an equivalent electrical circuit was proposed. It can be used to predict the behavior of SCs with this kind of non-conventional electrolytes.

Immiscible Redox Electrolytes and their Application in Membrane-Free Redox Flow Batteries

4) The feasibility of a new concept of Membrane-Free Redox Flow Battery which relies on immiscible redox electrolytes was demonstrated. The concept was firstly validated for one biphasic system in particular, based on aqueous-nonaqueous immiscible electrolytes. The electrochemical performance of this battery does not significantly differ from a conventional one since it maintains a stable discharge voltage profile, high capacity and good reversibility.

5) The versatility of this disruptive technology was validated, since it can be applied to other pairs of redox molecules and solvents, provided that the indispensable condition requiring a mutual immiscibility is met. Thus, different combinations of immiscible (aqueous/non-aqueous) redox electrolytes based on commercial available organic redox materials such as quinones, TEMPO and viologen derivatives and different supporting electrolytes based on ionic liquids, common organic solvents as propylene carbonate and aqueous solutions at different pHs were demonstrated in a Membrane-Free RFB configuration.

6) It was observed that the electrochemical behavior of the Membrane-Free RFB is strongly influenced by the composition of the electrolytes. Particularly, the dependence on the redox potential of the active species, their reversibility, their

electrochemical stability and their compatibility with the supporting electrolyte has found to be very significant and decisive.

7) It was revealed that Aqueous Biphasic Systems (ABS), which until now have been used in extraction/separation processes, are an efficient platform for developing Totally Aqueous Membrane-Free RFBs since they allow for controlling some important factors such as the partitioning of the active species and some physicochemical properties of the electrolytes/phases.

8) It has been demonstrated that the crossover at the interface between the electrolytes can be controlled through the determination of the partition coefficients of the active species in both phases.

9) The self-discharge by direct chemical reaction that leads to a direct electron exchange at the interface between the electrolytes has been revealed as an inherent aspect of this technology and will play a key role in future research lines.

Future Work and Recommendations

Redox Electrolytes for Hybrid SCs

As it has been analyzed in this thesis, one of the hurdles for the implementation of the hybrid SC is their moderate stability and cycle life that should be addressed in the future work. In this sense, one of the beneficial characteristics of this devices is that do not need highly concentrated electrolytes. Therefore, highly stable organic redox molecules might enhance the long-term performance of the SCs although, in low concentration. In this sense, the interface electrode/electrolyte must be deeply understood for controlling interfacial reactions, as well as electrolyte ion dynamics, solvation/desolvation and degradation mechanisms.

On the other hand the development of new organic redox molecules that can react in both electrodes (positive and negative one), having symmetric hybrid SC as well as those molecules that are able to undergo multiple electron exchange reactions should be considered and studied deeply, since these are strategies to enhance the performance of the hybrid SCs.

Immiscible Redox Electrolytes for Membrane Free Redox Flow Batteries

The study of the new Membrane-Free RFB concept has brought up new aspects that should be considered and further studied. Among these new factors, the partitioning of the active species between the immiscible electrolytes stands out as extremely relevant. Moreover, the effect of the supporting salt on the partition coefficients and its compatibility with the active species should be addressed.

Considering the performance demonstrated of the Membrane-Free RFB studied in this thesis, as an inherent aspect, the self-discharge phenomenon is one of the most important challenges that this new technology should address in near future. Thus, the study of the interface, its nature, the surface tension between the electrolytes and the ion exchanging passing through, can help to the development of this technology. In this sense, the study of triphasic systems in which a middle-liquid phase acts as liquid membrane can be an interesting topic.

Finally, since the Membrane-Free RFB presents new challenges compared to the conventional Redox Flow Battery technology, some aspects such as the position of the interface inside the cell, the area of the interface, the residence time of the electrolytes and their flowing regime that are factors closely related to the cell design and the operation conditions are going to have also an important effect on the self-discharge and of course, on the overall performance of the battery. Thus, the fluid dynamics of the immiscible electrolytes and new cell designs should be investigated and supported by the use of computational fluid dynamics (CFD) which can help in the simulation and modelling of the behavior of the components at certain scales and dimensions under different operational conditions. In addition, with the use of 3D printing, battery designs can be improved and fabricated easily which facilitates the scale-up process of a battery stack. Therefore, these tools could be implemented as part of the future work in this field.

Capítulo 6. Conclusiones Finales y Recomendaciones

En esta tesis doctoral se ha estudiado en profundidad el desarrollo de nuevos electrolitos redox y su aplicación en diferentes dispositivos de almacenamiento de energía electroquímica. Este trabajo ha demostrado la aplicación exitosa de electrolitos redox basados en moléculas redox orgánicas en SC híbridos y en un nuevo concepto de Batería de Flujo Redox Sin Membrana. En cada capítulo se han incluido conclusiones específicas de acuerdo a los resultados discutidos. Por ello, en este capítulo final, se han extraído las siguientes conclusiones generales para cada tecnología:

Electrolitos Redox en SC híbridos

1) El funcionamiento de supercondensadores híbridos con electrolitos redox basados en una molécula orgánica redox disuelta en un líquido iónico demostró dos mecanismos de almacenamiento de energía: la formación de doble capa característica de los SC basados en materiales carbonosos y las reacciones faradáicas características de las baterías. A través de la caracterización electroquímica de los SCs, se ha demostrado que las moléculas redox de pBQ disueltas en el electrolito líquido iónico proporcionan una mejora significativa en los SC híbridos en términos de capacitancia específica (C_s) y energía real específica (E_{real}). Además, se demostró que el uso de un líquido iónico como electrolito mejora el voltaje de operación y por consiguiente la E_{real} .

2) El análisis de la influencia de las propiedades texturales del material carbonoso del electrodo sobre el funcionamiento de supercondensadores híbridos evidenció que la contribución faradaica del electrolito redox depende del tipo de carbón usado en el electrodo. Específicamente las propiedades texturales del material del electrodo, particularmente la porosidad, tienen una influencia relevante en el comportamiento electroquímico del SC híbrido, especialmente cuando se usa un electrolito redox. Se descubrió que la presencia de pBQ aumenta notablemente la capacitancia en los carbones que tienen porosidad abierta con áreas superficiales específicas bajas-medias, tales como Vulcan. En el caso de materiales carbonosos microporosos como Pica, la contribución faradaica del electrolito redox se mostró menos significativa bajo alta polarización. Este comportamiento posiblemente se deba

a la obstrucción y a las mayores limitaciones de difusión en la estructura microporosa predominante en este tipo de material carbonoso.

3) Un análisis en profundidad utilizando espectroscopía de impedancia electroquímica demostró que el componente resistivo relacionado con la difusión tiene una fuerte dependencia del voltaje de polarización en los SC híbridos, mientras que otros componentes de la resistencia total permanecen prácticamente constantes. Por otro lado, los resultados indican que los procesos de formación de la doble capa y faradaicos ocurren a diferentes frecuencias y el funcionamiento de los SC híbridos está muy influenciado por esta diferencia. La tendencia de la capacitancia no es lineal con el voltaje de los dispositivos con electrolito quinónico; Se obtuvo un aumento de 7 veces el valor de la capacitancia a un voltaje de polarización de 1,25 V debido a los diferentes mecanismos de almacenamiento. Además, se propuso un circuito eléctrico equivalente que puede ser usado para predecir el comportamiento de SC con este tipo de electrolitos no convencionales.

Electrolitos Redox Inmiscibles y su Aplicación en Baterías de Flujo Redox Sin Membrana

4) La viabilidad de un nuevo concepto de Batería de Flujo Redox Sin Membrana, basada en electrolitos inmiscibles fue demostrada. El concepto se validó en primer lugar para un sistema bifásico en particular basado en electrolitos inmiscibles acuoso-no acuoso. El comportamiento electroquímico de esta batería no difiere significativamente de una convencional, ya que mantiene un perfil estable de voltaje de descarga, alta capacidad y buena reversibilidad.

5) La versatilidad de esta novedosa tecnología fue validada, ya que puede ser aplicada a otros pares de moléculas redox y disolventes, siempre que cumplan la condición indispensable de inmiscibilidad mutua. Así, diferentes combinaciones de electrolitos redox inmiscibles (acuoso-no acuoso) basados en materiales redox orgánicos disponibles comercialmente (quinonas, TEMPO y viológeno) y diferentes electrolitos soporte basados en líquidos iónicos, disolventes orgánicos comunes como carbonato de propileno y disoluciones acuosas con diferentes pH fueron demostrados en una configuración de Batería de Flujo Redox Sin Membrana.

6) Se observó que el comportamiento electroquímico de las Baterías de Flujo Redox Sin Membrana está fuertemente influenciado por la composición de los electrolitos, debido a su dependencia del potencial redox de las especies activas, su reversibilidad, su estabilidad electroquímica y su compatibilidad con el electrolito soporte, que ha demostrado ser muy significativa y determinante.

7) Se ha probado que los Sistemas Acuoso Bifásicos (SAB), que hasta ahora se han utilizado en los procesos de extracción / separación, son una herramienta eficiente para desarrollar Baterías de Flujo Redox Acuoso Sin Membrana ya que permiten controlar algunos factores importantes como la partición de las especies activas y algunas propiedades fisicoquímicas de los electrolitos/fases.

8) Se ha demostrado que el *crossover* a través de la interfase de los electrolitos puede ser controlado mediante la determinación de los coeficientes de reparto de las moléculas activas en las dos fases.

9) La autodescarga en la interfase entre los electrolitos mediante reacción química directa con intercambio de electrones entre las especies generadas ha sido revelado como un aspecto inherente de esta tecnología y jugará un papel clave en futuras líneas de investigación.

Trabajo Futuro y Recomendaciones

Electrolitos Redox para SCs Híbridos

Tal y como se ha analizado en esta tesis, uno de los obstáculos para la implementación de los SC híbridos es su todavía moderada estabilidad y ciclabilidad que deberían abordarse en el trabajo futuro. En este sentido, una de las características beneficiosas de estos dispositivos es que no necesitan electrolitos altamente concentrados. Así, moléculas redox orgánicas altamente estables podrían mejorar el rendimiento a largo plazo de los SCs aunque estén disueltas en baja concentración. En esta línea, la interfase electrodo/electrolito debe ser estudiada en profundidad para controlar las reacciones en la interfase, así como la dinámica de los iones del electrolito, los mecanismos de su solvatación/desolvatación y degradación.

Por otro lado, el desarrollo de nuevas moléculas orgánicas redox que puedan reaccionar en ambos electrodos (positivo y negativo), dando lugar a SC híbridos simétricos, así como aquellas moléculas que puedan experimentar reacciones de intercambio de múltiples electrones, deben ser consideradas y estudiadas profundamente, dado que son estrategias para mejorar el rendimiento de los SC híbridos.

Electrolitos Redox Inmiscibles para Baterías de Flujo Redox Sin Membrana

El estudio del nuevo concepto de Batería de Flujo Redox Sin Membrana ha planteado nuevos aspectos que deberían considerarse y estudiarse más a fondo. Entre estos nuevos factores, la partición de las especies activas entre los electrolitos inmiscibles destaca como altamente relevante. Además, debe abordarse el efecto de la sal soporte sobre los coeficientes de partición y su compatibilidad con las especies activas.

Teniendo en cuenta el comportamiento demostrado por las Baterías de Flujo Redox Sin Membrana estudiadas en esta tesis, como un aspecto inherente a este concepto, el fenómeno de autodescarga es uno de los desafíos más importantes que esta nueva tecnología debería abordar en un futuro próximo. Por lo tanto, el estudio de la interfase, su naturaleza, la tensión superficial entre los electrolitos y el intercambio de iones a través de la misma pueden ayudar al desarrollo de esta tecnología. En este sentido, el estudio de sistemas trifásicos en los que una fase líquida intermedia actúa como membrana líquida puede ser un tema interesante.

Finalmente, ya que el concepto de Batería de Flujo Redox Sin Membrana presenta nuevos retos comparado con la tecnología de las Baterías de Flujo Redox convencionales, algunos aspectos como la posición de la interfase dentro de la celda, el área de dicha interfase, el tiempo de residencia de los electrolitos y su régimen de flujo, que son factores estrechamente relacionados con el diseño de la celda y las condiciones de operación, van a tener también un efecto importante en la autodescarga y, por supuesto, en el rendimiento general de la batería. Por lo tanto, la fluidodinámica de los electrolitos inmiscibles y los nuevos diseños de celda deberían investigarse y apoyarse en el uso de fluidodinámica computacional (CFD en inglés), la cual puede ayudar en la simulación y modelado del comportamiento de los componentes en determinadas escalas y dimensiones bajo diferentes condiciones de operación. Además, con el uso de la impresión 3D, los diseños de batería pueden mejorarse y fabricarse fácilmente, lo que favorece el proceso de escalado de un *stack* de batería. Por ello, estas herramientas podrían ser implementadas como parte del trabajo futuro en este campo.

Appendix:

Scientific Contributions

The work presented in this doctoral thesis have given rise to several publications in peer-reviewed international scientific journals, contributions in international conferences and a patent. In addition, an international research stay was enjoyed.

- Publications

1. **Paula Navalpotro**, Jesús Palma, Marc Anderson, Rebeca Marcilla*; High Performance Hybrid Supercapacitors by using para-Benzoquinone Ionic Liquid Redox Electrolyte, *Journal of Power Sources*, **2016**, 711-717. (Impact Factor, IF 6.39, Q1)
2. G. Hernández, M. Isik, D. Mantione, A. Pendashteh, **P. Navalpotro**, S. Devaraj, R. Marcilla y D. Mecerreyes*; Redox-active poly(ionic liquid)s as active materials in energy storage applications, *Journal of Materials Chemistry A*, **2017**, 5, 16231-16240 (IF= 8.86, Q1)
3. **Paula Navalpotro**, Jesús Palma, Marc Anderson, Rebeca Marcilla*; A Membrane-Free Redox Flow Battery with Two Immiscible Redox Electrolytes *Angew. Chem.* **2017**, 129, 12634. Highlighted as Frontispiece (IF=11.99, Q1)
4. **Paula Navalpotro**, Rebeca Marcilla, Marc Anderson, Jesús Palma*; Insights into the Energy Storage Mechanism of Hybrid Supercapacitors with Redox Electrolytes by Electrochemical Impedance Spectroscopy. *Electrochim. Acta* **2018**, 263, 110-117 (IF= 4.79, Q1).
5. **Paula Navalpotro**, Jesús Palma, Marc Anderson, Rebeca Marcilla*; Exploring the Versatility of Membrane-Free Battery Concept Using Different Combinations of Immiscible Redox Electrolytes, (under revision in *Journal of Power Sources*, impact factor 6.39, Q1).
6. **Paula Navalpotro**, Catarina M. S. S. Neves, Jesus Palma, Mara G. Freire, João A. P. Coutinho, Rebeca Marcilla*. Pioneering use of Aqueous Biphasic Systems as Membrane-Free Batteries, (submitted to *Advance Science*, IF= 9.034, Q1).
7. **Paula Navalpotro**, Carlos Trujillo, Iciar Montes, Catarina M. S. S. Neves, Jesus Palma, Mara G. Freire, João A. P. Coutinho, Rebeca Marcilla*. High Performance of Membrane-Free Redox Battery based on two Immiscible Aqueous Phases. (submitted to *JACS*, IF =13.8, Q1).

- Patent

Spanish patent application: "Batería Redox Con Electrolitos Inmiscibles" (application num. 201630327. Priority date: March, 21st 2016. Publication date: ES2633601 (A1) September, 22nd 2017. Inventors: **Paula Navalpotro**, Jesús Palma, Marc Anderson, Rebeca Marcilla.

- Contributions to Conferences

- The 2nd *International Forum on Progress and Trends in Battery and Capacitor Technologies- Power Our Future 2014* held in Vitoria, (Spain). Poster contribution: *Electrochemical performance of Ionic Liquid based electrolytes in EDLCs. PYR₁₄TFSI, PYR₁₄FSI and their mixtures; a comparative study.* **Paula Navalpotro**, Jesús Palma, Marc Anderson, Rebeca Marcilla*. April-2014.

- 65th *Annual Meeting of International Society of Electrochemistry* held in Lausanne, (Switzerland). Poster contribution: *Electrochemical Performance of parabenzoquinone- PYR₁₄TFSI based Electrolyte in Redox Supercapacitor.* **Paula Navalpotro**, Jesús Palma, Marc Anderson, Rebeca Marcilla*.September-2014.

- 3rd *Annual workshop "Young Researchers"* held in IMDEA Energy Institute. Oral Contribution: *Electrochemical Performance of paraBenzoquinone- Ionic Liquid based Electrolyte in Supercapacitors.* **Paula Navalpotro**, Jesús Palma, Marc Anderson, Rebeca Marcilla*. December-2014.

- Seminar held in IMDEA Energy Institute. Oral Contribution: *A New Concept of Redox Ionic Liquid Electrolytes in Supercapacitor.* **Paula Navalpotro**, Jesús Palma, Marc Anderson, Rebeca Marcilla*. February-2015.

- *The Energy and Materials Research Conference*, held in Madrid (Spain). Oral Contribution: *Boosting the Performance of Supercapacitors by Using Redox Ionic liquids Electrolytes.* **Paula Navalpotro**, Jesús Palma, Marc Anderson, Rebeca Marcilla*. February-2015.

- *International Symposium on Enhanced Electrochemical Capacitors, ISEE'Cap15* held in Montpellier (France). Poster contribution: *High Performance of Quinoid-Ionic*

Liquid Redox Electrolyte in Supercapacitors. **Paula Navalpotro**, Jesús Palma, Marc Anderson, Rebeca Marcilla*. June-2015.

○ *4th Annual workshop “Young Researchers”* held in IMDEA Energy Institute. Oral Contribution: *Novel Concepts of Redox Flow Batteries (Breaking the Mold).* **Paula Navalpotro**, Jesús Palma, Marc Anderson, Rebeca Marcilla*. December-2015. (Best predoctoral presentation award)

○ *5th Annual workshop “Young Researchers”* held in IMDEA Energy Institute. Oral Contribution: *Membrane-Free Battery: A Paradigm Shift in Energy Storage.* **Paula Navalpotro**, Jesús Palma, Marc Anderson, Rebeca Marcilla* December-2016. (Best predoctoral presentation award)

○ *3rd International Forum on Progress and Trends in Battery and Capacitor Technologies- Power Our Future 2017* held in Vitoria, (Spain). Oral Contribution: *Proof-of-Concept of Membrane Free Flow Battery.* **Paula Navalpotro**, Jesús Palma, Marc Anderson, Rebeca Marcilla*. July-2017.

○ *6th Annual workshop “Young Researchers”* held in IMDEA Energy Institute. Oral Contribution: *Pioneering use of Aqueous Biphasic Systems in Electrochemical Energy Storage.* **Paula Navalpotro**, Catarina M. S. S. Neves, Jesus Palma, Mara G. Freire, João A. P. Coutinho, Rebeca Marcilla*. December-2017. (Best predoctoral presentation award).

- International Secondment

Research stay in the group of Processes and Products of Applied Thermodynamics (PATH) of the University of Aveiro and CICECO (Center for Research in Ceramic and Composite Materials) (Portugal) under the supervision of Prof. Joao A. P. Coutinho (March-June 2017).

The purpose of the stay was the evaluation of Aqueous Biphasic Systems as immiscible electrolytes for their application in a new concept of Membrane-Free Battery. Specifically, the effect of the nature of the components and the pH on the partition coefficient of several redox molecules was studied. This work gave rise to a scientific contribution entitled *Pioneering use of Aqueous Biphasic Systems as Membrane-Free Batteries* and the main results are gathered in the first part of Chapter 5 of this thesis.

Appendix B

In this Appendix the List of Figures, List of Tables and Acronyms used in this thesis are gathered.

List of Figures

CHAPTER 1: INTRODUCTION

Figure 1.1. Outlook of the power generation by source (left) and the total installed capacity (right) in 2040 for a Sustainable Development Scenario.....	2
Figure 1.2. Applications of energy storage systems.....	4
Figure 1.3. Classification of the energy storage systems. CAES in Compressed Air Energy Storage; LAES is Liquid Air Energy Storage; SMES is Superconducting Magnetic Electrical Systems; SNG is Synthetic Natural Gas.....	5
Figure 1.4. Relationship between the different technologies based on their energy capacity and time response. (PtG- H ₂ : hydrogen injected in the Natural gas network; PtG-SNG: hydrogen converted into methanol).....	8
Figure 1.5. Current global installed grid-connected electricity storage capacity in MW.....	9
Figure 1.6. Scheme of a supercapacitor.....	11
Figure 1.7. Classification of supercapacitors.....	13
Figure 1.8. Types of supercapacitors classified by their electrochemical response and storage mechanism.....	14
Figure 1.9. Scheme of EDLC and its behavior during charge and discharge processes.....	15
Figure 1.10. Stern model of the electrical double-layer formed at a positively charged electrode in an aqueous electrolyte. The electrical potential, ϕ , decreases from the electrode to the bulk electrolyte. The Stern plane marks the distance of closest approach of the ions to the charged surface. The diffuse layer starts in the range of 10 – 100 nm from the electrode surface.....	16
Figure 1.11. Schematic difference between ionic liquids and conventional electrolytes based on dissolved salts.....	20
Figure 1.12. Scheme of an EDLC and a pseudocapacitor.....	20
Figure 1.13. Scheme of the storage mechanism in a hybrid device.....	22
Figure 1.14. Illustration of the charge storage mechanisms in porous carbon based supercapacitor with a redox electrolyte.....	24
Figure 1.15. Illustration of different types of batteries.....	25
Figure 1.16. Illustration of an All-Vanadium Redox Flow Battery System.....	27
Figure 1.17. Components of a filter-press redox flow cell.....	28
Figure 1.18. Distribution of cost for all-V for a 1MW system (4MWh-450\$/kWh ⁻¹).....	30
Figure 1.19. Requirements and considerations for the development of flow batteries.....	32

Figure 1.20. Schematic Illustration of different design of redox flow batteries. a) semisolid Redox Flow Battery; b) Hybrid Redox Flow Battery; c) solar-Rechargeable Flow battery; d) metal-air Flow Battery; e) Detail of the reactor of Membrane-less Flow Battery design; f) Metal based complexes used in Non-aqueous Flow Battery.....	33
Figure 1.21. Schematic representation of redox organic molecules and their applications in energy storage.....	37
Figure 1.22. Molecular structure of different quinones.....	38
Figure 1.23. Mechanistic pathways of quinones.....	39
Figure 1.24. Schematic representation of the strategy for improving SC performance by adding organic redox molecules as active electrode material.....	40
Figure 1.25. Organic materials used in SC. a) 9,10-anthaquinone; b) catechol; c) 1,4-naphthoquinone; d) 9,10-phenanthraquinone; e) 4,5-pyrenedione; f) tetrachloro-1,4-benzoquinone; g) β -ketoenamine and 2,6-diamino anthraquinone linked COFs.....	41
Figure 1.26. Schematic representation of the use of redox electrolytes in SC.....	41
Figure 1.27. Charge-Discharge voltage profile of a hybrid SC using HQ-redox electrolyte and the potential profile of each electrode (in blue and grey).....	42
Figure 1.28. Schematic summary about the organic redox molecules used in Aqueous RFB and their characteristics.....	44
Figure 1.29. Schematic summary about the organic redox molecules used in Non-Aqueous RFB and their characteristics.....	46
 CHAPTER 3: ELECTROCHEMICAL STUDY OF HYBRID SUPERCAPACITORS BY USING PARA-BENZOQUINONE IONIC LIQUID REDOX ELECTROLYTE	
Figure 3.1. Mechanistic pathways of quinones. Blue arrow represents the reaction mechanism in protic media. Orange arrow indicates reaction mechanism in aprotic media.....	73
Figure 3.2. Cyclic voltammetry of a 20 mM solution of pBQ in PYR ₁₄ TFSI in 3 electrode cell at 10 mV·s ⁻¹ in glassy carbon electrode 3 mm diameter.....	74
Figure 3.3. Anodic and cathodic peak current dependence on the square root of scan rate. Inset: cyclic voltammetry obtained in a three electrode cell of 20 mM solution of pBQ in PYR ₁₄ TFSI at different scan rate.....	75
Figure 3.4. Real energy density (E_{real}) versus different concentration of pBQ dissolved into the IL. Obtained from galvanostatic Charge-Discharge experiments over a range in voltage from 0 V to 3 V at 10 mA·cm ⁻² . T ^a =60 °C. Electrode material: Vulcan carbon.....	76
Figure 3.5. Cyclic voltammetry of hybrid SCs at a scan rate of 5 mV·s ⁻¹ for (a) Pica activated carbon and (b) Vulcan carbon. Electrolytes: Redox electrolyte (0.4 M pBQ in PYR ₁₄ TFSI) and pure PYR ₁₄ TFSI. T=60°C.....	77
Figure 3.6. Specific capacitance (C_s) versus scan rate for SCs with different electrodes (Pica and Vulcan) and electrolytes (0.4 M pBQ in PYR ₁₄ TFSI and pure PYR ₁₄ TFSI). T=60°C.....	79

Figure 3.7. Voltage profiles plot up to 3 V at 60 °C and current density 10 mA·cm ⁻² : (a) Pica carbon (b) Vulcan carbon. Electrolytes: Pure PYR ₁₄ TFSI and 0.4 M pBQ in PYR ₁₄ TFSI	80
Figure 3.8. Real energy density (E_{real}) versus operating voltage of the SCs obtained from CD experiments: current density 5 mA·cm ⁻² . $T^a=60$ °C.	81
Figure 3.9. Real energy density (E_{real}) versus current density for different SCs. Obtained from CD experiments over a range in voltage from 0 V to 3 V. $T^a=60$ °C	83
Figure 3.10. Ragone plot of the SCs obtained from CD experiments over a voltage range from 0 to 3 V. $T^a=60$ °C.	84
Figure 3.11. Cycling stability of Vulcan SCs obtained from CD experiments from 0 to 3 V at 10 mA·cm ⁻² . $T^a=60$ °C.	85
Figure 3.12. Nyquist plot at different bias voltage for the SCs a) Pure IL. b) Pure IL-enlarged. Resistance contributions are labeled. c) Redox electrolyte. d) Redox electrolyte-enlarged. e) Bode plot at different bias voltage of Pure IL Electrolyte-SCs. f) Bode plot at different bias voltage of Redox Electrolyte – SCs	87
Figure 3.13. Resistance contributions and its dependence with bias voltage. a) Pure IL Electrolyte b) Redox Electrolyte.	89
Figure 3.14. Real part of the capacitance versus frequency plots recorded at various potential comprised between 0 V and 1.5 V. a) Pure IL electrolyte. b) Redox electrolyte. c) Evolution of the capacitance vs. potential extract from the low frequency values (0.01 Hz) of the impedance data for pure IL and redox electrolyte systems.	91
Figure 3.15. Imaginary capacitance versus frequency plots recorded at various bias voltages between 0 and 1.5 V. a) Pure IL electrolyte. b) Redox electrolyte. c) Evolution of the relaxation time constant vs bias voltage	93
Figure 3.16. Equivalent electrical circuit proposed for the devices under study.	95
Figure 3.17. Bode Plot model fitting validation at 0 V bias voltage. Fitting (Continuous line); Experimental data (dots). a) Pure IL SCs. b) Redox Electrolyte	95
Figure 3.18. Dependence on bias voltage of equivalent electrical circuit elements: a) resistance R1. b) capacitor C1. c) constant phase element 1/Q2. d) Warburg impedance W3. e) capacitor C4. f) resistance R5.	96
Figure 3.19. Picture of the electrodes after the preparation process.	102
Figure 3.20. MBraun glove box	103
Figure 3.21. Two electrodes configuration in a Swagelok® cell	103
Figure 3.22. Scheme of a cyclic voltammetry for: (right) Capacitive material; (left) Faradaic material.	104
Figure 3.23. Schematic illustration of a galvanostatic charge discharge curve of a supercapacitor	106
Figure 3.24. Schematic representation of Nyquist diagram (right) and Bode plot (left) for a supercapacitor.	107

CHAPTER 4: MEMBRANE-FREE REDOX FLOW BATTERIES BY USING TWO IMMISCIBLE REDOX ELECTROLYTES

Figure 4.1. Schematic illustration of different approaches to avoid the use of ion-exchange membrane. a) Hybrid RFB. b) Semi-solid RFB. c) Polymer RFB. d) Symmetric RFB. e) Microfluidic RFB.	119
Figure 4.2. a) Illustration of a “flow-capacitor”. b) Description of design of a hybrid SC with two redox molecules.	120
Figure 4.3. a) Schematic representation of the Membrane-Free Battery concept based on immiscible organic redox electrolytes. b) Illustration of a conventional Redox Flow Battery based on vanadium active species and having an ion-exchange membrane.	121
Figure 4.4. Proof-of Concept of Membrane-Free Battery	122
Figure 4.5. Electrochemical characterization of immiscible redox electrolytes. a) Cyclic voltammetry experiments of 20 mM pBQ in PYR ₁₄ TFSI (green) and 20 mM H ₂ Q in 0.1 M HCl (blue) performed in 3-electrode electrochemical cells (scan rate= 10 mV·s ⁻¹). b) and c) Redox-active organic species in both electrolytes and their corresponding redox mechanisms depending on the nature of the electrolyte.	123
Figure 4.6. Electrochemical investigation of redox electrolytes using a Rotating Disk Electrode (RDE). a) RDE experiments (LSV at 10 mV·s ⁻¹) of 5 mM pBQ in PYR ₁₄ TFSI. b) Levich plot of 5 mM pBQ in PYR ₁₄ TFSI and the line fit (red line) with its mathematical expression. c) RDE experiments (LSV at 10 mV·s ⁻¹) of 5 mM H ₂ Q in 0.1 M HCl. d) Levich plot of 5 mM H ₂ Q in 0.1 M HCl.	126
Figure 4.7. Experimental set-up of the Membrane-Free Battery.	126
Figure 4.8. Polarization curves of the Membrane-Free Battery at four different states of charge (SOC). All data were collected at room temperature using a 20 mM pBQ in PYR ₁₄ TFSI solution as the anolyte and 20 mM H ₂ Q in 0.1 M HCl as the catholyte.	127
Figure 4.9. Electrochemical Characterization of Membrane-Free Battery at 35 % SOC. Composition of the electrolytes: anolyte; 20 mM pBQ in PYR ₁₄ TFSI and catholyte; 20 mM H ₂ Q in 0.1 M HCl. a) Charge-discharge experiments at ±0.16 mA·cm ⁻² with a short OCV period. b) Polarization test. c) Discharge profiles of Membrane-Free Battery at different current densities.	128
Figure 4.10. Membrane-Free Battery performance at 35 % SOC. Composition of the electrolytes: 20 mM pBQ in PYR ₁₄ TFSI and 20 mM H ₂ Q in 0.1 M HCl. a) Cyclability test at ±0.16 mA·cm ⁻² using voltage cut-offs of 0.3 V in discharge and 2 V in charge (profound discharge). Discharge curves of 1 st , 10 th , 20 th and 30 th cycles with their individual profiles: Voltage of the full battery (continuous line), catholyte and anolyte individual voltages (dashed lines) and voltage drop at the interface (dotted line). b) Capacity retention vs. cycle number.	130
Figure 4.11. Membrane-Free Battery performance at 35% SOC. Composition of the electrolytes: 0.1 M pBQ in PYR ₁₄ TFSI and 0.1 M H ₂ Q in 0.1 M HCl. a) Cell potential and power density versus current density. b) A galvanostatic charge-discharge cycle with the individual potential profiles at ±0.16 mA·cm ⁻² . c) Discharge profiles of Membrane-Free Battery at different current densities.	131

Figure 4.12. Electrochemical Characterization of Membrane-Free Battery at 35 % SOC. Composition of the electrolytes: anolyte; 0.1 M pBQ in PYR ₁₄ TFSI and catholyte; 0.1 M H ₂ Q in 0.1 M HCl. Cyclability study at $\pm 0.66 \text{ mA}\cdot\text{cm}^{-2}$. Coulombic efficiency, energy efficiency and capacity retention versus cycles. Inset: Voltage profile of the battery for the first 5 cycles.....	132
Figure 4.13. Electrochemical investigation of the two immiscible electrolytes before and after cycling. Electrolyte active species concentration: 20 mM. a) CVs of catholyte. b) CVs of anolyte. c) Reaction mechanism and pathways for catholyte: Dissolved species (continuous line) and species coming from anolyte (dotted line). d) Reaction mechanism and pathways for anolyte: Dissolved species (continuous line) and species coming from catholyte (dotted line).....	133
Figure 4.14. Schematic representation of the versatility of Membrane-Free RFB concept.....	135
Figure 4.15. a) Schematic illustration of Membrane-Free Battery based on immiscible electrolytes. b), c), d) CVs of pairs of immiscible anolyte and catholyte (pBQ in green, H ₂ Q in blue, 2,3-DMAQ in pink, OilBlue N in purple). The composition of electrolytes is 20 mM of redox active specie. Scan rate: $10 \text{ mV}\cdot\text{s}^{-1}$	138
Figure 4.16. a) Scheme-of-squares for redox reaction of quinones in aprotic electrolyte. b) Reaction mechanism for pBQ (Proof-of-concept). c) Reaction mechanism for 2,3-DMAQ (Battery A).....	139
Figure 4.17. a) CVs of pairs of immiscible anolyte and catholyte (pBQ in green, TEMPO in red). Active species concentration: 20mM pBQ in the anolyte and 40mM TEMPO in the catholyte. Scan rate: $10 \text{ mV}\cdot\text{s}^{-1}$. b) Scheme of Redox reaction mechanism for TEMPO in 0.1 M NaCl.....	139
Figure 4.18. a), b) CVs of pairs of immiscible anolyte and catholyte (pBQ in green, H ₂ Q in blue). The composition of electrolytes is 20 mM of redox active specie. Scan rate: $10 \text{ mV}\cdot\text{s}^{-1}$	140
Figure 4.19. Comproportionation process mechanism suggested by some authors for pBQ ^{56,67}	140
Figure 4.20. CVs of pairs of immiscible anolyte and catholyte (pBQ in green, OH-TEMPO in orange). The composition of electrolytes is 20 mM of redox active specie. Scan rate: $10 \text{ mV}\cdot\text{s}^{-1}$	141
Figure 4.21. a), b), c), d) CVs of pairs of immiscible anolyte and catholyte (pBQ in green, 2,3-DMAQ in pink, OilBlue N in purple, OH-TEMPO in orange). The composition of electrolytes is 20 mM of redox active specie. Scan rate: $10 \text{ mV}\cdot\text{s}^{-1}$	142
Figure 4.22. Rotating Disk Electrode experiments. Electrolytes concentration: 5mM. Figures on the Left: LSV at $10 \text{ mV}\cdot\text{s}^{-1}$; Right: Levich plot (the mass-transport limited current vs. the square root of the rotation rate and the line fit (red line) with its mathematical expression. a and b) TEMPO in 0.1M NaCl. C and d) 2,3-Dimethylantraquinone in PYR ₁₄ TFSI. e and f) OilBlue N in PYR ₁₄ TFSI. g and h) pBQ in PC (0.1 M TBAPF ₆). i and j) OH-TEMPO (0.5 M NaCl). K and l) pBQ in PC + PYR ₁₄ TFSI (75:25 %wt).....	143

Figure 4.23. Performance of Battery A (SOC 35 %). Active species concentration: 20 mM in catholyte and anolyte. a) Galvanostatic charge-discharge cycle at 0.16 mA·cm ⁻² . b) Discharge voltage profiles of the battery at different current densities. c) Discharge individual voltage profiles of each electrolyte and the interface at different current densities. d) Polarization test during discharge. e) Discharge polarization test of battery and each individual profile (catholyte, anolyte and interface). f) Polarization test during charge. g) Individual voltages profiles of the cell, individual electrolytes and the interface during polarization test in charge.	147
Figure 4.24. Performance of the Battery B (SOC 35 %). Active species concentration: 20 mM in catholyte and anolyte. a) Discharge curves at different current densities. b) Discharge polarization test. c) Discharge curves of the individual potential profiles of each electrolyte and interface at different current densities. d) Discharge polarization test of battery and each individual profile (catholyte, anolyte and interface). e) Individual voltages profiles of the cell, individual electrolytes and the interface during polarization test in charge.	148
Figure 4.25. a) Comparison of CV for the anolytes and the catholyte used in the Batteries A, B and Proof-of-concept (H2Q in 0.1 M HCl in blue, 2,3-DMAQ in PYR14TFSI in grey, OilBlue N in PYR14TFSI in purple and pBQ in PYR14TFSI in green). b) Comparison between potential-capacity discharge profile at 0.08 mA·cm ⁻² (35 %SOC) for Batteries A, B and Proof-of-concept.	149
Figure 4.26. Performance of the Battery C (SOC 35%). Active species concentration: 40 mM in catholyte and 20 mM in anolyte. a) Galvanostatic charge-discharge cycle at 0.08 mA·cm ⁻² . b) Discharge voltage profiles of the battery at different current densities. c) Discharge individual voltage profiles of each electrolyte and the interface at different current densities. d) Polarization test during discharge. e) Discharge polarization test of battery and each individual phase (catholyte, anolyte and interface) at 35 % SOC. f) CV of the anolyte at positive potential range before operating (light green) and after battery operation (dark green), for comparison CV of TEMPO in PYR ₁₄ TFSI at 20 mM concentration was also included (orange).	151
Figure 4.27. Performance of the Battery E (SOC 25 %). Active species concentration: 20 mM in catholyte and anolyte. a) Galvanostatic charge-discharge cycle at 0.16 mA·cm ⁻² . b) Discharge voltage profiles of the battery at different current densities. c) Discharge individual voltage profiles of each electrolyte and the interface at different current densities. d) Polarization test during discharge. e) Discharge polarization test of battery and each individual profile (catholyte, anolyte and interface). f) Cycling stability (5 %SOC) at 0.16 mA·cm ⁻²	153
Figure 4.28. Performance Battery F (SOC 15%). Active species concentration: 0.1 M in catholyte and anolyte. a) Galvanostatic charge-discharge cycle at 1 mA·cm ⁻² for charging and 2 mA·cm ⁻² for discharging. b) Polarization test during discharge. c) Discharge voltage profiles of the battery at different current densities. d) Cycling stability (5 %SOC) at 1 mA·cm ⁻² for charging and 2 mA·cm ⁻² for discharging. e) Cycling performance (5%SOC) Discharge battery voltage in cycle 1 and cycle 300 versus % capacity utilization.	155
Figure 4.29. Rotating disk electrode setup and schematic representation of the working.	160

Figure 4.30. Schematic representation of the linear sweep voltammetry experiment result.....	161
Figure 4.31. Carbon Felt material used as electrodes.....	162
Figure 4.32. Schematic illustration of an assembled Membrane-Free Battery.....	163
CHAPTER 5: MEMBRANE-FREE REDOX FLOW BATTERIES BASED ON AQUEOUS BIPHASIC SYSTEMS	
Figure 5.1. Illustrated representation of a phase diagram.....	173
Figure 5.2. Phase diagrams according to the fitting of equation (5.1) to the experimental data obtained at 25°C and atmospheric pressure: a) in molality units; b) percentage by weight. Phase diagrams for [C ₄ mim][CF ₃ SO ₃], and [C ₄ mim][N(CN) ₂] were taken from literature.....	176
Figure 5.3. Partition coefficients (K) of the target molecules in ABS based on different ionic liquids or PEG ₁₀₀₀ and the partition coefficients in octanol water (K _{ow}).....	178
Figure 5.4. Selectivity of the target molecules with respect to MV.....	180
Figure 5.5. CV of each phase for the system based on [P ₄₄₄₁₄]Cl + Na ₂ SO ₄ with different active species at 20 mM concentration in the initial mixture; a) MV+AQ2S, b) MV+QUI, c) MV+H ₂ Q and d) MV+TEMPO.....	181
Figure 5.6. Redox reactions of the active species: a) TEMPO. b) Methyl viologen. Cyclic voltammetry of the phases separately of the systems based on IL+ Na ₂ SO ₄ + 20mM TEMPO-20mM MV. c) [P ₄₄₄₄]Br. d) [N ₄₄₄₄]Br. e) [P ₄₄₄₄][CF ₃ CO ₂]. f) [N ₄₄₄₄][CF ₃ CO ₂]. g) [C ₄ mim][CF ₃ SO ₃]. h) [P ₄₄₄₁₄]Cl. i) PEG ₁₀₀₀ . Scan rate 10 mV·s ⁻¹ . MV (in green) TEMPO (in blue).....	185
Figure 5.7. Binodal curve of the phase diagram of the ABS composed of PEG ₁₀₀₀ + Na ₂ SO ₄ + H ₂ O (blue dots + blue line), initial mixture composition (red dot) and composition of each phase (black dots and black line representing the respective tie-line, TLL =33.85; α=0.769).....	187
Figure 5.8. Partition coefficients of redox organic molecules between the PEG and salt-rich phases in the studied ABS. Chemical structures and abbreviations for the organic redox molecules are also given.....	188
Figure 5.9. CV of the immiscible phases of PEG-based ABS containing TEMPO (blue) and MV (light and dark green depending on the voltage limits) at 20 mM concentration. Reaction mechanism of MV and TEMPO.....	189
Figure 5.10. Rotating Disk Electrode Experiments. a), b) Linear Sweep Voltammetry (LSV) and Levich plot at 10 mV·s ⁻¹ of 5 mM MV in bottom phase. c), d) LSV and Levich plot at 10 mV·s ⁻¹ of 5 mM TEMPO in top phase.....	190
Figure 5.11. a) Schematic illustration of the Total Aqueous Membrane-Free Battery, b) Galvanostatic charge-discharge of the battery (20 %SOC) and individual potential profiles of each electrolyte and the interface; charge at C/4 and discharge at C/5.....	191
Figure 5.12. a) Polarization curve of the battery (20 %SOC) during discharge. b) Polarization curves including catholyte, anolyte and interface potential profiles during charge and c) discharge polarization.....	193

Figure 5.13. a) Discharge battery voltage profile at different current densities (20 %SOC). b) Capacity test at different current densities (20 %SOC).....	194
Figure 5.14. Schematic illustration of the self-discharge process.....	195
Figure 5.15. Self-discharge experiment (starting at 20 %SOC) consisting of monitoring the evolution of the OCV of the battery over time.....	196
Figure 5.16. Discharge battery voltage (20% SOC): a) Consecutive discharge experiments at C and C/2; b) Consecutive discharge experiments at 2C and C.....	196
Figure 5.17. Cyclability test of the battery (5 %SOC), charging at C/2 and discharging at C. a) Efficiency and capacity retention vs cycle number. b) Individual potential profiles during cycling.....	197
Figure 5.18. Schematic representation of partition coefficient determination method.....	204

List of Tables

CHAPTER 1: INTRODUCTION

Table 1.1. Comparison between batteries and supercapacitors.....	10
Table 1.2. General comparison between static and redox flow batteries.....	26
Table 1.3. Chemistry of the different developed RFB systems.....	29

CHAPTER 3: ELECTROCHEMICAL STUDY OF HYBRID SUPERCAPACITORS BY USING PARA-BENZOQUINONE IONIC LIQUID REDOX ELECTROLYTE

Table 3.1. Summary of reported redox-electrolytes based on organic molecules for supercapacitors.....	70
Table 3.2. Textural properties of Pica and Vulcan carbons.....	102

CHAPTER 4: MEMBRANE-FREE REDOX FLOW BATTERIES BY USING TWO IMMISCIBLE REDOX ELECTROLYTES

Table 4.1. Comparison of technical parameters and key factors of reported aqueous and nonaqueous ORFBs.....	116
Table 4.2. Diffusion Coefficients, kinetic rate constants, conductivity and viscosity of the anolyte and catholyte.....	125
Table 4.3. Different combination of immiscible anolyte and catholyte and theoretical OCV of the corresponding Membrane-Free RFBs.....	136
Table 4.4. Diffusion Coefficients and kinetic rate constants of the different electrolytes.....	145

CHAPTER 5: MEMBRANE-FREE REDOX FLOW BATTERIES BASED ON AQUEOUS BIPHASIC SYSTEMS

Table 5.1. Chemical structure of ionic liquids used to form ABS and their hydrogen bond basicity ¹⁹	174
Table 5.2. Parameters A, B and C obtained from Merchuk fitting ²⁰ (equation 5.1) for each ABS tested.....	176
Table 5.3. Partition coefficients (K) calculated as the ratio of concentrations of each compound in the two immiscible phases of all the studied ABS and octanol-water system.....	179
Table 5.4. Selectivity (S) calculated as the ratio of partition coefficient of the target molecule and MV ($K_{\text{molecule}}/K_{\text{MV}}$) in each ABS.....	180
Table 5.5. Potential redox reaction of majority species in each phase of a system based on [P ₄₄₄₁₄]Cl.....	182
Table 5.6. pH values of all the studied ABS.....	184
Table 5.7. Physicochemical properties of each phase of PEG-based ABS containing 0.1 M of TEMPO and MV in the initial mixture. Calculated Diffusion Coefficient (D) and Rate Constant (k^0) for MV and TEMPO in bottom and top phases, respectively.....	189

Acronyms

CAES	Compressed Air Energy Storage
LAES	Liquid Air Energy Storage
SMES	Superconducting Magnetic Electrical Systems
SNG	Synthetic Natural Gas
PHS	Pumped-Hydropower Storage
SC	Supercapacitor
ESW	Electrochemical Stability Window
EDLC	Electrical Double Layer Capacitor
C	Capacitance
ϵ_r	Permittivity
Q	Capacity
V	Voltage
C_H	Helmholtz Capacitance
C_{diff}	Diffusive-layer Capacitance
CDC	Carbide Derived Carbons
SWCNTs	Single Walled Carbon Nanotubes
MWCNTs	Multi-Walled Carbon Nanotubes
ESR	Equivalent Series Resistance
I	Current
σ	Ionic Conductivity
ILs	Ionic Liquids
RFB	Redox Flow Battery
F	Faraday's Constant
E^0	Standard Potential
E_{cell}	Cell Voltage
SHE	Standard Hydrogen Electrode
NHE	Standard Hydrogen Electrode
OCV	Open Circuit Voltage

EDG	Electron Donating Group
EWG	Electron Withdrawing groups
COFs	Covalent Organic Frameworks
E	Energy
E_{\max}	Maximum Energy
P	Power
P_{\max}	Maximum Power
CD	Charge-Discharge
CV	Cyclic Voltammetry
EIS	Electrochemical Impedance Spectroscopy
E_{real}	Real Energy
P_{real}	Real Power
Cs	Specific Capacitance
s	scan rate
T	Temperature
Z	Impedance
Z'	Real part of Impedance
Z''	Imaginary part of Impedance
R_s	Electric Resistance
R_c	Resistance at the electrode/electrolyte interface
R_d	Diffusion Resistance
f	Linear Frequency
ω	Angular Frequency
τ_R	Relaxation Time/Time Constant
C'	Real part of Capacitance
C''	Imaginary part of Capacitance
f_0	Characteristic Frequency
C_{am}	Specific Capacitance of the electrodes
C_{sc}	Capacitance of Supercapacitor
Q_0	Discharge capacity in the first cycle in the cycling test

Q_t	Theoretical Capacity
CE	Coulombic Efficiency
VE	Voltage Efficiency
EE	Energy Efficiency
RDE	Rotating Disk Electrode
LSV	Linear Sweep Voltammetry
D	Diffusion Coefficient
K^0	Rate Constant
SOC	State of Charge
e^-	Number of Electron Transferred
θ	Kinematic Viscosity
i_L	Limiting Current
i_k	Kinetic Current
ABS	Aqueous Biphasic System
K	Partition Coefficient
S	Selectivity
E_{pa}	Anodic Peak Potential
E_{pc}	Cathodic Peak Potential
E_p	Peak Potential
TL	Tie Line
TLL	Tie Line Length